

UNITED STATES AIR FORCE
SUMMER RESEARCH PROGRAM -- 1998
GRADUATE STUDENT RESEARCH PROGRAM FINAL REPORTS

VOLUME 10

WRIGHT LABORATORY

RESEARCH & DEVELOPMENT LABORATORIES

5800 Uplander Way
Culver City, CA 90230-6608

Program Director, RDL
Gary Moore

Program Manager, AFOSR
Colonel Jan Cervený

Program Manager, RDL
Scott Licoscó

Program Administrator, RDL
Johnetta Thompson

Program Administrator, RDL
Rebecca Kelly-Clemmons

Submitted to:

AIR FORCE OFFICE OF SCIENTIFIC RESEARCH

Bolling Air Force Base

Washington, D.C.

December 1998

20010319 020

AQM01-06-1212

PREFACE

Reports in this volume are numbered consecutively beginning with number 1. Each report is paginated with the report number followed by consecutive page numbers, e.g., 1-1, 1-2, 1-3; 2-1, 2-2, 2-3.

This document is one of a set of 15 volumes describing the 1998 AFOSR Summer Research Program. The following volumes comprise the set:

<u>VOLUME</u>	<u>TITLE</u>
1	Program Management Report
	<i>Summer Faculty Research Program (SFRP) Reports</i>
2	Armstrong Laboratory
3	Phillips Laboratory
4	Rome Laboratory
5A & 5B	Wright Laboratory
6	Arnold Engineering Development Center, Air Logistics Centers, United States Air Force Academy and Wilford Hall Medical Center
	<i>Graduate Student Research Program (GSRP) Reports</i>
7	Armstrong Laboratory
8	Phillips Laboratory
9	Rome Laboratory
10	Wright Laboratory
11	Arnold Engineering Development Center, and Wilford Hall Medical Center
	<i>High School Apprenticeship Program (HSAP) Reports</i>
12	Armstrong Laboratory
13	Phillips Laboratory
14	Rome Laboratory
15A, 15B & 15C	Wright Laboratory

REPORT DOCUMENTATION P

AFRL-SR-BL-TR-00-

Form Approved
AB No. 0704-0188

Public reporting burden for this collection of information is estimated to average 1 hour per response, including the collection of information. Send comments regarding this burden estimate or any other aspect of this collection of information, including suggestions for reducing the burden, to Washington Headquarters Services, Directorate for Information Operations and Reports, 1215 Jefferson Davis Highway, Suite 1204, Arlington, VA 22202-4302, and to the Office of Management and Budget, Paperwork Project, Washington, DC 20503.

the data needed, and completing and reviewing
Headquarters Services, Directorate for Information
Operations and Reports, 1215 Jefferson Davis Highway, Suite 1204, Arlington, VA 22202-4302, and to the Office of Management and Budget, Paperwork Project, Washington, DC 20503.

0786

1. AGENCY USE ONLY (Leave blank)		2. REPORT DATE December, 1998		3. REPORT TYPE AND DATES COVERED	
4. TITLE AND SUBTITLE 1998 Summer Research Program (SRP), Graduate Student Research Program (GSRP), Final Reports, Volume 10, Wright Laboratory				5. FUNDING NUMBERS F49620-93-C-0063	
6. AUTHOR(S) Gary Moore					
7. PERFORMING ORGANIZATION NAME(S) AND ADDRESS(ES) Research & Development Laboratories (RDL) 5800 Uplander Way Culver City, CA 90230-6608				8. PERFORMING ORGANIZATION REPORT NUMBER	
9. SPONSORING/MONITORING AGENCY NAME(S) AND ADDRESS(ES) Air Force Office of Scientific Research (AFOSR) 801 N. Randolph St. Arlington, VA 22203-1977				10. SPONSORING/MONITORING AGENCY REPORT NUMBER	
11. SUPPLEMENTARY NOTES					
12a. DISTRIBUTION AVAILABILITY STATEMENT Approved for Public Release				12b. DISTRIBUTION CODE	
13. ABSTRACT (Maximum 200 words) The United States Air Force Summer Research Program (USAF-SRP) is designed to introduce university, college, and technical institute faculty members, graduate students, and high school students to Air Force research. This is accomplished by the faculty members (Summer Faculty Research Program, (SFRP)), graduate students (Graduate Student Research Program (GSRP)), and high school students (High School Apprenticeship Program (HSAP)) being selected on a nationally advertised competitive basis during the summer intersession period to perform research at Air Force Research Laboratory (AFRL) Technical Directorates, Air Force Air Logistics Centers (ALC), and other AF Laboratories. This volume consists of a program overview, program management statistics, and the final technical reports from the GSRP participants at the Wright Laboratory.					
14. SUBJECT TERMS Air Force Research, Air Force, Engineering, Laboratories, Reports, Summer, Universities, Faculty, Graduate Student, High School Student				15. NUMBER OF PAGES	
				16. PRICE CODE	
17. SECURITY CLASSIFICATION OF REPORT Unclassified	18. SECURITY CLASSIFICATION OF THIS PAGE Unclassified	19. SECURITY CLASSIFICATION OF ABSTRACT Unclassified	20. LIMITATION OF ABSTRACT UL		

GENERAL INSTRUCTIONS FOR COMPLETING SF 298

The Report Documentation Page (RDP) is used in announcing and cataloging reports. -It is important that this information be consistent with the rest of the report, particularly the cover and title page. Instructions for filling in each block of the form follow. It is important to ***stay within the lines*** to meet ***optical scanning requirements***.

Block 1. Agency Use Only (*Leave blank*).

Block 2. Report Date. Full publication date including day, month, and year, if available
(e.g. 1 Jan 88). Must cite at least the year.

Block 3. Type of Report and Dates Covered. State whether report is interim, final, etc. If applicable, enter inclusive report dates (e.g. 10 Jun 87 - 30 Jun 88).

Block 4. Title and Subtitle. A title is taken from the part of the report that provides the most meaningful and complete information. When a report is prepared in more than one volume, repeat the primary title, add volume number, and include subtitle for the specific volume. On classified documents enter the title classification in parentheses.

Block 5. Funding Numbers. To include contract and grant numbers; may include program element number(s), project number(s), task number(s), and work unit number(s). Use the following labels:

C - Contract
G - Grant
PE - Program
Element

PR - Project
TA - Task
WU - Work Unit
Accession No.

Block 6. Author(s). Name(s) of person(s) responsible for writing the report, performing the research, or credited with the content of the report. If editor or compiler, this should follow the name(s).

Block 7. Performing Organization Name(s) and Address(es).
Self-explanatory.

Block 8. Performing Organization Report Number. Enter the unique alphanumeric report number(s) assigned by the organization performing the report.

Block 9. Sponsoring/Monitoring Agency Name(s) and Address(es).
Self-explanatory.

Block 10. Sponsoring/Monitoring Agency Report Number. (*If known*)

Block 11. Supplementary Notes. Enter information not included elsewhere such as: Prepared in cooperation with....; Trans. of....; To be published in.... When a report is revised, include a statement whether the new report supersedes or supplements the older report.

Block 12a. Distribution/Availability Statement. Denotes public availability or limitations. Cite any availability to the public. Enter additional limitations or special markings in all capitals (e.g. NOFORN, REL, ITAR).

DOD - See DoDD 5230.24, "Distribution Statements on Technical Documents."

DOE - See authorities.

NASA - See Handbook NHB 2200.2.

NTIS - Leave blank.

Block 12b. Distribution Code.

DOD - Leave blank.

DOE - Enter DOE distribution categories from the Standard Distribution for Unclassified Scientific and Technical Reports.

Leave blank.

NASA - Leave blank.

NTIS -

Block 13. Abstract. Include a brief (*Maximum 200 words*) factual summary of the most significant information contained in the report.

Block 14. Subject Terms. Keywords or phrases identifying major subjects in the report.

Block 15. Number of Pages. Enter the total number of pages.

Block 16. Price Code. Enter appropriate price code (*NTIS only*).

Blocks 17. - 19. Security Classifications. Self-explanatory. Enter U.S. Security Classification in accordance with U.S. Security Regulations (i.e., UNCLASSIFIED). If form contains classified information, stamp classification on the top and bottom of the page.

Block 20. Limitation of Abstract. This block must be completed to assign a limitation to the abstract. Enter either UL (unlimited) or SAR (same as report). An entry in this block is necessary if the abstract is to be limited. If blank, the abstract is assumed to be unlimited.

1. INTRODUCTION

The Summer Research Program (SRP), sponsored by the Air Force Office of Scientific Research (AFOSR), offers paid opportunities for university faculty, graduate students, and high school students to conduct research in U.S. Air Force research laboratories nationwide during the summer.

Introduced by AFOSR in 1978, this innovative program is based on the concept of teaming academic researchers with Air Force scientists in the same disciplines using laboratory facilities and equipment not often available at associates' institutions.

The Summer Faculty Research Program (SFRP) is open annually to approximately 150 faculty members with at least two years of teaching and/or research experience in accredited U.S. colleges, universities, or technical institutions. SFRP associates must be either U.S. citizens or permanent residents.

The Graduate Student Research Program (GSRP) is open annually to approximately 100 graduate students holding a bachelor's or a master's degree; GSRP associates must be U.S. citizens enrolled full time at an accredited institution.

The High School Apprentice Program (HSAP) annually selects about 125 high school students located within a twenty mile commuting distance of participating Air Force laboratories.

AFOSR also offers its research associates an opportunity, under the Summer Research Extension Program (SREP), to continue their AFOSR-sponsored research at their home institutions through the award of research grants. In 1994 the maximum amount of each grant was increased from \$20,000 to \$25,000, and the number of AFOSR-sponsored grants decreased from 75 to 60. A separate annual report is compiled on the SREP.

The numbers of projected summer research participants in each of the three categories and SREP "grants" are usually increased through direct sponsorship by participating laboratories.

AFOSR's SRP has well served its objectives of building critical links between Air Force research laboratories and the academic community, opening avenues of communications and forging new research relationships between Air Force and academic technical experts in areas of national interest, and strengthening the nation's efforts to sustain careers in science and engineering. The success of the SRP can be gauged from its growth from inception (see Table 1) and from the favorable responses the 1997 participants expressed in end-of-tour SRP evaluations (Appendix B).

AFOSR contracts for administration of the SRP by civilian contractors. The contract was first awarded to Research & Development Laboratories (RDL) in September 1990. After completion of the 1990 contract, RDL (in 1993) won the recompetition for the basic year and four 1-year options.

2. PARTICIPATION IN THE SUMMER RESEARCH PROGRAM

The SRP began with faculty associates in 1979; graduate students were added in 1982 and high school students in 1986. The following table shows the number of associates in the program each year.

YEAR	SRP Participation, by Year			TOTAL
	SFRP	GSRP	HSAP	
1979	70			70
1980	87			87
1981	87			87
1982	91	17		108
1983	101	53		154
1984	152	84		236
1985	154	92		246
1986	158	100	42	300
1987	159	101	73	333
1988	153	107	101	361
1989	168	102	103	373
1990	165	121	132	418
1991	170	142	132	444
1992	185	121	159	464
1993	187	117	136	440
1994	192	117	133	442
1995	190	115	137	442
1996	188	109	138	435
1997	148	98	140	427
1998	85	40	88	213

Beginning in 1993, due to budget cuts, some of the laboratories weren't able to afford to fund as many associates as in previous years. Since then, the number of funded positions has remained fairly constant at a slightly lower level.

3. RECRUITING AND SELECTION

The SRP is conducted on a nationally advertised and competitive-selection basis. The advertising for faculty and graduate students consisted primarily of the mailing of 8,000 52-page SRP brochures to chairpersons of departments relevant to AFOSR research and to administrators of grants in accredited universities, colleges, and technical institutions. Historically Black Colleges and Universities (HBCUs) and Minority Institutions (MIs) were included. Brochures also went to all participating USAF laboratories, the previous year's participants, and numerous individual requesters (over 1000 annually).

RDL placed advertisements in the following publications: *Black Issues in Higher Education*, *Winds of Change*, and *IEEE Spectrum*. Because no participants list either *Physics Today* or *Chemical & Engineering News* as being their source of learning about the program for the past several years, advertisements in these magazines were dropped, and the funds were used to cover increases in brochure printing costs.

High school applicants can participate only in laboratories located no more than 20 miles from their residence. Tailored brochures on the HSAP were sent to the head counselors of 180 high schools in the vicinity of participating laboratories, with instructions for publicizing the program in their schools. High school students selected to serve at Wright Laboratory's Armament Directorate (Eglin Air Force Base, Florida) serve eleven weeks as opposed to the eight weeks normally worked by high school students at all other participating laboratories.

Each SFRP or GSRP applicant is given a first, second, and third choice of laboratory. High school students who have more than one laboratory or directorate near their homes are also given first, second, and third choices.

Laboratories make their selections and prioritize their nominees. AFOSR then determines the number to be funded at each laboratory and approves laboratories' selections.

Subsequently, laboratories use their own funds to sponsor additional candidates. Some selectees do not accept the appointment, so alternate candidates are chosen. This multi-step selection procedure results in some candidates being notified of their acceptance after scheduled deadlines. The total applicants and participants for 1998 are shown in this table.

1998 Applicants and Participants			
PARTICIPANT CATEGORY	TOTAL APPLICANTS	SELECTEES	DECLINING SELECTEES
SFRP	382	85	13
(HBCU/MI)	(0)	(0)	(0)
GSRP	130	40	7
(HBCU/MI)	(0)	(0)	(0)
HSAP	328	88	22
TOTAL	840	213	42

4. SITE VISITS

During June and July of 1998, representatives of both AFOSR/NI and RDL visited each participating laboratory to provide briefings, answer questions, and resolve problems for both laboratory personnel and participants. The objective was to ensure that the SRP would be as constructive as possible for all participants. Both SRP participants and RDL representatives found these visits beneficial. At many of the laboratories, this was the only opportunity for all participants to meet at one time to share their experiences and exchange ideas.

5. HISTORICALLY BLACK COLLEGES AND UNIVERSITIES AND MINORITY INSTITUTIONS (HBCU/MIs)

Before 1993, an RDL program representative visited from seven to ten different HBCU/MIs annually to promote interest in the SRP among the faculty and graduate students. These efforts were marginally effective, yielding a doubling of HBCU/MI applicants. In an effort to achieve AFOSR's goal of 10% of all applicants and selectees being HBCU/MI qualified, the RDL team decided to try other avenues of approach to increase the number of qualified applicants. Through the combined efforts of the AFOSR Program Office at Bolling AFB and RDL, two very active minority groups were found, HACU (Hispanic American Colleges and Universities) and AISES (American Indian Science and Engineering Society). RDL is in communication with representatives of each of these organizations on a monthly basis to keep up with their activities and special events. Both organizations have widely-distributed magazines/quarterlies in which RDL placed ads.

Since 1994 the number of both SFRP and GSRP HBCU/MI applicants and participants has increased ten-fold, from about two dozen SFRP applicants and a half dozen selectees to over 100 applicants and two dozen selectees, and a half-dozen GSRP applicants and two or three selectees to 18 applicants and 7 or 8 selectees. Since 1993, the SFRP had a two-fold applicant increase and a two-fold selectee increase. Since 1993, the GSRP had a three-fold applicant increase and a three to four-fold increase in selectees.

In addition to RDL's special recruiting efforts, AFOSR attempts each year to obtain additional funding or use leftover funding from cancellations the past year to fund HBCU/MI associates.

SRP HBCU/MI Participation, By Year				
YEAR	SFRP		GSRP	
	Applicants	Participants	Applicants	Participants
1985	76	23	15	11
1986	70	18	20	10
1987	82	32	32	10
1988	53	17	23	14
1989	39	15	13	4
1990	43	14	17	3
1991	42	13	8	5
1992	70	13	9	5
1993	60	13	6	2
1994	90	16	11	6
1995	90	21	20	8
1996	119	27	18	7

6. SRP FUNDING SOURCES

Funding sources for the 1998 SRP were the AFOSR-provided slots for the basic contract and laboratory funds. Funding sources by category for the 1998 SRP selected participants are shown here.

1998 SRP FUNDING CATEGORY	SFRP	GSRP	HSAP
AFOSR Basic Allocation Funds	67	38	75
USAF Laboratory Funds	17	2	13
Slots Added by AFOSR (Leftover Funds)	0	0	0
HBCU/MI By AFOSR (Using Procured Addn'l Funds)	0	0	N/A
TOTAL	84	40	88

7. COMPENSATION FOR PARTICIPANTS

Compensation for SRP participants, per five-day work week, is shown in this table.

1998 SRP Associate Compensation

PARTICIPANT CATEGORY	1991	1992	1993	1994	1995	1996	1997	1998
Faculty Members	\$690	\$718	\$740	\$740	\$740	\$770	\$770	\$793
Graduate Student (Master's Degree)	\$425	\$442	\$455	\$455	\$455	\$470	\$470	\$484
Graduate Student (Bachelor's Degree)	\$365	\$380	\$391	\$391	\$391	\$400	\$400	\$412
High School Student (First Year)	\$200	\$200	\$200	\$200	\$200	\$200	\$200	\$200
High School Student (Subsequent Years)	\$240	\$240	\$240	\$240	\$240	\$240	\$240	\$240

The program also offered associates whose homes were more than 50 miles from the laboratory an expense allowance (seven days per week) of \$52/day for faculty and \$41/day for graduate students. Transportation to the laboratory at the beginning of their tour and back to their home destinations at the end was also reimbursed for these participants. Of the combined SFRP and GSRP associates, 65 % claimed travel reimbursements at an average round-trip cost of \$730.

Faculty members were encouraged to visit their laboratories before their summer tour began. All costs of these orientation visits were reimbursed. Forty-three percent (85 out of 188) of faculty associates took orientation trips at an average cost of \$449. By contrast, in 1993, 58 % of SFRP associates elected to take an orientation visits at an average cost of \$685; that was the highest

percentage of associates opting to take an orientation trip since RDL has administered the SRP, and the highest average cost of an orientation trip.

Program participants submitted biweekly vouchers countersigned by their laboratory research focal point, and RDL issued paychecks so as to arrive in associates' hands two weeks later.

This is the third year of using direct deposit for the SFRP and GSRP associates. The process went much more smoothly with respect to obtaining required information from the associates, about 15% of the associates' information needed clarification in order for direct deposit to properly function as opposed to 7% from last year. The remaining associates received their stipend and expense payments via checks sent in the US mail.

HSAP program participants were considered actual RDL employees, and their respective state and federal income tax and Social Security were withheld from their paychecks. By the nature of their independent research, SFRP and GSRP program participants were considered to be consultants or independent contractors. As such, SFRP and GSRP associates were responsible for their own income taxes, Social Security, and insurance.

8. CONTENTS OF THE 1998 REPORT

The complete set of reports for the 1998 SRP includes this program management report (Volume 1) augmented by fifteen volumes of final research reports by the 1998 associates, as indicated below:

1998 SRP Final Report Volume Assignments

LABORATORY	SFRP	GSRP	HSAP
Armstrong	2	7	12
Phillips	3	8	13
Rome	4	9	14
Wright	5A, 5B	10	15
AEDC, ALCs, USAFA, WHMC	6	11	

APPENDIX A -- PROGRAM STATISTICAL SUMMARY

A. Colleges/Universities Represented

Selected SFRP associates represented 169 different colleges, universities, and institutions, GSRP associates represented 95 different colleges, universities, and institutions.

B. States Represented

SFRP -Applicants came from 47 states plus Washington D.C. Selectees represent 44 states.

GSRP - Applicants came from 44 states. Selectees represent 32 states.

HSAP - Applicants came from thirteen states. Selectees represent nine states.

Total Number of Participants	
SFRP	85
GSRP	40
HSAP	88
TOTAL	213

Degrees Represented			
	SFRP	GSRP	TOTAL
Doctoral	83	0	83
Master's	1	3	4
Bachelor's	0	22	22
TOTAL	186	25	109

SFRP Academic Titles	
Assistant Professor	36
Associate Professor	34
Professor	15
Instructor	0
Chairman	0
Visiting Professor	0
Visiting Assoc. Prof.	0
Research Associate	0
TOTAL	85

Source of Learning About the SRP		
Category	Applicants	Selectees
Applied/participated in prior years	177	47
Colleague familiar with SRP	104	24
Brochure mailed to institution	101	21
Contact with Air Force laboratory	101	39
<i>IEEE Spectrum</i>	12	1
<i>BIIHE</i>	4	0
Other source	117	30
TOTAL	616	162

APPENDIX B -- SRP EVALUATION RESPONSES

1. OVERVIEW

Evaluations were completed and returned to RDL by four groups at the completion of the SRP. The number of respondents in each group is shown below.

Table B-1. Total SRP Evaluations Received

Evaluation Group	Responses
SFRP & GSRPs	100
HSAPs	75
USAF Laboratory Focal Points	84
USAF Laboratory HSAP Mentors	6

All groups indicate unanimous enthusiasm for the SRP experience.

The summarized recommendations for program improvement from both associates and laboratory personnel are listed below:

- A. Better preparation on the labs' part prior to associates' arrival (i.e., office space, computer assets, clearly defined scope of work).
- B. Faculty Associates suggest higher stipends for SFRP associates.
- C. Both HSAP Air Force laboratory mentors and associates would like the summer tour extended from the current 8 weeks to either 10 or 11 weeks; the groups state it takes 4-6 weeks just to get high school students up-to-speed on what's going on at laboratory. (Note: this same argument was used to raise the faculty and graduate student participation time a few years ago.)

2. 1998 USAF LABORATORY FOCAL POINT (LFP) EVALUATION RESPONSES

The summarized results listed below are from the 84 LFP evaluations received.

1. LFP evaluations received and associate preferences:

Table B-2. Air Force LFP Evaluation Responses (By Type)

Lab	Evals Recv'd	How Many Associates Would You Prefer To Get ? (% Response)											
		SFRP				GSRP (w/Univ Professor)				GSRP (w/o Univ Professor)			
		0	1	2	3+	0	1	2	3+	0	1	2	3+
AEDC	0	-	-	-	-	-	-	-	-	-	-	-	-
WHMC	0	-	-	-	-	-	-	-	-	-	-	-	-
AL	7	28	28	28	14	54	14	28	0	86	0	14	0
USAFA	1	0	100	0	0	100	0	0	0	0	100	0	0
PL	25	40	40	16	4	88	12	0	0	84	12	4	0
RL	5	60	40	0	0	80	10	0	0	100	0	0	0
WL	46	30	43	20	6	78	17	4	0	93	4	2	0
Total	84	32%	50%	13%	5%	80%	11%	6%	0%	73%	23%	4%	0%

LFP Evaluation Summary. The summarized responses, by laboratory, are listed on the following page. LFPs were asked to rate the following questions on a scale from 1 (below average) to 5 (above average).

2. LFPs involved in SRP associate application evaluation process:
 - a. Time available for evaluation of applications:
 - b. Adequacy of applications for selection process:
3. Value of orientation trips:
4. Length of research tour:
5.
 - a. Benefits of associate's work to laboratory:
 - b. Benefits of associate's work to Air Force:
6.
 - a. Enhancement of research qualifications for LFP and staff:
 - b. Enhancement of research qualifications for SFRP associate:
 - c. Enhancement of research qualifications for GSRP associate:
7.
 - a. Enhancement of knowledge for LFP and staff:
 - b. Enhancement of knowledge for SFRP associate:
 - c. Enhancement of knowledge for GSRP associate:
8. Value of Air Force and university links:
9. Potential for future collaboration:
10.
 - a. Your working relationship with SFRP:
 - b. Your working relationship with GSRP:
11. Expenditure of your time worthwhile:

(Continued on next page)

12. Quality of program literature for associate:
13. a. Quality of RDL's communications with you:
 b. Quality of RDL's communications with associates:
14. Overall assessment of SRP:

Table B-3. Laboratory Focal Point Responses to above questions

	<i>AEDC</i>	<i>AL</i>	<i>USAF</i>	<i>PL</i>	<i>RL</i>	<i>WHMC</i>	<i>WL</i>
	<i>A</i>						
<i># Evals Recv'd</i>	0	7	1	14	5	0	46
<i>Question #</i>							
2	-	86 %	0 %	88 %	80 %	-	85 %
2a	-	4.3	n/a	3.8	4.0	-	3.6
2b	-	4.0	n/a	3.9	4.5	-	4.1
3	-	4.5	n/a	4.3	4.3	-	3.7
4	-	4.1	4.0	4.1	4.2	-	3.9
5a	-	4.3	5.0	4.3	4.6	-	4.4
5b	-	4.5	n/a	4.2	4.6	-	4.3
6a	-	4.5	5.0	4.0	4.4	-	4.3
6b	-	4.3	n/a	4.1	5.0	-	4.4
6c	-	3.7	5.0	3.5	5.0	-	4.3
7a	-	4.7	5.0	4.0	4.4	-	4.3
7b	-	4.3	n/a	4.2	5.0	-	4.4
7c	-	4.0	5.0	3.9	5.0	-	4.3
8	-	4.6	4.0	4.5	4.6	-	4.3
9	-	4.9	5.0	4.4	4.8	-	4.2
10a	-	5.0	n/a	4.6	4.6	-	4.6
10b	-	4.7	5.0	3.9	5.0	-	4.4
11	-	4.6	5.0	4.4	4.8	-	4.4
12	-	4.0	4.0	4.0	4.2	-	3.8
13a	-	3.2	4.0	3.5	3.8	-	3.4
13b	-	3.4	4.0	3.6	4.5	-	3.6
14	-	4.4	5.0	4.4	4.8	-	4.4

3. 1998 SFRP & GSRP EVALUATION RESPONSES

The summarized results listed below are from the 120 SFRP/GSRP evaluations received.

Associates were asked to rate the following questions on a scale from 1 (below average) to 5 (above average) - by Air Force base results and over-all results of the 1998 evaluations are listed after the questions.

1. The match between the laboratories research and your field:
2. Your working relationship with your LFP:
3. Enhancement of your academic qualifications:
4. Enhancement of your research qualifications:
5. Lab readiness for you: LFP, task, plan:
6. Lab readiness for you: equipment, supplies, facilities:
7. Lab resources:
8. Lab research and administrative support:
9. Adequacy of brochure and associate handbook:
10. RDL communications with you:
11. Overall payment procedures:
12. Overall assessment of the SRP:
13.
 - a. Would you apply again?
 - b. Will you continue this or related research?
14. Was length of your tour satisfactory?
15. Percentage of associates who experienced difficulties in finding housing:
16. Where did you stay during your SRP tour?
 - a. At Home:
 - b. With Friend:
 - c. On Local Economy:
 - d. Base Quarters:
17. Value of orientation visit:
 - a. Essential:
 - b. Convenient:
 - c. Not Worth Cost:
 - d. Not Used:

SFRP and GSRP associate's responses are listed in tabular format on the following page.

Table B-4. 1997 SFRP & GSRP Associate Responses to SRP Evaluation

	Arnold	Brooks	Edwards	Eglin	Griffis	Hanscom	Kelly	Kirtland	Lackland	Robins	Tyndall	WPAFB	average
# res	6	48	6	14	31	19	3	32	1	2	10	85	257
1	4.8	4.4	4.6	4.7	4.4	4.9	4.6	4.6	5.0	5.0	4.0	4.7	4.6
2	5.0	4.6	4.1	4.9	4.7	4.7	5.0	4.7	5.0	5.0	4.6	4.8	4.7
3	4.5	4.4	4.0	4.6	4.3	4.2	4.3	4.4	5.0	5.0	4.5	4.3	4.4
4	4.3	4.5	3.8	4.6	4.4	4.4	4.3	4.6	5.0	4.0	4.4	4.5	4.5
5	4.5	4.3	3.3	4.8	4.4	4.5	4.3	4.2	5.0	5.0	3.9	4.4	4.4
6	4.3	4.3	3.7	4.7	4.4	4.5	4.0	3.8	5.0	5.0	3.8	4.2	4.2
7	4.5	4.4	4.2	4.8	4.5	4.3	4.3	4.1	5.0	5.0	4.3	4.3	4.4
8	4.5	4.6	3.0	4.9	4.4	4.3	4.3	4.5	5.0	5.0	4.7	4.5	4.5
9	4.7	4.5	4.7	4.5	4.3	4.5	4.7	4.3	5.0	5.0	4.1	4.5	4.5
10	4.2	4.4	4.7	4.4	4.1	4.1	4.0	4.2	5.0	4.5	3.6	4.4	4.3
11	3.8	4.1	4.5	4.0	3.9	4.1	4.0	4.0	3.0	4.0	3.7	4.0	4.0
12	5.7	4.7	4.3	4.9	4.5	4.9	4.7	4.6	5.0	4.5	4.6	4.5	4.6
Numbers below are percentages													
13a	83	90	83	93	87	75	100	81	100	100	100	86	87
13b	100	89	83	100	94	98	100	94	100	100	100	94	93
14	83	96	100	90	87	80	100	92	100	100	70	84	88
15	17	6	0	33	20	76	33	25	0	100	20	8	39
16a	-	26	17	9	38	23	33	4	-	-	-	30	
16b	100	33	-	40	-	8	-	-	-	-	36	2	
16c	-	41	83	40	62	69	67	96	100	100	64	68	
16d	-	-	-	-	-	-	-	-	-	-	-	0	
17a	-	33	100	17	50	14	67	39	-	50	40	31	35
17b	-	21	-	17	10	14	-	24	-	50	20	16	16
17c	-	-	-	-	10	7	-	-	-	-	-	2	3
17d	100	46	-	66	30	69	33	37	100	-	40	51	46

4. 1998 USAF LABORATORY HSAP MENTOR EVALUATION RESPONSES

Not enough evaluations received (5 total) from Mentors to do useful summary.

5. 1998 HSAP EVALUATION RESPONSES

The summarized results listed below are from the 23 HSAP evaluations received.

HSAP apprentices were asked to rate the following questions on a scale from 1 (below average) to 5 (above average)

1. Your influence on selection of topic/type of work.
2. Working relationship with mentor, other lab scientists.
3. Enhancement of your academic qualifications.
4. Technically challenging work.
5. Lab readiness for you: mentor, task, work plan, equipment.
6. Influence on your career.
7. Increased interest in math/science.
8. Lab research & administrative support.
9. Adequacy of RDL's Apprentice Handbook and administrative materials.
10. Responsiveness of RDL communications.
11. Overall payment procedures.
12. Overall assessment of SRP value to you.
13. Would you apply again next year? Yes (92 %)
14. Will you pursue future studies related to this research? Yes (68 %)
15. Was Tour length satisfactory? Yes (82 %)

	Arnold	Brooks	Edwards	Eglin	Griffiss	Hanscom	Kirtland	Tyndall	WPAFB	Totals
# resp	5	19	7	15	13	2	7	5	40	113
1	2.8	3.3	3.4	3.5	3.4	4.0	3.2	3.6	3.6	3.4
2	4.4	4.6	4.5	4.8	4.6	4.0	4.4	4.0	4.6	4.6
3	4.0	4.2	4.1	4.3	4.5	5.0	4.3	4.6	4.4	4.4
4	3.6	3.9	4.0	4.5	4.2	5.0	4.6	3.8	4.3	4.2
5	4.4	4.1	3.7	4.5	4.1	3.0	3.9	3.6	3.9	4.0
6	3.2	3.6	3.6	4.1	3.8	5.0	3.3	3.8	3.6	3.7
7	2.8	4.1	4.0	3.9	3.9	5.0	3.6	4.0	4.0	3.9
8	3.8	4.1	4.0	4.3	4.0	4.0	4.3	3.8	4.3	4.2
9	4.4	3.6	4.1	4.1	3.5	4.0	3.9	4.0	3.7	3.8
10	4.0	3.8	4.1	3.7	4.1	4.0	3.9	2.4	3.8	3.8
11	4.2	4.2	3.7	3.9	3.8	3.0	3.7	2.6	3.7	3.8
12	4.0	4.5	4.9	4.6	4.6	5.0	4.6	4.2	4.3	4.5
Numbers below are percentages										
13	60%	95%	100%	100%	85%	100%	100%	100%	90%	92%
14	20%	80%	71%	80%	54%	100%	71%	80%	65%	68%
15	100%	70%	71%	100%	100%	50%	86%	60%	80%	82%

**GROWTH AND CHARACTERIZATION OF 3-INCH NITRIDE
SEMICONDUCTING EPITAXIAL FILMS**

**Jeffrey C. Anderson
Department of Materials Science and Engineering**

**Clemson University
105 Riggs Hall
Clemson, SC 29631**

**Final Report for:
Summer Graduate Student Research Program
US Air Force Research Laboratory/SNHX, Hanscomb AFB**

**Sponsored by:
Air Force Office of Scientific Research
Bolling Air Force Base, DC**

and

US Air Force Research Laboratory/SNHX, Hanscomb AFB

August 1998

GROWTH AND CHARACTERIZATION OF 3-INCH NITRIDE SEMICONDUCTING EPITAXIAL FILMS

Jeffrey C. Anderson
Department of Materials Science and Engineering
Clemson University

Abstract

During the period from June 1998 to July 1998, my work was focused on : (1) modification of a MOCVD system located at the US Air Force Research Laboratory/SNHX, Hanscomb AFB to accommodate a new gallium nitride MOCVD reactor. The construction of the MOCVD reactor was completed and leak checking begun. (2) construction of a backup exhaust system for the preexisting vapor phase epitaxy (VPE) system used for gallium nitride (GaN.)

GROWTH AND CHARACTERIZATION OF 3-INCH NITRIDE SEMICONDUCTING EPITAXIAL FILMS

Jeffrey C. Anderson

Introduction

The ultimate goal of both projects is to develop techniques for the growth and characterization of gallium nitride (GaN) epitaxial films. As a first step, an aluminum-gallium arsenide (AlGaAs) MOCVD system was modified to accommodate a 3-inch GaN MOCVD reactor, manufactured by EMCORE Inc. as a SBIR deliverable product. In the future, the plan is to operate the system and gain growth experience on GaN films. After that, the reactor will be modified again into a close-spaced wafer-cooled injector reactor, similar to one constructed on site for growing GaAs films, to investigate the influence of the technology on the growth of GaN films.

The second project was the construction of a backup exhaust system for the existing VPE system. This is needed because the ammonia (NH_3) used in this process quickly degrades the current vacuum seals. Additionally, there are numerous possible leaks in the current system.

Procedure

The EMCORE's GaN stainless steel reactor is designed for growing films on a 3-inch substrate. A 3-inch molybdenum susceptor is capable of a rotation rate up to 1000 RPM. A tungsten heater, located under the susceptor, provides heating power up to 1050 C. The reactants and carrier gases are injected from the top of the reactor. The water, circulating around the injection head, the reactor wall, and the ferromagnetic fluid o-ring seal, provides maximum cooling power. The AlGaAs MOCVD system is used to supply reactant gases and control the flow. To combine the two systems, a number of things had to be done. The following is a list of those modifications performed during my time at the lab.

- The exhaust system for the GaN reactor was constructed. The exhaust line is composed of a particle flex trap, a MKS Baratron transducer for reading pressure of the reactor, a MKS Throttle valve controlling the system pressure, both inlet and outlet pump oil filters and an Edwards Two Stage-30 mechanical pump. To further trap particles and absorb ammonia, two oil bubblers connected in serial

are placed at the pump outlet. A purging line, used for purging the system when not the system is not running, was constructed using the same two bubblers.

- The cooling water supply was installed. The total water flow reached 1.6 G/m in which ~0.3 G/m of water goes to the gas burning unit located at the end of the exhaustion pipe to eliminate any hydrogen and ammonia going into the air. The other 1.3 G/m of water goes to the reactor unit.
- The leak check of the integrated systems was begun. Because of time constraints, this will be completed by Dr. Yang Ren Sun in the near future.

The backup exhaust system for the VPE system had a number of modifications over the current system. The following is a list of those modifications explored during my time at Rome Labs:

- A Welch pump with Viton seals was used to provide a vacuum. Viton provides a much higher resistance to ammonia than other type of rubber. A oil filter and cold trap were attached with a purging valve placed between them.
- The cold trap will be supported by a shelf being constructed by the machine shop. This will be a one piece unit attached to the pump itself.
- The HCl gas supply will be isolated in a nitrogen ambient glove box. This box will be constructed from preexisting materials and parts to be ordered based upon a decision from Dr. D. Weyburne.
- All Swagelock fittings will be replaced with Cajon fittings. This will greatly reduce the number of possible leaks in the system.

Modified Herriott Cell Interferometry for Pulsed Plasma Thruster
Neutral Density Measurements

Erik Antonsen
Department of Aeronautical and Astronautical Engineering

University of Illinois
306 Talbot Lab
Urbana, IL 61801

Final Report for:
Graduate Summer Research Program
Edwards Air Force Base

Sponsored by:
Air Force Office of Scientific Research
Bolling Air Force Base, DC
and
Air Force Research Lab

August 1998

Modified Herriott Cell Interferometry for Pulsed Plasma
Neutral Density Measurements

Erik Antonsen
Department of Aeronautical and Astronautical Engineering
University of Illinois, Urbana-Champaign

Abstract

A Modified Herriott Cell was designed, constructed, and implemented into a Heterodyne Quadrature Interferometer. This provided increased resolution of neutral density coming off of Pulsed Plasma Thrusters during firing. Two concave spherical mirrors were used to create a two dimensional plane measurement technique that allowed for large increases in path length by multiplying the number of passes that the laser made across the face of the thruster. Raytracing code was both written and purchased to calculate the possible configurations that could be used with this cell and to optimize solutions found. The solutions identified in the codes were demonstrated in the lab with the intent of making measurements at increased resolution. Lab vibrations were identified as a potentially large source of error and steps were taken to alleviate the error introduced. Final data was not taken on a PPT, as there was not enough time to complete these measurements. Another trip is being scheduled with the intent of taking the final data for demonstration of the validity of this diagnostic as well as using it on various thrusters.

Modified Herriott Cell Interferometry for Pulsed Plasma Thruster Neutral Density Measurements

Erik Antonsen

I. Introduction

The attraction of Pulsed Plasma Thrusters as a propulsion option on small satellites stems mainly from its design simplicity and use of solid, non-toxic propellant. However, in the past 30 years, research has failed to produce significant improvements in the overall performance of this thruster. Part of this is due to complex physics that are not completely understood at this point. Because of late time vaporization and small ionization fraction of the total propellant used per pulse, the typical efficiency of a PPT is around 10%. In order to improve this efficiency and harness the full potential of these thrusters, it is necessary to gain a more complete understanding of the physics behind their operation and of exactly how the propellant is being consumed. Heterodyne quadrature interferometry has been introduced at AFRL to determine electron and neutral densities during single pulses of PPTs. Unfortunately, at long timeframes room vibrations can introduce significant error reducing the resolution available to see the slow moving neutrals.

In order to compensate for this a modified Herriott Cell was designed and implemented in the interferometer setup to increase the laser path length exposed to the plasma thus increasing the spatial resolution of the system in spite of room vibrations at longer timeframes. Until now, Herriott Cell techniques have only been used in 3-dimensional applications for absorption measurements over volumes. For the purpose of this study, a 2-dimensional version was designed to take data over a specific plane normal to the thrust axis. The main issues were whether the phase front could be maintained over the curvature of the mirrors and whether the vibrations introduced into the extra optical equipment would be large enough to override the predicted gain in resolution.

It was determined that the phase front would be maintained as well as that the 2 Herriott Cell mirrors would not induce sufficient vibration to counteract the increase in resolution. The final goal of the Herriott Cell project was to demonstrate the ability to move from the 2-D plane measurement to a Point measurement and 3-D volume measurements. At this point only the plane measurements have been accomplished.

II. Herriott Cell Theory

Historically, the Herriott Cell has been limited to the domain of absorption measurements for gaseous emissions. However, because of its ability to confine a large number of passes to a small area, the Herriott Cell is an ideal candidate to replace multiple flat mirror and beamsplitter setups which can produce only limited numbers of passes and reduce intensity. The actual cell is simply two concave, spherical mirrors facing each other. One has a hole drilled off center for entrance and exit of the beam. Because of the curvature of the mirrors, there are many configurations that can confine the beam to within their diameter. By adjusting several key parameters the number of bounces can be increased and is limited by the size and location of the entrance hole. The entrance angle of the beam into the cell, the mirror separation, and the tilt of the mirrors in the beam plane all control the number of passes obtained. However, small errors in entrance angle and mirror tilt can be corrected by adjusting the mirror separation in most cases.

In order to calculate the number of passes that could be maintained within the cell, two ray-tracing codes were employed. The first was written at the University of Illinois specifically for determination of the best design specifications for the cell. This code allowed an input beam to enter the cell and continue bouncing within the cell until it left through the hole or over the side of the mirrors. Inputs included entrance angle, mirror separation, hole location, hole diameter, mirror radius of curvature, reflectivity, and mirror diameter. Outputs included number of passes, exit angle, exit light intensity, and average and rms beam coverage at the cell midline. This code was also used to determine rough parameters for specific numbers of bounces once the final mirror design had been frozen. In order to optimize the number of passes and determine the effects of small mirror tilts and slight changes in parameters, Beam3 code was used. This code was limited in the number of passes it could simulate, but had the added advantage of auto-optimizing specific variables for a desired output. With Beam3 software, planar solutions using total internal reflection modes of operation for the mirrors were identified and demonstrated in the lab. Figure 1 shows 6 passes in Retro-reflecting mode in the Herriott Cell.

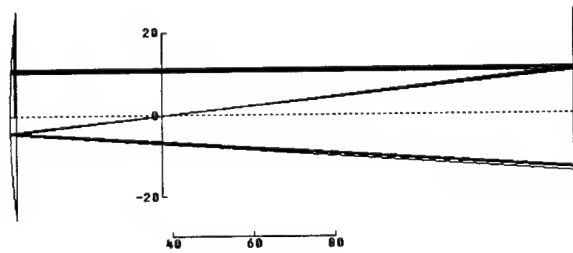


Fig. 1 Six Passes within the Herriott Cell

These modes were valuable to operation of the Herriott cell because they offset the focusing effect obtained from certain configurations through the curvature of the mirrors. The raytracing techniques were also applied to configurations showing 3-D volume measurements and point measurement possibilities. These configurations include entrance of the beam over the side of the mirrors as a possible solution. However, because of time constraints neither of these possibilities has been explored in depth.

The main issue in creating a 2-dimensional Herriott Cell for interferometry is the question of whether or not the phase front can be maintained over multiple passes through the cell. When the beams are recombined in heterodyne interferometry, an accurate alignment produces a fringe pattern that varies intensity with slight changes in path length. With a highly accurate alignment, the fringe pattern that is observed is reduced to one fringe that increases and decreases in intensity depending on how the electromagnetic fields add. Calculations were performed showing that the phase front could be maintained over large numbers of passes within the spherical mirrors and experimental verification of this was confirmed using a DieCam and beamsplitter setup. The DieCam was used because an acoustic modulation of 40 MHz is required for the detecting equipment. With the 40 MHz signal present, it is impossible to see the fringes. Pictures with the DieCam correlated with oscilloscope readings to determine that the best signal on the oscilloscope was indeed due to the minimum number of fringes obtained. Figure 2 shows some of the fringes at relatively poor alignment so that they can be distinguished easily.



Fig. 2 Fringes Showing Interference Pattern from Herriott Cell.

III. Experimental Apparatus

The Herriott Cell is intended for use on Pulsed Plasma Thrusters because it measures changes in phase shift from a baseline. This mode of operation is ideal for PPTs whose pulse widths are on the order of tens of microseconds. PPTs generally run on Teflon propellant and are simple in design and fabrication and highly reliable. XPPT-1A is a standard parallel plate PPT from AFRL that operates at around 20 Joules. Teflon is fed from the back by a spring to the electrodes where it is exposed to an arc, vaporized, and accelerated by a $j \times B$ force. There is a portion of the fuel that comes off late as a result of heating that is not ionized and therefore not accelerated by the electromagnetic force. It is this portion of neutral gas that comes off late in time that vibration can sometimes hide.

The Quadrature-Heterodyne Interferometer layout used is fairly straightforward. A 17mW HeNe is sent through an Isomet Bragg Cell where a 40MHz acoustic modulation is delivered and the beam is split into scene and reference. The scene beam passes through the tank and Herriott Cell and is recombined with the reference beam at equal path lengths on an Analog Modules 712 photodetector. The detector output is run into an analog oscilloscope for alignment purposes. When a clear 40 MHz signal is detected and stabilized, the output from the detector is run into a demodulating circuit that splits the signal into sine and cosine of the phase angle. These signals go to a digital scope that is triggered by the igniter circuit for the PPT. The data is then analyzed and the phase angle is output. This phase angle is linearly proportional to the electron and neutral densities. Figure 3 shows the interferometer layout with the Herriott Cell present.

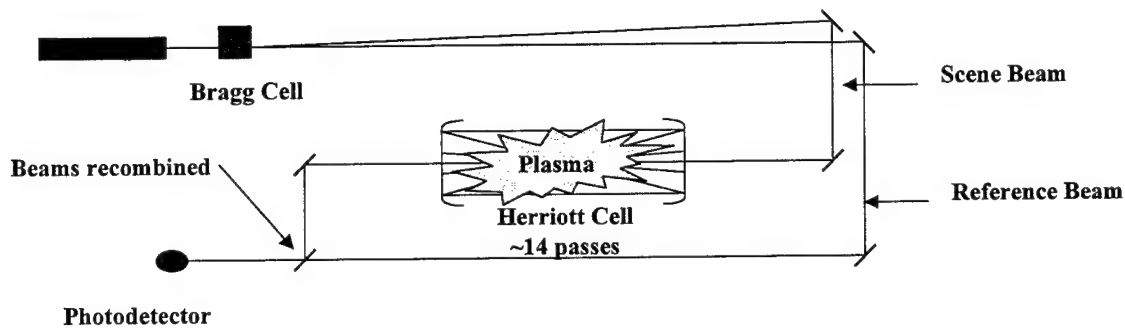


Fig. 3 Laboratory Setup for Interferometry

The Herriott Cell itself is two spherical mirrors with focal lengths of 100 mm each and 50.8 mm diameters. The focal lengths were chosen to have enough room to place the PPT between the mirrors comfortably. The mirror separation distance is limited to between f and $2f$. Originally, the hole was 3 mm diameter and 21 mm off center to provide a viewing area of about 42 mm vertically in front of the UIUC coaxial PPT. This was later redesigned to accommodate the AFRL XPPT-1A by moving the hole to 11 mm off center to provide a vertical viewing plane of 22 mm. After some concern about the diffraction effects from the beam passing through the hole, it was increased to a 5 mm diameter to allow a cleaner beam out of the cell. Both mirrors are mounted on Newport Ultima series mounts with high precision actuators which are in turn mounted on an optical rail to restrict the mirror motion. Finally, Intercavity Beam Shields were designed and built at the University of Illinois to keep the mirrors from becoming coated with Teflon. These are aluminum sheets mounted on the rail with the mirrors that allow a thin vertical plane for the laser to move within, but cover the rest of the mirror from the exhaust of the PPT. They also have two thin plates that cover the whole mirror but can be pulled off after the PPT has been burned in. Figure 3 shows the cell and shields.

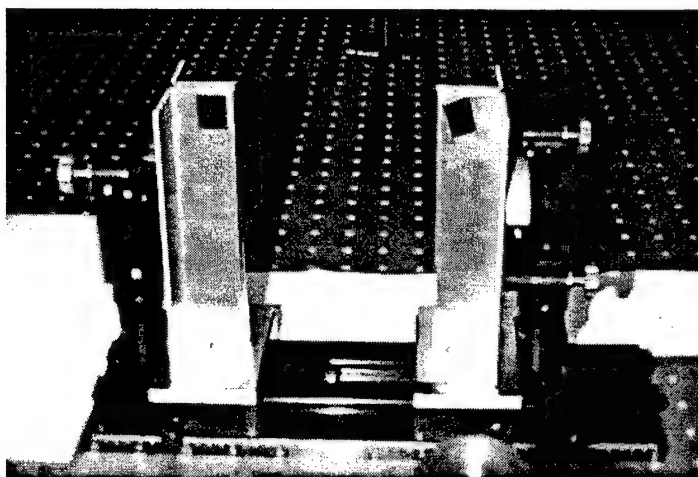


Fig. 4 Herriott Cell Equipped with Beam Shields

There is some concern that the shields may create an excessive amount of neutrals from impact of the plasma on the aluminum, but that can be determined with future testing. For all tests performed, the beam shields were not used.

IV. Experimental Results

The beam patterns created within the Herriott Cell were illuminated using vapor from liquid nitrogen. This technique allowed visual verification of the beam patterns predicted by the Beam3 and Illinois codes. Unfortunately, it was difficult to get a camera to focus on the laser light with the vapor and so pictures are not available at this time. Diffraction patterns out of the Herriott Cell were readily visible to the naked eye on white office paper. When the hole size was increased to 5 mm diameter the diffraction patterns became negligible. The final question was the fringe patterns from interference. While the Bragg cell is operating on the laser, the human eye can't distinguish the interference fringes due to the 40 MHz modulation. A DiCam was used with its shutter speed set at a 7 ns opening. This allowed visual inspection of the fringes to be correlated with the amplitude of the 40 MHz signal out of the detector. At the best signal out of the analog scope, one large fringe was noted over the detector area. As the signal was moved off of peak alignment, increased numbers of fringes were observed. These

observations along with the analytical solutions from above led to the conclusion that acceptable fringe patterns could be determined by the ability to acquire a 40 MHz signal out of the detector that is stable and above 1 V peak to peak. An unstable signal that fades in and out denotes a discrepancy of more than 5% of the coherence length of the laser between the scene and reference beam path lengths. Generally, the coherence length of the laser is around a meter. This suggests that a discrepancy of 2 inches in path length is acceptable for the purposes of this experiment.

The measured change in phase angle is related to the electron and neutral densities by equation 1:

$$\Delta\phi = 2.8 \times 10^{-15} \lambda \int n_e dl - \frac{3.9 \times 10^{-29}}{\lambda} \int n_n dl$$

Eqn. 1

In this case, $\lambda=632.8$ nm, and n_e and n_n are electron and neutral densities respectively. The integral over l becomes the path length exposed to the plasma multiplied by the number of passes. This is where the advantage of the Herriott Cell becomes apparent.

Another factor that comes into play here is external vibrations. Because of vibrations from outside sources, the mirrors move discrete amounts in random directions on the order of micrometers. These motions are larger than the wavelength of the laser and during longer time measurements can become significant. The resolution of the photodetector is 0.5 degrees. Depending on the quality of optical equipment and induced vibrations from sources such as vacuum pumps, air conditioning units, and activity of people nearby, these have been observed to contribute over 30 degrees of uncertainty in the measurements over a 200 μ s timescale. The vibrational contribution to the change in phase shift is $2\pi\Delta x/\lambda$. This is significant and steps must be taken to insure that uncertainty due to vibration does not override the actual density measurements. It is assumed at times past about 25 μ s that the electron density is zero and neutrals and vibrations are the only contributing factor. This assumption is based on the idea that after the current pulse is over, all electrons have been accelerated out and no more are being created. Assuming also that the path length exposed to plasma for one laser pass is one inch, the measurable neutral density is:

$$n_n = \frac{\Delta\phi}{N} .388 \times 10^{15} \text{ cm}^{-3}$$

Eqn. 2

Where N is the number of passes, and $\Delta\phi$ is the change in phase shift. By taking data over a larger number of bounces, the resolution can be greatly increased depending on how low the vibration data is. Taking shots over a specific amount of time without firing the PPT will yield a $\Delta\phi$ that determines the vibrational limit to the PPT data taken. This sets the lower limit to resolvable neutral density. Any data that falls below this vibration limit is within the error bars and therefore unresolvable. Because of the pulsed nature of the PPT, it is not highly repeatable from pulse to pulse. The vibration error bars are then simply the standard deviation from 20+ measurements taken without the PPT firing. Over long times, the vibrational data will accumulate and swamp the neutral data.

V. Conclusions

The research performed here was not completed in the sense that actual data on a PPT was not taken when the program ended. However, a trip is being planned to take the final data necessary to validate the experiment. At this point, there were large amounts of error introduced into the experiment during PPT firings. At first these were mistaken for late time ablation of the teflon propellant, but when the thruster was covered so that no exhaust could cross the laser, the discrepancies were still measured. By taking the thruster off the optics table within the tank and firing, mechanical vibrations from the thruster were isolated and the anomalies were not present. It was therefore concluded that the false readings were due to induced vibrations from the thruster. In order to compensate for this, the thruster must be mechanically isolated from the optics table on which the Herriott Cell is mounted. This is a simple task, but due to time constraints was not performed. A final report on this diagnostic will be tendered when the actual PPT data is taken and verified.

VI. References

1. G. Spanjers, et al, "Investigation of Propellant Inefficiencies in a Pulsed Plasma Thruster" AIAA-96-2723.
2. J. Altmann, et al, "Two-mirror multipass absorption cell" Applied Optics, 1981, Vol. 20, No. 6, pp. 995-999.

MDICE ANALYSIS OF AN F-18C WING

Daniel J. Bodony
Graduate Student
Aeronautical and Astronautical Engineering

Purdue University
1282 Grissom Hall
West Lafayette, Indiana 47907-1282

Final Report for:
Summer Graduate Research Fellowship
Air Force Research Laboratory

Sponsored by:
Air Force Office of Scientific Research
Bolling Air Force Base, DC

and

Air Force Research Laboratory
AFRL/VAAC CFD Research Branch

August 1998

MDICE ANALYSIS OF AN F-18C WING

Daniel J. Bodony
Graduate Student
Aeronautical and Astronautical Engineering
Purdue University

Abstract

In this report, the process of creating a geometric model of an F-18C wing, gridding with structured and unstructured grids, and using the grids in a flow computation is described for a new methodology designed for aeroelastic computations. The new methodology, called MDICE, is a paradigm of distributed processing over a heterogeneous network with all processes controlled by one interface. Through MDICE, the user has control of geometry modeling, grid production, flow solving, and post-process visualization. Successes and failures of a first-time user of MDICE are presented and solutions to encountered problems are given where available. Project limitations resulted in not reaching an aeroelastic computation.

MDICE ANALYSIS OF AN F-18C WING

Daniel J. Bodony

Introduction

In an effort to better understand the aeroelastic behavior of an F-18C wing with missile pylons and to evaluate and refine a multi-platform methodology for aeroelastic computations, an analysis project was undertaken at Wright-Patterson Air Force Base, Dayton, Ohio, in the CFD Research Branch of the Air Force Research Laboratory (AFRL). The project, in conjunction with the Computational Fluid Dynamics Research Corporation (CFDRC) of Huntsville, Alabama, was to provide baseline experience with MDICE (Multi-Disciplinary Computing Environment), an integrated heterogeneous network analysis package, and to evaluate the overall performance and applicability of the MDICE suite by providing feedback to CFDRC and expertise to AFRL. The expertise developed at AFRL will then be used in future projects involving MDICE for more complex aeroelastic computations.

The project was divided into three segments as follows: first, an external grid was used to re-create the wing geometry, including rib- and section-cuts. Second, the wing geometry was used to produce a suitable grid for computation. Both unstructured and structured grids will be needed in the future but currently only a structured grid was used. Finally, the computational grid was input into a flow solver and a suitable test case was run.

Geometry Creation

Using an Air Force provided structured F-18C grid composed of 12 zones, the first task was to use CFDRC's CFD-GEOM¹ to re-create the underlying wing geometry for use in creating structured and unstructured grids. The main purpose for re-creating the grid was two-fold: first, the original grid was defined in such a way as to be incompatible with the FASTRAN flow solver (a few negative volume cells were present); and second, with aeroelastic computations in mind, point-to-point matching between a minimal number of logically placed zonal interfaces is a more efficient means of using a grid mover as the wing deflects. With point-to-point matching, the transfer of information from one zone to a

¹Unless otherwise specified, the following programs are part of the CFDRC MDICE suite: CFD-GEOM, CFD-FASTRAN, CFD-GUI, CFD-VIEW, LSS, and VCE

neighboring zone is done exactly without the need for complicated algorithms to ensure that mass, momentum, and energy are conserved over the zonal boundaries. Although MDICE has this ability built in, it was decided to avoid the problem altogether.

As this was the first time using GEOM, a couple of weeks were spent learning GEOM's capabilities and habits by going through the available documentation and tutorials. The learning curve was mildly quick for basic geometry and gridding functions but it was later found out that the higher level geometry commands, such as those controlling surface generation, were poorly documented, if at all. In addition to learning GEOM, the simple geometries and grids created were fed into the flow solver and used as sample cases with which to learn the MDICE scripting language as well as the overall picture of the interplay between the MDICE suite programs.

To create the geometry, the program CFD-GEOM was used to read in the external grid and then create appropriate rib- and cross-sections at various points on the wing and missile pylon. Initially all points were entered by clicking on the external grid points and then curves were manually created by "connecting the dots." A more efficient method was discovered by which GEOM would connect two points on the same i-, j-, or k-line with a B-spline curve, thus permitting two points to be used to create entire geometry curves. The wing geometry was defined using approximately 500 independent curves based on the external grid points. It should be noted that the geometry used is only as accurate as the provided grid, as the original IGES surfaces could not be obtained.

Once the curves were finished, the next task was to assemble them into usable surfaces from which the overall wing geometry could be constructed and eventually gridded. Creating the surfaces proved to be a difficult task due to the inconsistent definitions of the geometry curves. Because the external grid did not have point-to-point matching between zones, a zonal boundary curve could have a multitude of definitions, depending on which zone was used to create the curve. Thus, at zonal interfaces, the surfaces on one side of the zone would not match those on the other side because of the definition preference of the bounding curve. Surfaces created in this manner often had skewed grid points (control points) that resulted in unsatisfactory surfaces in regions of high curvature (see Figure 1). Although this problem is not substantial for creation of structured grids, the unstructured grid algorithm has significant difficulty resolving the surface oscillations, often causing the algorithm to fail.

The solution to the surface problem was discovered late in the project. By creating surfaces that did not have zonal boundary curves as boundaries and making small surfaces near the zone interfaces, a suitable surface could be created by "patching" surfaces together.

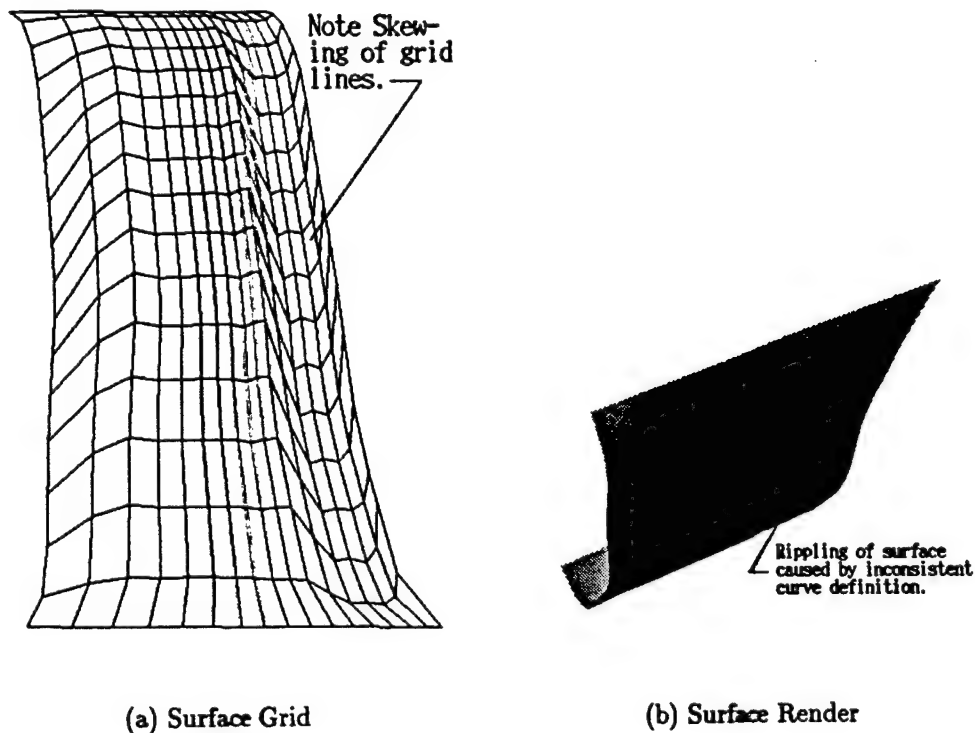


Figure 1: Surface creation problems with inconsistently defined curves. (a) shows original surface. (b) is the rendered version of (a), rotated for clarity.

Patching surfaces together, as discussed with a representative of CFDRC, causes GEOM to re-parameterize the boundary curves such that curves on opposite sides of a surface are parameterized in the same way, ridding the surface of ripples.

With the geometry curves and surfaces created, the wing was placed inside a computational domain of reasonable size to isolate the wing from non-freestream conditions. The overall domain is six span-widths wide, six span-widths tall, and nine chord lengths long, with three chords in front of the wing and five chords behind the wing. This domain allows for the top, bottom, and side farfield face to be treated as freestream with the front and rear faces as inlet and outlet boundaries, respectively. The wing root was treated as a symmetry boundary.

Grid Generation

With the wing geometry available, it was decided to create a structured grid first to more quickly reach the goal of aeroelastic computations. From previous in-house experience with aeroelastic analyses, the structured grid was required to have point-to-point matching between a minimal number of zones. In addition, the zones were to be defined such that a wing tip deflection would not create large included angles between the original and deflected grid lines. There were no other explicit grid requirements.

Using the upper- and lower surfaces of the wing as natural dividing surfaces, the subsequent portions of the domain were treated as separate. Starting with the wing geometry curves, a set of edges, curves that carry point distribution information, were created where necessary to resolve local regions of curvature while not putting too many grid points near the farfield boundaries to keep the total number of grid points feasible. Then, from the edge set, a number of surface grids (not the same as geometry surfaces) were defined to begin dividing the computational domain into six-sided boxes from which a structured grid could be created. In regions of high curvature, such as near the missile pylon nose, the surface grid did not accurately reflect the true geometry. To resolve this, surface grids were "associated" with underlying geometric surfaces onto which surface grid points are projected onto the geometry surfaces by solving the projection theorem optimization problem. In this manner, the surface grid is made to follow the geometry to within the tolerances defined in GEOM. There was a bit of problem, however, in this projection process near the missile pylon nose where the surface grid is required to undergo a ninety degree bend: the projection algorithm would consistently choose the wrong geometric surface to project onto. This problem was fixed by noting the algorithm chooses the correct geometric surface based on minimum normal distances so subdividing the surface grids near the nose met the required distance conditions.

Another problem area involved resolving a feature of the wing's geometry that needed degenerate surface grids to properly define. Shown in Figure 2 is the intersection of the outer and inner wing panels near the trailing edge. At the intersection, both the wing chord and thickness change discontinuously resulting in the degenerate faces shown. A surface grid spanning the intersection is unable to correctly resolve the geometry, so a separate surface, and eventually a separate zone, was used. GEOM's capabilities were limited in degenerate surface creation with the user having no control on choosing which side of the surface was degenerate. It was discovered, however, that by isolating the geometry, GEOM was capable

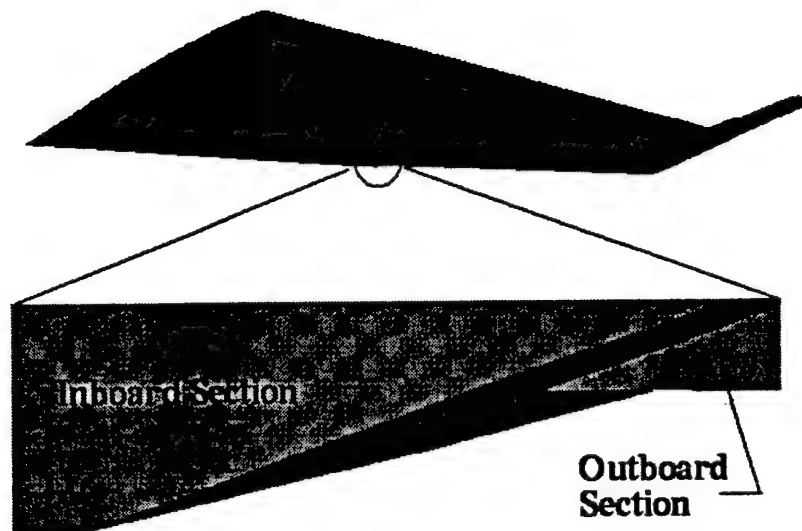


Figure 2: Detailed view of wing panel intersection.

of creating the required surface but necessitated copying the degenerate surface back into the original geometry. While workable, this method is problematic for very complex geometries and is undesirable for a finished product.

With the surface grids created, they were assembled into blocks that represent the (i, j, k) computational structure while describing the domain geometry. GEOM has the ability to composite blocks, allowing a large number of individual zones to be grouped together as a single structured entity. The domain was split into 20 total zones (10 on the upper half of the domain, 10 on the lower), each with point-to-point matching over interfaces. With this number blocks, a variety of grids could be created, depending on the application. An aeroelastic grid with two zones, one for the entire upper domain, one for the lower, met the requirements as stated previously by having only one zonal interface and, by placing the zonal boundaries at the edges of the domain, result in very small deflection angles. Both Euler and viscous grids were created to reflect the different resolution requirements imposed by the separate formulations, with the viscous grid packing 12 points at a spacing of $y^+ = 10$ near the wing surface, as suggested by the FASTRAN flow solver. Initial Euler computations

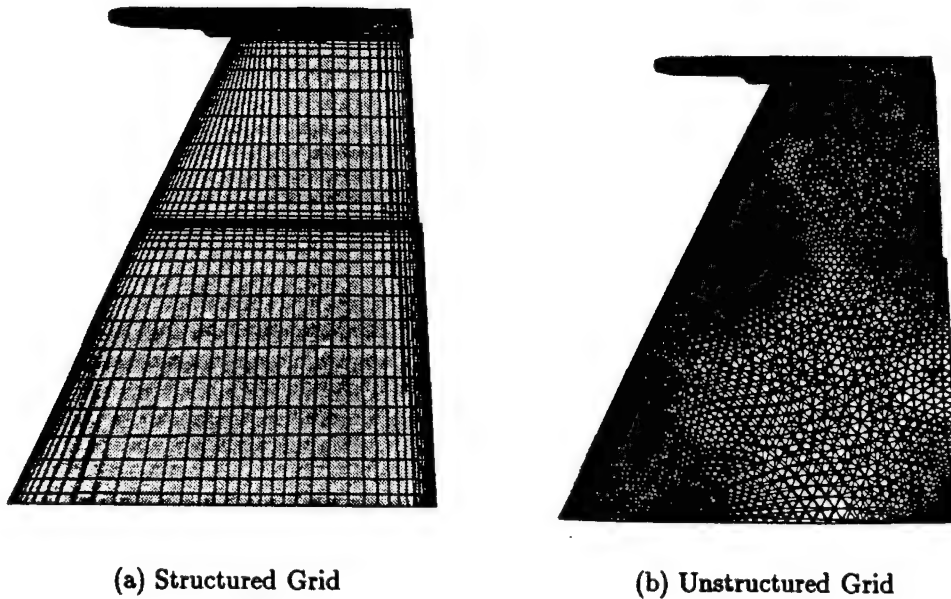


Figure 3: Example of grids created in GEOM.

showed that a shock existed on the upper and lower surfaces of the wing so both grids were adjusted to better resolve the compression region.

As a sidelight, an unstructured grid was produced to test out GEOM's unstructured functionality and to gain experience in grid generation. After patching to ensure all geometric surfaces did not have skewed grid lines, GEOM's unstructured algorithm was employed. A successful grid was created although no further work was done with it. Figures 3(a) and 3(b) show the wing surface with the two grids.

Computation

Continuing with the project, the next step was to run the grids through a flow solver using a set of freestream and boundary conditions. To save overall project time, the same set of freestream conditions to be run for the aeroelastic analysis were used to test out the grids, allowing a couple of refinement iterations. The conditions to be run were:

Mach 0.90 at 10,000 feet $AOA=0.675\text{deg}$

Mach 1.20 at 10,000 feet $AOA=1.109\text{deg}$.

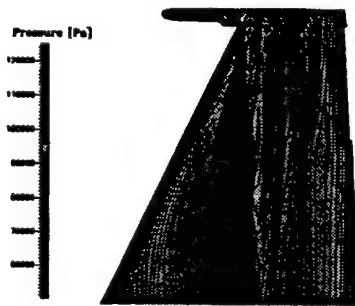
Starting with the Mach 0.90 case, the Euler grid was run to gain a feeling of how the

flow solver worked. The original two zone domain was broken up into six zones to permit splitting the workload between six SGI machines—three Octanes, two Origins, and one R10000 Indigo²—thus decreasing total computation time. Using VCE (Visual Computing Environment) as the parent process, the six flow solvers were started and controlled using a single interface that allowed dynamic passing of information between the flow solvers and visualization programs such as XMGR and CFD-VIEW. The solution was watched iteration by iteration in CFD-VIEW to witness the boundary condition influences and to stop the solutions at any point and make necessary grid refinements. In this manner, the solution was stopped three times to change grid spacing near the compression zone to reduce shock smearing. By following this method, convergence was not required before grid changes could be implemented.

Using ideas learned from the Euler computations, the viscous grid was attempted in the flow solver but without success. The flow solver was unable to start the solution with the viscous flags turned on so no viscous solution is available. However, the viscous grid was run inviscidly to 2000 iterations using a fully implicit scheme so that the inviscid solution could be used as a starting solution for future viscous runs. Figures 4-5 demonstrate various field variables in the computational domain.

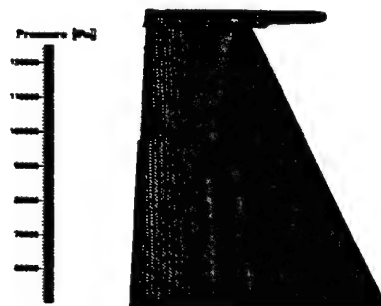
With the rigid, inviscid cases run as described above, it was next hoped to begin aeroelastic computations using the two-zone grid and the previous solution as a start. In discussions with AFRL personnel, a finite-element model of the F-18C wing was to be used to create the deflection mode shapes to be used in conjunction with the structural solver part of the MDICE suite. These mode shapes would be taken from the F-18C wing and mapped to a flat plate such that all structural modeling would use the flat plate with deflections and twistings computed from that plate and mapped back to the wing surface. Unfortunately, the structural information was unavailable at the time of this report and so no aeroelastic computations have been attempted.

M=0.90 @ 10Kft AOA=0.675deg



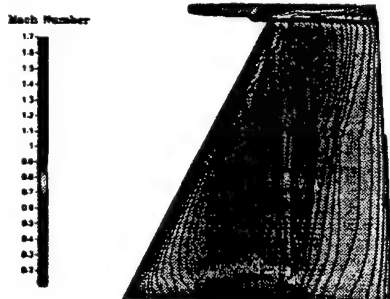
(a) Upper surface pressure contours

M=0.90 @ 10Kft AOA=0.675deg



(b) Lower surface pressure contours

M=0.90 @ 10Kft AOA=0.675 deg
(top view)



(c) Upper surface Mach contours

M=0.90 @ 10Kft AOA=0.675 deg
(bottom view)



(d) Lower surface Mach contours

Figure 4: Pressure and Mach number contours for inviscid solution.

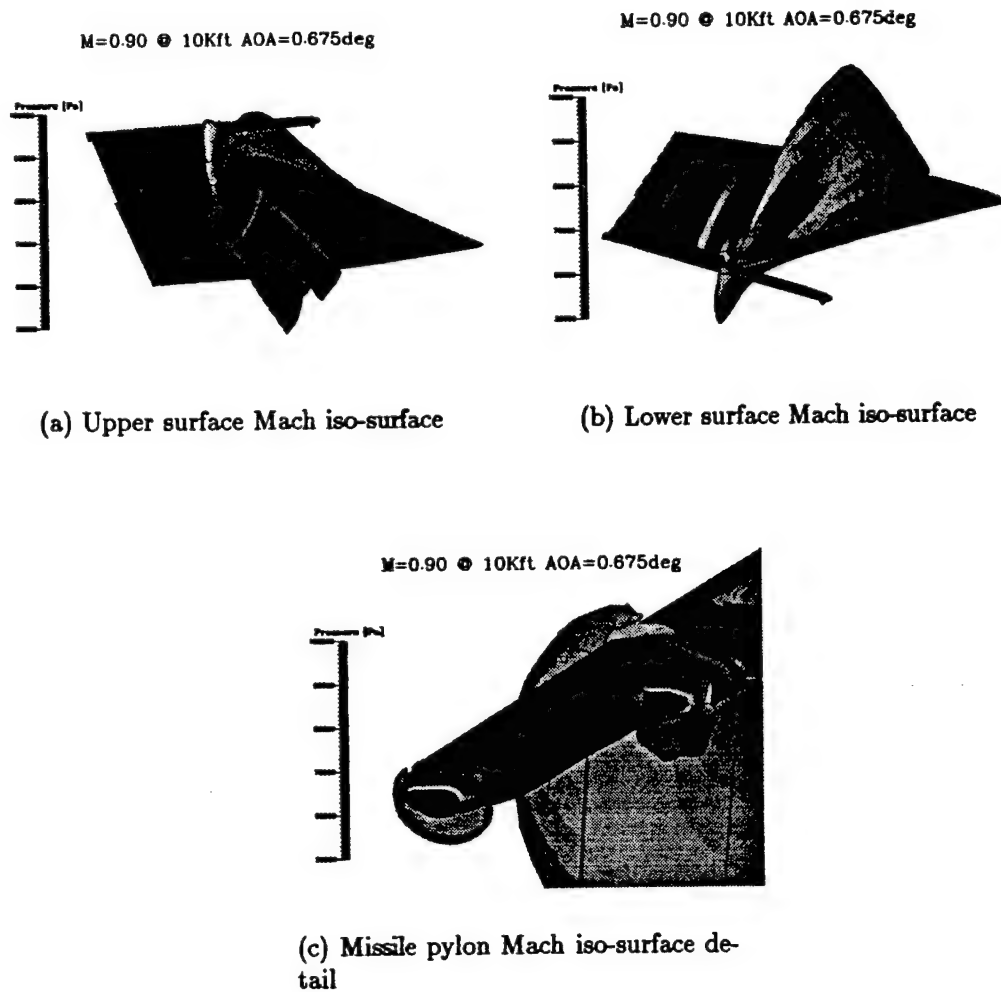


Figure 5: Mach one iso-surfaces for inviscid solution.

Conclusions

Although the project goals were not met in their entirety, the act of going through the process from geometry creation to post-processing with the MDICE suite has given AFRL an expertise for future attempts and has given CFDRC, the MDICE creator, valuable feedback for future revisions of the software. It was shown that given an external grid, it was possible to re-create the underlying geometry of an F-18C wing, produce both structured and unstructured grids, and apply a flow solver within a single interface. Additionally, all data was visualized and processed using the same interface.

When applied with all needed resources available, MDICE is capable of providing a single interface for aeroelastic computation. Moreover, given the structure of MDICE as an object-oriented interface, it is not limited to only aerodynamic problems; electromagnetic and orbit mechanic problems could be as easily attempted. Future projects with MDICE should involve the following steps:

1. Successful completion of the aeroelastic analysis described in this report,
2. Electromagnetic computation involving the coupling of fluid dynamics, as in magneto-hydrodynamics,
3. Application of Electrodynamics and orbit mechanics for a satellite in orbit, and
4. Extension of previous item to include free molecular dynamics and ion interaction with an orbiting satellite.

INTERACTIONS BETWEEN WEAKLY IONIZED GAS PLASMAS AND SHOCK WAVES,
A REVIEW

Gregory C. Harding*
Graduate Student
Aerospace Engineering Program
Division of Engineering Sciences

Florida Institute of Technology
150 W. University Blvd.
Melbourne, FL 32901-6988

Final Report for:
Graduate Student Research Program
Wright-Patterson Air Force Base, OH

Sponsored by:
Air Force Office of Scientific Research
Bolling Air Force Base, Washington, DC

and

Wright-Patterson Air Force Base, OH

August 1998

*Current Address:
The George Washington University
Joint Institute for Advancement of Flight Sciences
NASA-Langley Research Center
60 E. Taylor St.
Hampton, VA 23666

INTERACTIONS BETWEEN WEAKLY IONIZED GAS PLASMAS AND SHOCK WAVES, A REVIEW

Gregory C. Harding
Graduate Student
Aerospace Engineering Program
Division of Engineering Sciences
Florida Institute of Technology

ABSTRACT

Investigators have observed "anomalous" interaction effects between shock waves and weakly ionized gas plasmas (WIGs). The contribution of thermal inhomogeneities to the phenomena is unclear, but the observed effects exceed those that would occur in the case of simple heat addition. Characteristic phenomena include increased shock velocity, increased shock standoff distance, shock weakening, shock front dispersion, as well as other effects. Several models are presented which may describe mechanisms that could cause the observed "anomalous" effects. Observations of key issues and suggestions for future experiments are also included.

1.0 INTRODUCTION

The phenomena accompanying shock wave propagation through weakly ionized gas plasmas (WIGs) have recently received considerable attention in the United States. Russian scientists have researched the subject for approximately twenty years, and their studies have produced some striking experimental data. Now, both Russian and American data show that the use of WIGs on aerospace vehicles may significantly enhance vehicle performance by reducing drag, heat transfer, and by improving stability and control. Saeks [1] produced a thorough literature survey that summarized the major experimental phenomena observed by the Russian scientists and reproduced by investigators in the United States. Adamovich et al. [2] and Cambier [3] have also summarized the major experimental observations. A compilation of their summaries [1-3] is as follows:

1. Shocks accelerate in the plasma with an apparent change in the speed of sound.
2. The shock front widens (disperses), its amplitude decreases, and two or three shocks may form.
3. The shock standoff distance from a body increases with an accompanying decrease in supersonic drag.
4. A precursor wave develops ahead of the shock.
5. The effect occurs in a variety of gases: Air, H₂, N₂, CO₂, Ar, Ne, Xe, and He in longitudinal, transverse, DC and RF (radio frequency) discharges, and erosive plasma jets.
6. Evidence exists of an increase in electron density and conductivity upstream of the shock and a decrease in electron density and conductivity downstream of the shock.
7. The effect begins approximately 10^{-4} seconds after the start of the plasma discharge and disappears at approx. 10^{-2} seconds after discharge stops. This particular phenomenon has given rise to the term "plasma memory."
8. The effect is reduced in the presence of a transverse magnetic field.

Currently, investigators have not developed adequate models to describe the observed phenomena, and the physics behind the observed effects still remains a partial mystery. Since conventional physics can't, as of yet explain the observed phenomena, some researchers have dubbed it "anomalous." Thus, many investigators have relied on thermal models to explain the observed effects since linear electro-gasdynamics has so far failed to develop a sufficient theory [4]. Interestingly, a recent computational study [5] claims that much of the observed effects can be described by thermal inhomogeneities alone, but it does concede that thermal phenomena can't explain some of the observed effects.

2.0 DISCUSSION

Many researchers believe that they understand how much energy it takes to cause the observed "anomalous" effects. Consequently, many proposed mechanisms fall short on the grounds of insufficient available energy. Adamovich et al. [2] have stated the standard by which models are investigated: the general mechanism must release energy comparable to the incident flow energy flux or the incident flow enthalpy. As a result, researchers adopt theories and models with mechanisms capable of providing energy of such magnitude and discard ones with seemingly inadequate potential energy. The following paper discusses several models that have received considerable attention in the literature, both for and against, on the basis of postulated available energy.

2.1 DOUBTS ON PURELY THERMAL MODELS

It is well known that shock strength can be reduced by adding thermal energy to the flow, but researchers have not reached a consensus on the extent of the thermal contribution to the WIG/shock interaction phenomena. However, support for possible non-thermal contributions continues to mount [4-10,12,14-19]. Hilbun's thermal simulation [5] makes a case for thermal inhomogeneities as the primary cause of the observed phenomena, but others, such as Ganguly and Bletzinger [6], favor a combination of plasma and

thermal effects. Although Hilbun's thermal simulation [5] showed good agreement with density gradient photo-deflection and other experimental data of [6], he does make it clear that it cannot account for the observed phenomena of "plasma memory."

Malmuth et al. [7] note that shock wave velocity increases by approximately the same amount in both WIGs with gas temperatures of 1500-2000 K or cold discharge WIGs of 350-400 K. Thus, a purely thermal model will have difficulty reconciling these two cases.

Saeks and Kunhardt [8] report on experiments and simulations done by the USAF Arnold Engineering and Development Center that show a greater shock weakening due to WIG interaction than the weakening due to simple heat addition. Furthermore, Vuskovic and Popovic [4] reason that a completely thermal model cannot account for the reduced wave propagation velocity and dispersion in the presence of a transverse magnetic field or the apparent strengthening of the phenomena by the addition of ultraviolet light. In conjunction, Mishin [9] cites data that shows a speed of sound increase with ultraviolet irradiation. Vuskovic and Popovic further suggest that the electrodynamic nature of the observed effects is non-negligible, and that researchers must pay attention to the local charge separation across the shock.

2.2 ELECTRODYNAMIC EFFECTS & THE ELECTRONIC DOUBLE LAYER

The realization that electrodynamic effects may play an important role in WIG/shock interactions has prompted several other studies in this area. Some studies have produced new notions of plasmas that have internal structure. Mishin [10] has proposed a modified Van der Waals equation as the equation of state in the plasma that implies the formation of "quasi-structures" within the plasma. Mishin's model shows that increases in the specific heat ratio, γ , between 2 and 4 in the WIG are possible [9]. Furthermore, Froning and Roach [11] performed a complementary simulation where γ was artificially increased up to 4 in the vicinity of an airfoil. The simulation produced preliminary results which show a decrease in drag

with increasing gamma. In addition, Bose and Murthy [12] show that treating the WIG as a Van der Waals gas with repulsive forces shifts the shock front away from a body. Similarly, shock standoff distance also increases due to the estimated internal body force that develops from charge separation. Also, Adamovich et al. [2] cite a Russian work [13] that discusses the formation of a "polymer" structure with anomalous properties in the shock propagating through the plasma. Additionally, Cambier [3] suggests the existence of a "heterogeneous phase" of the plasma consisting of a network of electronic double layers arranged in a fractal structure.

Several recent papers and presentations [1-4,14,16,22] have addressed the notion of the electronic double layer (EDL) and its candidacy as a possible mechanism for the "anomalous" phenomena. Simply stated, an EDL is a region of positive space charge layered next to a region of negative space charge in a plasma that gives rise to localized electric fields. Different theories exist on how EDLs contribute to the observed effects. Both Sacks [1] and Cambier [14] have developed interesting models.

EDL Model 1:

Sacks and Kunhardt [16] posit the existence of an EDL at the shock surface itself. They cite experimental work by Mishin [15] that shows an increase in electron density and conductivity ahead of the shock front and a similar decrease behind the shock front. Sacks and Kunhardt theorize that once a shock wave passes into a glow discharge, the free electrons in the plasma remain in front of the shock due to their high drift velocity and low collision cross-section, while the relatively large and slow ions get carried behind the shock front by the neutral particle flow. Thus, a negative space charge forms ahead of the shock and a positive space charge forms behind it as in Figure 1.

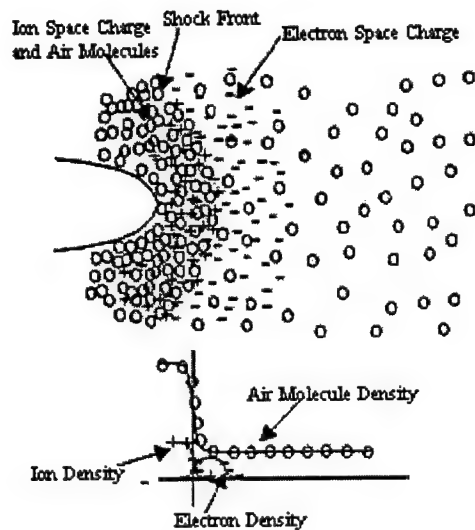


Figure 1. Sketch of an EDL at a Shock Front from Sacks and Kunhardt [16]

Sacks' and Kunhardt's model depends on two interrelated effects: mechanical and electric. The mechanical effect (based on collision cross-sections) will see an enhancement or degradation depending on the direction of the electric field. An enhancement will occur when the electrons drift in a direction upstream of the shock front since the natural drift will augment the modeled charge separation at the front. Sacks and Kunhardt reference the fact that many of the related experiments use a longitudinal electric field with the cathode located closest to the origin of the shock wave. Thus the drift of the electrons toward the downstream anode may enhance the charge separation in the EDL.

Although Adamovich et al. [2] found that the kinetic energy inherent in an EDL effect was insufficient to create the observed effects, Sacks and Kunhardt [16] point out that their analysis didn't account for the Coulomb forces in the EDL. Accounting for the Coulomb forces may explain the observed shock standoff distance increase. This may occur due to the mechanical coupling between the positive ions and neutrals

behind the shock combined with the attraction due to electrons ahead of the shock that pulls the shock upstream.

Furthermore, Saeks and Kunhardt [8,16] show the appreciable effect of the repulsive Coulomb forces within the EDL. They have also developed an expression for the speed of sound in the space charge. From Saeks and Kunhardt [8,16], the speed of sound in a space charge is

$$c_{SC} = \sqrt{\frac{\gamma K_n + \gamma K_i + \gamma Q_i + \gamma K_e + \gamma Q_e}{N_n m_n}}$$

$$= \sqrt{g \frac{N_n m_n v_n^2}{3 N_n m_n} + g \frac{N_i m_i v_i^2}{3 N_n m_n} + g \frac{e^2 k [N_i - N_e] N_i^{2/3}}{N_n m_n} G_{SC} + g \frac{N_e m_e v_e^2}{3 N_n m_n} + g \frac{e^2 k [N_e - N_i] N_e^{2/3}}{N_n m_n} G_{SC}}$$

where subscripts n , i , and e indicate neutral, ion, or electron respectively. K represents the kinetic pressure term, k is the Coulomb's Law constant, e is the charge of an ion ($1.60 \times 10^{-19} C$), and Q represents the additional effective ion or electron pressures due to the Coulomb forces in the space charge of the EDL. N , m , and v represent the concentration, mass, and velocity of the particles, and γ is the ratio of specific heat of the gas at constant pressure and volume. G_{SC} represents a volume integral which incorporates the electron field geometry and Coulomb's Law. From Saeks and Kunhardt [8,16], for the case of the positive space charge behind the shock front, the above equation for the speed of sound becomes

$$c_{PSC} = \sqrt{401 \times T_n + 1.95 \times \frac{N_{if}^{5/3}}{N_{nf}} \times 10^{-2}}$$

where the first term in the expression is the neutral particle kinetic pressure, and the second represents the additional effective Coulomb pressure arising from the EDL. T_n is the gas temperature, N_{if} and N_{nf} are the freestream concentrations of ions and neutrals respectively. Thus, the space charge is shown to have a "non-trivial" effect on the local speed of sound for an ionization level of one part in 10^5 - 10^6 . However,

the formula for the speed of sound in the positive space charge assumes a uniform distribution of neutrals and electrons which will probably not occur in reality [8].

EDL Model 2:

Cambier [14] argues that due to the low ionization fraction in the WIG, an EDL at the shock front would need to have a potential on the order of 50 kV if it was responsible for the observed effects. He also cites work by Chutov [17] that measured shock polarization and found it to be only a few Volts. Instead, Cambier suggests that the “anomalous” effects might be explained if the plasma were composed of EDLs linked together in a fractal structure throughout the medium. The network would provide a means for rapid upstream heat conduction to create the precursor wave. The precursor will propagate with a speed which behaves as a function of the network connectivity with its upper bound as the propagation speed in an electron gas. Since the electrons carry out the heat conduction in this model, a transverse magnetic field would cause them to spiral around its field lines and thereby inhibit the upstream propagation of precursors.

From Cambier [14], the scaling law that relates the width L and potential ϕ of the double layer is:

$$\frac{e\phi}{T_e} = 0.1 L^2 \lambda_{De}^{-2},$$

where T_e is the electron temperature and λ_{De} is the Debye length. From the above equation for constant electron temperature and EDL potential, the Debye length and EDL width will increase with decreasing electron density. Thus, for low currents the EDLs may be thicker thereby forming a denser fractal network. The heat conduction might then be more difficult to suppress with a transverse magnetic field. This may explain the observed phenomenon that the magnetic field strength required for suppression increases with decreasing current [3, 15]. The present model requires that the EDLs break down in order to release their electrostatic energy into the shock itself. However, the mechanism by which the fractal network might form and break down remains unclear [14].

Further indirect support for EDL models, particularly Saeks' and Kunhardt's, comes from Klimov [18] who points out that WIG/shock experiments involving supersonic drag reduction achieved maximal results when the direction of the electric current was optimal. As an aside, Klimov also notes that the drag reduction was better for an AC discharge than a DC discharge.

2.3 EFFECTS OF HEAVY PARTICLES ON WIG PROPERTIES

Biturin et al. [19] simulated WIG/shock interactions with the addition of micro- and nano-particles to the plasma. The results of their analysis further enhance the model of the space charge at the shock front. The apparent effect of the micro- and nano-particles was to enhance the charge separation thereby creating a strong electric field and high voltage across the shock front. This creates a significantly different plasma system with drastically different properties than a pure plasma. For a particular case of a Mach 2.5 flow with a molecular weight ratio of $2 \times 10^6:40:1$ for the super-heavy particles, heavy particles, and the neutral gas respectively, a potential difference of nearly 3000 Volts develops across the shock front as seen in Figure 3. Biturin et al. state that their simulations of electric field strength and voltage, Figures 2 and 3 respectively, across a shock front are in good agreement with experimental observations of [13] and [20].

Note: The natural log of the normalized distance, ξ , represents the distance from the shock front normalized to the mean free path length of the neutrals.

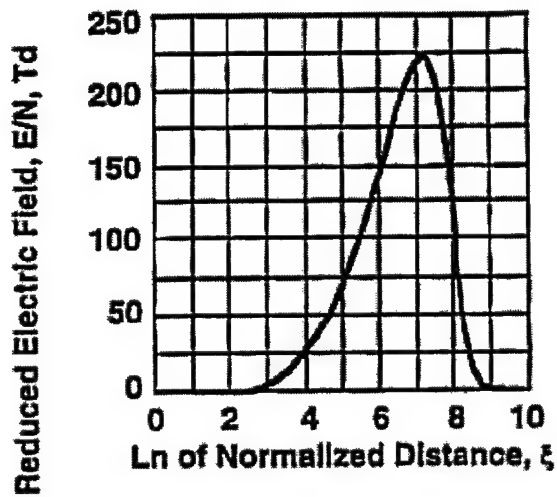


Figure 2. Reduced Electric Field Distribution from Bityurin et al. [19]

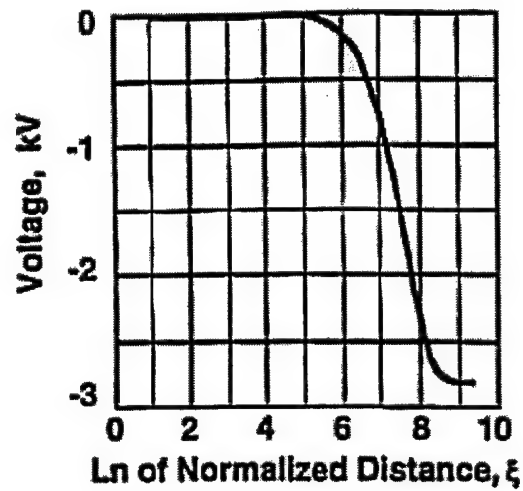


Figure 3. Electric Potential Distribution from Bityurin et al. [19]

Figures 4 and 5 show the results for electron density and electric field respectively for a five component plasma including the main gas, heavy negative ions, positively charged heavy molecules (clusters and nano-particles), main gas ions, and electrons.

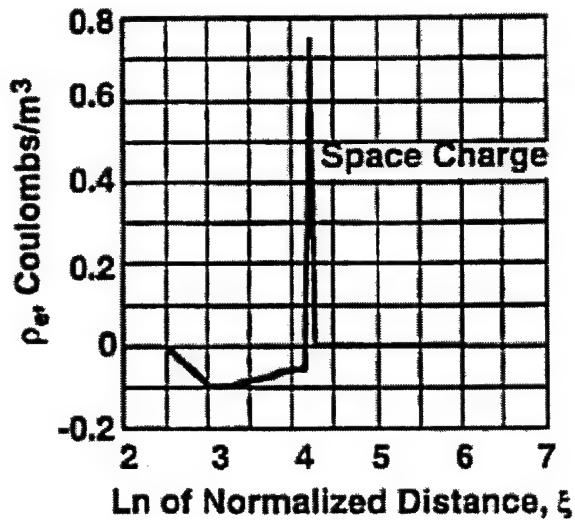


Figure 4. Space Charge Distribution for the Five Component Plasma from Bityurin et al. [19]

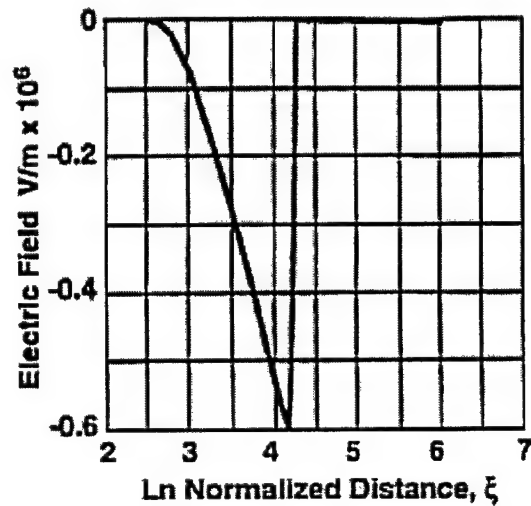


Figure 5. Electric Field Distribution for the Five Component Plasma from Bityurin et al. [19]

The potential difference across the shock presented by Bityurin et al. is in contrast to the work by Chutov [17] that measured the polarization of the shock and found it to be only a few Volts. Furthermore, Macheret et al. [22] have calculated the potential drop across an EDL to be 1 - 5 Volts for a typical glow discharge (assumed to be a pure plasma). However, independent research in dusty plasmas may provide some insight into the discrepancies. Yu et al. [21] studied plasmas near conducting boundaries with minute amounts of dust. Their work shows that the presence of dust will lead to vastly different behavior than that of a pure electron-ion plasma. Goree [23] cites several sources which show that charged dust grains in low-temperature plasmas can modify or dominate "wave propagation, wave scattering, ionization balance, shock propagation, and gradient and velocity-space-driven instabilities." Thus, the purity of the WIGs comes into question.

Even though Macheret et al. [22] calculated a potential drop across an EDL of only 1 - 5 Volts, they subsequently calculated the energy flux imparted to the shock via ion-neutral collisions induced by their pure plasma EDL potential. Due to the small ionization fraction of the WIG, this energy flux was determined to be small. However, another subsequent calculation shows that this small energy flux could begin to weaken the shock in as little as 1 - 10 cm. For some Mach numbers, this range of distances would correspond to the observed time constant of 10^{-4} seconds before the "anomalous" effects begin to occur.

2.4 KINETIC MODELS OF HIGHLY EXCITED ELECTRONIC STATES

Another possible mechanism for the observed "anomalous" effects in WIG/shock interaction is energy storage in highly excited electron states within the WIG [3,7,14]. However, Adamovich et al. [2] and Cambier [3, 14] have shown that highly excited Rydberg states do not couple strongly to neutrals or exist in sufficient density to cause the observed effects respectively. Nonetheless, Cambier [14] suggests that highly excited Rydberg states could have a high density and appreciable effect on the system if the electron

densities are in equilibrium with the electron temperature where inelastic collisions are dominated by electron impact (suppression of quenching from de-excitation by atomic collisions).

Malmuth et al. [7] studied a model of highly excited electronic states where electrons have a dominant role and atomic quenching is limited. However, Malmuth et al. caution that the model is only a first rough approximation since they consider the upper bound of energy stored in highly excited states. For the case considered (typical of most glow discharge conditions), the energy available from highly excited states was estimated to be approximately 3×10^{16} eV/cm³ most of which could be released as heat behind the shock wave. They found that inclusion of this energy greatly improved agreement with experimental data of a 1-D shock and a hypersonic sphere penetrating a plasma. The following figures contain notations marked "Experiment [4]" and "Experiment [8]" which correspond to references [25] and [26] of this paper respectively. Figures 6 and 7 below show the improved agreement of the present model with experimental data.

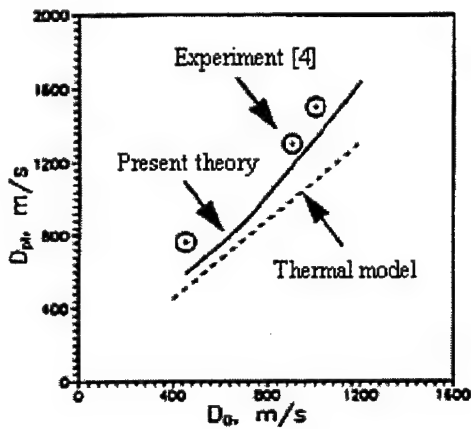


Figure 6. Dependence of Shock Speed in Plasma Versus the Initial Shock Speed in a Gas from Malmuth et al.[7]

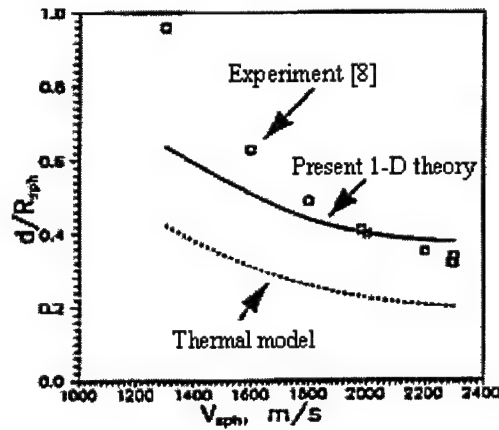


Figure 7. Dependence of Normalized Shock standoff Distance from a Sphere Versus the speed of a Sphere from Malmuth et al.[7]

3.0 OBSERVATIONS

Through the course of the present review, the author has noticed various trends and assumptions in the literature which warrant comment. First, the pure electron-ion plasmas analyzed in theory and the plasmas which exist in the laboratory may have greatly varying properties. Secondly, the plasmas generated for experiment may not have spatially homogeneous properties as is often implied. Lastly, many researchers believe that the low ionization fraction in a WIG remains constant as the shock passes through it.

Most analytical, computational, and experimental studies [2,3,5-8,14,22] consider pure electron-ion plasmas (ions, electrons, and neutrals) as their basis, while relatively few [13,19,20] consider contaminated plasmas in which heavy microscopic particles also exist in the system. In light of studies that show that microscopic particles can greatly influence the behavior of a plasma system [19,21,23], the question of plasma purity in experiments, analytical or computational studies, and in possible application environments becomes important. If plasma generators are used in the atmosphere on aircraft, impurities will certainly play a part in the system. When WIGs are created in the laboratory by electrodes exposed to the gas, electrode erosion will certainly contaminate the system. If erosive plasma jets are used, then contaminants will be present in large quantities. Hence, the inclusion of measured or probable amounts of micro- and nano-particles in the WIG system may modify the existing models of WIG/shock interaction or shed new light on the existing phenomena. The question is then to what extent do dust grains effect the plasma system, and at what point are their particle densities low enough to neglect their presence?

In terms of plasma homogeneity, the weakly ionized gases involved in the relevant experiments and simulations are labeled "glow discharges." The use of the term "glow discharge" implies that the electric field within the plasma is nominally uniform (distortions do exist due to space charges). Mishin [9] supports this assumption by reasoning that the plasma properties in the WIG "should be isotropic, except of course for the electrode zones." However, if the geometry of the electrodes is at all sharp as in [6], the probability of a corona discharge occurring increases. A corona discharge is also a weakly ionized gas like the glow discharge, but due to the sharpness of one electrode, locally intense ionization, serious electric

field distortion due to highly dense space charges, intense ultraviolet light emission, and secondary ionization can occur [24].

Charged particles can also produce intense non-uniform electric fields which resemble those of corona discharges [27]. The charged particle effectively acts like the sharp needle point used to create corona discharges in the laboratory. If a negatively charged cluster of particles with an appreciable electric field (microscopic dust) existed at a shock front in a plasma, then ions, electrons, and neutral polar molecules would be subject to its strong field. The positive ions and electrons will then experience body forces toward and away from the charged cluster respectively. Therefore, even if the electric field does not cause a local corona discharge, the charged cluster will enhance charge separation and precursor development.

If the WIGs under consideration possess corona-like characteristics, then the current models for WIG/shock interaction that assume a uniform electric field may need to be modified. Furthermore, if corona-like regions occurred at the shock front, then the local ionization fraction could increase to a much higher level than in the freestream. Since corona discharges emit intense ultraviolet light, the corona-like shock front notion fits well with the observation that the "anomalous" effects are augmented with the addition of ultraviolet light. As above, charged dust grains may act as a stimulant for corona-like occurrences at the shock front by appearing like sharply pointed miniature electrodes.

A common problem with many models under consideration in the literature is that they apparently produce only small energy fluxes which appear insufficient to cause the observed effects. Many of these "failed" models might provide sufficient energy flux at higher ionization levels which are not characteristic of weakly ionized gas plasmas. If there was in fact intense local ionization due to some mechanism, then many of the models might begin to show appreciable effects.

4.0 SUGGESTIONS FOR FURTHER WORK

Although the models primarily discussed in this paper deserve further consideration based on initial analysis, the thermal effects have not yet been sufficiently separated from other "plasma" effects. A fundamental experiment which finally separates thermal effects (pure heat addition and temperature gradients) from plasma effects must be performed. In a shock tube apparatus such as [6], one could perform a series of three experiments in an attempt to determine which effects are thermal and which are not. The general procedure might consist of the following:

1. Quantify the behavior of a shock in a no plasma, non-thermal environment in the shock tube (baseline measurements).
2. Quantify the behavior in a "plasma off," thermal environment where the thermal equilibrium environment is created by the plasma and then the plasma is turned off shortly before the test. The remaining thermal environment might be very close to the "plasma on" environment if the rate of thermal dissipation is slow.
3. Quantify the behavior in the "plasma on" environment and compare the differences between steps 1, 2 and 3.

Following the differentiation between thermal and plasma effects, the same apparatus could be used to measure the effects of microscopic particles in the system and the effects of electrode polarity. Finally, a measurement of electron and ion concentrations locally fore and aft of the shock wave front would be critical for determining the cause of the plasma effects [28].

ACKNOWLEDGMENTS

This work was sponsored by the Air Force Office of Scientific Research, Bolling AFB, Washington, DC. The author also wishes to thank Dr. Paavo Sepri and Dr. Richard Rivir for many fruitful discussions.

REFERENCES

- [1] Saks, R., "Weakly Ionized Gas Drag Reduction Tutorial," Addendum to the Final Report on Air Force Contract F33615-97-C-2739, 1998.
- [2] Adamovich, I.V., J.W. Rich, V.V. Subramaniam, and S.O. Macheret, "Shock Wave Propagation in Weakly Ionized Plasmas," *Proceedings of the Workshop on Weakly Ionized Gases*, USAF Academy, Colorado Springs, CO, Paper Y, June 9-13, 1997.
- [3] Cambier, J., "Shock Dispersion in Weakly Ionized Non-Equilibrium Plasmas: Evidence of a New Heterogeneous Phase?" *Proceedings of the Workshop on Weakly Ionized Gases*, USAF Academy, Colorado Springs, CO, Paper C, June 9-13, 1997.
- [4] Vuskovic, L., and Popovic, S., "Supersonic Motion of a Spherical Body in Weakly ionized Gas," *Proceedings Supplement of the 2nd Workshop on Weakly Ionized Gases*, Norfolk, VA, pp. 101-111, April 24-25, 1998.
- [5] Hilbun, M., *Shock Waves in Nonequilibrium Gases and Plasmas*. Ph.D. Dissertation, Air Force Institute of Technology, pp. 194-196, October, 1997.
- [6] Ganguly, B.N., and P. Bletzinger, A. Garscadden, *Physics Letters A* 230 (1997) 218-222, June, 1997.
- [7] Malmuth, N., V. Soloviev, V. Bytchkov, H. Hornung, V. Krivtsov, A. M. Konchakov, A. Tsekis, S. Palinswamy, K. Lee, S. Ramakrishnan, D. Ota, I. Goldberg, A. Fedorov, and P. Bellan, "Plasma Aerodynamics Research at the Rockwell Science Center," *Proceedings of the 2nd Workshop on Weakly Ionized Gases*, Norfolk, VA, pp. 69-99, April 24-25, 1998.
- [8] Saks, R., and E. Kunhardt, "On the Speed of Sound in a Weakly Ionized Gas," Accurate Automation Corp. Technical Report, October, 1997.
- [9] Mishin, G.I., "Equation of State for a Weakly Ionized Gas-Discharge Plasma," *Tech. Phys. Lett.* Vol. 23 (7), pp. 570-572, July 1997.
- [10] Mishin, G.I., "Sonic and shock waves in gas-discharge plasma," *Appl. Phys. Lett.* 71 (1), July 7, 1997.
- [11] Froning, H.D., Jr., and R.L. Roach, "Transonic and Supersonic Drag Reduction by Electro-Magnetic Discharges and Heat Addition," *Proceedings of the 2nd Weakly Ionized Gases Workshop*, Norfolk, VA, April 24-25, 1998.
- [12] Bose, T.K. and S.N.B. Murthy, "Blunt Body Shock in Weakly Ionized Air," Unpublished Paper, NASA Grant No. NAG 1 1601.
- [13] Klimov, A.I., Gridin, A.Yu., and Mishin, G.I., "Plasma Condensation behind Shock Wave in Non-equilibrium Discharge and Ball Lightning," in "Ball Lightning in Laboratory," Khimiya, Moscow, 1994, pp. 175-183 (in Russian).

- [14] Cambier, J-L, "On the Possibility of an Heterogeneous Plasma Phase and its Effectss in Weakly Ionized Non-Equilibrium Plasmas," *Proceedings of the 2nd Workshop on Weakly Ionized Gases*, Norfolk, VA, pp. 165-188, April 24-25, 1998.
- [15] Mishin, G. I., "Sonic and Shock Wave Propagation in a Weakly Ionized Plasma," in *Gas Dynamics* (ed. Yu. I. Koptev), Nova Science Publishers, Commack, pp. 81-95, 1992.
- [16] Saeks, R., and E. Kunhardt, "Analysis of the Electronic Double Layer Effect in Weakly Ionized Gas Drag Reduction," *Proceedings of the 2nd Weakly Ionized Gases Workshop*, Norfolk, VA, April 24-25, pp. 113-117, 1998.
- [17] Chutov, Yu., I., *Prikl. Mathem. Tekhn. Fiz.*, No. 1, pp. 124-130, 1979 (In Russian).
- [18] Klimov, A., "Key Experiments in the Field of Plasma Gas Dynamics. Comparison of Experimental and Theoretical Results," *Proceeding Supplement of the 2nd Workshop on Weakly Ionized Gases*, Norfolk, Virginia, Page 61, April 24-25, 1998.
- [19] Bityurin, V.A. , V.Yu. Velikodnyi, and J.T. Lineberry, "On Structure of Shock Waves and Related Effects in Weakly Ionized Ionic Plasmas with Nano-Particle Admixture," *Proceedings Supplement of the 2nd Workshop on Weakly Ionized Gases*, Norfolk, VA, pp. 303-308, April 24-25, 1998.
- [20] Mishin, G.I., A.I. Klimov, and A. Yu. Gridin, "Pressure and Density Measurements in Shock Waves in Gas Discharge Plasma," *Sov. Tech. Phys. Lett.*, Vol. 17, No. 8, pp. 413-416, 1991.
- [21] Yu, M.Y, H. Saleem, and H. Luo, "Dusty Plasma Near a Conducting Boundary," *Phys. Fluids B* Vol. 4 (10), pp. 3427-3431, October 1992.
- [22] Macheret, S., L. Martinelli, and R. Miles, "Shock Wave Propagation in Non-Uniform Plasmas and Gases," *Proceedings of the 2nd Workshop on Weakly Ionized Gases*, Norfolk, VA, pp. 95-120, April 24-25, 1998.
- [23] Goree, J., "Ion Trapping by a Charged Dust Grain in a Plasma," *Physical Review Letters*, Volume 69, Number 2, pp. 277-280, 13 July 1992.
- [24] Arthur, K., *Fundamentals of Electricity and Magnetism*. McGraw-Hill, pp. 346-347, 1962.
- [25] Mishin, G.I., A.I. Klimov, and A. Yu. Gridin, *Sov. Tech. Phys. Lett.*, Vol. 17, p. 602, 1992.
- [26] Klimov, A.I., G.I. Mishin, A.B. Fedotov, and I.P. Yavor, *Sov. Tech. Phys. Lett.*, Vol. 15, p. 800, 1989.
- [27] Velkoff, H.R., *Investigation of the Effects of Electrostatic Fields on Heat Transfer and Boundary Layers*. Ph.D. Dissertation, The Ohio State University, 1962.
- [28] Ganguly, B. N., Bletzinger, P., Private Communication, June, 1998.

THE PHYSICAL BASIS OF BOID AND CROTALINE INFRARED DETECTION

John L. Hazel
Graduate student
CMD dept.

College of Engineering & Applied Sciences,
Western Michigan University,
Kalamazoo, MI 49908

Final Report for:
Summer Graduate Research Program
Wright Lab MLPJ

Sponsored by:
Air Force Office of Scientific Research
Bolling Air Force base, DC

And

Wright Lab MLPJ
Wright Patterson Air Force Base

September 30, 1998

THE PHYSICAL BASIS OF BOID AND CROTALINE INFRARED DETECTION

J. Hazel

Graduate student

CMD dept.

College of Engineering & Applied Sciences,
Western Michigan University,
Kalamazoo, MI 49908

Abstract

A hypothesis for the physical basis of neuronal action potential frequency shift due to changes in temperature of vertebrate thermoreceptors is presented. The mechanism of heat generation in the IR receptor organ of pit vipers is shown through finite element modeling of the receptor structure. The adsorption of IR radiation from a mammal is shown to give sufficient heating of the pit organ for supra-threshold stimulation of non-specialized thermoreceptor neurons present in the receptor organ.

THE PHYSICAL BASIS OF BOID AND CROTALINE INFRARED DETECTION

J. Hazel

Introduction

The snake pit organ is a fascinating adaptation that has been studied from the beginning to the end of the 20th century.^{1,2} Although it had been identified as a sensory organ, the particular stimuli that induced a response from the pit organ was not known until 1937 when Noble and Schmidt showed that the pits were sensitive to heat.³ In 1956, further studies by Bullock and Diecke using electrodes implanted in related neurons showed that the pit organs responded to IR radiation and temperature changes.⁴ Odor, sounds, visible light, air currents and moderate air temperature changes near the pit were shown to be ineffective stimuli. The mechanism of transduction has not been established; however a general consensus was established that the pit receptor functioned by detecting changes in pit temperature rather than by direct sensing of IR light.^{5,6,7,8}

The morphology of the neurons in the pit are very similar to vertebrate cutaneous "warm" thermoreceptors.(fig 1) Cutaneous "warm" thermoreceptors have highly branched, unmyelinated free nerve endings with high concentrations of mitochondria. Many studies of the morphology in snake IR pit receptors have been conducted.^{9,10} No specialized structure for snake IR receptor organs has been reported other than highly branched, unmyelinated free nerve endings and high mitochondrial density.

Recordings of pit neuronal action potentials taken during step changes in IR illumination compared to action potentials during heating and cooling of vertebrate cutaneous thermoreceptors support this consensus (Fig 2: a Hartline sci am; b spray or schmit?). These recordings displayed the dependence neuron action potential frequency had with respect to temperature. An increase in action potential frequency occurs with

increasing temperature. Using a stream of water flowing over the IR pit, Bullock showed that a change of 0.003C in 0.06 seconds (0.05C/sec) produced a detectable change in action potential frequency of the pit receptor neurons.¹¹ They also demonstrated that the radiation from a human hand 40 cm distant is enough to be detected via the pit receptor.

Methodology

Standard methods of calculation for radiation exchange between two circular disks¹² can be used to model the system of hand to pit radiation. A human hand has area of about 150 cm² which is approximately equal to the area of a 7cm radius disk. The crocotaline IR receptor pit has a radius of about 0.1cm. Figure 3 shows pit membrane heating rate calculations for a hand 50 cm away from the IR receptor organ. This calculation shows that a hand radiates enough energy to exceed the experimentally determined pit membrane threshold heating rate of 0.05C/s. Thus the change in temperature due to IR radiation exchange alone is sufficient stimuli for detection. The alternative model of retina-like direct IR photon sensing mechanism is not supportable by energy calculations. Calculations for the molecular conformational change induced by photons striking rhodopsin show that 2×10^{-19} Joule per molecule is required¹³. This compares favorably with the 3.7×10^{-19} Joule energy of a 535 nm visible wavelength photon. However the 3.6×10^{-20} Joule energy of a 6 m wavelength IR photon is much lower than needed to cause a conformational change. This six-fold energy deficit is a strong argument against any proposed photon detection mechanism existing in the IR pit receptor. The IR pit membrane can be viewed as a collector of energy that functions by conversion and accumulation of the photons' energy into more easily stored thermal energy. The summed energy of many weak photons is then much easier to detect.

Terashima¹⁴ measured the pit receptor generator potential versus time by exposing the pit to 3.7 second IR pulses. (Fig 4) This data showed a difference in the time constant

for the response of the generator potential during heating and cooling. Hartline suggested that this data indicated a nonlinear process. To test this hypothesis, we created a finite element computer model of the pit receptor membrane. This model was a one dimensional cross section approximation of a crocodile pit membrane. The 100 element layer model allowed specification of density, heat capacity and conductivity, and optical absorption. The radiation and convective components of the pit-air surface were also modeled. The innermost layer was given high values of heat conduction and capacity to account for the high density of blood vessels.

Results

From this model it became clear that if all the IR radiation was absorbed by the pit and then re-radiated from the membrane surface (corresponding to the receptor being modeled as a set of lumped parameters), one could expect the heating and cooling time constants to be nearly equal. The actual case is much more complex than this symmetric mode of heating and cooling. First, the IR radiation is not absorbed at the surface. The pit material is partially translucent so one can expect a large amount of the radiated heat conversion to occur inside the pit membrane. Figure 5 shows the dramatic heating differences between pit membrane models having constant-property (top panel) composition versus the more realistic, variable-property (bottom panel) composition. Second, the mode of cooling is dominated by conduction to the blood and convection from the surface, which contrasts with the radiation absorption being dominant during heating. Fig 6a shows a cycle of IR radiation applied to a constant property, partially translucent, membrane at $t = 0$ seconds and then removed halfway through the time course of the graph. Fig 6b is a trace along the temperature profile of Fig 6a showing the obvious difference in heating- versus cooling-rates due only to differences in mode of heat gain and loss. This simple version of the pit simulation could be developed in to a

much more representative model with additional parameters for input and measured values of pit thermal characteristics.

Discussion

From the above arguments, we propose that pit receptors operate as phasic thermal detectors. This leads to the question of how thermal energy is transduced into a neuronal action potential. This question is unanswered for vertebrate thermoreception in general.¹⁵ One difficulty is the well-established fact that no specialized structures exist in vertebrate thermoreceptors. This might beg the hypothesis that some specialized physiology, such as a special ion channel, would be responsible for the thermal responsiveness of these unspecialized neurons. No such channels or organelles have been found to date.¹⁶

The theory presented here assumes no specialization of the physiology in the warm receptor. We used only well established characteristics of neuronal components to explain the thermosensitive response of warm receptors. Two morphologic features associated with thermoreceptors can account for their thermal behavior. These features are the highly tapered/highly branched free nerve endings and lack of myelination. For simplicity, only "warm" thermoreceptors will be discussed in detail here although the response of other thermoreceptors may be explained by similar means.

Here the neuron must be viewed as a system in dynamic equilibrium with a characteristic frequency of action potentials. The dominant components of this model are the sodium channels, sodium-potassium ATPase, calcium channels and mitochondria. This model depends on the Na^+ permeability being controlled by diffusion, the probability of the channel being open, the rate of Na^+-K^+ being regulated by ATP concentration, oscillations of Ca^{++} resulting from action potentials¹⁷, and the recently discovered mitochondrial ATP production response to calcium concentration oscillations.

Fig 7 depicts the sequence of events responsible for maintaining the frequency of action potentials.

Since no special mechanism for thermoreception is specified, the above model should be true for all neurons; therefore, some differentiation between non-thermoresponsive neurons and thermoreceptors needs to be established. Recall that the sodium permeability of the neuron is controlled by diffusion and the probability of the channel being open. The channel-open probability function has a very high thermal response with a measured Q_{10} (the change in rate of reaction resulting from a 10C change in temperature) around 40 for the slow inactivating channel. This characteristic causes a relatively large increase of inward Na^+ current (I_{in}). Conversely, the Na^+-K^+ pump rate (I_{out}), which is controlled by the concentration of ATP, has a measured Q_{10} of 2.2. Therefore, the net inward current (I_{net}) increases with an increase in temperature causing the depolarizing of the neuron to proceed much more quickly, which in turn causes an increase in action potential frequency. This increased AP frequency is maintained until the mitochondria are able to react with an increased ATP production rate. This increases the Na^+-K^+ pumping rate and reduces I_{net} with a reestablishment of the steady-state action potential frequency. A temperature decrease produces a reduced action potential frequency until the mitochondria react with a reduced ATP production rate.

The change in mitochondrial ATP production is associated with a conformational change in the inner membrane (fig 8). The condensed state is associated with active respiration and a high ATP production rate. The "resting" state is associated with a low rate of ATP production. The conformational change in the inner membrane obviously has some time constant and this delayed response is critical in establishing the phasic thermal response of action potential frequency. A highly tapered structure, as in warm thermoreceptors, increases the surface area to volume ratio in the cell and therefore the Na^+/K^+ ATPase to mitochondria ratio. This higher ratio causes the necessary response in

ATP production per mitochondria to be greater than in an untapered neuron. This larger response takes longer and therefore enhances the thermal sensitivity of the action potential frequency.

Conclusion

The pit organs of crotaline and boid snakes are specialized structures designed to detect small changes in heat that result from impinging IR radiation from mammals. This function can be accomplished by the “warm” thermoreceptor neurons common to invertebrates. No specialized physiology is required to attain the high IR sensitivity. The high packing density and proximity to the surface of these common neurons is sufficient to explain the receptor function. However the physiology of thermoreception has not been elucidated. A new hypothesis presented here is that the thermoreceptor neuron acts as a self stabilizing oscillator through shifts in mitochondrial ATP production in response to thermally induced changes in action potential frequency. A possible biomimetic thermoreceptor could be produced by employment of slow inactivating sodium channels in a reconstituted or artificial cell membrane. The ion current through this membrane would change with changes in temperature and thus provide a detectable signal. The first step in developing this receptor would be to establish the structure of a suitable host membrane for the ion channels.

Fig 1. "warm" thermoreceptor neuron

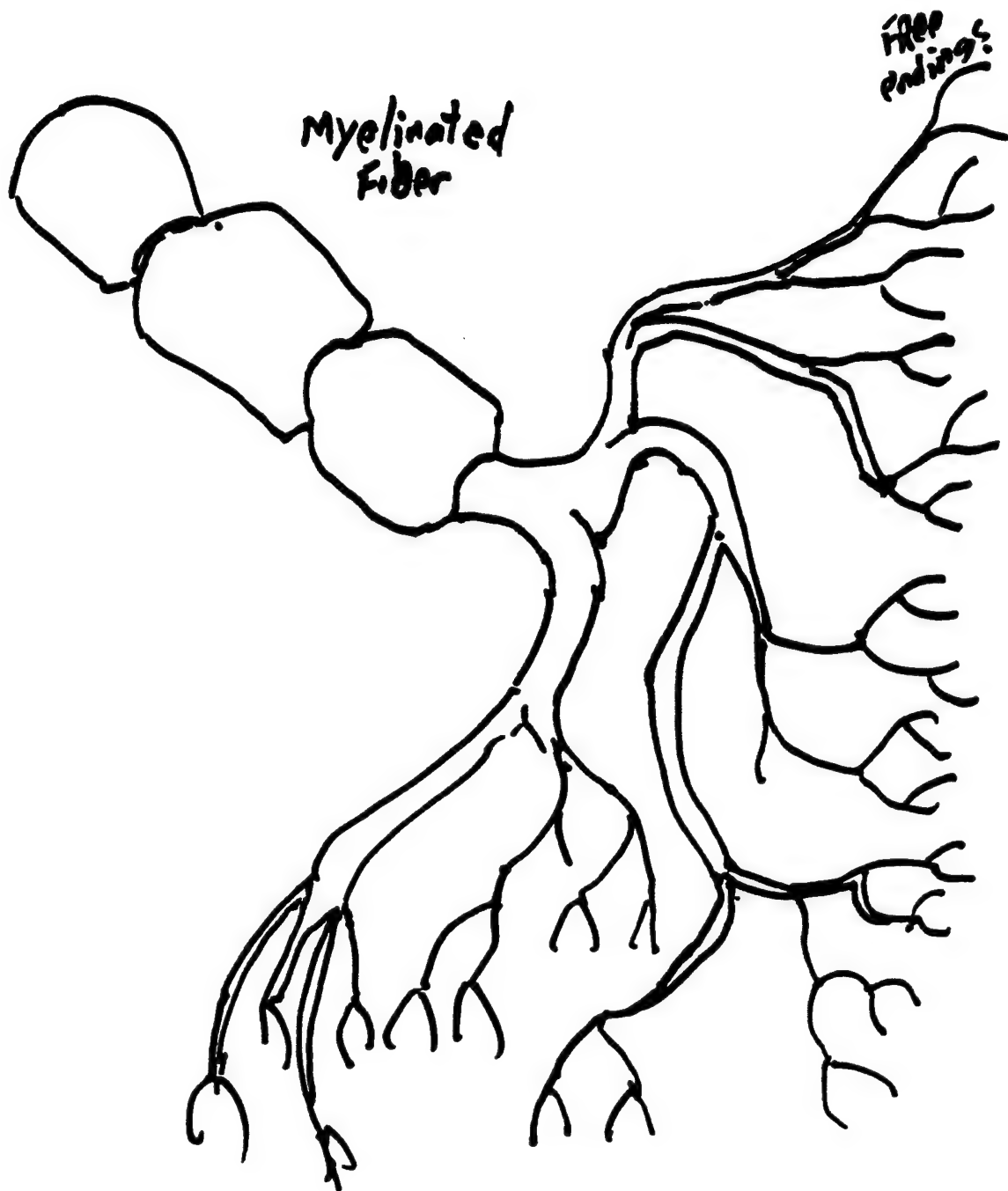
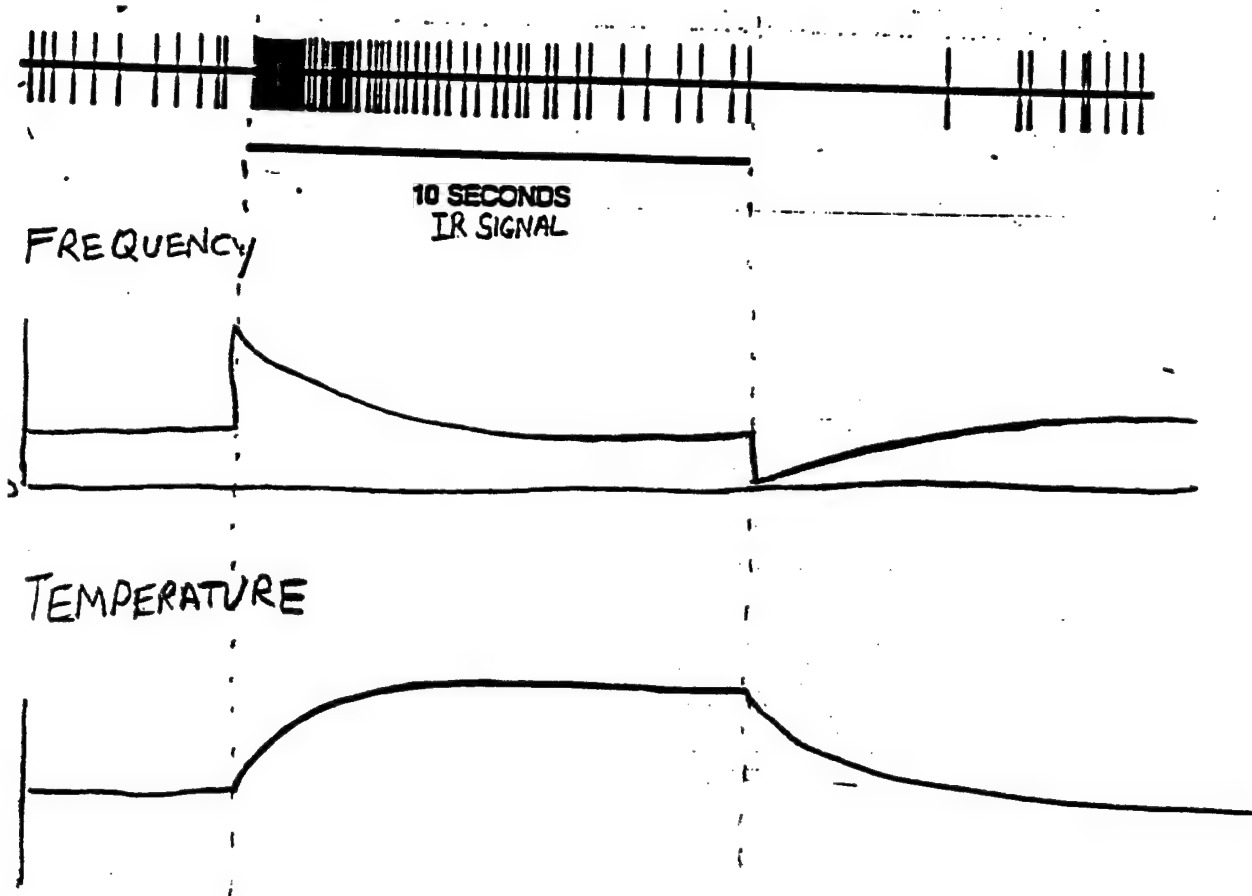


Fig 2.
ACTION POTENTIALS (NERVE FIRING)



John Hazel

Fig 3.

Human Hand Radiation to Crotaline Pit Membrane Calculation

T1= 310 K =hand temperature
T2= 295 K =pit temperature
h= 5.67E-12 W/(cm²*K⁴)

Power between infinite black plates $W=h(T1^4-T2^4)$

W= 9.42E-03 W/cm²

Shape Factor for Radiation Between Two Coaxial Parallel Disks

r1= 7 cm =radius of disk with same area as a human hand
r2= 0.1 cm =radius of pit receptor organ
L= 50 cm =pit to hand distance

R1= 0.14 =r1/L
R2= 0.002 =r2/L
S= 5.20E+01 = 1+(1+R2²)/(R1²)

F= 3.92E-06 =shape factor for pit-hand geometry
=0.5*(S-(S²-4*(r2/r1)²)^{0.5})

Total Heat Flux from Hand to Pit $Q= \text{area1} * F * W$

area1= 153.94 =hand area

Q= 5.69E-06 Watts

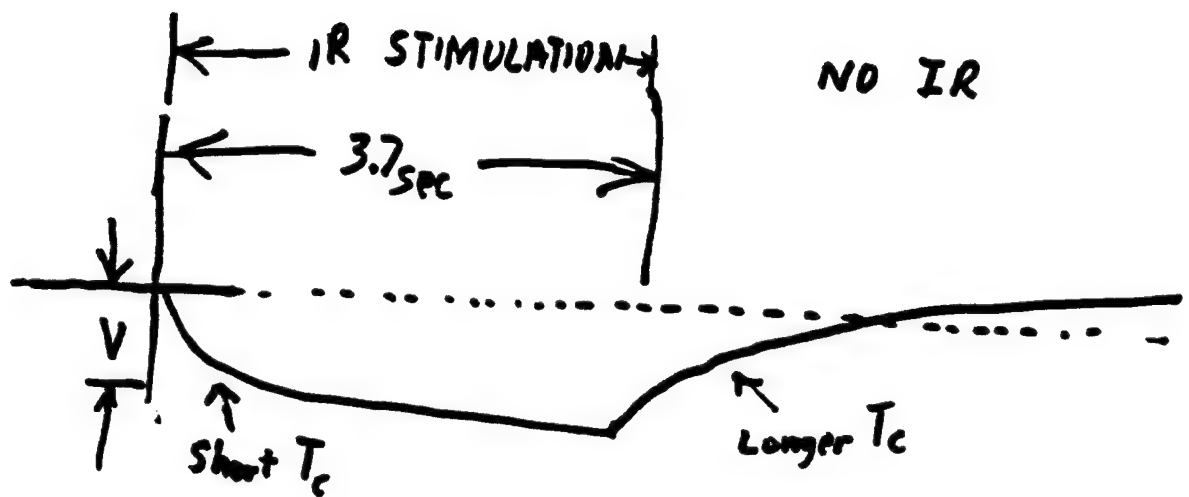
Initial Heating rate on Pit Membrane $Q/(Cp * m2)$

thick= 0.0015 cm =pit membrane thickness
area2= 0.0314 cm² =pit membrane area
rho= 1 g/cm³ =density of pit material
Cp= 2.2 J/g =Heat capacity of pit material

dT/dt= 0.0549 K/s

ref: Infrared Handbook

Fig 4.

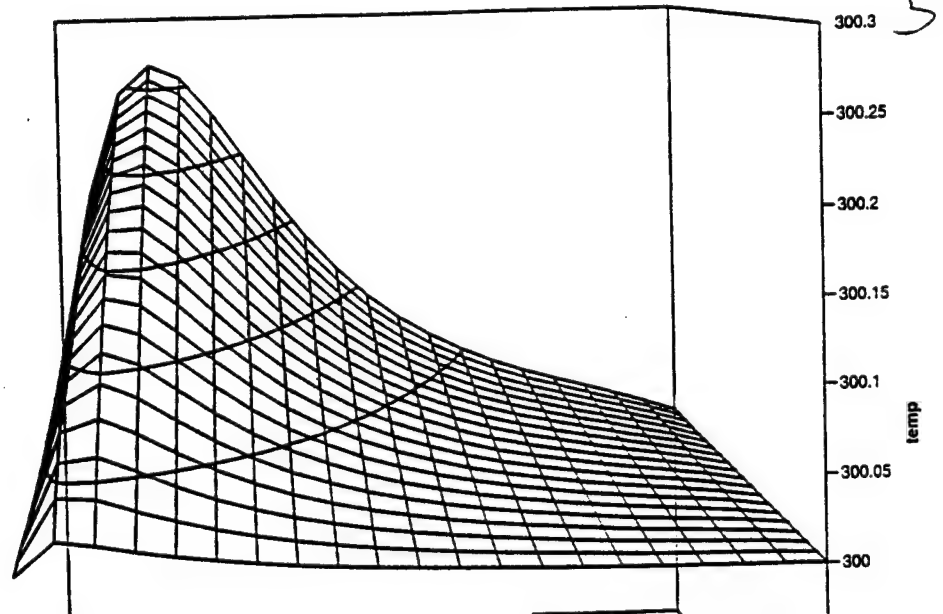


Receptor potential
response
after Tprashima 1968

Fig. 5

in thermal response

CONST



VARI

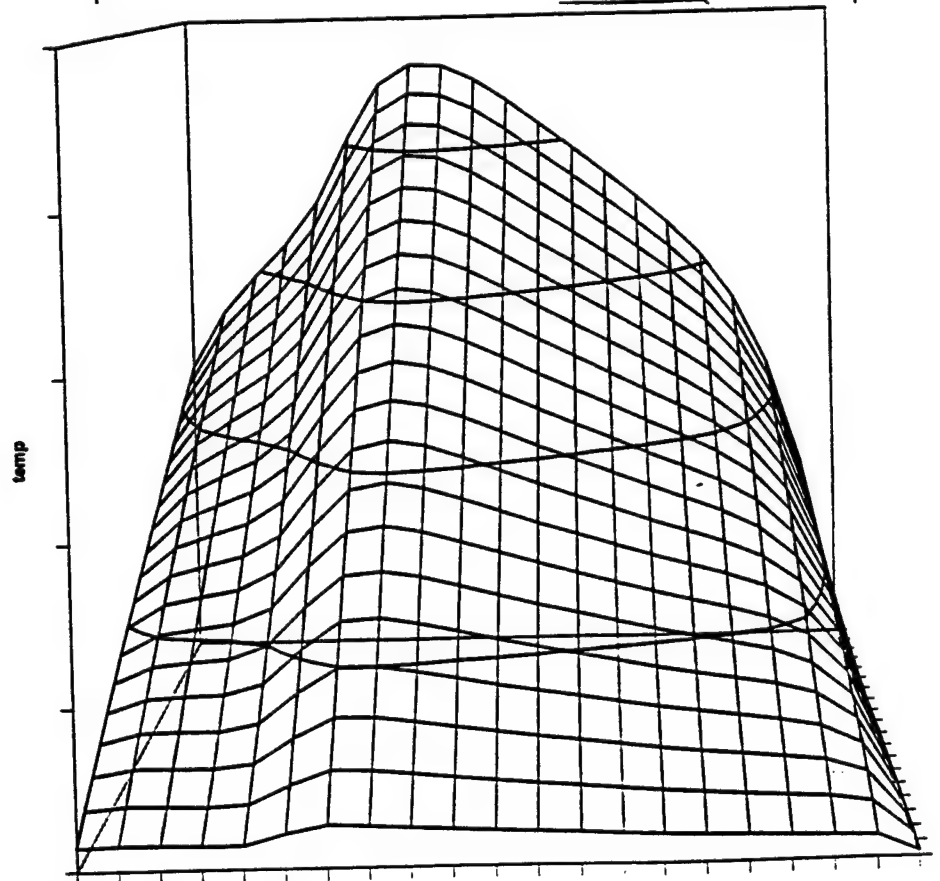
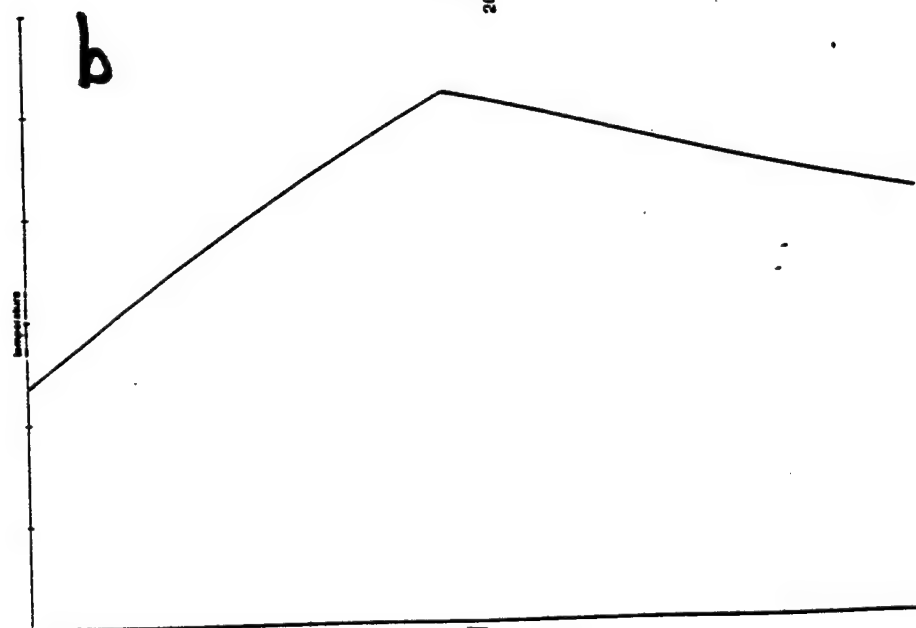
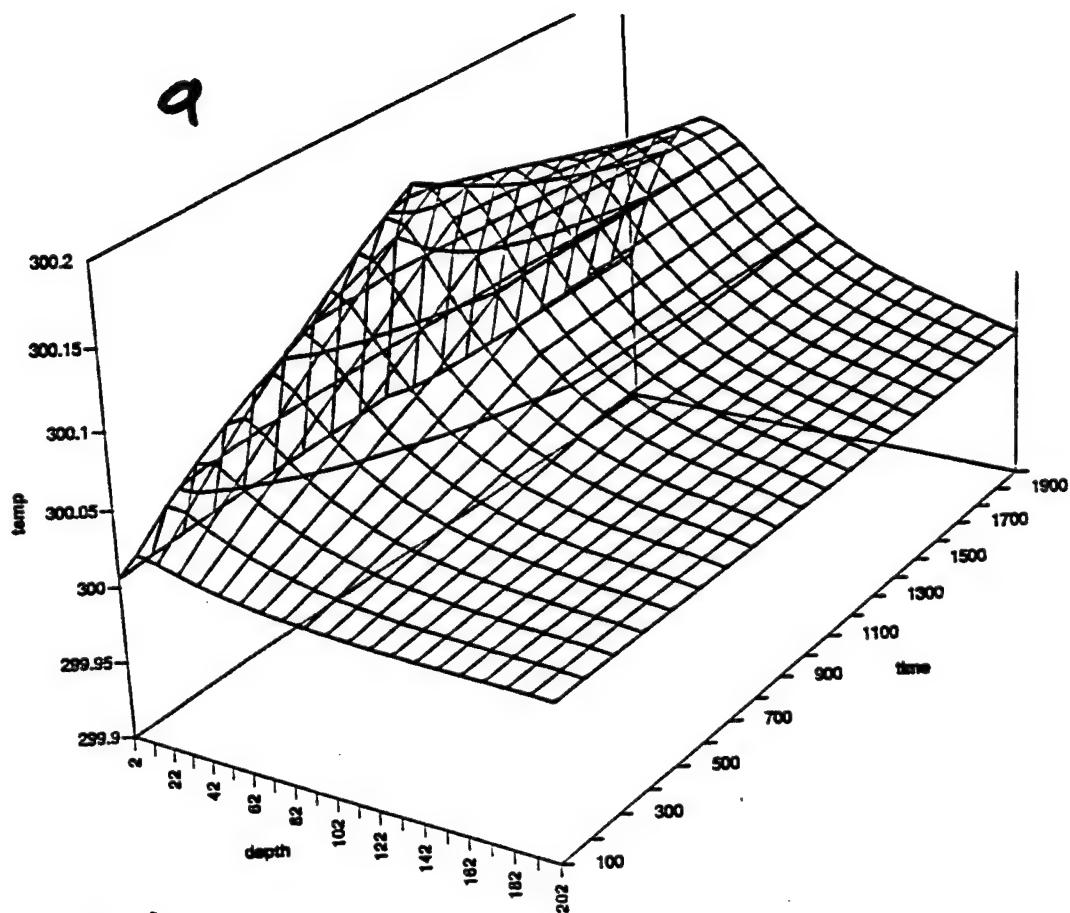


Fig 6.



ACTION POTENTIAL FREQUENCY REGULATION BY MITOCHONDRIA

If the frequency of action potential is too high (low), the $[Ca^{++}]$ oscillations in the cytoplasm stimulate the mitochondria to increase (decrease) production of ATP.



The increased (decreased) ATP production increases (decreases) $[ATP]$ in the cytoplasm.



Increased (decreased) $[ATP]$ increase (decreases) $Na^{+} - K^{+}$ ATPase pumping rate. (I_{out})



Increased (decreased) I_{net} caused a reduction (increase) in I_{net} .



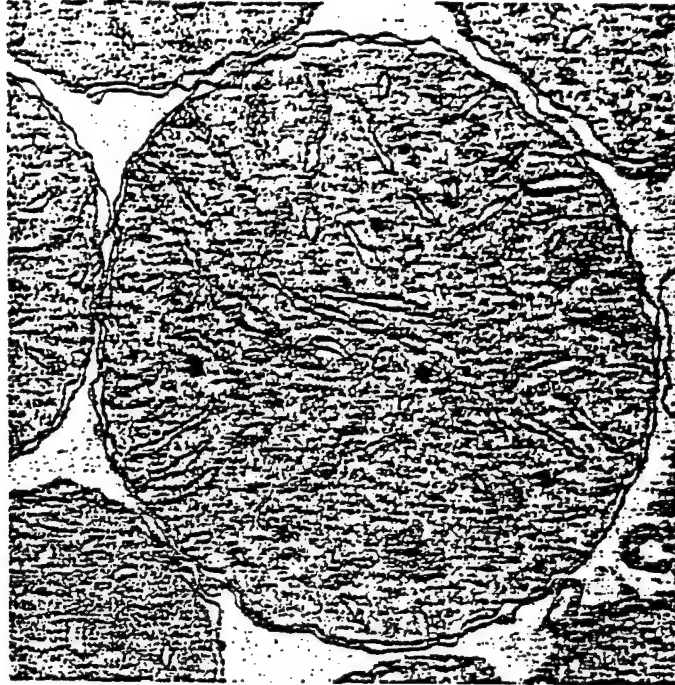
Lower (higher) I_{net} reduces cell depolarization rate.



Reduced (increased) cell depolarization rate increases (decreases) the time to reach the threshold voltage so action potential frequency is reduced (increased).

Fig 7.

Fig. 8



(b)



(a)

Figure 8-8-14

Electron micrographs of mouse liver mitochondria in (a) the actively respiring state and (b) the resting state. The cristae in actively respiring mitochondria are far more condensed than they are in resting mitochondria. [Courtesy of Charles Hackenbrock, University of North Carolina Medical School.]

ENHANCEMENTS TO A DIRECT AEROELASTIC STABILITY COMPUTATIONAL MODEL

Tim J. Leger
Graduate Research Assistant

J. Mitch Wolff
Assistant Professor

Department of Mechanical and Materials Engineering

Wright State University
3640 Colonel Glenn Hwy.
Dayton, Ohio 45435-0001
Ph: (937) 775-5040
Fax: (937) 775-5009

Final Report for:
Graduate Student Research Program
Summer Faculty Research Program
Wright Laboratories

Sponsored by:
Air Force Office of Scientific Research
Bolling Air Force Base, DC

and

Wright Laboratories
Wright Patterson Air Force Base, OH

December 1998

ENHANCEMENTS TO A DIRECT AEROELASTIC STABILITY COMPUTATIONAL MODEL

Tim J. Leger
Graduate Student

J. Mitch Wolff
Assistant Professor

Department of Mechanical and Materials Engineering
Wright State University

Abstract

The ability to accurately and efficiently predict transonic flutter boundaries is investigated using an enhanced direct computational method. Steady characteristic and unsteady approximate non-reflecting characteristic farfield boundary conditions are utilized to more accurately model the aerodynamic flow physics in a direct method. In addition, the aerodynamic model is modified to lock the movement of the farfield grid points while allowing the airfoil surface points to move freely. This is accomplished by introducing a linear weighting function in the grid deformation model. The direct method is based on a discretization of the Euler equations and a coupled set of structural dynamics equations representative of a pitch-and-plunge airfoil with trailing edge flap. The coupled equations are expanded to specify a Hopf-bifurcation point, which defines an incipient flutter state. Since the enhanced farfield boundary conditions improve the modeling of the flow physics, the computational domains can be reduced in size over similar models with simple freestream conditions. A flapped NACA 64A006 airfoil, executing pitching and plunging motion, is utilized to demonstrate the ability of the enhanced direct method to accurately and efficiently calculate flutter boundaries for reduced domain sizes. Both zero and non-zero angle of attack results are shown to highlight the improved accuracy and efficiency of the enhanced model. Each model modification resulted in analysis improvements, with the steady characteristic model demonstrating significant improvements in the nonlinear flow regime. For a 1° static pre-twist analysis at a transonic freestream Mach number of 0.84, the enhanced model resulted in over a 75% decrease in the flutter speed error. Therefore, the capability to more accurately and efficiently model transonic flow conditions with strong shock interaction has been shown.

ENHANCEMENTS TO A DIRECT AEROELASTIC STABILITY COMPUTATIONAL MODEL

Tim J. Leger
J. Mitch Wolff

Introduction

In the design of flexible aircraft structures, it is important to determine accurately and efficiently the flutter boundaries within which aircraft can safely operate. Using conventional computational fluid dynamics (CFD) methods, these boundaries are estimated through time integration of the governing dynamical (fluid and structure) equations. In a design environment, where a large number of configurations are examined, time integration with CFD techniques can be unsystematic and prohibitively inefficient. However, efficient aerodynamic methods currently used within aeroelastic design procedures are typically based on linear aerodynamics and, thus, are not well suited to transonic flutter computations. There is a need for a robust method of flutter prediction of sufficiently high fidelity to capture properly the nonlinear aerodynamics characteristic of transonic flight, but with sufficient efficiency to bring nonlinear aerodynamics to the design environment.

Recently, direct, or non-time-integration, methods have been developed that are suitable for both flutter prediction and steady aeroelastic analysis. Morton and Beran (1995,1996A) developed, implemented and validated the first direct method for the calculation of flutter points in 2-D transonic flow. The implicit methodology provides the ability to compute the critical speed, as an unknown of an expanded system of equations, at which the equilibrium fluid-structure system loses stability to periodic motions. For a soft flutter condition, the critical speed is the speed at which limit-cycle oscillation (LCO) is first possible, and becomes critical at a supercritical Hopf-bifurcation point.

There are advantages and disadvantages of the use of direct methods for flutter prediction relative to that of time-integration methods. The advantages are primarily three-fold: (1) direct methods avoid the need for bracketing, i.e., the repetitious application of a time-integration method to obtain stable and unstable equilibrium solutions about a presumed critical state, (2) the computational effort of direct methods is not time-step sensitive, whereas the computational effort of time integration is inversely proportional to the time step, (3) direct methods obtain an explicit representation of the aeroelastic mode that is associated with the loss of stability in the system. The primary disadvantage of direct methods to date has been the fully implicit and computationally expensive solution strategies employed to compute simultaneously the aeroelastic solution, critical aeroelastic mode, flutter speed, and flutter frequency. Still, for grids typical of inviscid, 2-D,

transonic airfoil calculations (2000-3000 grid points), Beran (1998) observed significant improvements (a factor of 50) in computational performance of a direct approach over an explicit, total-variation diminishing, time-integration scheme.

Direct methods based on bifurcation analysis have been improved and applied in several recent studies. Beran and Morton (1997) added a solution-path tracing capability to the direct solver called BIFAE to allow flutter boundaries to be automatically computed, and made numerous fundamental improvements to their algorithmic procedure. Morton and Beran (1996B) studied the flutter characteristics of an airfoil with bi-linear structural coupling, including freeplay, and later (1997) implemented a deforming mesh strategy and investigated the effect of a trailing-edge flap on airfoil flutter speed. Beran (1998) developed a new direct methodology within BIFAE that allowed robust computation of flutter states throughout the transonic regime and at angle-of-attack, and adopted a block-relaxation strategy that reduced computational work and storage requirements, especially for large grids. Most recently, Lee, Jiang, and Wong (1998) applied a similar bifurcation analysis to a pitch-and-plunge airfoil with a cubic nonlinear restoring force. In this work, the aerodynamics was modeled (i.e., not computed with CFD), allowing a system of reduced order to be studied. They also applied asymptotic theory to the computation of LCO amplitude for the supercritical, hard-spring case.

Beran and Morton (1997) noted flutter-speed sensitivity to domain size in the transonic regime, which resulted from the following: growth of the lateral length scale in the transonic regime; the relatively small domains used in their analysis (6 to 12 airfoil chords), and the enforcement of far-field conditions based on freestream conditions and extrapolation. To minimize the sensitivity in the transonic regime, a corrective action is required. Grid insensitivity could be achieved through domain enlargement. However, owing to the current use of a fully implicit solution methodology, direct flutter analysis with computational grids of increased size incurs significant performance penalties (these penalties are reduced with a domain decomposition procedure, but not eliminated). A more reasonable approach to reducing grid sensitivity is to improve the analytical formulation of the farfield boundary conditions.

One of the most important factors determining the success or failure of a CFD code is the boundary conditions. The far field boundaries are usually set to freestream values. Although appropriate, these boundary conditions require domain enlargement as previously discussed. Theoretically, a more appropriate boundary condition for the far field boundary is the characteristic variable method (Janus (1984)), which is consistent with the concept of upwinding. Therefore, characteristic variable boundary conditions are implemented giving a more efficient smaller computational domain. In addition, moving airfoils are known to generate unsteady disturbances, which propagate from the airfoil. These propagating waves must not be reflected back into the solution domain by the farfield boundary conditions. This problem is avoided by utilizing

approximate non-reflecting boundary conditions for the unsteady aerodynamic analysis (Giles (1990)).

The objective of this research is to implement and verify improvements obtained by utilizing higher fidelity farfield boundary conditions. Characteristic variable and approximate non-reflecting farfield boundary conditions for steady and unsteady flows, respectively, will be implemented in the direct BIFAE aeroelastic model. A NACA 64A006 flapped airfoil executing pitching and plunging motion will be utilized for both zero and non-zero static pretwist configurations to demonstrate the accuracy and efficiency improvements. In particular, a nonlinear transonic flow configuration will be investigated to highlight improvements in the transonic analysis capability of the enhanced model.

Methodology

In this section, the mathematical model for a pitch-and-plunge airfoil in inviscid flow is briefly summarized, and the analytical conditions satisfied at flutter points provided. Further details are given in the references cited above.

The rigid, pitch-and-plunge airfoil with flap is constrained to plunge along a vertical line and is allowed to pitch about an elastic axis. See Figure 1. Linear and torsional springs, with specified stiffness and damping constants (K_α , K_h , K_β , D_α , D_h , D_β), mediate the motion of the airfoil according to three linear, non-homogeneous, second-order ordinary differential equations for pitch (represented by the angle of attack, α), plunge (represented by the vertical displacement, h), and flap deflection, β . These equations are expressed as six, first-order differential equations, and are a function of the reduced velocity, $u = v_\infty / (b\omega_\alpha)$, where v_∞ is the freestream velocity, b is the semi-chord, and ω_α is the pitch natural frequency.

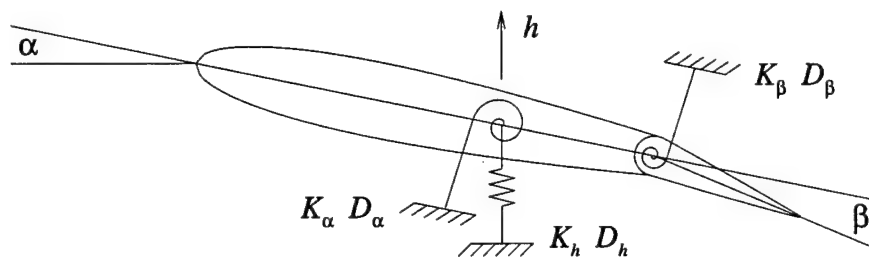


Figure 1: Schematic pitch-and-plunge airfoil with flap.

The governing aerodynamic equations are the Euler equations, cast in strong-conservative form for a general curvilinear coordinate system. These equations are placed in discrete form using a moving grid-point form of a standard upwind total-variation diminishing (TVD) scheme (Morton and Beran (1996A)). The systems of discretized fluid-dynamic equations and structural equations are combined into a single time-dependent system,

$$Y_t = G(y; u) \quad (1)$$

where Y is an array containing all the aerodynamic and structural dynamic variables, and G is an array of all the model equations. Equilibrium solutions of Equation 1 satisfy the nonlinear system $G(y; u) = 0$, and are computed with Newton's method. In this computation, the Jacobian G_y is calculated numerically to second-order accuracy and fully stored. The structure of G_y is that of a bordered, banded matrix.

The aeroelastic system governed by Equation 1 is also simulated through time integration following the approach detailed by Beran and Morton (1997). Using this approach, validation of stable equilibrium solutions obtained with Newton's method can be obtained, as well as validation of computed flutter points.

The equations representative of a Hopf-bifurcation, or flutter, point are developed by applying an assumed form of the solution Y . At a Hopf point, a steady-state solution transitions to an oscillatory solution with zero amplitude. The Hopf-point solution is assumed to be of the form, $Y(t; u) = Y_0(u) + \varepsilon P e^{\beta t}$, where ε is some small parameter and P is a coefficient vector. Substitution of this assumed form into Equation 1 yields the eigen-problem

$$G_y Y P = \beta P \quad (2)$$

The Hopf-point condition is satisfied when the real part of β vanishes for some complex pair of eigenvalues:

$$\beta = i\Theta \quad (3)$$

where i is the imaginary number and Θ is the flutter frequency. With Eqn. 2 and Eqn. 3, the discrete equations $G = 0$ are expanded to yield a system of equations, approximately three times the size of the original discrete system, for the critical aeroelastic state, Y^* , the critical aeroelastic mode, P^* , the flutter velocity, u^* , and the flutter frequency, Θ^* :

$$F(x) = \begin{bmatrix} G \\ (G_y - i\Theta)P \\ q^T P - I \end{bmatrix} = 0, \quad X = \begin{bmatrix} Y \\ P \\ u \\ \Theta \end{bmatrix} \quad (4)$$

with q defined as a user specified constant array. The solution of this expanded system within BIFAE is described in detail by Beran (1998).

Boundary Conditions

Theoretically speaking the characteristic variable boundary conditions should more accurately model nature due to the ability to pass information into and out of the computational domain. In order to correctly implement these characteristic variable boundary conditions however, the outer boundary of the computational domain must remain fixed in space. To accomplish this while allowing the airfoil to move, a weighting function grid deformation technique is employed.

Grid Deformation

In the deforming grid technique, the outer boundary remains fixed in space, with a deforming grid method used to locate the position of the airfoil. The grid lines connecting the inner and outer boundaries deform with the airfoil motion. Figure 2 shows a reduced computational grid with an exaggerated airfoil motion, which highlights the deforming grid method. The amount of deformation is a function of the distance from the airfoil surfaces. The grid deformation is defined as

$$\Delta x_{i,j} = W_{i,j} (\Delta x_{i,j}) \quad (5a)$$

$$\Delta y_{i,j} = W_{i,j} (\Delta y_{i,j}) \quad (5b)$$

where $\Delta x_{i,j}$ and $\Delta y_{i,j}$ are the spatial differences that would exist between successive time steps if the entire grid were to move as a rigid body. The weighting function, W , is defined as

$$W_{i,j} = W(\xi, \eta) = \left| \frac{s(\xi, \eta)}{s(\xi, \eta_{\max})} - 1 \right| \quad (6)$$

where s is the arc length of a grid line from the airfoil surface, $\eta = 1$, to some grid point along $\xi = \text{constant}$, and η_{\max} is the outer boundary grid line as shown in Figure 2.

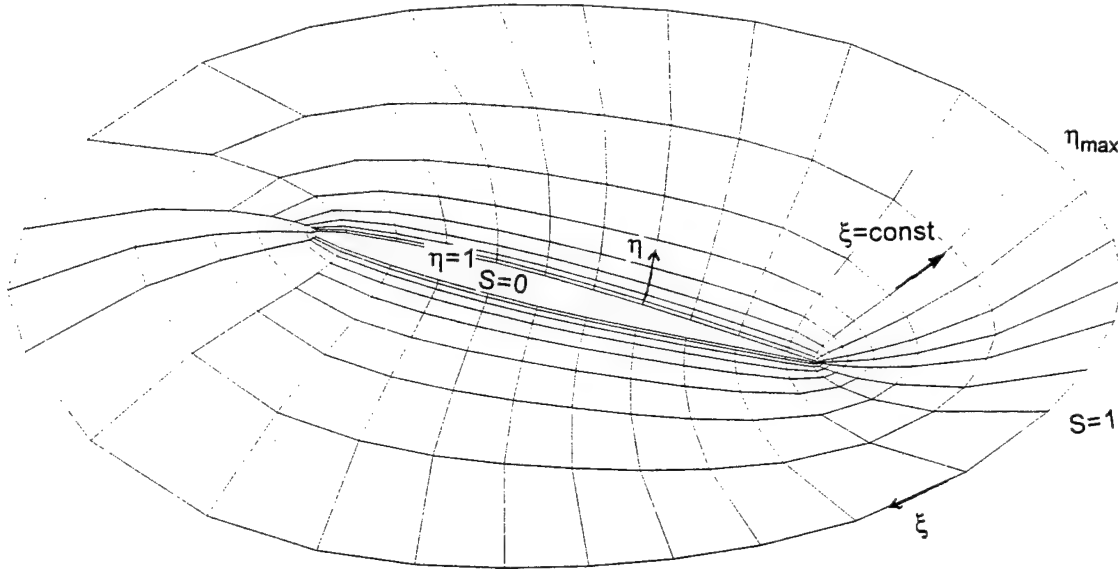


Figure 2: Deforming grid geometry.

From Equations 5 and 6, the nodes at the inner boundary, $s = 0$, give $W_{i,j} = 1$, which means the airfoil surface is deformed completely, as a rigid body motion. Conversely, the outer boundary nodes give $W_{i,j} = 0$, which signifies that these nodes remain fixed in space at their initial specified locations. The interior nodes shear in space relative to the initial grid as $W_{i,j}$ varies from 0 to 1. The grid speeds are then calculated by dividing the grid deformation by the time step used.

Steady State – Janus Characteristic Variable Method

The steady state characteristic variable boundary conditions are consistent with the concept of upwinding in which the signs of the characteristic velocities determine the appropriate propagation directions (Janus, 1984). A summary of their derivation is given in the following. The Euler equations written in their non-conservative form are

$$q_\tau + aq_\xi + bq_\eta = 0 \quad (7)$$

with the matrices a and b determined through an eigenvalue analysis.

The far field boundary conditions are obtained by multiplying Equation 7 by P_η^{-1} and neglecting the derivatives in the normal ξ direction to give

$$P_\eta^{-1} q_\tau + P_\eta^{-1} P_\eta \Lambda_\eta P_\eta^{-1} q_\eta = 0 \quad (8)$$

where Λ_η is a diagonal matrix containing the eigenvalues, λ_η , and P_η and P_η^{-1} are the left and right eigenvectors, respectively.

The characteristic vector is defined as

$$W_\eta = P_\eta^{-1} q \quad (9)$$

P_η is such that the elements of the characteristic vector become

$$w_\eta^1 = \frac{J}{|\nabla \eta|} \left[\eta_x \left(\rho - \frac{P}{c_i^2} \right) \right] \quad (10a)$$

$$w_\eta^2 = \frac{J}{|\nabla \eta|} \left[\eta_y \left(\rho - \frac{P}{c_i^2} \right) \right] \quad (10b)$$

$$w_\eta^3 = \frac{J}{\sqrt{2}|\nabla \eta|} \left[\frac{P \nabla \eta}{\rho_i c_i} + (\eta_x u + \eta_y v) \right] \quad (10c)$$

$$w_\eta^4 = \frac{J}{\sqrt{2}|\nabla \eta|} \left[\frac{P \nabla \eta}{\rho_i c_i} - (\eta_x u + \eta_y v) \right] \quad (10d)$$

The corresponding eigenvalues are

$$\lambda_\eta^1, \lambda_\eta^2 = \eta_x u + \eta_y v \quad (11a,b)$$

$$\lambda_\eta^3 = (\eta_x u + \eta_y v) + c|\nabla \eta| \quad (11c)$$

$$\lambda_\eta^4 = (\eta_x u + \eta_y v) - c|\nabla \eta| \quad (11d)$$

The implementation of the steady state far field characteristic variable boundary conditions is accomplished by computing the sign of λ to determine the directions of the characteristics. The subscript "a" denotes approaching the boundary, "b" refers to on the boundary, and "l" leaving the boundary. Then the characteristics approaching the boundary are set equal to the characteristics on the boundary using Equation 10.

$$\left[\eta_x \left(\rho - \frac{P}{c_1^2} \right) \right]_a = \left[\eta_x \left(\rho - \frac{P}{c_1^2} \right) \right]_b \quad (12a)$$

$$\left[\eta_y \left(\rho - \frac{P}{c_1^2} \right) \right]_a = \left[\eta_y \left(\rho - \frac{P}{c_1^2} \right) \right]_b \quad (12b)$$

$$\left[\frac{P \nabla \eta}{\rho_1 c_1} + \text{sign}(\lambda_n^1) (\eta_x u + \eta_y v) \right]_a = \left[\frac{P \nabla \eta}{\rho_1 c_1} + \text{sign}(\lambda_n^1) (\eta_x u + \eta_y v) \right]_b \quad (12c)$$

$$\left[\frac{P \nabla \eta}{\rho_1 c_1} + \text{sign}(\lambda_n^1) (\eta_x u + \eta_y v) \right]_i = \left[\frac{P \nabla \eta}{\rho_1 c_1} + \text{sign}(\lambda_n^1) (\eta_x u + \eta_y v) \right]_b \quad (12d)$$

The metrics at points "a" and "i" are assumed to be the same as those at point "b". Combining Equations 12(c,d) gives Equation 13a, with the remaining flow variables at the far field boundary found by simultaneous solution of Equations 12(a-d).

$$P_b = \frac{1}{2} (P_a + P_i - \rho_1 c_1 [\eta_x (u_a - u_i) + \eta_y (v_a - v_i)]) \quad (13a)$$

$$\rho_b = \rho_a + \frac{P_b - P_a}{c_1^2} \quad (13b)$$

$$u_b = u_a - \eta_x \frac{P_a - P_b}{\rho_1 c_1} \quad (13c)$$

$$v_b = v_a - \eta_y \frac{P_a - P_b}{\rho_1 c_1} \quad (13d)$$

Unsteady Flows – Giles Approximate Non-Reflecting Characteristic Method

Approximate non-reflecting unsteady farfield boundary conditions are developed by assuming that linear theory can be applied. Giles (1990) derived "non-reflecting" boundary conditions for a general turbomachinery Euler solver. First the steady flow is solved using the previously presented characteristic variable boundary conditions. The linearized Euler equations are then solved at the farfield boundary to determine the perturbation flow variables in terms of the characteristic variables. This allows time variations of static pressure at the farfield and reduces reflections from the boundaries. A brief outline of this method is given below.

The linearized, two-dimensional Euler equations are written in terms of primitive small-perturbation variables as

$$Q_t + A Q_x + B Q_y = 0 \quad (14)$$

where

$$Q = (\delta p, \delta u, \delta v, \delta p)^T \quad (15)$$

$$A = \begin{bmatrix} u & \rho & 0 & 0 \\ 0 & u & 0 & \frac{1}{P} \\ 0 & 0 & u & 0 \\ 0 & \gamma P & 0 & u \end{bmatrix}, \quad B = \begin{bmatrix} v & 0 & \rho & 0 \\ 0 & v & 0 & 0 \\ 0 & 0 & v & \frac{1}{P} \\ 0 & 0 & \gamma P & v \end{bmatrix} \quad (17)$$

The elements of the vector Q' represent perturbations from uniform flow conditions

$$\rho = \rho_0 + \delta\rho \quad (18a)$$

$$u = u_0 + \delta u \quad (18b)$$

$$v = v_0 + \delta v \quad (18c)$$

$$P = P_0 + \delta P \quad (18d)$$

where ρ_0 , u_0 , v_0 , and P_0 specify the steady solution.

The matrices A and B are evaluated using these same conditions. The analysis is greatly simplified if the unsteady perturbations and the steady variables in A and B are nondimensionalized using the steady density and speed of sound. With this choice of nondimensionalization, the final forms of the matrices A and B are

$$A = \begin{bmatrix} M_x & 1 & 0 & 0 \\ 0 & M_x & 0 & 1 \\ 0 & 0 & M_x & 0 \\ 0 & 1 & 0 & M_x \end{bmatrix}, \quad B = \begin{bmatrix} M_y & 0 & 1 & 0 \\ 0 & M_y & 0 & 0 \\ 0 & 0 & M_y & 1 \\ 0 & 0 & 1 & M_y \end{bmatrix} \quad (19)$$

where M_x and M_y are the Mach numbers in the x and y directions.

A set of eigenvectors representing an entropy wave, a vorticity wave and an upstream/downstream running pressure waves are determined by Fourier analysis of these equations. Using these eigenvectors and assuming locally one-dimensional flow at the boundary, the characteristic variables for unsteady flows are written in terms of the perturbation variables as

$$\begin{bmatrix} C_1 \\ C_2 \\ C_3 \\ C_4 \end{bmatrix} = \begin{bmatrix} -1 & 0 & 0 & 0 \\ 0 & 0 & 1 & 1 \\ 0 & 1 & 0 & 1 \\ 0 & -1 & 0 & 0 \end{bmatrix} \begin{bmatrix} \delta\rho \\ \delta u \\ \delta v \\ \delta P \end{bmatrix} \quad (20)$$

For a subsonic freestream flow, the amplitudes of the incoming unsteady characteristics (C_1 , C_2 , C_3) are set to zero and the outgoing characteristic (C_4) is computed using Equation 20. For subsonic downstream flow, $C_4=0$ and the remaining characteristics are computed. Once the characteristics are known, the perturbation variables are found using an inverse transform

$$\begin{bmatrix} \delta\rho \\ \delta u \\ \delta v \\ \delta P \end{bmatrix} = \begin{bmatrix} -1 & 0 & \frac{1}{2} & \frac{1}{2} \\ 0 & 0 & \frac{1}{2} & -\frac{1}{2} \\ 0 & 1 & 0 & 0 \\ 0 & 0 & \frac{1}{2} & \frac{1}{2} \end{bmatrix} \begin{bmatrix} C_1 \\ C_2 \\ C_3 \\ C_4 \end{bmatrix} \quad (21)$$

The primitive flow variables are found using Equation 18. With the non-conservative flow variables found, the conservative dependent variables are easily computed for the farfield boundaries.

Results

The direct computational procedure BIFAE has been successfully validated against other inviscid methods, including Euler and transonic small-disturbance methods (Morton and Beran (1997) and Beran and Morton (1997)). Validation of BIFAE was also the subject of work by Buxton and Beran (1997). In this report, both equilibrium and flutter point solutions are obtained for these

same configurations to validate the new farfield boundary condition modifications. The sensitivity of these new boundary conditions to domain size is examined through the use of flutter boundaries and Cp distributions. Results were obtained using a standardized set of structural and aerodynamic parameters for a baseline configuration of the BIFAE algorithm.

NACA 64A006 Flapped Airfoil Pitching and Plunging

The enhanced Hopf-bifurcation analysis is applied to a NACA 64A006 flapped airfoil with pitching and plunging motion for various computational grids and aerodynamic parameters. The structural parameters were not varied in this research, because the improvements to the analysis were related to the aerodynamic model. Therefore, only variations in the aerodynamic parameters were required to demonstrate the successful implementation of the improved flow physics model.

The structural parameters utilized for all the computational results are presented in Table 1.

Symbol	Description	Value
x_{cg}	center of gravity (from LE)	0.5
ζ_α, ζ_h	airfoil damping ratios	0.0
ζ_β	flap damping ratio	0.01
ω_h/ω_α	natural frequency ratio	0.3
$\omega_\beta/\omega_\alpha$	flap natural frequency ratio	1.5
x_α	elastic-axis location	-0.2
μ	airfoil-fluid mass ratio	50

Table 1: NACA 64A006 Structural Parameter Values

To demonstrate the increased solution accuracy obtained by modifying the farfield boundary conditions, three different computational domains were utilized. Table 2 gives specific details about each computational grid used to model the NACA 64A006 airfoil.

Grid	Δ_{le}	Δ_{te}	Δ_w	R_{max}	I	J
G-1	0.0010	0.0005	0.0006	5	84	31
G-3	0.0010	0.0005	0.0006	50	84	43
G-4	0.0010	0.0005	0.0006	150	84	49

Table 2: NACA 64A006 Computational Grids

As shown in Table 2, the three computational grids used are the same grid except for the location of the farfield boundary. The G-1 grid has a domain size of 5 airfoil chords with the G-3 and G-4 grids having 50 and 150 chords domain sizes, respectively. Utilizing the same grids except for in the J direction, ensures that any difference in the predictions is caused by modifications to the farfield boundary condition or boundary location.

Since the direct hopf-bifurcation model is optimized for calculating flutter boundaries, then flutter boundary studies will be utilized to demonstrate the enhancements to the model accuracy obtained with the new farfield boundary conditions. These results are typically obtained by

establishing all the aerodynamic parameters, then incrementally modifying only one parameter. Traditionally, the parameter which is incremented is the freestream Mach number. The initial investigation of the enhanced analysis was accomplished by varying the freestream Mach number from 0.7 to 0.9 with a static pre-twist angle of attack of 0° . The continuation feature designed into the analysis was utilized for these investigations. After the flutter point was calculated for the 0.7 Mach case, the Mach number was incremented by 0.01 with the previous flutter point solution used to begin the solution. The analysis was continued until the solution did not converge on a flutter point for a particular Mach number.

Initially, obtaining a flutter boundary that is independent of the computational domain size was accomplished. Figures 3 & 4 shows the flutter boundary analysis of the flutter speed and reduced frequency variation with Mach number for the 84x43 and 84x49 grids, which have domain sizes of 50 and 150 chords, respectively. The analysis did not converge above a Mach number of 0.88. The flutter boundaries for both domains are exactly the same. Therefore, the baseline grid independent solution for the specified structural and aerodynamic parameters is known. The flutter bucket for this configuration occurs between 0.83 and 0.85 Mach number. The flutter bucket location is of primary interest when flutter boundaries are analyzed.

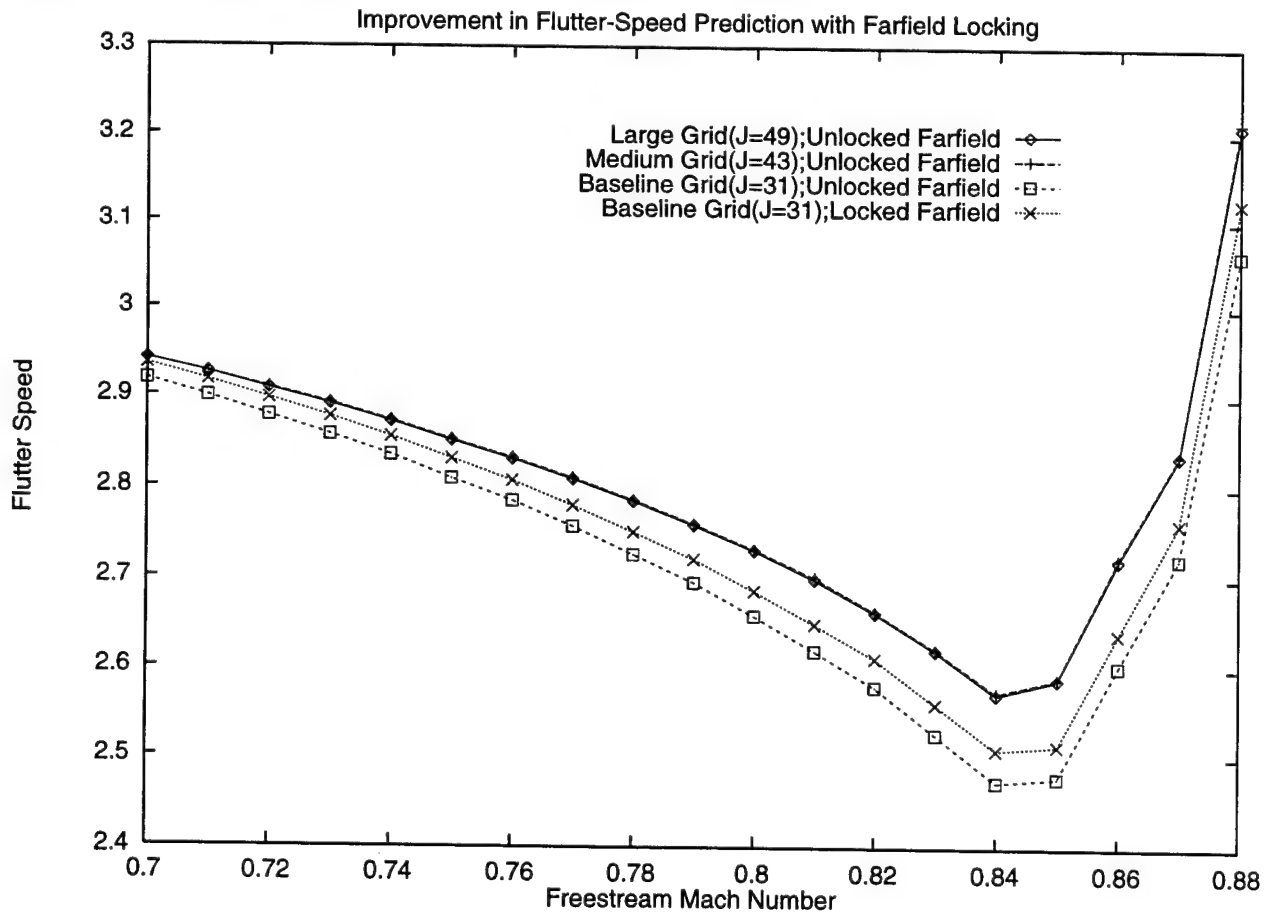


Figure 3: Reduced Velocity Flutter Boundary for a NACA 64A006 Airfoil with Flap

Included in Figures 3 & 4 is the unmodified BIFAE analysis using an 84x31 computational grid, which has a domain size of 5 chords. As shown in Figure 3, the 5 chord domain results under predict the flutter speed slightly at $M=0.7$ (0.8%), but the prediction is off by 3.8% at $M=0.84$, which is in the flutter bucket. With regards to the reduced frequency, shown in Figure 4, the unmodified model over predicts the correct frequency by 1.0 % for all Mach numbers. The difference in the model predictions just discussed are entirely attributed to the reduction in domain size from 50 chords to 5 chords. This means that the solution is dependent on the domain size of 5 chords for the farfield boundary.

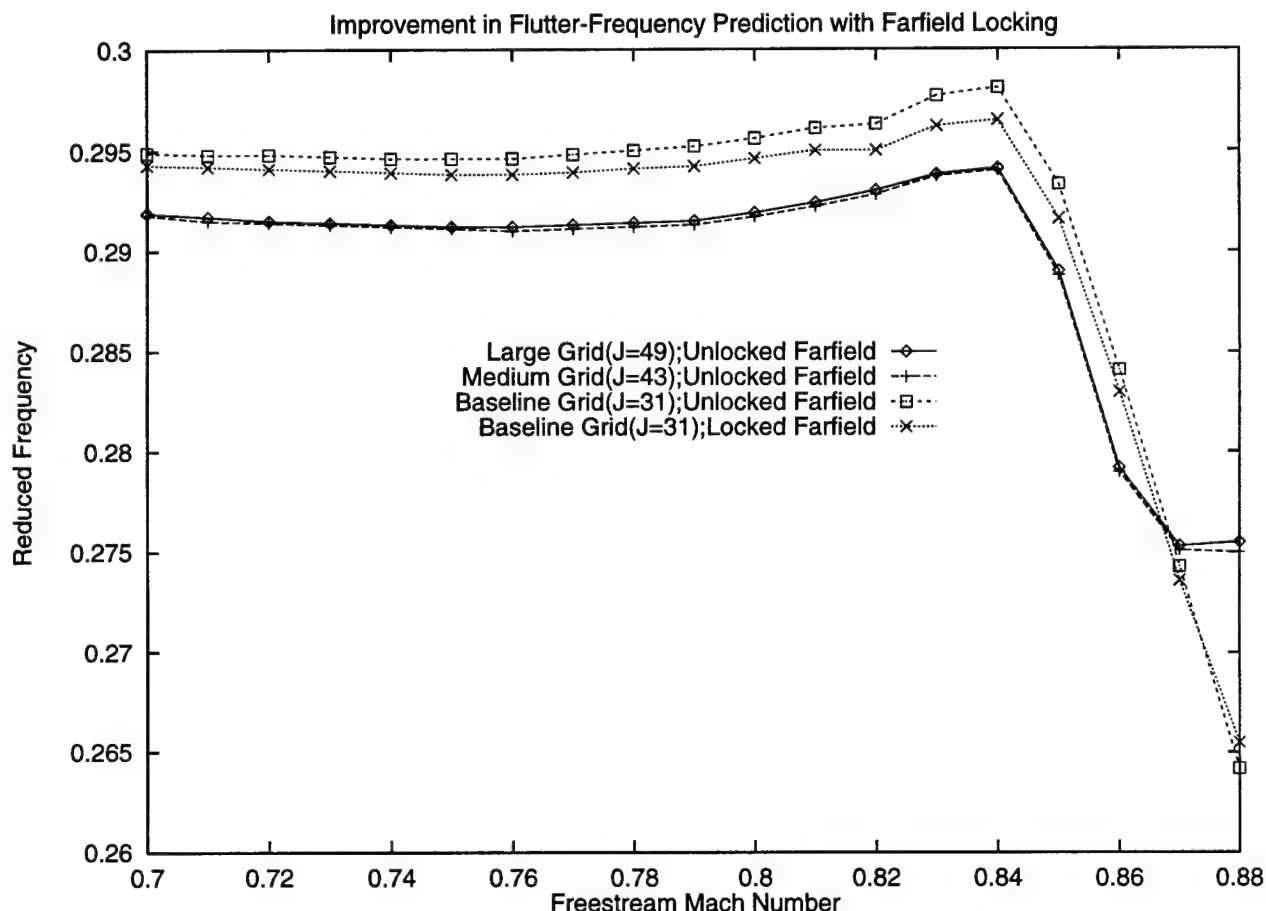


Figure 4: Reduced Frequency Flutter Boundary for a NACA 64A006 Airfoil with Flap

In addition, Figures 3 & 4 show the BIFAE analysis obtained with the grid deformation modification implemented. This modification locks the movement of the grid at the farfield boundary using a weighting function. As shown in Figure 3, the flutter speed prediction is improved at all Mach numbers. At $M=0.7$ the solution is off by 0.2% and at $M=0.84$ the reduced velocity predicted is off by 2.4%. Therefore, the percentage improvement increased with increasing Mach number. For the reduced frequency, Figure 4, the improvement was fairly uniform with Mach number, the predicted value was off by 0.8% from the grid independent analysis. These results show the improvement in the BIFAE model obtained by incorporating the grid deformation model.

The improvements in both the flutter speed and reduced frequency obtained by modifying the grid deformation model are more significant than expected.

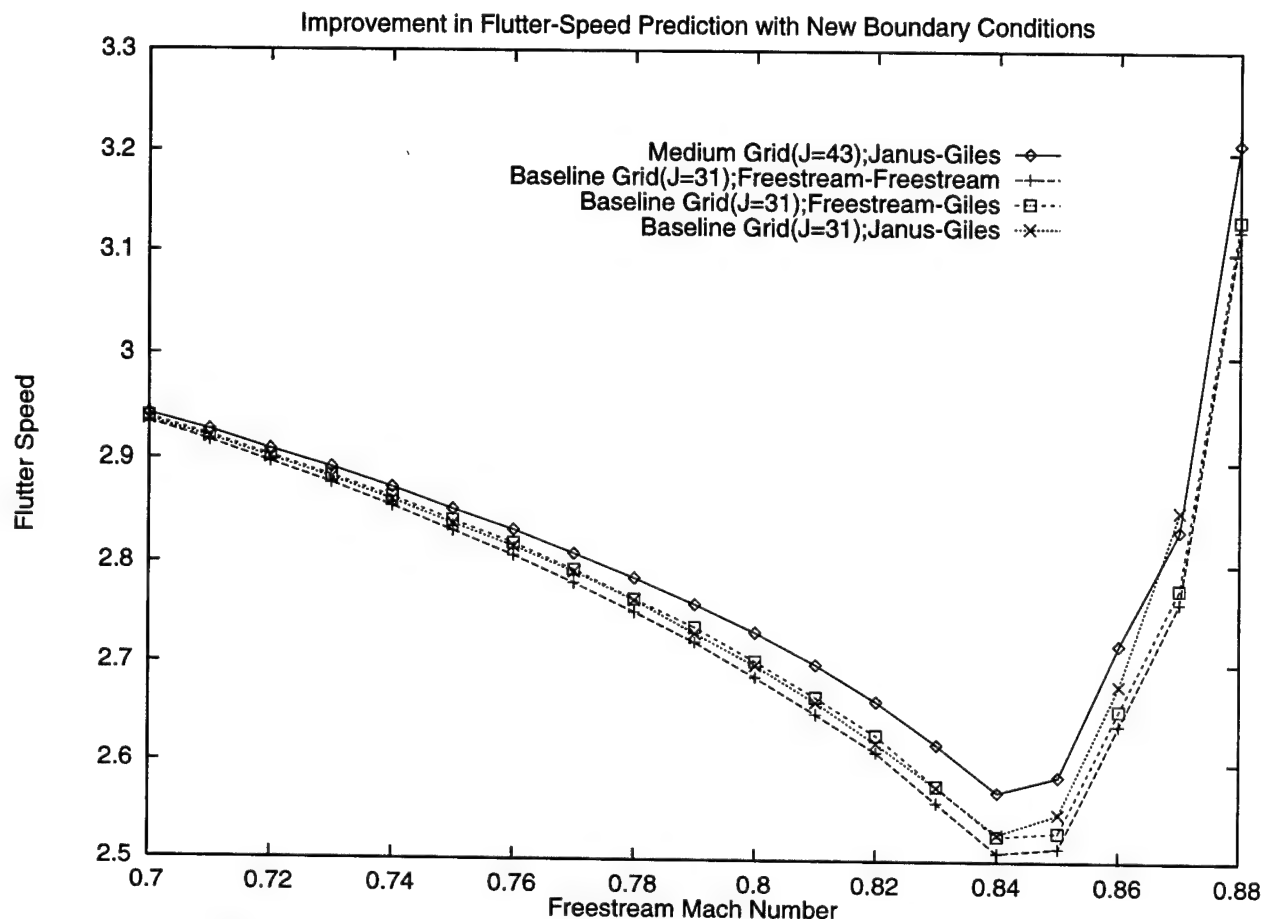


Figure 5: Reduced Velocity Flutter Boundary Effect of New Unsteady Boundary Conditions

To investigate the influence of improvements to the farfield boundary conditions, various combinations of the original freestream, the steady characteristic, and the unsteady approximate conditions are shown in Figures 5 and 6 for flutter speed and reduced frequency, respectively. All the results shown utilize the locked grid deformation model with the different farfield boundary condition. The grid independent result from a 50 chord domain analysis ($J=43$) is given as the reference solution for this configuration. Also, the locked original boundary condition solution shown in Figures 3 and 4 is given (i.e. 'Baseline Grid($J=31$);Freestream-Freestream'). At an inlet Mach number of 0.7 the flutter speed is only slightly off with the original boundary conditions, using both the steady characteristics of Janus and the unsteady approximate of Giles boundary conditions give a more accurate prediction, but the improvement is modest. As the Mach number is increased the improvement in the predictions of both flutter speed and reduced frequency from the original freestream to Janus-Giles conditions gets more significant. For the flutter speed prediction at $M=.85$, see Figure 5, utilizing the Giles unsteady conditions alone results in a 0.6% improvement while using both Janus's steady and Giles unsteady results in a 1.4% improvement in

flutter speed. While for the reduced frequency analysis, see Figure 6, the improvements were 0.2% and 0.8%, respectively. It is important to note, at a freestream Mach number of 0.84 the improvement from using Janus's steady boundary conditions is nearly zero in the flutter speed prediction (Figure 5), but is quite significant in terms of the reduced frequency prediction (Figure 6). These results warrant a more detailed investigation at this Mach number.

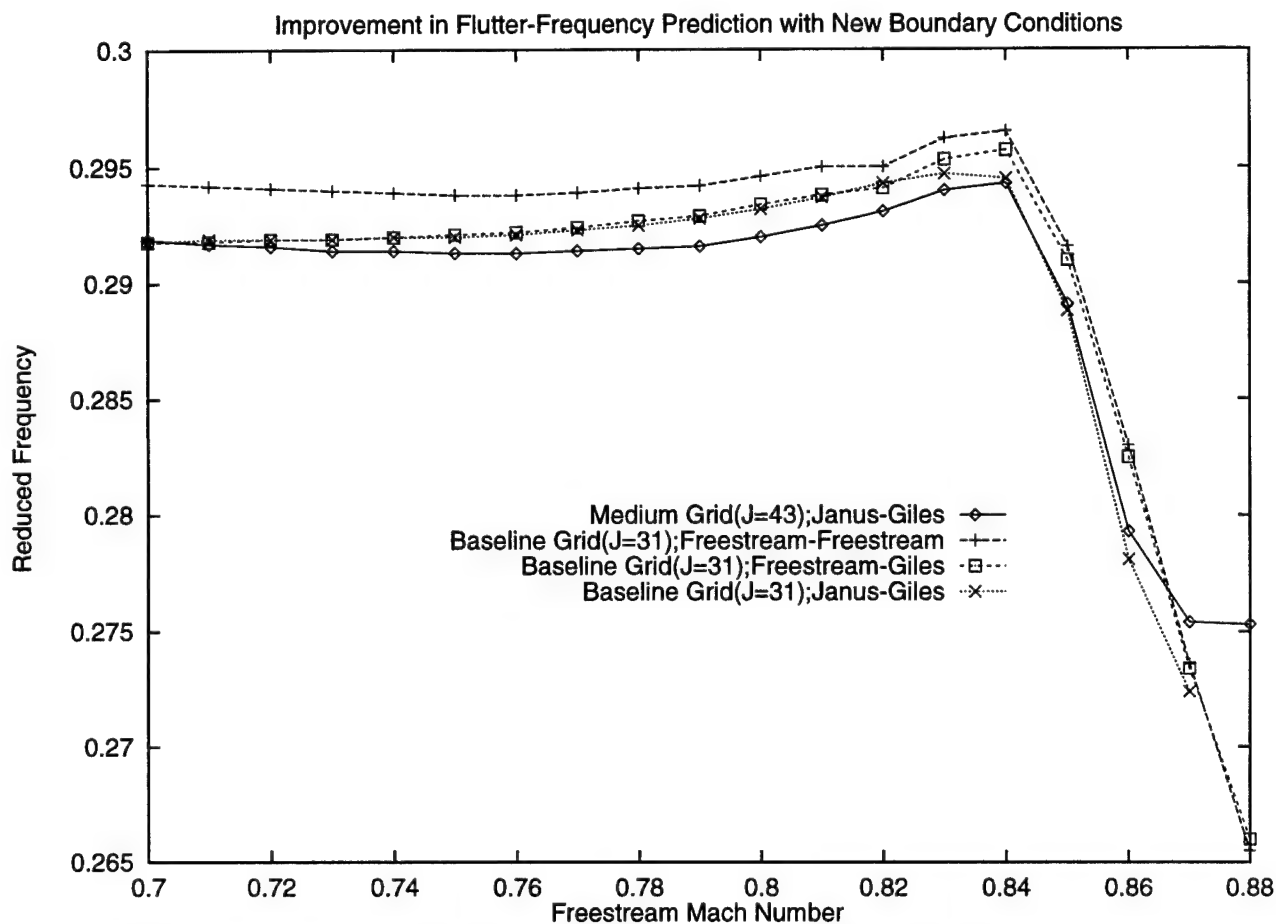


Figure 6: Reduced Frequency Flutter Boundary Effect of New Unsteady Boundary Conditions

Since the accurate prediction of the flutter bucket is of significant interest when doing flutter boundary studies, the significant change in solution accuracy from $M=0.84$ to $M=0.85$ was investigated in more detail. The only change between the results at $M=0.85$ and $M=0.84$ was in the steady farfield boundary conditions. At $M=0.85$ a significant effect was seen when Janus conditions were utilized but at $M=0.84$ no effect was shown. Therefore, the steady surface pressure distribution was investigated for differences as shown in Figure 7. It is quite apparent from Figure 7 that there is no effect on the steady pressure distribution no matter which farfield boundary conditions are used. Another interesting feature to note shown in Figure 7 is the lack of a shock wave. It is well known that the freestream boundary conditions have problems accurately modeling nonlinear flow phenomena. All the results given have been for zero static pre-twist. By increasing the airfoil angle of attack, a shock wave will form on the suction surface therefore, giving a better test of the

improved analysis model. Since the predictions at a freestream Mach number of 0.84 did not show a significant improvement in the flutter speed, the angle of attack is varied for this speed by increasing the static pre-twist angle in 0.1° increments until 1.0° is reached.

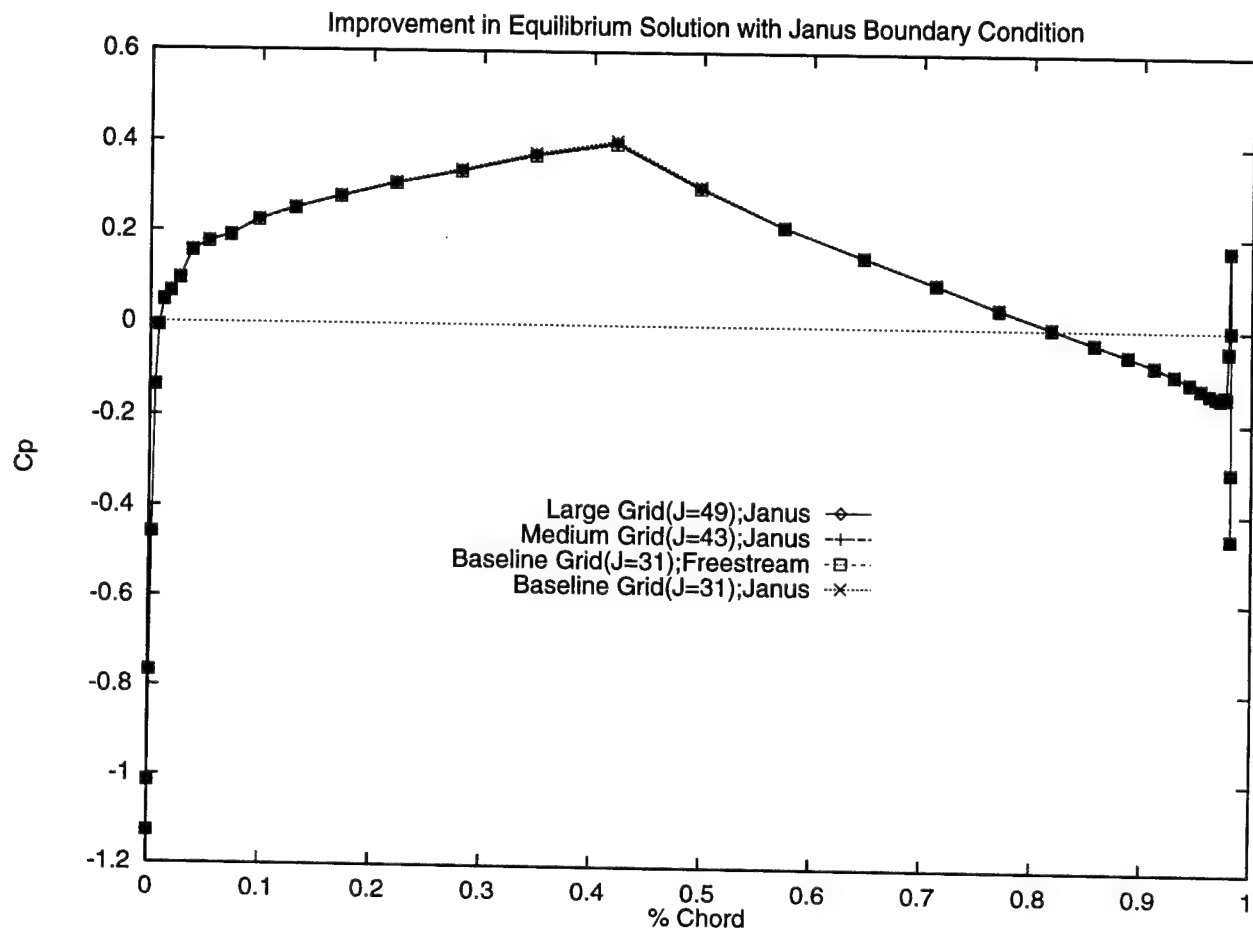


Figure 7: Steady C_p Distribution for $M=0.84$ and $\alpha_0 = 0^\circ$

Figure 8 shows the steady surface pressure distribution for the 1° static pre-twist analysis for 150, 50, and 5 chord domain sizes for both Janus and the original freestream farfield boundary conditions. At this angle of attack, the solution is grid independent at the 50 chord domain size as shown by comparing the 150 and 50 (i.e. $J=49$ and $J=43$, respectively) chord results. In addition, Figure 8 shows a normal shock on the suction surface at 75% of the airfoil chord. Comparing the predictions with Janus steady boundary conditions to the original freestream conditions shows a significant improvement in the C_p distribution at the shock location. The original freestream conditions predicted the shock starting at the 60% chord location, while the Janus conditions predicted the shock starting at 70% chord. In addition, the Janus calculations predicted the same ending location for the shock wave as the 50 chord solution, while the freestream conditions were 8% chord upstream.

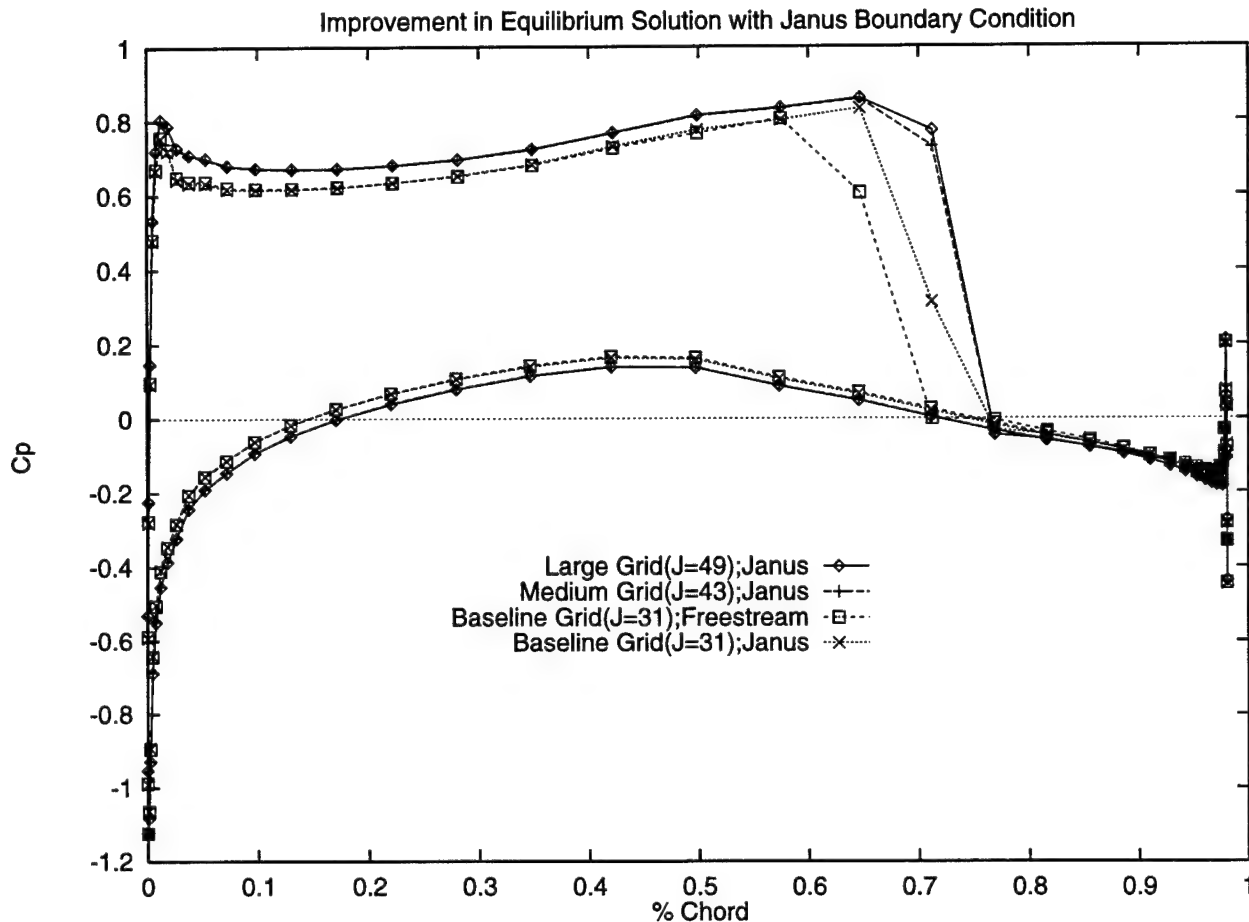


Figure 8: Steady C_p Distribution for $M=0.84$ and $\alpha_0 = 1^\circ$

Figure 9 shows the flutter speed variation with the different static pre-twist angles for a freestream Mach number of 0.84. Grid independence was achieved for the 150 and 50 chord domains solutions as shown in Figure 9. For the 5 chords domain ($J=31$) results, all the different model configurations are shown for the direct solver. The solution improvement from utilizing the locked grid deformation model is fairly consistent with changes in static pre-twist. Therefore, these improvements are not related to the nonlinear effects introduced by the strong shock wave. Comparing the approximate non-reflecting unsteady boundary conditions with the original freestream conditions resulted in another constant improvement in the flutter speed prediction for all static pre-twist values. Again, the conclusion is drawn that the approximate non-reflecting unsteady boundary conditions are not being significantly affected by the nonlinear nature of the flow physics.

When the steady characteristic boundary conditions are introduced with Giles unsteady conditions the improvement in flutter speed increases with increasing static pre-twist. At 0° static pre-twist, the improvement is nearly zero while at 1° the flutter speed prediction is 2.954 versus 2.812 without the new steady boundary conditions. The grid independent flutter speed is 3.005 at 1° . Therefore, the solution error is reduced nearly 60% by introducing the steady characteristic

boundary conditions, while each of the other modifications result in a 10% reduction, respectively. This is a strong indication that the steady characteristic boundary conditions do a significantly better job of modeling the nonlinear shock effects. Accurate shock predictions are required for transonic flight and beyond.

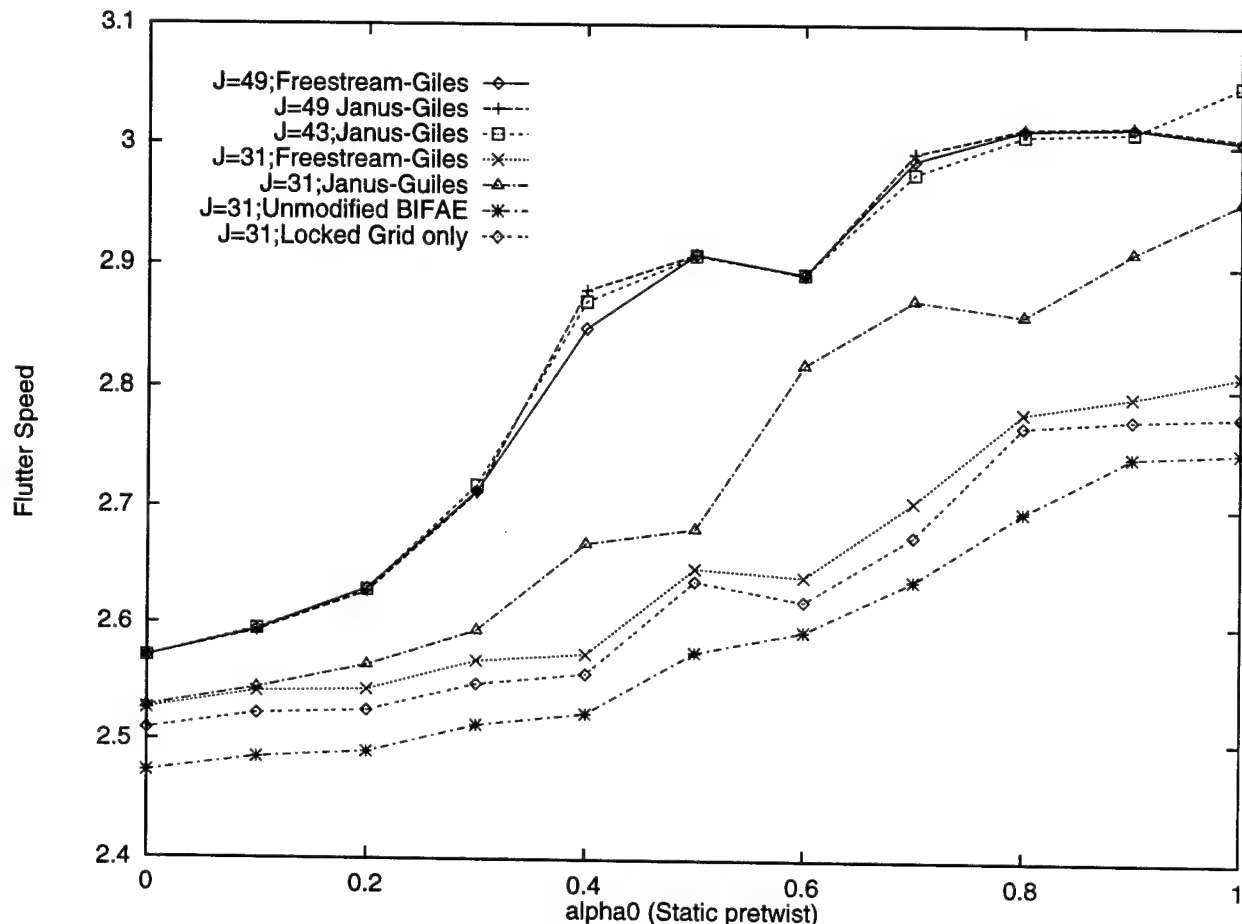


Figure 9: Flutter Speed Variations for M=0.84 with Static Pre-Twist

In addition, it is interesting to note the slight scatter in the results at 0.4° and 0.7° . For these conditions the analysis required reducing the CFL number, the under-relaxation parameter and increasing the number of iterations to get a converged flutter point solution. Typically, the flutter speed variation with static pre-twist is a smoother curve. Several possible reasons for the results shown in Figure 9 are inaccuracies in the trailing edge model and resolution of the shock location on the suction surface. As shown in Figure 8, the shock wave was smeared over three grid points. The shock position is extremely important in the calculation of the flutter speed, therefore any error in its location will have significant effects on the aeroelastic analysis.

Summary and Conclusion

The direct computational procedure BIFAE has been successfully enhanced by improved flow physics models of the farfield boundary conditions. In particular, a deforming grid model was

implemented which locks the farfield grid while allowing the grid near the airfoil surface to deform with the airfoil movement. In addition, steady characteristic and approximate non-reflecting unsteady farfield boundary conditions have been incorporated into the BIFAE model. A NACA 64A006 flapped airfoil, executing pitching and plunging motion, was utilized for verifying the successful implementation of these higher fidelity models. Both zero and non-zero angle of attack results were shown to highlight the improved efficiency of the enhanced model. For a 1° static pre-twist analysis at a freestream Mach number of 0.84, the new model resulted in over a 75% decrease in the flutter speed error. Therefore, the capability to more accurately model transonic flow conditions with strong shock interaction has been shown.

Potential enhancements to the direct BIFAE model as a consequence of the research described in this report are as follows: 1) implementation of the approximate non-reflecting unsteady 2-D farfield boundary conditions of Giles; 2) implement the Giles steady farfield boundary conditions; and 3) implement the geometric conservation law to properly account for the grid deformation. The results presented in this report could be improved by investigating the rounded trailing edge and chordwise grid resolution. In addition, it would be beneficial to identify the precise computational domain size required with the new farfield boundary conditions for a grid independent solution. These improvements were not completed in the current investigation because of a lack of time.

Acknowledgements

The authors would like to thank Dr. Phil Beran for providing this excellent educational opportunity and the Air Vehicles Directorate for the funding support required. In addition, we acknowledge all the support given us during this appointment by the other members of the Air Vehicles – Aeroelasticity Group. We have felt like one of the team and this has made the experience very rewarding. Finally, we appreciate the manner in which we have been able to continue working on this challenging and rewarding research after our summer appointment has ended.

References

Beran, P.S., *A Domain-Decomposition Method for Airfoil Flutter Analysis*, 36th AIAA Aerospace Sciences Meeting, Reno, NV, Jan. 12-15, 1998, AIAA 98-0098.

Beran, P.S. and Morton, S.A., *A Continuation Method for the Calculation of Airfoil Flutter Boundaries*, Journal of Guidance, Control and Dynamics, Vol. 20, No. 6, Nov.-Dec., 1997, pp. 1165-1171.

Buxton, B.J. and Beran, P.S., *Validation of Two Shock-Capturing Methods for Calculation of Transonic Airfoil Flutter*, 35th AIAA Aerospace Sciences Meeting, Reno, NV, Jan. 6-10, 1997, AIAA 97-0834.

Giles, M.B., *Non-Reflecting Boundary Conditions for Euler Equation Calculations*, AIAA Journal, Vol. 28, No. 12, 1990, pp. 2050-2058.

Janus, J.M., *The Development of a Three-Dimensional Split Flux Vector Solver with Dynamic Grid Applications*, MS Thesis, Mississippi State University, August, 1984.

Lee, B.H.K., Yang, L.Y., and Wong, Y.S., *Flutter of an Airfoil with a Cubic Nonlinear Restoring Force*, Proceedings of the 39th AIAA/ASME/ASCE/AHS/ASC Structures, Structural Dynamics, and Materials Conference and Exhibit, Long Beach, CA, April 20-23, 1998, AIAA 98-1725-CP, pp. 237-257.

Morton, S.A. and Beran, P.S., *Hopf Bifurcation Analysis Applied to Deforming Airfoils at Transonic Speeds*, 13th AIAA Computational Fluid Dynamics Conference, Snowmass, CO, June 29-July 2, 1997, AIAA 97-1772.

Morton, S.A. and Beran, P.S., *Hopf-Bifurcation Analysis of Airfoil Flutter at Transonic Speeds*, 34th AIAA Aerospace Sciences Meeting and Exhibit, Reno NV, Jan. 15-18, 1996A, AIAA 96-0060.

Morton, S.A. and Beran, P.S., *Effects of Structural Nonlinearity in the Bifurcation Analysis of Transonic Airfoil Flutter*, 27th AIAA Fluid Dynamics Conference, New Orleans, LA, June 17-20, 1996B, AIAA 96-1975.

Morton, S.A. and Beran, P.S., *Nonlinear Analysis of Airfoil Flutter at Transonic Speeds*, Proceedings of the 13th AIAA Applied Aerodynamics Conference, San Diego, CA, June 19-22, 1995, AIAA 95-1905-CP, pp. 1169-1179.

**A DETAILED STUDY OF THE NUMERICAL PROPERTIES
OF FDTD ALGORITHMS FOR DISPERSIVE MEDIA**

**Ronald O. Nelson
Graduate Research Assistant
Department of Electrical Engineering**

**University of Idaho
Moscow, ID 83844-1023**

**Final Report for:
Summer Faculty Research Program
Air Force Research Laboratory**

**Sponsored by:
Air Force Office of Scientific Research
Bolling Air Force Base, DC**

and

Air Force Research Laboratory, Air Vehicles Directorate

August 1998

A DETAILED STUDY OF THE NUMERICAL PROPERTIES OF FDTD ALGORITHMS FOR DISPERSIVE MEDIA

**Ronald Nelson
Graduate Student**

Department of Electrical Engineering
University of Idaho

Abstract

Numerous finite-difference, time-domain (FDTD) algorithms for dispersive media are presented and studied. To limit the scope of the discussion, only direct integration and recursive convolution techniques are considered in conjunction with the following media types: the isotropic cold plasma and the multi-pole Debye dielectric. The study primarily focuses on the numerical permittivity calculation that results from the discretization procedure. Where appropriate, this permittivity is used to quantify the temporal error mechanisms of the scheme. Discussions are provided that assess the overall strengths and weaknesses of each scheme.

A DETAILED STUDY OF THE NUMERICAL PROPERTIES OF FDTD ALGORITHMS FOR DISPERSIVE MEDIA

Ronald Nelson

1 Introduction

The finite-difference, time-domain method (FDTD) has emerged as a leading numerical tool for the solution of the temporally dependent Maxwell's equations [1, 2]. Originally the scheme was created to discretize Maxwell's equations, with the assumption that the medium that hosted the electromagnetic wave was isotropic, non-dispersive, linear and time-invariant. In many applications that arise in the study of electromagnetic waves, such assumptions are indeed valid.

As the method grew in popularity and proved its worth in the prediction of scattering, diffraction and propagation events, many researchers postulated and then devised ways that the algorithm could be applied to problems for which the medium was no longer simple in its composition. Such media types include the ionosphere, biological tissues, crystalline structures, ferrites, optical fibers, and radar absorbing materials, to name a few. Whatever the case may be, however, these media are subsets of what is generally termed as *complex* media – media that is described by one or many of the following descriptors: dispersive, anisotropic, nonlinear and time-variant [3].

This report examines the most recent and popular advances in FDTD algorithm development as applied to electromagnetic wave propagation in complex media. Several methodologies are presented and comparisons are made in order to demonstrate the strengths and weaknesses of the various approaches. Particularly, direct integration and recursive convolution schemes associated with wave propagation in a cold plasma and a Debye dielectric are considered.

Error analyses are also provided. Since the discretized equations are approximations of Maxwell's equations, the data obtained from the FDTD algorithm will be corrupted by errors of the dissipative or dispersive kind. These errors linearly accumulate after each time step and hence, the data will be attenuated and out of phase with the data obtained from the exact solution. To quantify these errors, numerical dispersion relationships are derived. These same dispersion relationships also provide information on the stability of the scheme; this information is couched in terms of a Courant-Friedrichs-Lewy (CFL) number [4]. Thus, for those schemes for which the stability properties are known, that information is also provided.

2 Maxwell's Equations and Complex Media

According to Maxwell, the electromagnetic field is comprised of an electric field $\mathbf{E}(\mathbf{x}, t)$ and a magnetic field $\mathbf{B}(\mathbf{x}, t)$ that satisfy, at a point, two curl equations and two divergence equations [5]:

$$\nabla \times \mathbf{E} = -\frac{\partial \mathbf{B}}{\partial t} - \mathbf{M}, \quad (1)$$

$$\nabla \times \mathbf{H} = \frac{\partial \mathbf{D}}{\partial t} + \mathbf{J}, \quad (2)$$

$$\nabla \cdot \mathbf{D} = 0 \quad (3)$$

and

$$\nabla \cdot \mathbf{B} = 0. \quad (4)$$

Here \mathbf{D} is the electric flux density and \mathbf{H} is the magnetic intensity. The terms \mathbf{J} and \mathbf{M} are often regarded as source terms, and in that context they are the electric and magnetic current densities, respectively. For purposes of numerical computation, the two curl equations are discretized and advanced in time; the two divergence equations are additional constraints imposed upon the fields. To bring closure to this system of equations, a set of constitutive relationships are imposed that quantify the effects of a material medium on an applied electromagnetic field. In general, we write

$$\mathbf{D} = \mathbf{D}(\mathbf{E}, \mathbf{H}) \quad \mathbf{B} = \mathbf{B}(\mathbf{E}, \mathbf{H}). \quad (5)$$

In addition, the currents may also be coupled to the fields, in which case

$$\mathbf{J} = \mathbf{J}(\mathbf{E}, \mathbf{H}) \quad \mathbf{M} = \mathbf{M}(\mathbf{E}, \mathbf{H}). \quad (6)$$

It is in this latter context that we will invoke the notion of current. That is, rather than the current being typified as *impressed*, it will be considered *induced* – a current generated by a field. For example, in the study of wave propagation in a cold plasma, \mathbf{J} is replaced with \mathbf{J}_p , the polarization current generated in the plasma by an applied field. By definition, the polarization current is viewed as the time rate of change of the polarization vector \mathbf{P} (i.e. $\mathbf{J}_p = \partial \mathbf{P} / \partial t$). The inclusion of \mathbf{P} into the field description proves useful when studying propagation in Debye-type materials.

If the material is *simple* and source-free, the previous relationships reduce to $\mathbf{D} = \epsilon \mathbf{E}$, $\mathbf{B} = \mu \mathbf{H}$, $\mathbf{J} = \sigma \mathbf{E}$ and $\mathbf{M} = 0$, where the constants ϵ , μ and σ are the electric permittivity, magnetic permeability and electric conductivity, respectively. Written as such, \mathbf{J} is now interpreted as the induced conduction current. For *complex* materials, the constitutive relationships do not reduce to such simple forms. Instead, the relationships may be cast in terms of convolution integrals, matrices or derivatives. For these situations, the material may be characterized as dispersive, anisotropic, or non-linear, to name a few possibilities.

3 FDTD Method

Consider a medium that is simple and source-free, but lossy. The FDTD method is based upon the application of central differences for both temporal and spatial discretization [6] which, for the sake of future developments, will be considered separately. With respect to the former, the temporal discretization of Maxwell's curl equations yields

$$\mu \left(\frac{\mathbf{H}^{n+1/2} - \mathbf{H}^{n-1/2}}{\delta_t} \right) = -\nabla \times \mathbf{E}^n \quad (7)$$

and

$$\epsilon \left(\frac{\mathbf{E}^{n+1} - \mathbf{E}^n}{\delta_t} \right) = \nabla \times \mathbf{H}^{n+1/2} - \sigma \left(\frac{\mathbf{E}^{n+1} + \mathbf{E}^n}{2} \right), \quad (8)$$

where we have employed central averages for the loss term in Ampere's law. Here δ_t is the time increment and \mathbf{E}^n denotes the value of \mathbf{E} at time $n\delta_t$. Upon the rearrangement of terms,

$$\mu \mathbf{H}^{n+1/2} = \mu \mathbf{H}^{n-1/2} - \delta_t \nabla \times \mathbf{E}^n \quad (9)$$

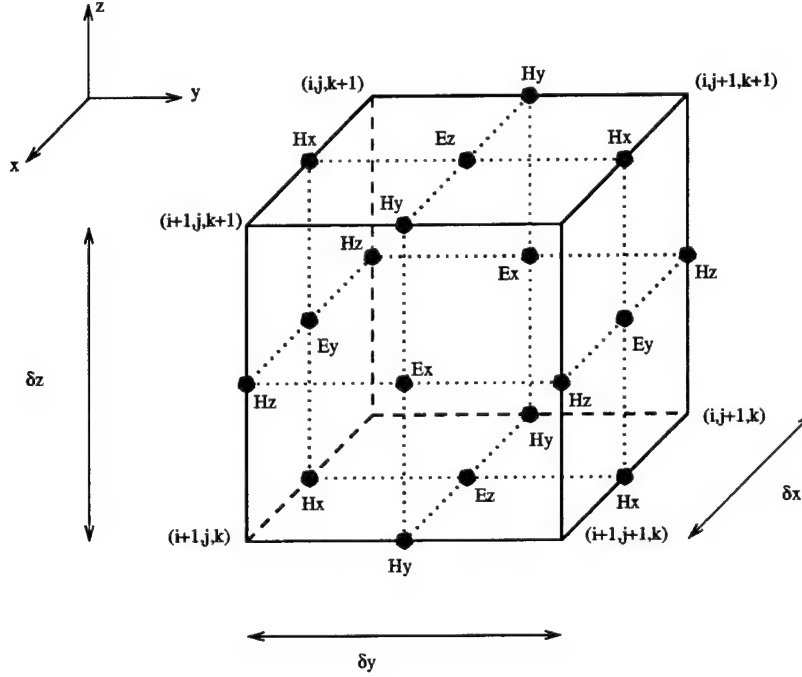


Figure 1: The Yee cell

and

$$\epsilon \mathbf{E}^{n+1} = \epsilon \left(\frac{1 - \sigma \delta_t/2}{1 + \sigma \delta_t/2} \right) \mathbf{E}^n + \left(\frac{\delta_t}{1 + \sigma \delta_t/2} \right) \nabla \times \mathbf{H}^{n+1/2}. \quad (10)$$

Whence, the update equation for the field constituents is readily observed. Given that \mathbf{E} and \mathbf{H} are synchronized, but syncopated by a half-time step, this type of integration scheme is commonly referred to as leap-frog integration. The previous equations constitute a second-order temporal method, as deduced from the truncation term of the central difference and average approximations.

To accomplish the spatial discretization, the Yee grid is invoked, as shown in Figure 1. The components of the Yee grid are arranged in accordance with the natural rotational structure of the curl operator acting upon \mathbf{H} , which is also spatially proportional to \mathbf{E} (or vice-versa). For example, upon the spatial discretization of the z -component of Ampere's law, we obtain,

$$\mathbf{a}_z \cdot \nabla \times \mathbf{H} \Big|_{i+1/2, j+1/2, k} = \left[\frac{H_y|_{i+1} - H_y|_i}{\delta_x} \right]_{j+1/2, k} - \left[\frac{H_x|_{j+1} - H_x|_j}{\delta_y} \right]_{i+1/2, k}. \quad (11)$$

The indices (i, j, k) denote the spatial coordinates $(i\delta_x, j\delta_y, k\delta_z)$ with δ_x , δ_y and δ_z being the length of the cell in the x, y, z directions, respectively. The remaining five components of electromagnetic field are derived in a similar manner.

To quantify the FDTD method in terms of its dissipation and dispersion errors, consider a plane wave propagating in the \mathbf{k} direction and in an homogeneous open domain. That is, let $\mathbf{E} = \mathbf{E}_0 e^{-j\mathbf{k} \cdot \mathbf{x}} e^{j\omega t}$ and $\mathbf{H} = \mathbf{H}_0 e^{-j\mathbf{k} \cdot \mathbf{x}} e^{j\omega t}$; \mathbf{E}_0 and \mathbf{H}_0 are constant vectors. If \mathbf{E} and \mathbf{H} are to be solutions of the discretized form of Maxwell's equations, then

$$-j\mathbf{K} \times \mathbf{E}_0 = -j\Omega\mu\mathbf{H}_0. \quad (12)$$

and

$$-j\mathbf{K} \times \mathbf{H}_o = j\Omega\epsilon\mathbf{E}_o + \Lambda\sigma\mathbf{E}_o; \quad (13)$$

moreover, $\mathbf{K} \cdot \mathbf{E}_o = 0$ and $\mathbf{K} \cdot \mathbf{H}_o = 0$. Here

$$\mathbf{K} = \left(\frac{2}{\delta_x}\right) \sin\left(\frac{k_x\delta_x}{2}\right) \mathbf{a}_x + \left(\frac{2}{\delta_y}\right) \sin\left(\frac{k_y\delta_y}{2}\right) \mathbf{a}_y + \left(\frac{2}{\delta_z}\right) \sin\left(\frac{k_z\delta_z}{2}\right) \mathbf{a}_z, \quad (14)$$

$$\Omega = \left(\frac{2}{\delta_t}\right) \sin\left(\frac{\omega\delta_t}{2}\right) \quad (15)$$

and

$$\Lambda = \cos\left(\frac{\omega\delta_t}{2}\right). \quad (16)$$

Obviously, $\mathbf{K} \rightarrow \mathbf{k}$, $\Omega \rightarrow \omega$ and $\Lambda \rightarrow 1$ as $\delta_x, \delta_y, \delta_z, \delta_t \rightarrow 0$, as required for a consistent scheme. Further manipulation of Eqns. (12) and (13) leads to the equation

$$\mathbf{K} \cdot \mathbf{K} = -j\Omega\mu(j\Omega\epsilon + \Lambda\sigma) = \Omega^2\mu\hat{\epsilon}, \quad (17)$$

which is the numerical dispersion equation and is the counterpart of the analytical dispersion equation $\mathbf{k} \cdot \mathbf{k} = -j\omega\mu(j\omega\epsilon + \sigma)$; here $\hat{\epsilon} = [\epsilon + \Lambda\sigma/(j\Omega)]$. In many of the subsequent sections this same equation will be referenced, but different permittivity relationships will be supplied. Whatever the case may be, Eqn. (17) provides the necessary information for understanding the scheme's dispersion, dissipation, anisotropy and stability properties [7, 8].

Stability (i.e., non-exponential growth in time) is insured if $\text{Im}\{\omega\delta_t\} > 0$. From Eqn. (17) and for $\sigma = 0$, this constraint is satisfied for all directions of propagation provided that [2]

$$\delta_t < \frac{1}{v_p} \left[\left(\frac{1}{\delta_x}\right)^2 + \left(\frac{1}{\delta_y}\right)^2 + \left(\frac{1}{\delta_z}\right)^2 \right]^{-1/2}. \quad (18)$$

Here $v_p = 1/\sqrt{\mu\epsilon}$, which is the phase velocity (if $\epsilon = \epsilon_o$ and $\mu = \mu_o$ then $v_p = c$, the speed of light). Note: If Eqn. (18) is satisfied, $\text{Im}\{\omega\delta_t\} = 0$, which implies a dissipationless numerical scheme. Finally, given that the FDTD method is both consistent and stable, Lax's theorem states that the data will converge to the exact solution as the cell and time-step become infinitesimally small [9].

In the ensuing sections, the FDTD method will be modified or extended to model wave propagation in complex media. However, in all cases considered, the Yee grid of Figure 1 and the discretization of the curl operators will be retained.

4 Cold Plasma

To demonstrate the wide variety of techniques available to model numerically wave propagation in linearly dispersive media, the case of wave propagation in an isotropic, lossy, cold plasma is considered next. For this scenario, Ampere's law and the momentum equation are [10]

$$\epsilon_o \frac{\partial \mathbf{E}}{\partial t} = \nabla \times \mathbf{H} - \mathbf{J}_p \quad (19)$$

and

$$\frac{\partial \mathbf{J}_p}{\partial t} = -\nu \mathbf{J}_p + \epsilon_o \omega_p^2 \mathbf{E}, \quad (20)$$

where \mathbf{J}_p is the polarization current, ν is the collision frequency and ω_p is the plasma frequency; specifically $\mathbf{J}_p = -n_o q \mathbf{u}$ and $\omega_p = \sqrt{n_o q^2 / (m \epsilon_o)}$. For time-harmonic signals of dependence $e^{j\omega t}$, it is a simple exercise to show that the momentum equation can be embedded into Ampere's law, from which a scalar frequency domain permittivity $\hat{\epsilon}$ can be defined. Suppressing that analysis, one finds that

$$\hat{\epsilon} = \epsilon_o \left(1 + \frac{\omega_p^2}{\omega(j\nu - \omega)} \right) = \epsilon_o (1 + \hat{\chi}(\omega)), \quad (21)$$

where $\hat{\chi}$ is the scalar frequency domain susceptibility. Since $\hat{\mathbf{D}} = \hat{\epsilon} \hat{\mathbf{E}}$, the corresponding time-domain constitutive relationship, cast in terms of a convolution integral, is deducible from Fourier theory [11]:

$$\mathbf{D}(\mathbf{x}, t) = \epsilon_o \mathbf{E}(\mathbf{x}, t) + \epsilon_o \int_{-\infty}^t \chi(\tau) \mathbf{E}(\mathbf{x}, t - \tau) d\tau, \quad (22)$$

where

$$\chi(\tau) = \frac{\omega_p^2}{\nu} [1 - e^{-\nu\tau}] U(\tau). \quad (23)$$

Here U is the unit step function.

Each equation in the previous development gives a different insight into the phenomenology of wave propagation in a cold plasma. And, for each of those insights, there exists a corresponding FDTD discretization methodology. In this section, we will explore several such methodologies and will classify those methodologies into two categories: Direct integration methods and recursive convolution methods. The direct integration methods are either based on the fundamental state equations of Eqns. (19) and (20) or on the constitutive relation $\hat{\mathbf{D}} = \hat{\epsilon} \hat{\mathbf{E}}$. The recursive methods incorporate the convolution integral of Eqn. (22) into the FDTD paradigm¹. Although each discretization procedure is consistent with the governing equations, their accuracy order and memory requirements are different. Such similarities and differences are documented in the last subsection.

In the following subsections, Eqn. (9) is the temporally discretized form of Faraday's law. Additionally, the components of \mathbf{J}_p , \mathbf{D} and \mathbf{E} are assumed to occupy the same locations in the Yee grid.

4.1 Direct Integration Method One: CP-DIM1

Consider first a state-space integration technique. For this situation, Eqns. (19) and (20) are discretized using central differences for the derivatives and central averages for the collision term. To maintain synchronization with the FDTD leap-frog integrator, the momentum equation and Faraday's law are advanced simultaneously and collectively leaped with Ampere's law. For source-free media, this procedure results in the following system of equations [15]:

$$\frac{\mathbf{J}_p^{n+1/2} - \mathbf{J}_p^{n-1/2}}{\delta_t} = -\nu \left(\frac{\mathbf{J}_p^{n+1/2} + \mathbf{J}_p^{n-1/2}}{2} \right) + \epsilon_o \omega_p^2 \mathbf{E}^n \quad (24)$$

and

$$\epsilon_o \left(\frac{\mathbf{E}^{n+1} - \mathbf{E}^n}{\delta_t} \right) = \nabla \times \mathbf{H}^{n+1/2} - \mathbf{J}_p^{n+1/2}. \quad (25)$$

Given the simplicity of the algebraic manipulations that solve for $\mathbf{J}_p^{n+1/2}$ in Eqn. (24), the final expression is not given. This will be the case for many of the other direct integration methods as well.

¹Since the Z -transform method is a subset of the recursive method, it will not be documented herein. For more information on using Z -transforms in conjunction with the FDTD method consult [12]–[14].

4.2 Direct Integration Method Two: CP-DIM2

Instead of averaging the loss term, as in CP-DIM1, averaging the current term in Ampere's law is equally possible. For this case, the momentum equation and Ampere's law are synchronized and collectively leaped with Faraday's law [16]. That is,

$$\frac{\mathbf{J}_p^{n+1} - \mathbf{J}_p^{n-1}}{2\delta_t} = -\nu\mathbf{J}_p^n + \epsilon_o\omega_p^2\mathbf{E}^n \quad (26)$$

and

$$\epsilon_o \left(\frac{\mathbf{E}^{n+1} - \mathbf{E}^n}{\delta_t} \right) = \nabla \times \mathbf{H}^{n+1/2} - \left(\frac{\mathbf{J}_p^{n+1} + \mathbf{J}_p^n}{2} \right). \quad (27)$$

4.3 Direct Integration Method Three: CP-DIM3

Next consider the case in which the polarization current in Ampere's law, the electric field term in the momentum equation and the dissipation term in the momentum equation are all time averaged. The synchronization of the momentum equation and Ampere's law is maintained [17]. The resulting scheme is

$$\frac{\mathbf{J}_p^{n+1} - \mathbf{J}_p^n}{\delta_t} = -\nu \frac{\mathbf{J}_p^{n+1} + \mathbf{J}_p^n}{2} + \epsilon_o\omega_p^2 \left(\frac{\mathbf{E}^{n+1} + \mathbf{E}^n}{2} \right) \quad (28)$$

and

$$\epsilon_o \left(\frac{\mathbf{E}^{n+1} - \mathbf{E}^n}{\delta_t} \right) = \nabla \times \mathbf{H}^{n+1/2} - \left(\frac{\mathbf{J}_p^{n+1} + \mathbf{J}_p^n}{2} \right). \quad (29)$$

4.4 Direct Integration Method Four: CP-DIM4

Observing that the momentum equation has solutions that decay exponentially like $e^{-\nu t}$, Cummer suggests that exponential fitting is necessary, particularly when the dissipation term is large [17]. To that end, the exponentially fitted equation is

$$\mathbf{J}_p^{n+1} = e^{-\nu\delta_t} \mathbf{J}_p^n + \frac{\epsilon_o\omega_p^2}{\nu^2\delta_t} (\nu\delta_t + e^{-\nu\delta_t} - 1) \mathbf{E}^{n+1} + \frac{\epsilon_o\omega_p^2}{\nu^2\delta_t} (1 - e^{-\nu\delta_t} - \nu\delta_t e^{-\nu\delta_t}) \mathbf{E}^n. \quad (30)$$

Ampere's law still requires the averaging of the polarization current:

$$\epsilon_o \left(\frac{\mathbf{E}^{n+1} - \mathbf{E}^n}{\delta_t} \right) = \nabla \times \mathbf{H}^{n+1/2} - \left(\frac{\mathbf{J}_p^{n+1} + \mathbf{J}_p^n}{2} \right). \quad (31)$$

4.5 Direct Integration Method Five: CP-DIM5

The next direct integration technique considers the frequency domain constitutive relationship $\hat{\mathbf{D}} = \hat{\epsilon}\hat{\mathbf{E}}$ and Eqn. (21) as the basis of temporal discretization [18]. Combining these two equations, we obtain

$$(\omega^2 - j\omega\nu)\hat{\mathbf{D}} = \epsilon_o(\omega^2 - j\omega\nu - \omega_p^2)\hat{\mathbf{E}}. \quad (32)$$

Since multiplications of $j\omega$ in the frequency domain are equivalent to time derivatives in the time-domain, Eqn. (32) is equivalent to

$$\frac{\partial^2 \mathbf{D}}{\partial t^2} + \nu \frac{\partial \mathbf{D}}{\partial t} = \epsilon_o \frac{\partial^2 \mathbf{E}}{\partial t^2} + \epsilon_o \nu \frac{\partial \mathbf{E}}{\partial t} + \epsilon_o \omega_p^2 \mathbf{E}. \quad (33)$$

Discretization of Eqn. (33) with second-order central differences, along with Eqn. (2), yields the following system of semi-discrete numerical equations:

$$\mathbf{D}^{n+1} = \mathbf{D}^n + \delta_t \nabla \times \mathbf{H}^{n+1/2}, \quad (34)$$

and

$$\begin{aligned} \epsilon_o(2 + \nu\delta_t)\mathbf{E}^{n+1} &= (2 + \nu\delta_t)\mathbf{D}^{n+1} - 4\mathbf{D}^n + (2 - \nu\delta_t)\mathbf{D}^{n-1} \\ &- 2\epsilon_o(\omega_p^2\delta_t^2 - 2)\mathbf{E}^n - \epsilon_o(2 - \nu\delta_t)\mathbf{E}^{n-1}. \end{aligned} \quad (35)$$

4.6 Recursive Convolution Method One: CP-RCM1

The recursive convolution method is based upon the discretization of the convolution integral of Eqn. (22) [19]. At time $n\delta_t$,

$$\mathbf{D}(\mathbf{x}, n\delta_t) = \epsilon_o \mathbf{E}(\mathbf{x}, n\delta_t) + \epsilon_o \int_0^{n\delta_t} \mathbf{E}(\mathbf{x}, n\delta_t - \tau) \chi(\tau) d\tau. \quad (36)$$

Under the assumption that \mathbf{E} is piece-wise constant,

$$\mathbf{D}^n = \epsilon_o \mathbf{E}^n + \epsilon_o \sum_{m=0}^{n-1} \mathbf{E}^{n-m} \int_{m\delta_t}^{(m+1)\delta_t} \chi(\tau) d\tau. \quad (37)$$

Likewise,

$$\mathbf{D}^{n+1} = \epsilon_o \mathbf{E}^{n+1} + \epsilon_o \sum_{m=0}^n \mathbf{E}^{n-m+1} \int_{m\delta_t}^{(m+1)\delta_t} \chi(\tau) d\tau. \quad (38)$$

The discretization of Ampere's law, as given by Eqn. (2), requires us to take the difference of the two preceding equations. Doing so and replacing that difference into Ampere's law, we obtain

$$\mathbf{E}^{n+1} = \alpha \mathbf{E}^n + \alpha \Psi^n + \frac{\alpha \delta_t}{\epsilon_o} \nabla \times \mathbf{H}^{n+1/2}, \quad (39)$$

where

$$\Psi^n = \sum_{m=0}^{n-1} \mathbf{E}^{n-m} \Delta \chi^m \quad (40)$$

and

$$\alpha = \frac{1}{1 + \chi^0}. \quad (41)$$

Here

$$\Delta \chi^m = \chi^m - \chi^{m+1} \quad (42)$$

and

$$\chi^m = \int_{m\delta_t}^{(m+1)\delta_t} \chi(\tau) d\tau. \quad (43)$$

Performing the calculation for χ^0 and $\Delta \chi^m$ in conjunction with Eqn. (23), we obtain

$$\chi^0 = \frac{\omega_p^2 \delta_t}{\nu} - \left(\frac{\omega_p}{\nu} \right)^2 (1 - e^{-\nu \delta_t}) \quad (44)$$

and

$$\Delta \chi^m = - \left(\frac{\omega_p}{\nu} \right)^2 e^{-m\nu \delta_t} (1 - e^{-\nu \delta_t})^2 = \Delta \chi^0 e^{-m\nu \delta_t}. \quad (45)$$

Although Maxwell's equations are temporally discretized, they are not in a form suitable for computation. For we note that to compute Eqn. (40), one would have to store the complete time history of \mathbf{E} . However, given the exponential form of $\Delta\chi^m$,

$$\Psi^n = \Delta\chi^0 \sum_{m=0}^{n-1} \mathbf{E}^{n-m} e^{-m\nu\delta_t}; \quad (46)$$

whence,

$$\Psi^n = \Delta\chi^0 \mathbf{E}^n + e^{-\nu\delta_t} \Psi^{n-1}. \quad (47)$$

Thus, the equation for Ψ reduces to a simple recursive relationship.

4.7 Recursive Convolution Method Two: CP-RCM2

Numerical accuracy of CP-RCM1 can be increased by assuming piecewise linear line segments in the integration of the convolution integral [20]. For this situation, one approximates \mathbf{E} over the interval $[n\delta_t, (n+1)\delta_t]$ with

$$\mathbf{E}(\mathbf{x}, t) = \mathbf{E}(\mathbf{x}, n\delta_t) + (t - n\delta_t) \left(\frac{\mathbf{E}(\mathbf{x}, (n+1)\delta_t) - \mathbf{E}(\mathbf{x}, n\delta_t)}{\delta_t} \right). \quad (48)$$

Substitution of this approximation into Eqn. (36) yields the following result:

$$\mathbf{D}^n = \epsilon_0 \mathbf{E}^n + \epsilon_0 \sum_{m=0}^{n-1} \mathbf{E}^{n-m} \chi^m + \epsilon_0 \sum_{m=0}^{n-1} (\mathbf{E}^{n-m-1} - \mathbf{E}^{n-m}) \xi^m, \quad (49)$$

where χ^m is given by Eqn. (43) and

$$\xi^m = \frac{1}{\delta_t} \int_{m\delta_t}^{(m+1)\delta_t} (\tau - m\delta_t) \chi(\tau) d\tau. \quad (50)$$

As before, the time derivative of \mathbf{D} at time $(n+1/2)\delta_t$ is approximated to second-order by $(\mathbf{D}^{n+1} - \mathbf{D}^n)/\delta_t$. From Eqn. (2) and Eqn. (49),

$$\mathbf{E}^{n+1} = \alpha(1 - \xi^0) \mathbf{E}^n + \frac{\alpha\delta_t}{\epsilon_0} \nabla \times \mathbf{H}^{n+1/2} + \alpha \Psi^n. \quad (51)$$

Here

$$\Psi^n = \sum_{m=0}^{n-1} \mathbf{E}^{n-m} \Delta\chi^m + (\mathbf{E}^{n-m-1} - \mathbf{E}^{n-m}) \Delta\xi^m, \quad (52)$$

$$\alpha = \frac{1}{(1 + \chi^0 - \xi^0)} \quad (53)$$

and

$$\Delta\xi^m = \xi^m - \xi^{m+1}. \quad (54)$$

The expression for $\Delta\chi^m$ is given by Eqn. (45).

For the time-domain susceptibility function given by Eqn. (23), it is a simple matter to show that

$$\xi^m = \frac{\omega_p^2}{\delta_t \nu} \left[\frac{\delta_t^2}{2} + \frac{e^{-\nu m \delta_t}}{\nu} \left(\delta_t e^{-\nu \delta_t} + \frac{e^{-\nu \delta_t}}{\nu} - \frac{1}{\nu} \right) \right] \quad (55)$$

Method	Numerical Permittivity: $\hat{\epsilon}$
CP-DIM1	$\hat{\epsilon} = \epsilon_0 \left(1 + \frac{\omega_p^2}{\Omega(j\nu\Lambda - \Omega)} \right)$
CP-DIM2	$\hat{\epsilon} = \epsilon_0 \left(1 + \frac{\omega_p^2 \Lambda}{\Omega(j\nu - \Omega\Lambda)} \right)$
CP-DIM3	$\hat{\epsilon} = \epsilon_0 \left(1 + \frac{\omega_p^2 \Lambda^2}{\Omega(j\nu\Lambda - \Omega)} \right)$
CP-DIM4	$\hat{\epsilon} = \epsilon_0 \left[1 + \frac{\Lambda\omega_p^2 \{ \nu \sin[(\omega - j\nu)\delta_t/2] - \Omega \sinh(\nu\delta_t/2) \}}{j\Omega\nu^2 \sin[(\omega - j\nu)\delta_t/2]} \right]$
CP-DIM5	$\hat{\epsilon} = \epsilon_0 \left(1 + \frac{\omega_p^2}{\Omega(j\nu\Lambda - \Omega)} \right)$
CP-RCM1	$\hat{\epsilon} = \epsilon_0 \left(1 + \frac{\chi^0 e^{j\omega\delta_t/2}}{j\Omega\delta_t} + \frac{\Delta\chi^0 e^{\nu\delta_t/2}}{2\Omega\delta_t \sin[(\omega - j\nu)\delta_t/2]} \right)$
CP-RCM2	$\hat{\epsilon} = \epsilon_0 \left[1 - \xi^0 + \frac{\chi^0 e^{j\omega\delta_t/2}}{j\Omega\delta_t} + \left(\frac{\Delta\chi^0 - j\Omega\delta_t \Delta\xi^0 e^{-j\omega\delta_t/2}}{2\Omega\delta_t \sin[(\omega - j\nu)\delta_t/2]} \right) e^{\nu\delta_t/2} \right]$

Table 1: Numerical permittivities for various schemes associated with propagation in an isotropic cold plasma.

and

$$\Delta\xi^m = \frac{\omega_p^2}{\delta_t\nu^2} \left(\delta_t e^{-\nu\delta_t} + \frac{e^{-\nu\delta_t}}{\nu} - \frac{1}{\nu} \right) (1 - e^{-\nu\delta_t}) e^{-m\nu\delta_t} = \Delta\xi^0 e^{-m\nu\delta_t}. \quad (56)$$

Finally, the summation over all time in Eqn. (52) is replaced with a recursive factor – to wit,

$$\Psi^n = \Delta\chi^0 \mathbf{E}^n + (\mathbf{E}^{n-1} - \mathbf{E}^n) \Delta\xi^0 + e^{-\nu\delta_t} \Psi^{n-1}. \quad (57)$$

The expression for $\Delta\chi^0$ is given by Eqn. (45) when $m = 0$.

Although the previous equation appears to require an additional storage location for \mathbf{E}^{n-1} , such is not the case. As pointed out by Kelley *et al.* [20], a low storage implementation is possible by making judicious use of a temporary variable.

4.8 Comparative Analysis

The numerical errors of each of the aforementioned schemes are deduced in a similar way as in Section Three. Assuming again plane wave propagation and an unbounded domain, the numerical dispersion relationship is similar to that given by Eqn. (17). Of course, each scheme produces a different $\hat{\epsilon}$, as seen in Table 1. Note the equivalence between CP-DIM1 and CP-DIM5. Even though both of these procedures are derived from different equations, the final numerical permittivities are identical. However, as seen in Table 3, CP-DIM5 requires more memory. Next, as pointed out by Cummer [17], there exists an equivalence between exponential differencing (i.e., CP-DIM4) and the recursive convolution methods; this observation is confirmed in Table 1, where it is seen that the numerical permittivities bear some semblance to one another. Finally, if $\xi^0 = \Delta\xi^0 = 0$, CP-RCM1 and CP-RCM2 are one and the same, as expected.

To appreciate the subtle differences between each of the schemes, Table 2 is provided. In this table, each entry corresponds to the leading term of the Taylor series of the function $\Omega^2\hat{\epsilon}/\epsilon_0$. As seen from Eqn. (17), the function $\Omega^2\hat{\epsilon}$ contains the complete temporal information of the numerical scheme. Except for CP-RCM1, these numerical permittivity relationships reduce to the exact analytical permittivity relationship to the order of δ_t^2 ; CP-RCM1 is temporally accurate to first-order. Of course, for certain choices of ω , ω_p , ν , δ_t , the scheme with lowest truncation term is deemed temporally best, from an accuracy point of view.

Method	Truncation Term	Truncation Term: $\nu = 0$
CP-DIM1	$\frac{(\nu^2\omega^4 + 2j\nu\omega^5 - \omega^6 + j\nu\omega^3\omega_p^2)\delta_t^2}{12(\omega - j\nu)^2}$	$\frac{-\omega^4\delta_t^2}{12}$
CP-DIM2	$\frac{(\nu^2\omega^4 + 2j\nu\omega^5 - \omega^6 - 2j\nu\omega^3\omega_p^2)\delta_t^2}{12(\omega - j\nu)^2}$	$\frac{-\omega^4\delta_t^2}{12}$
CP-DIM3	$\left(-\omega^4 + \frac{2j\omega^3\omega_p^2}{\nu + j\omega} - \frac{\omega^4\omega_p^2}{(\nu + j\omega)^2}\right)\left(\frac{\delta_t^2}{12}\right)$	$\frac{\omega^2(-\omega^2 + 3\omega_p^2)\delta_t^2}{12}$
CP-DIM4	$\left(-\omega^4 + \frac{3j\omega^3\omega_p^2}{\nu + j\omega}\right)\left(\frac{\delta_t^2}{12}\right)$	$\frac{\omega^2(-\omega^2 + 3\omega_p^2)\delta_t^2}{12}$
CP-DIM5	$\frac{(\nu^2\omega^4 + 2j\nu\omega^5 - \omega^6 + j\nu\omega^3\omega_p^2)\delta_t^2}{12(\omega - j\nu)^2}$	$\frac{-\omega^4\delta_t^2}{12}$
CP-RCM1	$\frac{\omega_p^2\omega^2\delta_t}{2(\nu + j\omega)}$	$\frac{\omega_p^2\omega\delta_t}{2j}$
CP-RCM2	$\left(-\omega^4 + \frac{2j\omega^3\omega_p^2}{\nu + j\omega}\right)\left(\frac{\delta_t^2}{12}\right)$	$\frac{\omega^2(-\omega^2 + 2\omega_p^2)\delta_t^2}{12}$

Table 2: Truncation term from the Taylor analysis of $\Omega^2\hat{\epsilon}/\epsilon_0$: Cold plasma.

A special case of interest is when $\nu = 0$. From Table 2, it is readily seen that CP-DIM1, CP-DIM2 and CP-DIM5 all have the same leading truncation term, which is independent ω_p . CP-DIM3 and CP-DIM4 also have the same truncation term; the truncation term for CP-RCM2 is close in value to that of CP-DIM3 and CP-DIM4. Since the truncation term for CP-DIM3, CP-DIM4 and CP-RCM2 are dependent on ω_p^2 , the truncation terms are smaller than those associated with CP-DIM1, CP-DIM2 and CP-DIM5. Moreover, there exists a frequency for which the truncation terms of CP-DIM3, CP-DIM4 and CP-RCM2 vanish. Finally, if $\omega_p^2\delta_t^2 \ll 1$, then all of the second order schemes produce a truncation term of $-\omega^4\delta_t^2/12$, which is the truncation term of the standard FDTD algorithm.

Other properties of these algorithms, including memory and one-dimensional CFL equations are shown in Table 3 [17]. As expected from the previous discussion on the truncation terms, CP-DIM1, CP-DIM2 and CP-DIM5 have the same stability equations, which are dependent on the plasma frequency, when $\nu = 0$. When $\nu \neq 0$, CP-DIM2 is unconditionally unstable. CP-DIM3 and CP-DIM4 have a CFL of unity. This is to be expected since the leading truncation term of $\Omega^2\hat{\epsilon}/\epsilon_0$ for CP-DIM3 and CP-DIM4 contains the factor $(\omega_p\delta_t/2)^2$, which is also the same factor that appears in the CFL equation for CP-DIM1, CP-DIM2 and CP-DIM5. As for CP-RCM1 and CP-RCM2, the CFL is found experimentally to be near unity [17]. From a memory point of view, CP-DIM2 and CP-DIM5 require additional memory (compared to the other schemes) for the back storage of a vector.

5 Debye Dielectric

The Debye dielectric has received considerable attention in the literature due to the fast growing interest in electromagnetic wave interactions with biological and water-based substances [21]–[23]. Given the water content of these substances, they are well modeled by a combination of single-pole models, which account for permanent dipole moments established within the water [3]. Moreover, since the Debye model is consistent with the requirements associated with the Kramers–Kronig relationships, the model inherently satisfies causality requirements. For this reason, an M -pole model is often used to construct an analytical model

Method	3D Memory/Cell	1D Stability
CP-DIM1	9	$\delta_t < (\delta_x/c)\sqrt{1 - (\omega_p\delta_t/2)^2}; \nu = 0$
CP-DIM2	12	$\delta_t < (\delta_x/c)\sqrt{1 - (\omega_p\delta_t/2)^2}; \nu = 0$
CP-DIM3	9	$\delta_t < \delta_x/c$
CP-DIM4	9	$\delta_t < \delta_x/c$
CP-DIM5	12	$\delta_t < (\delta_x/c)\sqrt{1 - (\omega_p\delta_t/2)^2}; \nu = 0$
CP-RCM1	9	$\delta_t^{max} \approx \delta_x/c$
CP-RCM2	9	$\delta_t^{max} \approx \delta_x/c$

Table 3: Comparison table of various schemes in terms of memory per cell and stability equations: Cold plasma.

from empirical data. Since in the frequency-domain the permittivity of the Debye dielectric is given by

$$\hat{\epsilon} = \epsilon_o \epsilon_\infty + \epsilon_o \sum_{k=1}^M \frac{\epsilon_{sk} - \epsilon_\infty}{1 + j\omega\tau_k} = \epsilon_o (1 + \hat{\chi}(\omega)), \quad (58)$$

the modeling task is to deduce values for τ_k , ϵ_∞ and ϵ_{sk} that best fit $\hat{\epsilon}$ to the data [24]. Here τ_k is the k th relaxation time, $\epsilon_o \epsilon_\infty$ is the value of $\hat{\epsilon}$ at infinite frequency and $\epsilon_{sk} \epsilon_o$ is the zero frequency permittivity of the k th relaxation. Note: In the time-domain,

$$\chi(t) = \sum_{k=1}^M \left(\frac{\epsilon_{sk} - \epsilon_\infty}{\tau_k} \right) e^{-t/\tau_k} U(t). \quad (59)$$

The Debye dielectric may also be characterized in state variable form (excluding Faraday's law) in terms of the polarization vector \mathbf{P} [25]:

$$\epsilon_o \epsilon_\infty \frac{\partial \mathbf{E}}{\partial t} = \nabla \times \mathbf{H} - \sum_{k=1}^M \frac{1}{\tau_k} [(\epsilon_{sk} - \epsilon_\infty) \epsilon_o \mathbf{E} - \mathbf{P}_k] \quad (60)$$

and

$$\frac{\partial \mathbf{P}_k}{\partial t} = \frac{1}{\tau_k} [(\epsilon_{sk} - \epsilon_\infty) \epsilon_o \mathbf{E} - \mathbf{P}_k], \quad (61)$$

where $k = 1, 2, \dots, M$ in the last equation (Note: The subscript k denotes the pole number, not the spatial index of z). These latter two equations form the basis for two of the direct integration schemes.

5.1 Direct Integration Method One: D-DIM1

For the first direct integration technique, consider initially a single-pole model. Then

$$\epsilon_o \epsilon_\infty \frac{\partial \mathbf{E}}{\partial t} = \nabla \times \mathbf{H} - \frac{1}{\tau} [(\epsilon_s - \epsilon_\infty) \epsilon_o \mathbf{E} - \mathbf{P}] \quad (62)$$

and

$$\frac{\partial \mathbf{P}}{\partial t} = \frac{1}{\tau} [(\epsilon_s - \epsilon_\infty) \epsilon_o \mathbf{E} - \mathbf{P}]. \quad (63)$$

The components of \mathbf{P} and \mathbf{E} are conjoined on the Yee grid and the discretization of the curl operators is accomplished in the usual manner. Regarding the temporal discretization, we invoke the notion of the central difference and average approximations and the leap-frog time advancement [26]. To this end,

$$\frac{\mathbf{P}^{n+1/2} - \mathbf{P}^{n-1/2}}{\delta_t} = \frac{1}{\tau} \left[(\epsilon_s - \epsilon_\infty) \epsilon_o \mathbf{E}^n - \left(\frac{\mathbf{P}^{n+1/2} + \mathbf{P}^{n-1/2}}{2} \right) \right] \quad (64)$$

and

$$\epsilon_o \epsilon_\infty \left(\frac{\mathbf{E}^{n+1} - \mathbf{E}^n}{\delta_t} \right) = \nabla \times \mathbf{H}^{n+1/2} - \frac{1}{\tau} \left[(\epsilon_s - \epsilon_\infty) \epsilon_o \left(\frac{\mathbf{E}^{n+1} + \mathbf{E}^n}{2} \right) - \mathbf{P}^{n+1/2} \right]. \quad (65)$$

The proceeding equations can be algebraically arranged so that only $\mathbf{P}^{n+1/2}$ and \mathbf{E}^{n+1} appear on the left-hand side of the equations; see [26]. Note that in this implementation, the polarization vector \mathbf{P} and the magnetic field vector \mathbf{H} are advanced simultaneously and leaped with \mathbf{E} .

The basic strategy for M -poles is essentially the same as before, with the exception that all of the polarization equations are advanced simultaneously with Faraday's law [26]. When temporal averaging is invoked, the discretized temporal form becomes

$$\frac{\mathbf{P}_k^{n+1/2} - \mathbf{P}_k^{n-1/2}}{\delta_t} = \frac{1}{\tau_k} \left[(\epsilon_{sk} - \epsilon_\infty) \epsilon_o \mathbf{E}^n - \left(\frac{\mathbf{P}_k^{n+1/2} + \mathbf{P}_k^{n-1/2}}{2} \right) \right] \quad (66)$$

and

$$\epsilon_o \epsilon_\infty \left(\frac{\mathbf{E}^{n+1} - \mathbf{E}^n}{\delta_t} \right) = \nabla \times \mathbf{H}^{n+1/2} - \sum_{k=1}^M \frac{1}{\tau_k} \left[(\epsilon_{sk} - \epsilon_\infty) \epsilon_o \left(\frac{\mathbf{E}^{n+1} + \mathbf{E}^n}{2} \right) - \mathbf{P}_k^{n+1/2} \right]. \quad (67)$$

Further manipulation of Eqns. (66) and (67) leads to the following update equations for \mathbf{P} and \mathbf{E} :

$$\mathbf{P}_k^{n+1/2} = \alpha_k \mathbf{P}_k^{n-1/2} + \beta_k \delta_t \tau_k^{-1} (\epsilon_{sk} - \epsilon_\infty) \epsilon_o \mathbf{E}^n, \quad (68)$$

where

$$\alpha_k = \frac{2\tau_k - \delta_t}{2\tau_k + \delta_t}, \quad (69)$$

and

$$\beta_k = \frac{2\tau_k}{2\tau_k + \delta_t}; \quad (70)$$

$$\mathbf{E}^{n+1} = c_1 \mathbf{E}^n + c_2 \delta_t \nabla \times \mathbf{H}^{n+1/2} + c_2 \delta_t \sum_{k=1}^M \tau_k^{-1} \mathbf{P}_k^{n+1/2}, \quad (71)$$

where

$$c_1 = \left[\epsilon_\infty - \frac{\delta_t}{2} \sum_{k=1}^M \frac{\epsilon_{sk} - \epsilon_\infty}{\tau_k} \right] \left[\epsilon_\infty + \frac{\delta_t}{2} \sum_{k=1}^M \frac{\epsilon_{sk} - \epsilon_\infty}{\tau_k} \right]^{-1} \quad (72)$$

and

$$c_2 = \left[\epsilon_\infty \epsilon_o + \frac{\delta_t}{2} \sum_{k=1}^M \frac{(\epsilon_{sk} - \epsilon_\infty) \epsilon_o}{\tau_k} \right]^{-1}. \quad (73)$$

5.2 Direct Integration Method Two: D-DIM2

To have greater control over the stability properties of the scheme, semi-implicit schemes, such as those proposed by Kashiwa [25] and Petropoulos [27] must be considered. (The reader may also consult [28] for further information on the semi-implicit approach.) For example, for M th-order media,

$$\epsilon_o \epsilon_\infty \left(\frac{\mathbf{E}^{n+1} - \mathbf{E}^n}{\delta_t} \right) + \sum_{k=1}^M \left(\frac{\mathbf{P}_k^{n+1} - \mathbf{P}_k^n}{\delta_t} \right) = \nabla \times \mathbf{H}^{n+1/2} \quad (74)$$

and

$$\left(\frac{\mathbf{P}_k^{n+1} - \mathbf{P}_k^n}{\delta_t} \right) = \frac{1}{\tau_k} \left[(\epsilon_{sk} - \epsilon_\infty) \epsilon_o \left(\frac{\mathbf{E}^{n+1} + \mathbf{E}^n}{2} \right) - \left(\frac{\mathbf{P}_k^{n+1} + \mathbf{P}_k^n}{2} \right) \right]; \quad (75)$$

here $k = 1, 2, \dots, M$.

5.3 Direct Integration Method Three: D-DIM3

Before leaving this section on direct integration techniques, we wish to consider an integration technique based upon the frequency domain permittivity relationship: $\hat{\mathbf{D}} = \hat{\epsilon} \hat{\mathbf{E}}$ [18]. As an example, consider the technique for a one-pole Debye dielectric. For this situation, the constitutive relationship can be written as

$$\hat{\mathbf{D}} = \epsilon_o \left[\epsilon_\infty + \frac{\epsilon_s - \epsilon_\infty}{1 + j\omega\tau} \right] \hat{\mathbf{E}}. \quad (76)$$

Or, in the time-domain,

$$\mathbf{D} + \tau \frac{\partial \mathbf{D}}{\partial t} = \epsilon_s \epsilon_o \mathbf{E} + \epsilon_\infty \epsilon_o \tau \frac{\partial \mathbf{E}}{\partial t}. \quad (77)$$

As before, central differences and averages are applied to the previous ordinary differential equation, whereby an update equation for \mathbf{E} is obtained. Using this update equation and the corresponding update equation for Ampere's law, we obtain

$$\mathbf{D}^{n+1} = \mathbf{D}^n + \delta_t \nabla \times \mathbf{H}^{n+1/2} \quad (78)$$

and

$$\mathbf{E}^{n+1} = \left(\frac{\delta_t + 2\tau}{\epsilon_o(2\tau\epsilon_\infty + \epsilon_s\delta_t)} \right) \mathbf{D}^{n+1} + \left(\frac{\delta_t - 2\tau}{\epsilon_o(2\tau\epsilon_\infty + \epsilon_s\delta_t)} \right) \mathbf{D}^n + \left(\frac{2\tau\epsilon_\infty - \epsilon_s\delta_t}{2\tau\epsilon_\infty + \epsilon_s\delta_t} \right) \mathbf{E}^n. \quad (79)$$

Note: The update equation for \mathbf{E}^{n+1} must be rederived for each additional pole considered in the dielectric model.

5.4 Recursive Convolution Method One: D-RCM1

The formulation of the recursive convolution method follows one-for-one with that of CP-RCM1. The only difference in that formulation and the one presented below is the equation for the accumulator, since the time-domain susceptibility function is different. To account for ϵ_∞ , the first-order update equation is rewritten as [29]

$$\mathbf{E}^{n+1} = \epsilon_\infty \alpha \mathbf{E}^n + \alpha \Psi^n + \frac{\alpha \delta_t}{\epsilon_o} \nabla \times \mathbf{H}^{n+1/2}, \quad (80)$$

where

$$\alpha = \frac{1}{\epsilon_\infty + \chi^0}; \quad (81)$$

here

$$\chi^0 = (\epsilon_s - \epsilon_\infty) (1 - e^{-\delta_t/\tau}). \quad (82)$$

With respect to the accumulator,

$$\Psi^n = \Delta\chi^0 \mathbf{E}^n + e^{-\delta_t/\tau} \Psi^{n-1}, \quad (83)$$

where

$$\Delta\chi^0 = \chi^0 (1 - e^{-\delta_t/\tau}). \quad (84)$$

5.5 Recursive Convolution Method Two: D-RCM2

To improve the temporal accuracy, a piecewise linear model may be employed in the integrand of the convolution integral [20]. (See also CP-RCM2 for the cold plasma.) The final equations are

$$\mathbf{E}^{n+1} = \alpha(\epsilon_\infty - \xi^0) \mathbf{E}^n + \frac{\alpha\delta_t}{\epsilon_0} \nabla \times \mathbf{H}^{n+1/2} + \alpha \Psi^n, \quad (85)$$

where

$$\alpha = \frac{1}{(\epsilon_\infty + \chi^0 - \xi^0)} \quad (86)$$

and

$$\Psi^n = \Delta\chi^0 \mathbf{E}^n + (\mathbf{E}^{n-1} - \mathbf{E}^n) \Delta\xi^0 + e^{-\delta_t/\tau} \Psi^{n-1}. \quad (87)$$

Here χ^0 and $\Delta\chi^0$ are given by Eqns. (82) and (84), respectively. As for ξ^0 and $\Delta\xi^0$,

$$\xi^0 = -(\epsilon_s - \epsilon_\infty) \left(\frac{\tau}{\delta_t} \right) \left[\left(\frac{\delta_t}{\tau} + 1 \right) e^{-\delta_t/\tau} - 1 \right] \quad (88)$$

and

$$\Delta\xi^0 = \xi^0 (1 - e^{-\delta_t/\tau}). \quad (89)$$

5.6 Comparative Analysis

As with the cold plasma, Table 4 documents the numerical permittivities for the previously reported schemes. From this table, the equivalence between D-DIM2 and D-DIM3 is seen. However, since D-DIM3 is constructed from the frequency-domain constitutive equation, D-DIM3 requires more memory than D-DIM2. Finally, D-RCM1 is first-order accurate in time; all other schemes are temporally second-order accurate.

To appreciate many of the subtle features of each of the aforementioned schemes, Tables 5 and 6 are given. These tables show the leading truncation term of the function $\Omega^2 \hat{\epsilon}/\epsilon_0$. From a temporal accuracy point of view, the scheme with the lowest truncation term for a given ω , τ , ϵ_s , ϵ_∞ and δ_t is deemed best. Consider Table 6, which shows the leading truncation term for the two cases $\omega\tau \ll 1$ and $\omega\tau \gg 1$. Except for D-RCM1, all other schemes have identical high-frequency truncation terms. These terms are the same truncation terms that the standard FDTD algorithm would produce in a dielectric of permittivity $\epsilon_\infty\epsilon_0$. In the low-frequency limit only D-DIM2 and D-DIM3 predict the anticipated truncation term. Thus it can be argued that D-DIM2 and D-DIM3 are the most compatible with the standard FDTD algorithm.

A summary of the stability properties and memory requirements of the various methodologies is provided in Table 7. Here we note that D-DIM2 is the most memory intensive. With respect to the stability equations,

Method	Numerical Permittivity: $\hat{\epsilon}$		
D-DIM1	$\hat{\epsilon} = \epsilon_\infty \epsilon_0 + \epsilon_0 (\epsilon_s - \epsilon_\infty)$	$\frac{\Lambda + j(\delta_t/2)^2(\Omega/\tau)}{\Lambda + j\Omega\tau}$	
D-DIM2	$\hat{\epsilon} = \epsilon_\infty \epsilon_0 + (\epsilon_s - \epsilon_\infty) \epsilon_0$	$\frac{\Lambda}{\Lambda + j\Omega\tau}$	
D-DIM3	$\hat{\epsilon} = \epsilon_\infty \epsilon_0 + (\epsilon_s - \epsilon_\infty) \epsilon_0$	$\frac{\Lambda}{\Lambda + j\Omega\tau}$	
D-RCM1	$\hat{\epsilon} = \epsilon_0$	$\epsilon_\infty + \frac{\chi^0 e^{j\omega\delta_t/2}}{j\Omega\delta_t} - \frac{\Delta\chi^0 e^{\delta_t/(2\tau)}}{2j\Omega\delta_t \sinh[(\delta_t/\tau)(1+j\omega\tau)/2]}$	
D-RCM2	$\hat{\epsilon} = \epsilon_0$	$\epsilon_\infty - \xi^0 + \frac{\chi^0 e^{j\omega\delta_t/2}}{j\Omega\delta_t} - \left(\frac{\Delta\chi^0 - j\Omega\delta_t \Delta\epsilon^0 e^{-j\omega\delta_t/2}}{2j\Omega\delta_t \sinh[(\delta_t/\tau)(1+j\omega\tau)/2]} \right) e^{\delta_t/(2\tau)}$	

Table 4: Numerical permittivities for various schemes associated with propagation in single-pole Debye dielectric.

Method	Truncation Term	
D-DIM1	$\frac{\omega^4 \delta_t^2}{12}$	$(\epsilon_s - \epsilon_\infty) \left(\frac{3j}{\omega\tau} + \frac{j}{j-\omega\tau} - \frac{1}{(j-\omega\tau)^2} \right) - \epsilon_\infty$
D-DIM2	$\frac{\omega^4 \delta_t^2}{12}$	$(\epsilon_\infty - \epsilon_s) \left(\frac{2j}{j-\omega\tau} + \frac{1}{(j-\omega\tau)^2} \right) - \epsilon_\infty$
D-DIM3	$\frac{\omega^4 \delta_t^2}{12}$	$(\epsilon_\infty - \epsilon_s) \left(\frac{2j}{j-\omega\tau} + \frac{1}{(j-\omega\tau)^2} \right) - \epsilon_\infty$
D-RCM1	$\frac{j\omega^3 \delta_t}{2}$	$\frac{\epsilon_s - \epsilon_\infty}{1+j\omega\tau}$
D-RCM2	$\frac{\omega^4 \delta_t^2}{12}$	$\frac{j(\epsilon_\infty - 2\epsilon_s) + \epsilon_\infty \omega\tau}{j-\omega\tau}$

Table 5: Truncation term from the Taylor analysis of $\Omega^2 \hat{\epsilon}/\epsilon_0$: Debye dielectric.

Method	Truncation Term: $\omega\tau \ll 1$	Truncation Term: $\omega\tau \gg 1$
D-DIM1	$\left(\frac{\omega^4 \delta_t^2}{12} \right) [(\epsilon_s - \epsilon_\infty) (2 + \frac{3j}{\omega\tau}) - \epsilon_\infty]$	$\frac{-\omega^4 \delta_t^2 \epsilon_\infty}{12}$
D-DIM2	$\frac{-\omega^4 \delta_t^2 \epsilon_s}{12}$	$\frac{-\omega^4 \delta_t^2 \epsilon_\infty}{12}$
D-DIM3	$\frac{-\omega^4 \delta_t^2 \epsilon_s}{12}$	$\frac{-\omega^4 \delta_t^2 \epsilon_\infty}{12}$
D-RCM1	$\left(\frac{j\omega^3 \delta_t}{2} \right) (\epsilon_s - \epsilon_\infty)$	$\left(\frac{\omega^2 \delta_t}{2\tau} \right) (\epsilon_s - \epsilon_\infty)$
D-RCM2	$\left(\frac{\omega^4 \delta_t^2}{12} \right) (\epsilon_\infty - 2\epsilon_s)$	$\frac{-\omega^4 \delta_t^2 \epsilon_\infty}{12}$

Table 6: Truncation term from the Taylor analysis of $\Omega^2 \hat{\epsilon}/\epsilon_0$ for two special cases: Debye dielectric.

Method	3D Memory/Cell	1D Stability
D-DIM1	9	$\delta_t < \delta_x / v_p^{max}$
D-DIM2	9	$\delta_t < \sqrt{\epsilon_\infty} \delta_x / c$
D-DIM3	12	$\delta_t < \sqrt{\epsilon_\infty} \delta_x / c$
D-RCM1	9	$\delta_t < \delta_x / v_p^{max}$
D-RCM2	9	$\delta_t < \delta_x / v_p^{max}$

Table 7: Comparison table of various schemes in terms of memory per cell and stability equations: Single-pole Debye dielectric.

the entries for D-DIM1, D-RCM1 and D-RCM2 have not been rigorously established. The entry for D-DIM3 follows directly from the semi-implicit nature of the scheme [30]. Finally, since D-DIM2 and D-DIM3 are equivalent to one another, they also have the same stability equation.

To close this section, a comment on multi-pole Debye dielectrics is in order. Each of the schemes reviewed herein are capable of modeling the multi-pole dielectric. Some schemes like D-DIM1, D-RCM1 and D-RCM2 can be directly extended without any special treatment. Other schemes like D-DIM3 require a new derivation for each new pole added to the model. As for D-DIM2, the semi-implicit nature requires the loading and the inverting of a new matrix (each time a pole is added) to find the necessary coefficients of the algorithm.

5.7 Parameter Selection

To set the parameters δ_t and δ_x for the simulation, consider the example in which muscle is the medium. For a two-pole model, $\epsilon_\infty = 40$, $\epsilon_{s1} = 3948$, $\epsilon_{s2} = 59.09$, $\tau_1 = 46.25$ ns and $\tau_2 = .0907$ ns [23]. One possible way to deduce a value for δ_t is to make it a fraction of the smallest relaxation; for this example, let $\delta_t = \tau_2/10 = 9.07$ ps. To minimize dispersion errors, the CFL number should be maximized. Thus, from the definition of CFL let $\delta_x = \delta_t v_p^{max} = .430$ mm, where, for this example, $v_p^{max} = 4.74 \times 10^7$ m/s. A second way is to set δ_x in accordance with the minimum wavelength of interest. Let $\delta_x = \lambda^{min}/20$, where λ^{min} is the minimum wavelength at some angular frequency; for this example let $\omega = 10/\tau_2$, in which case $\lambda^{min} = 2.69$ mm and $\delta_x = .135$ mm. Finally, from the stability relationship, the maximum time step is $\delta_t = \delta_x/v_p^{max} = 2.84$ ps.

Based upon the previous example, the more conservative choice for the values of δ_x and δ_t is based upon the minimum wavelength argument. Unfortunately, this argument produces a time-step that over-resolves the time-domain driving signal. Moreover, by doing so, we incur the cost of increasing the simulation time by about a factor of 3.2 and the computational memory by a factor of 32.8 (three-dimensional domain), as compared with the other method. Had we chosen the first method, the high-frequency information of the medium would not be capture and hence, the early-time information of the output data would be in error. One possible way to resolve these contrary specifications is to increase the spatial accuracy order of the scheme [27]. For example, if a fourth-order in space and a second-order in time scheme is employed, the sampling requirements on the minimum wavelength can be relaxed and the resulting time-step will be commensurate with the smallest relaxation.

6 Summary

A survey of some of the more popular schemes associated with FDTD analysis of electromagnetic wave propagation in complex media has been given. These schemes have been characterized in terms of their numerical permittivities in conjunction with a numerical dispersion relationship. In addition, the CFL number of each scheme is given or postulated when such information has been provided in the literature. In some cases, discussions on memory requirements have also been provided.

It is not the intention of this report to rank such schemes in terms of *best* or *worst*. Such terms are subjective, since best or worst designators require one to quantify both the tangible (e.g., accuracy) and intangible (e.g., simplicity) features of a scheme into a single number. Instead, each scheme should be analyzed with a particular application in mind and, from that analysis, an informed selection can be made.

References

- [1] K. S. Yee, "Numerical solution of initial boundary value problems involving Maxwell's equations in isotropic media," *IEEE Trans. Ant. Propagat.*, vol. 14, no. 3, pp. 302-307, 1966.
- [2] A. Taflov and M. E. Brodwin, "Numerical solution of steady-state electromagnetic scattering problems using the time-dependent Maxwell's equations," *IEEE Trans. Microwave Theory Tech.*, vol. 23, no. 8, pp. 623-630, 1975.
- [3] A. Ishimaru, *Electromagnetic Wave Propagation, Radiation and Scattering*, Prentice-Hall, Englewood Cliffs, NJ, 1991.
- [4] R. Richtmyer and K. Morton, *Difference Methods for Initial-Value Problems*, Wiley, New York, NY, 1967.
- [5] R. F. Harrington, *Time-Harmonic Electromagnetic Fields*, McGraw-Hill, New York, NY, 1961.
- [6] K. S. Kunz and R. J. Luebbers, *The Finite Difference Time Domain Method for Electromagnetics*, CRC Press, Boca Raton, FL, 1993.
- [7] Y. Liu, "Fourier analysis of numerical algorithms for the Maxwell equations," *31st Aerospace Sciences Meeting & Exhibit*, AIAA-93-0368, Reno, NV, 1993.
- [8] A. Taflov and K. R. Umashankar, "The finite-difference time-domain method for numerical modeling of electromagnetic wave interactions," *Electromagnetics*, vol. 10, no. 1/2, pp. 105-126, 1990.
- [9] D. A. Anderson, J. C. Tannehill and R. H. Pletcher, *Computational Fluid and Mechanics and Heat Transfer*, Taylor & Francis, Bristol, PA, 1984.
- [10] J. R. Wait, *Electromagnetic Waves in Stratified Media*, Pergamon Press, Oxford, UK, 1970.
- [11] Jackson, J. D., *Classical Electrodynamics*, Wiley, New York, NY, 1975.
- [12] D. M. Sullivan, "Frequency-dependent FDTD methods using Z transforms," *IEEE Trans. Ant. Propagat.*, vol. 40, no. 10, pp. 1223-1230, 1992.
- [13] D. M. Sullivan, "Z-transform theory and the FDTD method," *IEEE Trans. Ant. Propagat.*, vol. 44, no. 1, pp. 28-34, 1996.
- [14] W. H. Weedon and C. M. Rappaport, "A general method for FDTD modeling of wave propagation in arbitrary frequency-dependent media," *IEEE Trans. Ant. Propagat.*, vol. 45, no. 3, pp. 401-410, 1997.
- [15] J. L. Young, "A full finite difference time domain implementation for radio wave propagation in a plasma," *Radio Sci.*, vol. 29, no. 6, pp. 1513-1522, 1994.
- [16] L. J. Nickisch and P. M. Franke, "Finite-difference time-domain solution of Maxwell's equations for the dispersive ionosphere," *IEEE Ant. Propagat. Mag.*, vol. 34, no. 5, pp. 33-39, 1992.
- [17] S. A. Cummer, "An analysis of new and existing FDTD methods for isotropic cold plasma and a method for improving their accuracy," *IEEE Trans. Ant. Propagat.*, vol. 45, no. 3, pp. 392-400, 1997.
- [18] R. M. Joseph, S. C. Hagness and A. Taflov, "Direct time integration of Maxwell's equations in linear dispersive media with absorption for scattering and propagation of femtosecond electromagnetic pulses," *Opt. Lett.*, vol. 16, no. 18, pp. 1412-1414, 1991.
- [19] R. J. Luebbers, F. Hunsberger, and K. S. Kunz, "A frequency-dependent finite-difference time-domain formulation for transient propagation in plasma," *IEEE Trans. Ant. Propagat.*, vol. 39, no. 1, pp. 29-34, 1991.
- [20] D. F. Kelley and R. J. Luebbers, "Piecewise linear recursive convolution for dispersive media using FDTD," *IEEE Trans. Ant. Propagat.*, vol. 44, no. 6, pp. 792-797, 1996.
- [21] D. M. Sullivan, "A frequency-dependent FDTD method for biological applications," *IEEE Trans. Microwave Theory Tech.*, vol. 40, no. 3, pp. 532-539, 1992.
- [22] O. P. Gandhi and C. M. Furse, "Currents induced in the human body for exposure to ultrawideband electromagnetic pulses," *IEEE Trans. Electromagn. Compat.*, vol. 39, no. 2, pp. 174-180, 1997.

- [23] C. M. Furse, J.-Y. Chen and O. P. Ghandi, "The use of frequency-dependent finite-difference time-domain method for induced current and SAR calculations for a heterogeneous model of the human body," *IEEE Trans. Electromagn. Compat.*, vol. 36, no. 2, pp. 128-133, 1994.
- [24] W. D. Hurt, "Multiterm Debye dispersion relations for permittivity of muscle," *IEEE Trans. Biomed. Engr.*, vol. 32, no. 1, pp. 60-64, 1985.
- [25] T. Kashiwa, N. Yoshida and I. Fukai, "A treatment by the finite-difference time-domain method of the dispersive characteristics associated with orientation polarization," *IEICE Transactions*, vol. E73, no. 8, pp. 1326-1328, 1990.
- [26] J. L. Young, "Propagation in linear dispersive media: Finite difference time-domain methodologies," *IEEE Trans. Ant. Propagat.*, vol. 43, no. 4, pp. 422-426, 1995.
- [27] P. G. Petropoulos, "The computation of linear dispersive electromagnetic waves," *Applied Computational Electromagnetics Society Journal*, vol. 11, no. 1, pp. 8-16, 1996.
- [28] M. Okoniewski, M. Mrozowski and M.A. Stuchly, "Simple treatment of multi-term dispersion in FDTD," *IEEE Microwave Guided Wave Lett.*, vol. 7, no. 5, pp. 121-123, 1997.
- [29] R. Luebbers, F. P. Hunsberger, K. S. Kunz, R. B. Standler and M. Schneider, "A frequency-dependent finite-difference time-domain formulation for dispersive materials," *IEEE Trans. Electromagn. Compat.*, vol. 32, no. 3, pp. 222-227, 1990.
- [30] P. G. Petropoulos, "Stability and phase error analysis of FD-TD in dispersive dielectrics," *IEEE Trans. Ant. Propagat.*, vol. 42, no. 1, pp. 62-69, 1994.

THE DESIGN OF A DOUBLE STRUT SUPPORT SYSTEM
FOR LOW SPEED WIND TUNNEL TESTING OF
ROTATING, AXISYMMETRIC LIGHTCRAFT MODEL

Andrew D. Panetta
Graduate Student
Department of Mechanical Engineering,
Aeronautical Engineering, and Mechanics

Rensselaer Polytechnic Institute
110 8th Street
Troy, NY 12180-3590

Final Report for:
Graduate Student Research Program
Edwards Research Site

Sponsored by:
Air Force Office of Scientific Research
Bolling Air Force Base
Washington, DC

And

Edwards Research Site

September 1998

THE DESIGN OF A DOUBLE STRUT SUPPORT SYSTEM FOR LOW SPEED WIND TUNNEL TESTING OF ROTATING, AXISYMMETRIC LIGHTCRAFT MODEL

Andrew D. Panetta
Graduate Student
Department of Mechanical Engineering,
Aeronautical Engineering, and Mechanics
Rensselaer Polytechnic Institute

Abstract

An inline, double strut support system and Lightcraft test model were designed, and partially constructed, for use with the Rensselaer Polytechnic Institute Low Speed Wind Tunnel. The support system was designed especially for rotating, axisymmetric bodies, particularly the Lightcraft model.^{1,2} By attaching the system to the existing yoke balance system; it is possible to experimentally measure the aerodynamic forces on the rotating model. The apparatus maintains a constant angle of attack, while the yaw angle may be varied.

THE DESIGN OF A DOUBLE STRUT SUPPORT SYSTEM FOR LOW SPEED WIND TUNNEL TESTING OF ROTATING, AXISYMMETRIC LIGHTCRAFT MODEL

Andrew D. Panetta

Introduction

The Lightcraft Technology Demonstrator (LTD) is currently being flight tested at the High Energy Laser Systems Test Facility at White Sands Missile Range, NM.^{1,2} The Lightcraft, depicted in Fig. 1, uses a ground based laser as a means of propulsion. For stability, the LTD is spun to approximately 6000 rpm just prior to launch. During a recent spin-stabilized test, a 10 kW pulsed carbon dioxide laser has propelled the 1.45-oz vehicle to an altitude in excess of 98 ft.²

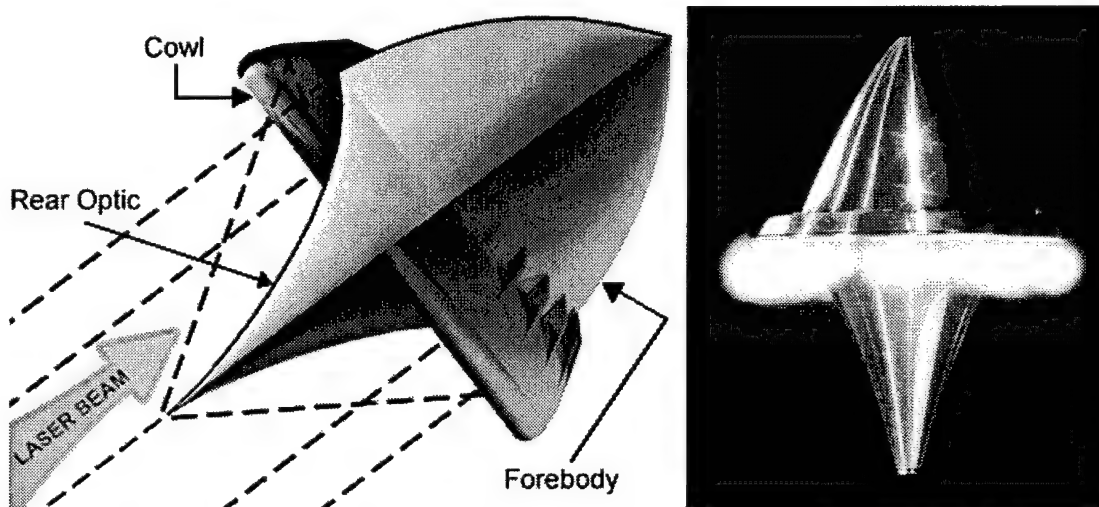


Fig. 1 a) Schematic of Lightcraft b) Photograph of Lightcraft With Plasma Created by Laser Pulse

Tests on the Lightcraft were also performed in the Rensselaer Polytechnic Institute 24-in. Hypersonic Shock Tunnel (HST).³ The HST is capable of producing free stream Mach numbers up to 25 and stagnation temperatures to

4,100 K. These tests were used to measure the surface pressure on the Lightcraft forebody at hypersonic speeds. The experimental results were then compared to computational solutions obtained by NPARC.⁴

Experiments measuring the low speed aerodynamic characteristics of the Lightcraft have yet to be performed. The experimental results can then be used to provide insight, as to what changes can be made, to improve the overall performance of the Lightcraft. They can also provide test cases to be used to validate computational results as well as coefficients necessary for stability calculations. This paper will focus on the efforts undertaken to design and construct the experimental apparatus, thus far, to accomplish this goal.

Experimental Apparatus

The Rensselaer Polytechnic Institute (RPI) Low Speed Wind Tunnel (LSWT) is located in the Aeronautical Engineering Laboratory at RPI. Built in the early 1930's, it is a closed circuit tunnel with a 4-ft. by 6-ft. test section. The

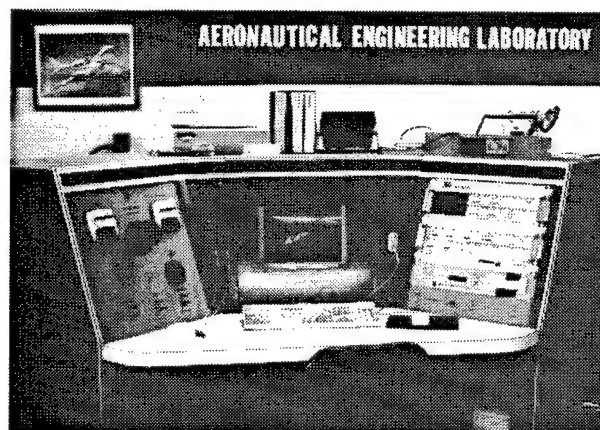


Fig. 2 Wind Tunnel Control Panel

facility has been used for a wide variety of experiments, ranging from wings in the rain to sports aerodynamics. Recent upgrades allow the tunnel to be completely controlled by a personal computer using the LabView program, cf. Fig. 2.

A fixed pitch, multi-blade axial fan is capable of producing flow speeds on the order of 150 mph. Turning vanes rotate the flow 180° from the fan exit. The flow then passes through turbulence screens before it enters the contraction, and later the test section. A schematic of the tunnel is shown by Fig. 3. The test section, cf. Fig. 4, has a turbulence factor of 1.06^5 and is equipped with large windows for viewing and photographing the model. An external yoke balance system is used to measure the aerodynamic forces.

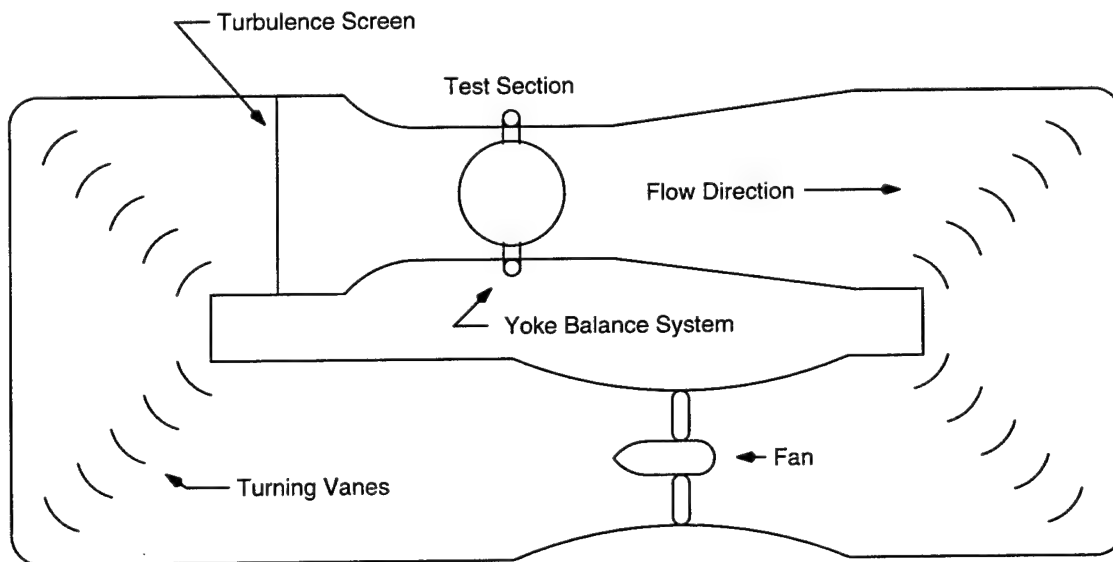


Fig. 3 Schematic of Closed Circuit Wind Tunnel

The yoke, illustrated by Fig. 5, contains 6 Lebow Associates, Inc. Load Cells, model 3167. The load cells are capable of measuring forces up to 300 lbs. By using the algebraic manipulations listed below, where A, B, C, D, E, and F

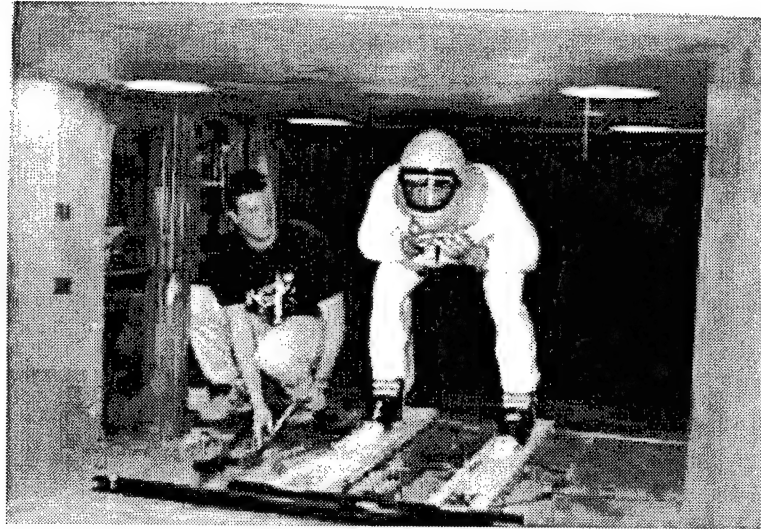


Fig. 4 Test Section With Speed Skier, Mike Skakel

represent the forces exerted on the load cells, the aerodynamic forces are calculated:

$$\text{Lift} = A + B + C$$

$$\text{Drag} = D + E$$

$$\text{Side Force} = F$$

$$\text{Rolling Moment} = (B - A) \cdot (z / 2)$$

$$\text{Pitching Moment} = C \cdot m$$

$$\text{Yawing Moment} = (D - C) \cdot (z / 2)$$

The double strut support, as designed, connects directly to the yoke, cf. Figs. 6-8. An inline design was chosen to reduce the interference drag. Interference drag is difficult to distinguish from the actual drag of the model and that of the struts. It can be estimated, but by reducing the interference drag, the relative error of the measurements will decrease. Because of the turbulence factor of the RPI LSWT, the vortices produced by the vertical struts will have a

significant effect even at relatively low speeds. Inserting the vertical struts into an aerodynamic shell will reduce the drag of the struts by reducing the trailing vortices.

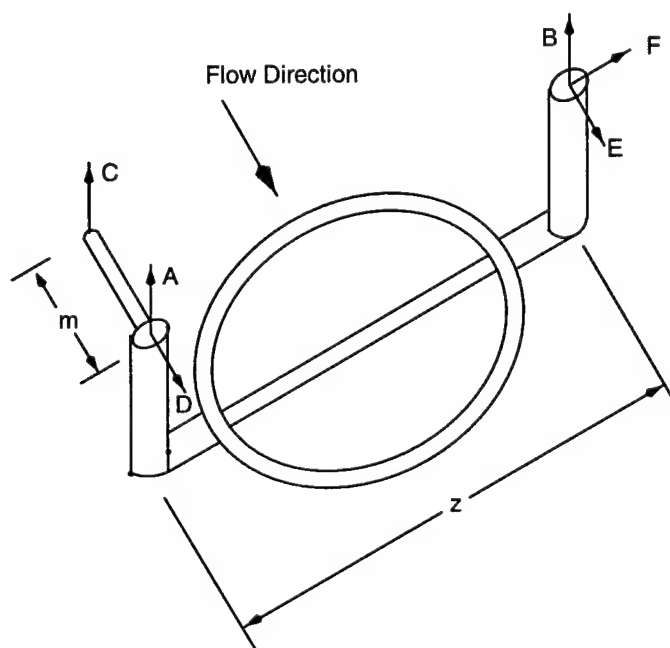


Fig. 5 Schematic of Yoke Balance System

Since the Lightcraft test model is axisymmetric, it will be possible to maintain a constant angle of attack and allow for a variable yaw angle. The benefits of this are twofold. With the yoke being circular, the entire system may be rotated about the yoke, giving the model the appropriate yaw angle. This simplified the design and the manufacturing of the support apparatus. Also, due to gyroscopic effects, the forces due to the yaw angle will manifest themselves as lift, acting in the vertical direction. Because the struts are in line, it is less capable of withstanding excessive side forces, which would be produced due to the gyroscopic effect, if the model is given a pitch angle.

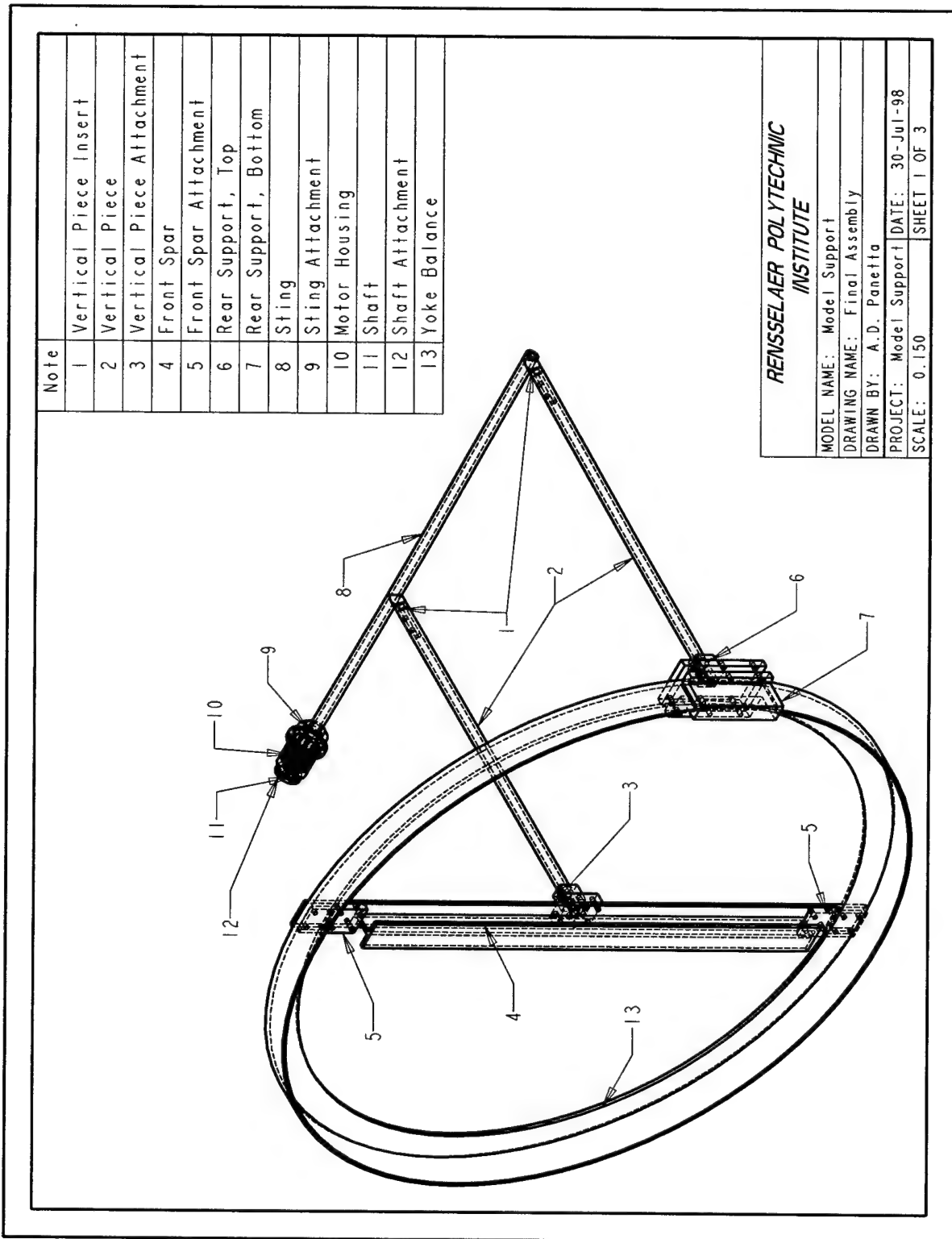


Fig. 6 Double Strut Support Attached to Yoke

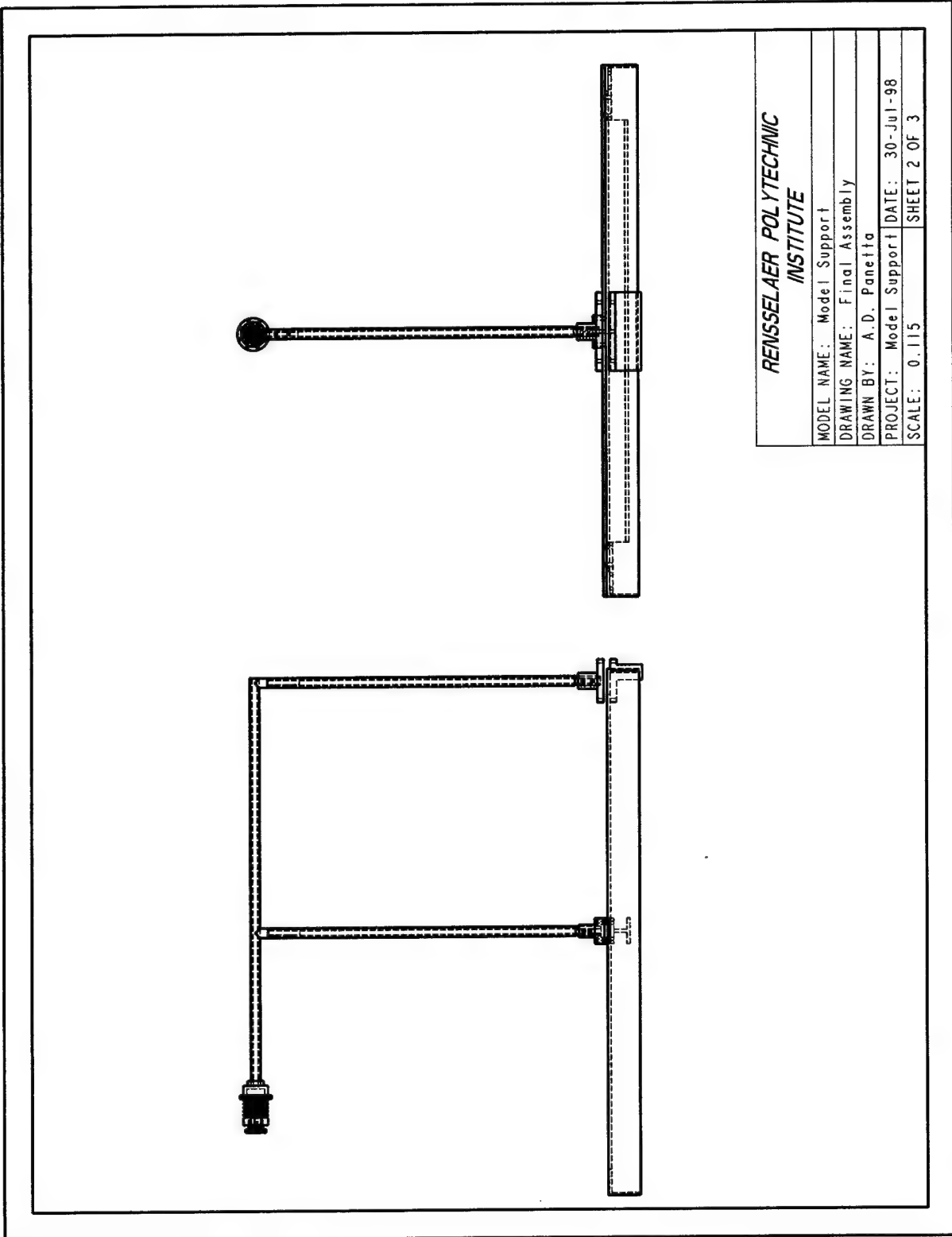


Fig. 7 Side and Front View of Model Support

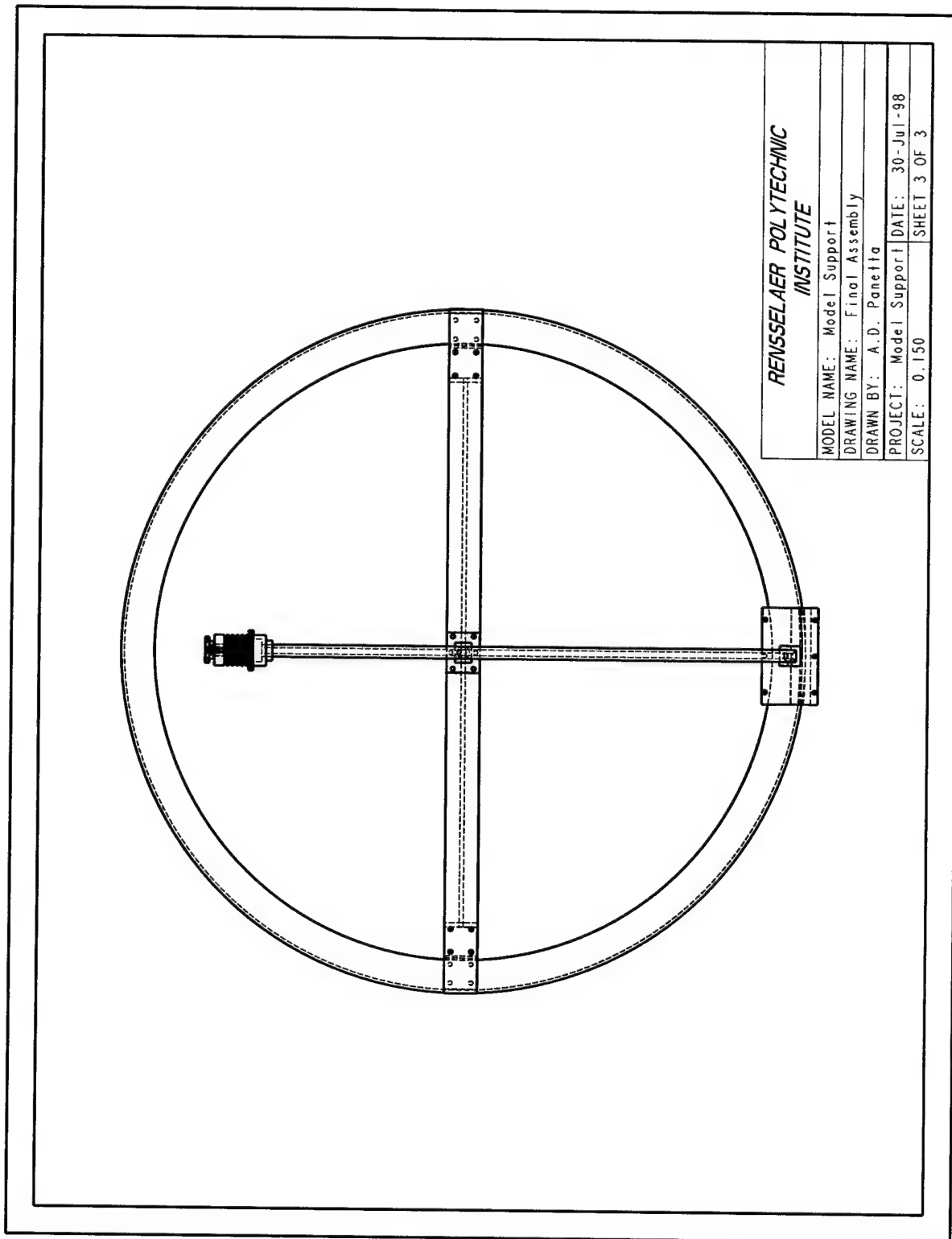


Fig. 8 Top View of Double Strut Support

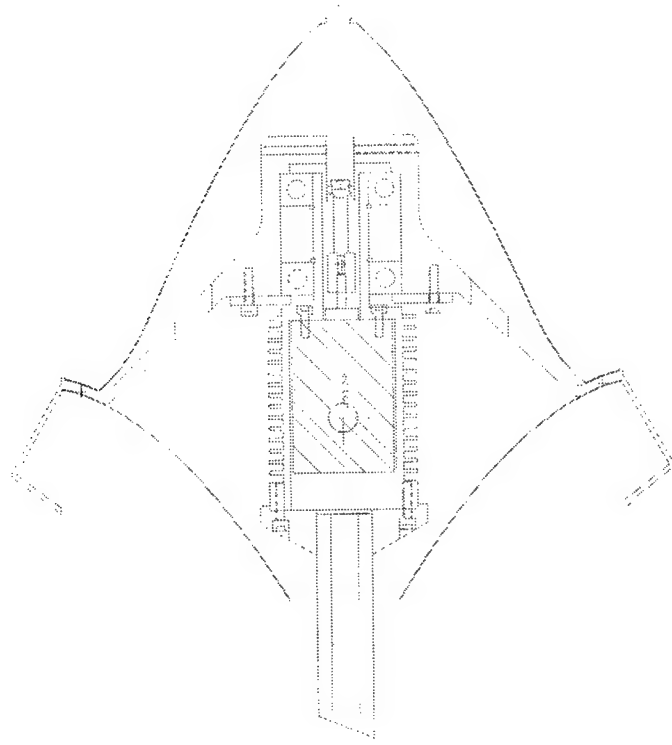


Fig. 9 Lightcraft Model and Motor Mount

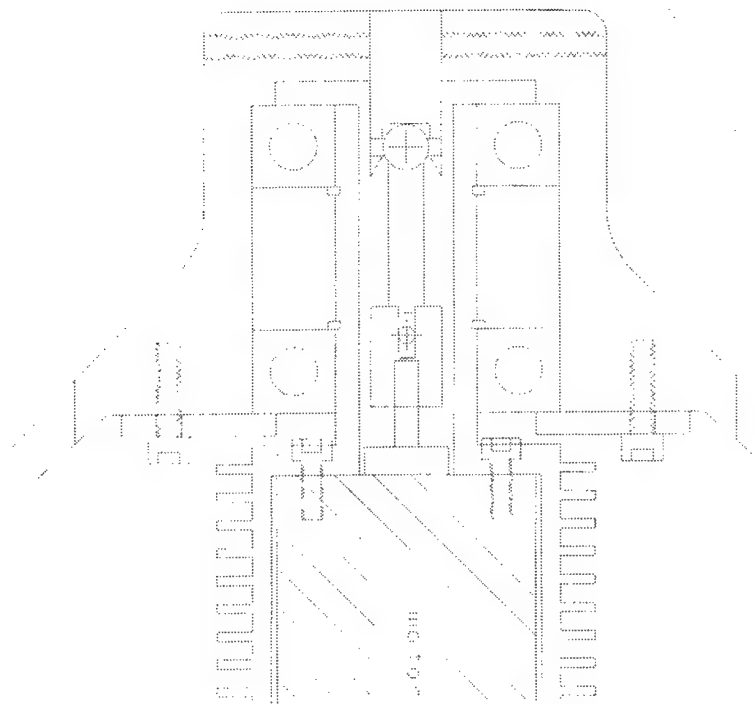


Fig. 10 Close-up of Bearing and Shaft Assembly

To estimate the loads on the Lightcraft test model and the mounting system, the drag coefficient was taken to be 0.5. This was chosen because the fineness ratio is 1:1, similar to a sphere. Loads were calculated for a non-rotating model. The support system was designed with a factor of safety of roughly 3 for a non-rotating model with a flow speed of 150 mph. The deflection of the struts, in the worst case scenario, was calculated to be 0.4 in. The energy expended to deflect the struts, or any other portion of the assembly, is not transferred to the balance system, resulting in inaccurate measurements of the aerodynamic forces.

The motor housing is located at the end of the sting, cf. Figs. 6 and 9. Since the sting is hollow, power cables may be passed through the center and exit the test section via a strut. A bulkhead in the Lightcraft model is attached to the armature of the motor.

A Putnam Pro-Pulsion DC motor, powered by a BK Precision Model 1686 power supply, is used to spin the LTD model to 4-6,000 rpm. A current limiting feature on the power supply provides protection against short circuit and excessive current output. Because of this feature, a direct connection from the motor to the power supply can not be made. Upon startup, the motor draws a high initial current compared to steady state operation. This is interpreted as an overload by the power supply, resulting in the shut down of the power supply. This problem was remedied by the construction of a simple control circuit, cf. Fig. 11. The resistor is used to limit the initial inrush of current.

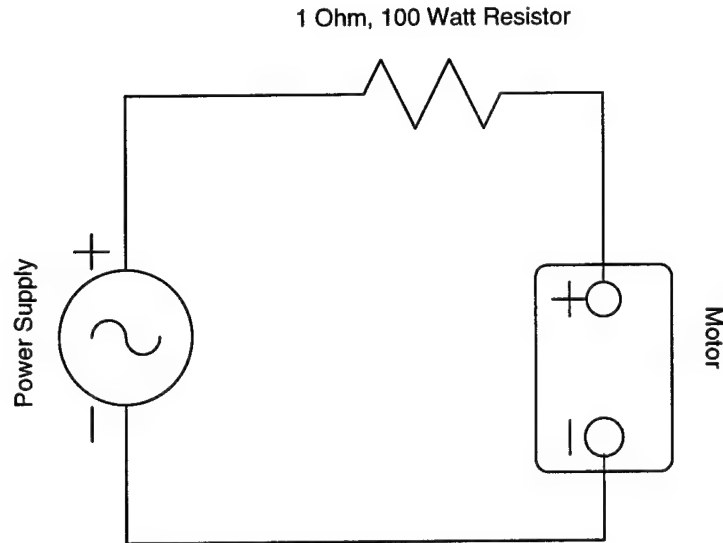


Fig. 11 Motor Control Circuit

The Lightcraft test model is based on the LTD Model 200 Series with a length and diameter of 5.5 in.² The test model has been scaled to a 9 in. diameter and is approximately 8.5 in. long. The end of the rear optic was shortened to allow clearance for the sting. From valuable lessons learned in Ref. 6, the separation distance between the optic and the sting is half the diameter of the sting. The forebody and optic of the model are very thin to reduce the weight of the model, cf. Fig. 9.

A series of bearings distribute the aerodynamic loads to the sting, rather than to the motor, cf. Figs. 9 and 10. Since the motor will be operated for short periods of time, the motor housing is a sufficient heat exchanger. By mounting a Hall effect sensor on a portion of the sting inside the model, it is possible to measure the revolutions per second and then calculate the angular velocity.

Conclusions

An inline, double strut support system for low speed wind tunnel testing was designed and partially constructed. The Lightcraft model was designed, and much of the material and equipment for the future experiments has been procured.

This served as the first step to wind tunnel testing the model. With the designing of the model and experimental apparatus nearly completed, the next logical step would be to test the model in the wind tunnel. These experimental results could be used to validate a computational fluid dynamics code, such as WIND.⁷

Acknowledgments

The author wishes to thank the Air Force Office of Scientific Research and Edwards Research Site for supporting this investigation, and Dr. Franklin B. Mead, Jr., of Edwards Air Force Base, for acting as the laboratory focal point. Acknowledgments are also due to Mark Mickiewicz, of Rensselaer Polytechnic Institute, whose machining expertise and insight were extremely useful. Finally, the author wishes to thank the Rensselaer Hypersonic Gasdynamics Research Team, especially Drs. Henry T. Nagamatsu, Leik N. Myrabo, and Marco A. S. Minucci.

References

1. Myrabo, L.N., Messitt, D.G., and Mead, F.B., "Ground and Flight Tests of a Laser Propelled Vehicle," AIAA Paper 98-1001, Jan. 1998.

2. Mead, F.B., Myrabo, L.N., and Messitt, D.G., "Flight and Ground Tests of a Laser-Boosted Vehicle," AIAA Paper 98-3735, July 1998.
3. Messitt, D.G., "Computational and Experimental Investigation of 2- and 3-D Scramjet Inlets and Flow Over a Sharp Flat Plate at Mach Numbers From 10 to 25 in a Hypersonic Shock Tunnel," Ph.D. Thesis Dissertation, Rensselaer Polytechnic Institute, Troy NY, Sept. 1998.
4. Power, G.D., Cooper, G.K., and Sirbaugh, J.R., "NPARC 2.2 – Features and Capabilities," AIAA Paper 95-2609, 1995.
5. Rae, W.H. and Pope, A., *Low-Speed Wind Tunnel Testing*, Second Edition, John Wiley & Sons, Inc., 1984.
6. Kelly, H.R., "The Subsonic Aerodynamic Characteristics of Several Spin-Stabilized Rocket Models. II Magnus Coefficients," TM-376, U.S. Naval Ordnance Test Station, Inyokern, China Lake, CA, Nov. 1953.
7. Bush, R.H., Power, G.D., and Towne, C.E., "WIND: The Production Flow Solver of the NPARC Alliance," AIAA Paper 98-0935, 1998.

**A GREEDY RANDOMIZED ADAPTIVE SEARCH PROCEDURE
FOR THE MULTI-CRITERIA
RADIO LINK FREQUENCY ASSIGNMENT PROBLEM**

**E.L. Pasiliao
Graduate Student
Department of Industrial and Systems Engineering**

**University of Florida
303 Weil Hall
P.O.Box 116595
Gainesville FL 32611-6595**

**Final Report for:
Graduate Student Research Program
Eglin Research Site Center**

**Sponsored by:
Air Force Office of Scientific Research
Bolling Air Force Base DC
and
Eglin Research Site Center**

September 1998

A GREEDY RANDOMIZED ADAPTIVE SEARCH PROCEDURE
FOR THE MULTI-CRITERIA
RADIO LINK FREQUENCY ASSIGNMENT PROBLEM

E.L. Pasiliao
Graduate Student
Department of Industrial and Systems Engineering
University of Florida

Abstract

A Greedy Randomized Adaptive Search Procedure (GRASP) is presented for computing approximate solutions to the NP -hard Radio Link Frequency Assignment Problem (RLFAP). The purpose is to allocate a limited number of frequency channels to a given set of transceivers needing to establish communication links. An RLFAP solution is termed feasible if no two frequencies within the network interfere with each other and all other constraints are satisfied. If a feasible solution does exist, the objective would be the minimization of both the order and the span of the solution set. GRASP is shown to be an efficient and robust method for solving the RLFAP. The paper also shows the advantages of solving a multi-criteria function in finding the most beneficial optimal solution.

Keywords: Radio link frequency assignment problem, Combinatorial Optimization, GRASP, heuristics, computational results

A GREEDY RANDOMIZED ADAPTIVE SEARCH PROCEDURE
FOR THE MULTI-CRITERIA
RADIO LINK FREQUENCY ASSIGNMENT PROBLEM

E.L. Pasiliao

1 Introduction

The Radio Link Frequency Assignment Problem (RLFAP) addresses the issue of establishing communication links for a network of transmitters and receivers. It is a special case of the general Frequency Assignment Problem (FAP) [8] in which a limited number of frequency channels must be allocated to a set of requesting transmitters so that interference between any transmitters and receivers is negligible. To help explain the RLFAP, a cursory discussion of an FAP application is presented.

A well known application of the FAP is the radio station channel assignment. Figure 1 shows six radio stations requiring transmission channels for each to serve their respective listening population. Unfortunately, the stations' broadcasting areas often overlap with one another. These common listening populations may experience interference problems if there are two or more transmission signals operating within a narrow frequency band.

The FAP is mathematically represented as a graph with transmitters and receivers as nodes and possible interference as arcs. For example, stations 1 and 2 have an overlap in their transmission regions. The possible signal interference arising in their intersection is described by drawing an arc between nodes 1 and 2.

As previously stated, the RLFAP is a special case of the FAP. The RLFAP requires that every node is both a transmitter and a receiver (transceiver) and each node must establish a communication link to one and only one other node. Figures 2 and 3 illustrate the formulations of the RLFAP equality and inequality constraints. In this simple version of a four node RLFAP, there are two pairs of transceivers needing to establish a communication link. Parallel or duplex links are formulated with $|f_i - f_j| = d_{i,j}$, where the separation distance, $d_{i,j}$, is an arbitrarily agreed upon channel distance between transceivers i and j .

Because of the relatively small physical distance between radio links $\{1, 2\}$ and $\{3, 4\}$, a possibility exists that intolerable interference between each other may occur. For example, node 1 communicates with node 2 but may also receive unintentional noise from node 3. If the transmissions emanating from nodes 2 and 3 are too close in the frequency band, then node 1 will have a low signal to noise ratio and the communication link between nodes 1 and 2 will be compromised. Arcs that represent possible interference are formulated with $|f_i - f_j| > d_{i,j}$. Here, the separation distance, $d_{i,j}$, is the channel distance at

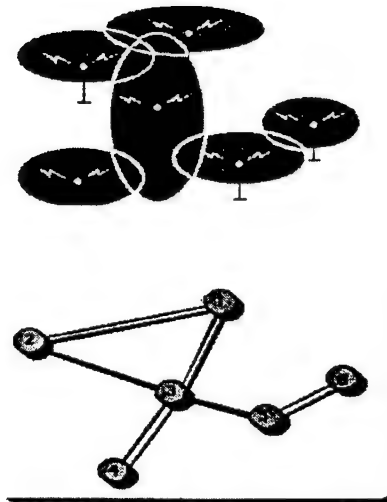


Figure 1: Graph Representation

which the interference between nodes i and j becomes intolerable.

The separation distance may be limited by government regulations, technological characteristics of the transceivers, geological or other physical barriers, etc. Any one or combination of these factors may explain why node 2 does not receive transmission from node 3 or why node 1 cannot hear node 4's signal.

Hale [9] describes two objectives for the FAP — the minimum order and the minimum span assignment problems. Order is the number of unique channels assigned to the communication network, and span is the largest frequency value.

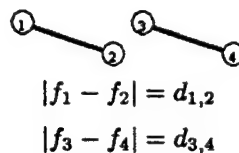


Figure 2: Communication Links

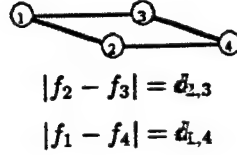


Figure 3: Interference Links

The mathematical formulation of the minimum order RLFAP is the following:

$$\begin{aligned} \min \quad & \left| \bigcup_i \{f_i\} \right| \\ \text{s.t.} \quad & |f_i - f_j| = d_{i,j} \quad \forall \{i, j\} \in U \\ & |f_i - f_j| > d_{i,j} \quad \forall \{i, j\} \in V \\ & f_i \in D_i \quad \forall i \in N \end{aligned}$$

where $N \equiv$ set of transceivers,
 $U \equiv$ set of communication links,
 $V \equiv$ set of interference links, and
 $D_i \equiv$ set of frequency channels available for node i .

The minimum span RLFAP has the same constraints, but its objective function is the following:

$$\min \max_i f_i.$$

In the problem instances that are investigated in this paper, the primary objective is the minimization of the solution set's order. However, in the case where there exists multiple RLFAP solutions with the same minimum order value, the minimum span problem may be solved to determine which of these solutions would be preferred. By adding a secondary objective function to the original, the RLFAP becomes a two dimensional multi-criteria problem. The sorting of optimal primary solutions according to their secondary objective function value is termed lexicographic ordering. A feasible solution s is lexicographically less than another feasible solution t if $f_1(s) = f_1(t)$ for the primary function and $f_2(s) < f_2(t)$ for the secondary objective function. This relation is then denoted by $f(s) \prec f(t)$. In other words, solution s is preferred over t . Raychaudhuri [2] introduces the notions of a restricted order and a restricted span assignment problems to describe these multi-criteria problems.

ONE CRITERION		
minimum order	⇒	finds the smallest number of frequency channels necessary to avoid interference
minimum span	⇒	finds the smallest maximum frequency value necessary to avoid interference
TWO CRITERIA		
restricted order	⇒	same as the minimum span problem with the added constraint that the order is fixed at its minimum
restricted span	⇒	same as the minimum order problem with the added constraint that the span is fixed at its minimum

Figure 4: Objective Functions for RLFAP

This paper provides a brief description of a generic Greedy Randomized Adaptive Search Procedure (GRASP) and then explains in detail its implementation for the RLFAP. GRASP is a meta-heuristic algorithm thoroughly described by Feo and Resende [6] and has been successfully applied to many combinatorial optimization problems [10, 12]. As a benchmark for qualifying GRASP's suitability for the RLFAP, results obtained by the T.U. Eindhoven RLFAP Group [3] through the use of two widely implemented heuristic algorithms, Simulated Annealing [1] and Taboo Search [4, 5], are presented. Computational results indicate that GRASP provides good approximate solutions within a relatively short amount of time in several real life and computationally generated RLFAP instances. Results also show that multi-criteria optimization is indeed a powerful tool in defining the most beneficial optimal solution.

2 GRASP

GRASP is an iterative procedure with each iteration consisting of two stages: a construction phase and a local search phase. At each iteration a solution is found and the best solution of all iterations is stored as the final solution. It is a heuristic algorithm which has been shown to produce good quality solutions with relatively short computation times. The generic GRASP procedure is presented in pseudo-code in Figure 5 while the two stages are described in Figure 6.

The construction phase builds a feasible solution through the use of a greedy randomized function. The "greedy" part of the function makes sure the feasible solution generated is of low cost. The random component is included to prevent entrapment in any local minima and is therefore one of the keys to the performance of GRASP. The construction of a feasible solution begins with a selected number of the best of all costs gathered in a restricted candidate list (RCL).

```

PROCEDURE GRASP(ListSize,MaxIter,RandomSeed)
1  InputInstance( );
2  DO  $k = 1, \dots, \text{MaxIter} \rightarrow$ 
3    Construction(ListSize,RandomSeed);
4    LocalSearch(BestSolutionFound);
5    UpdateSolution(BestSolutionFound);
6  OD;
7  RETURN BestSolutionFound
END GRASP;

```

Figure 5: GRASP pseudo-code

From the RCL, a candidate is randomly selected. Then the RCL is updated, i.e. all costs that no longer are feasible choices are removed from the RCL and new ones are entered. This procedure is repeated until the last assignment is made and a feasible solution is obtained.

The local search phase attempts to improve upon the greedy feasible solution by searching the neighborhood of the current solution to see if a better solution can be found. If an improvement is found, this solution is then kept as the current solution and a new neighborhood is searched. When no better solution can be found, the search is terminated and a local minimum is returned.

The test instances used in the analysis of the GRASP algorithm are three real-life instances provided by the EUCLID (European Cooperation for the Long term In Defence) program for the CALMA (Combinatorial Algorithms for Military Applications) project. An additional five artificially generated instances with the same characteristics as the real-life instances are also studied. All eight instances are known to have assignment solutions with zero level interference. The original objective of these instances is to minimize the order. However, the minimum span objective is also applied as a secondary function to evaluate the multi-criteria properties of the RLFAP instances. This paper analyzes an implementation of GRASP to a minimum order RLFAP and examines the relevance of multi-criteria optimization.

The remainder of this section describes in detail a GRASP implementation for the RLFAP. In section 2.1, the first of the two GRASP stages, the construction phase, is presented. The second GRASP stage, the local search is described in section 2.2.

2.1 RLFAP Construction Phase

The GRASP construction phase for the RFLAP in Figure 7 begins by initializing all the transceiver assignments. This process, in addition to a randomized

```

PROCEDURE Construction(Solution)
1  Solution = {};
2  for Solution construction not done;
3    MakeRCL(RCL);
4    s = SelectElementAtRandom(RCL);
5    Solution = Solution ∪ {s};
6    AdaptGreedyFunction(s);
7  ROF;
8  RETURN;
END Construction;

```

```

PROCEDURE LocalSearch(P, N(P), s)
1  for s not locally optimal;
2    Find a better solution t ∈ N(s);
3    Let s = t;
4  ROF;
5  RETURN(s as local optimal for P);
END LocalSearch;

```

Figure 6: GRASP phases

```

PROCEDURE Construction( )
{  Initialize all the nodes with frequency value of zero
  While there are unlabeled nodes and iter < max
  {  Create RCL according to the following priorities:
    [ List all unlabeled nodes linked to the largest number
      of labeled nodes first.
      If ties exist → list unlabeled nodes with a duplex link
      to a labeled node first. ]
    s=randomly select a node from the RCL
    Assign s with a random and non-interfering channel
    [ If all choices of channels lead to interference →
      randomly assign s with a channel
      and reinitialize every node that interferes with s. ]
  } }

```

Figure 7: Construction Phase for RLFAP

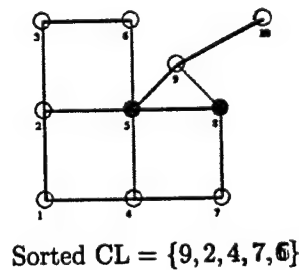
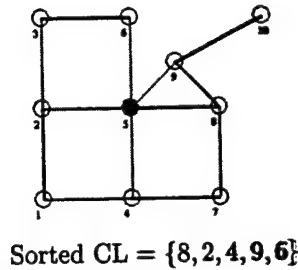


Figure 8: Candidate List Examples

starting node, ensures that each GRASP iteration always starts from scratch and provides a high probability that the resulting solution from the current iteration will be different from any prior solution obtained thus far. The iteration is repeated until all the transceivers or nodes have been assigned a frequency channel and there are no violated constraints. Figure 8 illustrates how the candidate lists are obtained. The hollow circles are nodes that are still waiting for a frequency channel assignment. Whenever a channel assignment to a transceiver causes interference to a neighboring transceiver, a simple form of backtracking is performed. The interfered transceiver is reinitialized and removed from the current solution set. When all communication and interference constraints are satisfied, the construction phase returns a feasible assignment solution with reliable communication links. This solution is then processed by the local search phase for further improvements.

```

PROCEDURE LocalSearch( )
{ For every channel  $f_i$  in the frequency domain
  { Re-initialize all nodes that are assigned channel  $f_i$ 
  While there are unlabeled nodes and  $iter < max$ 
    { Create RCL according to the same previous priorities
     $s$ =randomly select a node from the RCL
    Assign  $s$  with a non-interfering random channel
    [ If all choices of channels lead to interference  $\rightarrow$ 
      randomly assign  $s$  with any feasible channel
      and re-initialize every node that interferes with  $s$ . ]
    }
  If all nodes are labeled  $\rightarrow$  update current solution
} }

```

Figure 9: Local Search Phase for RLFAP

2.2 RLFAP Local Search Phase

The GRASP local search phase in Figure 9 is similar to the construction phase. Since the objective is to minimize the total number of frequency channels in use, the local search phase attempts to eliminate each channel from the communication network. This process begins by choosing a channel currently in use and re-initializing all transceivers that are allocated that channel. If no feasible solution can be found with the diminished set of available frequency channels, then the removed channel is reinstated into the solution set and another channel is chosen to be removed from the set. This process is repeated until an attempt to eliminate every single frequency in the solution set has been made.

When solving the minimum order RLFAP, frequency channels that are available to the least number of transceivers are the first to be selected for possible elimination. For the minimum span problem, the frequency channel with the largest values are selected first. The minimum span local search phase requires less computation time since the elimination process terminates as soon as it encounters a channel that cannot be eliminated from the solution set. The minimum order search has to check every channel in the entire set. The results described in Section 3 show that GRASP can be efficiently and robustly implemented to the RLFAP.

3 Results

Compared to the Simulated Annealing and Taboo Search benchmarks, GRASP proved to be an effective method for solving the RLFAP. Grasp was coded in C and tested on a SUN SPARCstation. Simulated Annealing and Taboo Search

real life	variables	constraints	Simulated annealing		Taboo search		GRASP			
			min. order	time [sec]	min. order	time [sec]	order			time [sec]
							minimum	average	maximum	
1	916	5548	16*	396	16*	705	16*	16.16	18	97.48
2	200	1235	14*	2	14*	7	14*	14.10	16	27.30
3	400	2760	16	6	16	32	14*	15.88	18	83.22

generated										
1	200	1134	18*	---	18*	---	18*	18.00	18	11.19
2	400	2245	14*	---	14*	---	14*	14.38	16	15.03
3	680	3757	18*	---	18*	---	18*	19.88	24	94.24
4	916	5246	18*	---	22	---	18*	19.66	26	190.90
5	916	4638	10*	---	10*	---	10*	11.60	12	31.71

Table 1: Minimum Order RLFAP

real life	span		order
	span	order	
1	680^	16*	
2	394^	14*	
3	722^	14*	
	708	16*	
	694	16	
	680	16	
	666^	16	

generated			
1	652^	18*	
2	652^	14*	
3	750	18*	
	736	20	
	722^	24	
4	764	18*	
5	750^	20	
	390	10*	
	380^	12	

^ minimum span solution
* minimum order solution

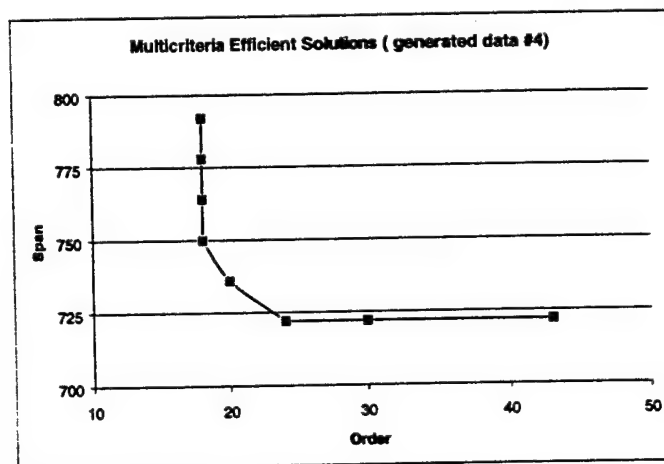


Table 2: Multi-criteria RLFAP

results come from the T.U.Eindhoven RLFAP Group and were also tested on SUN SPARCstations. Because the two benchmark algorithms are tested on the same type but different machines, care should be taken in any running time comparisons. The benchmarks, however, do provide a good basis for qualifying the GRASP results. Table 1 compares the performance of all three algorithms using three real life instances from the CALMA project and five artificially generated instances with similar properties. The size of instances ranged from a manageable graph of 200 nodes with 1,235 constraints to an extremely complex graph of 916 nodes with 5,543 constraints. Since GRASP is comprised of a series of construction and local search phases with each iteration having a high probability of giving different results, the average optimum value returned and the average computational time obtained from 100 GRASP iterations are reported.

From the real life instances, the GRASP results compare more favorably to both the Simulated Annealing and Tabu Search algorithms as the size of the RLFAP instance increases. GRASP running times did not increase as dramatically as the two benchmarks when the communication network size became larger. Even in the artificially generated instances, GRASP running times remained relatively short and predictable. The GRASP average optimal values also stayed close to the true optimal solutions, denoted with asterisks, while the maximum optimal value returned from all the iterations still provided a reliable approximation.

Multi-criteria results for the RLFAP instances are mixed. Restricted span solutions are given in Table 2. To create the efficient solutions, the minimum order algorithm was continually applied to the RFLAP instances while the frequency channel span was decreased. The table reports data from the smallest span at which the optimal order was still obtained through the smallest span at which a feasible solution still existed. Since the RLFAP instances tested had a limited number of available channels, it turns out that the original span could not be significantly limited without causing interference in the network. The best results came from the fourth generated instance. For these, we plotted the efficient solutions with span as the ordinate and order as the abscissa. The curve gives the values of restricted span solutions as well as restricted order solutions. From this plot, a decision may be made as to which assignment solution would be most appropriate and beneficial. Multi-criteria optimization would be an invaluable tool in decision making when the cost of obtaining frequency channels depends on both the number of channels and the range of these channels.

4 Discussion

The primary advantage of GRASP over other heuristics is that many solutions may be generated within a short amount of time. GRASP is also easily implemented on a parallel processor [11] by simply providing each processor with its

own copy of the process, the instance data, and an independent random number sequence. Only a single global variable is needed to keep track of the best current solution. GRASP has few parameters that need to be set and tuned which leads to the robustness of the algorithm. The power of the GRASP heuristics is that the best of many GRASP solutions is generally significantly better than any single solution produced by other heuristics.

The FAP is especially important for Air Force Munitions. One of these applications is in the LOCAAS system which provides an affordable standoff miniature munitions to autonomously search, detect, attack, and destroy TMD (Theater Missile Defence), SEAD (Suppress Enemy Air Defense), and ground mobile targets of military interest. A wireless data network that allows target and munitions information to be exchanged between munitions significantly improves their weapon to target assignment and their target location, recognition, and tracking capabilities. GRASP is an attractive algorithm for the LOCUS system since the best current solution may be always be obtained from a running GRASP procedure. Even after only one construction phase, a solution is already available for use. A good approximation is obtained after only one local search phase. Multi-criteria optimization is also advantageous because restricted order solutions are almost always preferred over minimum order solution, and restricted span solutions are almost always preferred over minimum span solutions. Since communication networks that require a smaller spectrum and a smaller number of channels to operate are more robust to jamming and fading, restricted order and restricted span solutions are remarkably beneficial in establishing and maintaining reliable communication links. Multi-criteria solutions are particularly useful to the LOCUS system where the choice of an efficient solution depends on how the radio communication links are being attacked or compromised.

Future research should extend multi-criteria optimization to three dimensions by adding the additional objective of minimizing the network interference. It would also be good to apply the same algorithm to data that more closely resembles the properties of a three dimensional mobile network such as the LOCAAS system.

5 Acknowledgements

I would like to take this opportunity to thank Robert Murphey for his assistance with the computations and for our valuable discussions and Dr. Dennis Goldstein for securing and arranging my stay at Eglin Air Force Base during the Summer of 1998. Thanks are also due to my faculty advisor, Dr. Panos Pardalos, for giving me motivation and direction.

References

- [1] E.H.L. AARTS AND J.H.M. KORST (1989), *Simulated annealing and Boltzmann machines: a stochastic approach to combinatorial optimization and neural networks*, Wiley, Chichester.
- [2] A. RAYCHAUDHURI (1985), *Intersection assignments, T-coloring, and powers of graphs*, Ph.D. Thesis, Department of Mathematics, Rutgers University, New Brunswick NJ.
- [3] T.U. EINDHOVEN RLFAP GROUP (1989), *Radio Link Frequency Assignment Project*, Technical Annex T-2.3.3.
- [4] F. GLOVER (1989), *Tabu search - Part I*, ORSA Journal on Computing 1: 190-206.
- [5] F. GLOVER (1990), *Tabu search - Part II*, ORSA Journal on Computing 2: 4-32.
- [6] T. FEO AND M. RESENDE (1995), *Greedy randomized adaptive search procedures*, Journal of Global Optimization 16: 109-133.
- [7] D.H. SMITH, S. HURLEY, AND S.U. THIEL (1998), *Improving heuristics for the frequency assignment problem*, European Journal of Operational Research 107: 76-78.
- [8] R.A. MURPHEY, P.M. PARDALOS, AND M. RESENDE (1998), *Frequency assignment problem*, Handbook of Combinatorial Optimization (Eds: D-Z. Du and P.M. Pardalos), Kluwer Academic Publishers.
- [9] W.K. HALE (1980), *Frequency assignment: theory and applications*, Proceedings of the IEEE 68(12): 1497-1514.
- [10] T. MAVRIDOU, P.M. PARDALOS, L. PITSOULIS, AND M.G.C. RESENDE (1996), *A GRASP for the Quadratic Assignment Problem*, Submitted to EJOR.
- [11] P. M. PARDALOS, L.S. PITSOULIS, T.D. MAVRIDOU, AND M.G.C. RESENDE (1995), *Parallel search for combinatorial optimization: genetic algorithms, simulated annealing, tabu search and GRASP*, Springer-Verlag, Lecture Notes in Computer Science 980: 317-331.
- [12] P.M. PARDALOS, L. PITSOULIS AND M.G.C. RESENDE (1995), *A parallel GRASP implementation for the quadratic assignment problem*, Solving Irregular Problems in Parallel: State of the Art (Eds: A. Ferreira and J. Rolim), Kluwer Academic Publishers.

IN-SITU SYNTHESIS OF DISCONTINUOUSLY REINFORCED TITANIUM ALLOY
COMPOSITES VIA BLENDED ELEMENTAL POWDER METALLURGY PROCESSING

Craig A. Riviello
Ph. D. Candidate
Department of Materials and Mechanical Engineering
Wright State University

Wright State University
Department of Materials and Mechanical Engineering
204 Russ Center
3640 Colonel Glenn Highway
Dayton OH 45435-0001

Final Report for the
Graduate Student Research Program
Air Force Research Laboratory
Materials Directorate

Sponsored by the
Air Force Office of Scientific Research
Bolling AFB, Washington, DC

September 1998

IN-SITU SYNTHESIS OF DISCONTINUOUSLY REINFORCED TITANIUM ALLOY COMPOSITES VIA BLENDED ELEMENTAL POWDER METALLURGY PROCESSING

Craig A. Riviello
Ph. D. Candidate
Department of Materials and Mechanical Engineering
Wright State University

Abstract

Discontinuously reinforced titanium (DRTi) matrix composites offer higher specific modulus, specific strength, wear resistance and thermal stability as compared to the unreinforced titanium alloys. The powder processing approach can offer better distribution of the reinforcement particles than conventional casting techniques.

In this study two alloys were selected for investigation; Ti-6Al-4V and Ti-10V-2Fe-3Al, both reinforced with 15 volume percent titanium boride (TiB). The composites were processed via a powder metallurgy technique by in-situ synthesis of the TiB from titanium diboride (TiB₂). The elemental powders were blended, compacted and extruded to obtain a fully dense material. Microstructural characterization of the as-extruded and heat treated specimens was performed to understand the transformation kinetics. The composites were also made using hot isostatic pressing to compare with the extruded material.

IN-SITU SYNTHESIS OF DISCONTINUOUSLY REINFORCED TITANIUM ALLOY COMPOSITES VIA BLENDED ELEMENTAL POWDER METALLURGY PROCESSING

Craig A. Riviello

Introduction

There is a broad range of Air Force requirements for discontinuously reinforced metals (DRX), where 'X' can be Al, Mg, Ti, etc., with improved properties. The successful development and implementation of discontinuously reinforced aluminum (DRA) alloys under the Air Force's Title III Program has paved the way for other DRX alloys. Established applications of DRA include the fan exit guide vanes of the PW4084 turbofan engine and the ventral fin and fuel access door covers of the F-16 fighter aircraft. Typically, the selection of materials for commercial, military and space-related applications often involves a compromise between performance and cost [1]. A moderate increase in fracture toughness, from ~20 to ~30 MPa√m, is a trigger point for critical components while a moderate increase in temperature capability over discontinuously reinforced aluminum alloys by 150-250°C will allow substitution for titanium alloys. Highly loaded structures require DRX with improved strength; i.e., discontinuously reinforced titanium alloys.

Discontinuously reinforced titanium (DRTi) matrix composites offer higher specific modulus, specific strengths, wear resistance and thermal stability as compared to the unreinforced titanium alloys. These materials also offer the significant advantages of nearly isotropic properties and the ability to be processed using conventional metal working techniques which make them cost competitive for aerospace applications. These properties are achieved through the introduction of a high strength and high modulus reinforcement phase in the discontinuous form of whiskers, platelets, and/or particles [1-3]. The ideal reinforcement should meet the following conditions [3-5]:

- High strength and stiffness, as well as the capability to maintain higher strength at higher temperatures,
- Thermodynamic stability in titanium alloys from room to sintering temperatures;

- Insolubility of the elements comprising the reinforcing compound in the titanium matrix and the titanium atoms in the reinforcing compound; i.e., mutual insolubility;
- A coherent boundary between the matrix and reinforcing compound, and
- Minimal difference in thermal expansion between the matrix and reinforcing compound.

Discussion of Problem

Previous studies have shown that titanium (mono) boride (TiB) is a superior reinforcement compound for titanium alloys for the reasons outlined above [1-3]. However, TiB is a line compound formed by a peritectic reaction and cannot be obtained in powder form, therefore an in-situ synthesis of TiB is required by the addition of titanium diboride (TiB₂). It is much more advantageous to introduce the reinforcement phase through in-situ processing. These advantages compared with conventional powder metallurgy and casting particulate approaches include cost-effectiveness, homogeneous distribution of reinforcement, finer particles, improved wettability between the reinforcement and matrix, and elimination of the deleterious interface reaction [2].

The blended elemental (BE) powder metallurgy approach allows more control of alloy microstructure and a wider range of reinforcement volume percentage than conventional casting techniques or prealloyed powder techniques. Typically, morphology, not volume percentage, of the reinforcement phase is limited by the phase diagram for casting approaches. Hypereutectic compositions with primary TiB particles are likely to have poor fatigue properties. Needle morphology, better for strength and fatigue, can most likely be obtained for hypereutectic compositions only by in-situ reaction with TiB₂.

Additionally, the use of conventional ingot metallurgy titanium products has lead to higher costs at almost every production stage when compared to powder metallurgy techniques. A major incentive is to reduce the cost of the processing steps or to eliminate them altogether [3-5], while maintaining superior properties over conventional ingot metallurgy products. The BE powder metallurgy process has been identified as a promising approach to overcome the high production cost of titanium alloy parts for the following reasons [3]:

- A cheap by-product of the production of sponge titanium, sponge fines, can be used directly as the raw material (cost savings);

- The melting and hot production processes which contribute to the high cost can be eliminated (cost savings);
- Near net shape capability achieves extremely high material yields (exceeding 90% for the BE method compared to just 20% to 50% for normal ingot forging methods) allowing a considerable reduction in post-processing costs for machining and grinding operations (cost savings); and
- Powder metallurgy methods can produce compositions difficult to achieve by conventional ingot metallurgy, resulting in a dramatic increase in freedom of control of the microstructure (performance improvement)

Methodology

Two alloys were selected for this investigation; Ti-6Al-4V and Ti-10V-2Fe-3Al, both reinforced with 15 volume percent TiB.

Powder Morphology

The BE powder metallurgy approach was used in this study to make the composites. The following elemental powders were obtained: titanium, aluminum, titanium diboride, vanadium, iron, and aluminum/vanadium master alloy. The titanium powder was obtained in -100 mesh (≤ 150 microns) while the other powders, except for the master alloy, were obtained in -325 mesh (≤ 45 microns). The master alloy ranged in size from +30 mesh (≤ 600 microns) to -200 mesh (≥ 75 microns). The titanium powder was gas-atomized, spherical particles whereas the other powders ranged from irregular to blocky in morphology. The goal was to enable the smaller powders to fill the voids between the titanium particles to increase the overall packing density which, in hindsight, had deleterious effects on the processed microstructure for reasons that will be discussed later. One of the reasons for using this titanium powder was its lower oxygen content. The titanium powder contained approximately 800 wppm oxygen. Figures 9-1 through 9-6 document the powder morphology.

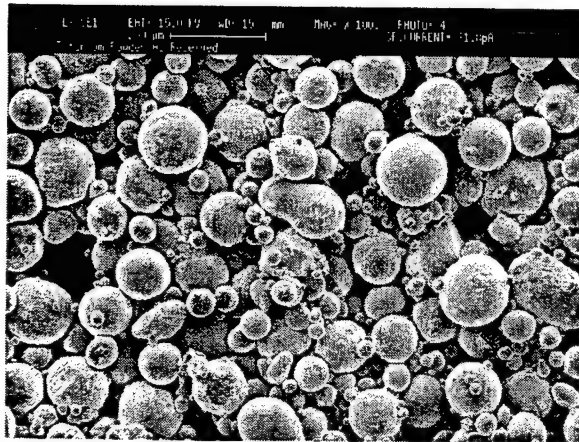


Figure 9-1

-100 mesh Titanium

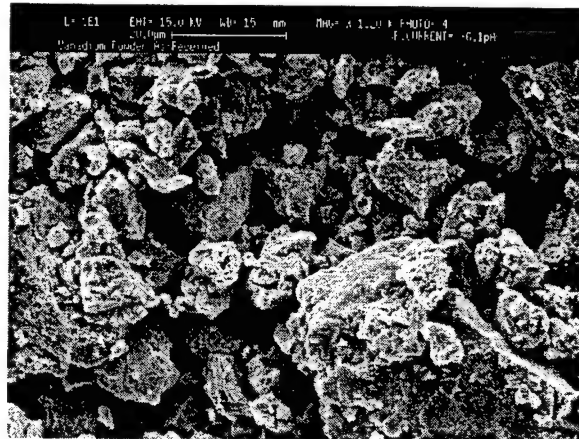


Figure 9-2

-325 mesh Vanadium

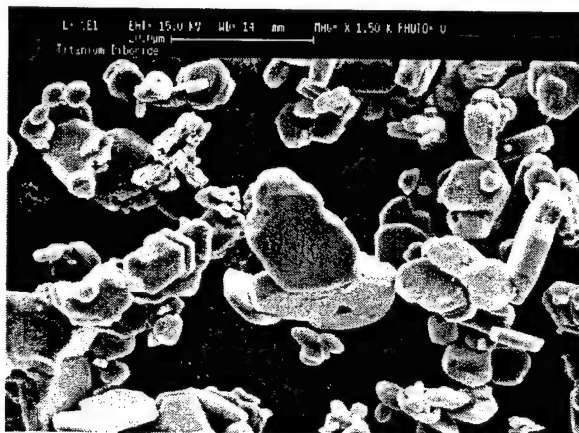


Figure 9-3

-325 mesh Titanium Diboride

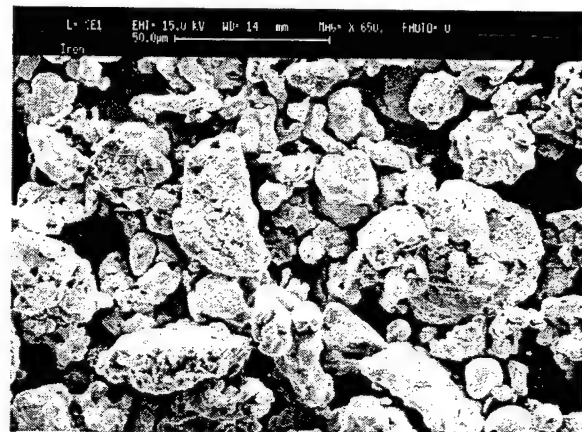


Figure 9-4

-325 mesh Iron

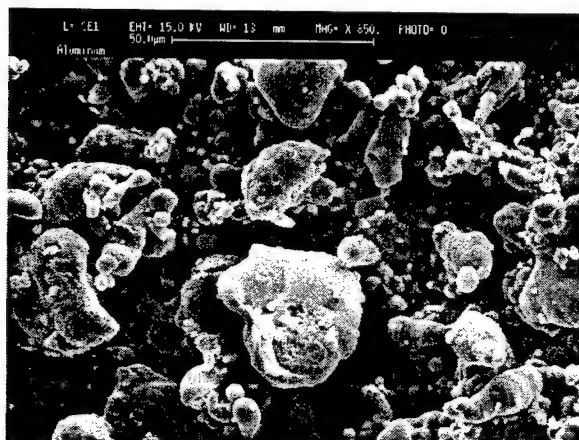


Figure 9-5

-325 mesh Aluminum

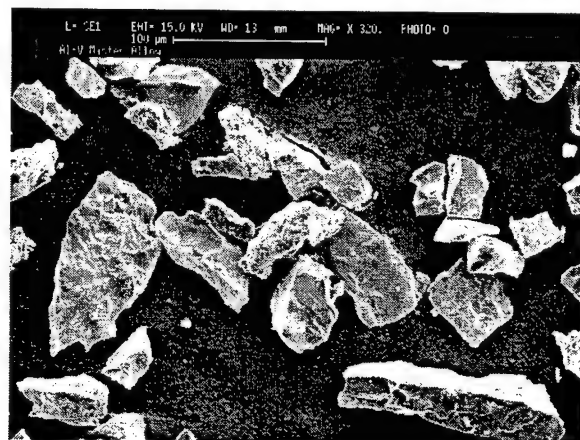


Figure 9-6

-30/+200 mesh Aluminum/Vanadium

Powder Blending

Calculations based on the required reinforcement volume percentage were performed to obtain the necessary powder weights to blend together. The powders were weighed and initially dry blended for 24 hours at 176 RPM on a jar mill. This speed was based on the following formula which balances gravitational and centrifugal forces acting on the powder [6]:

$$N_o = 32/d^{1/2}$$

where d is the container diameter and N_o is the optimal rate of rotation in RPM. Stainless steel spheres were then added to the mix and the powder was dry blended for an additional 24 hours. Figures 9-7 and 9-8 document the powder distribution after mixing. The preliminary assessment indicated that the powder was evenly distributed with the smaller particles filling in the voids between the titanium particles.

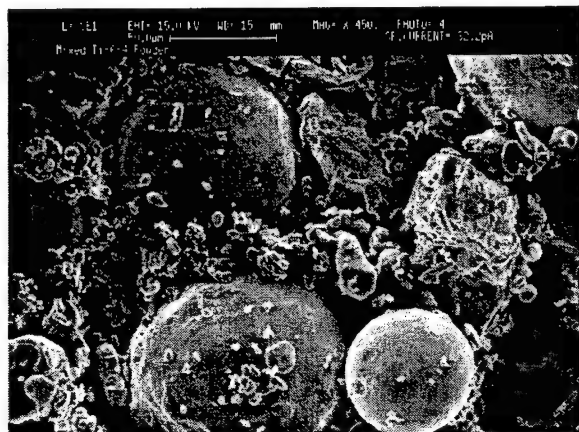


Figure 9-7

Blended Ti-6Al-4V/TiB₂

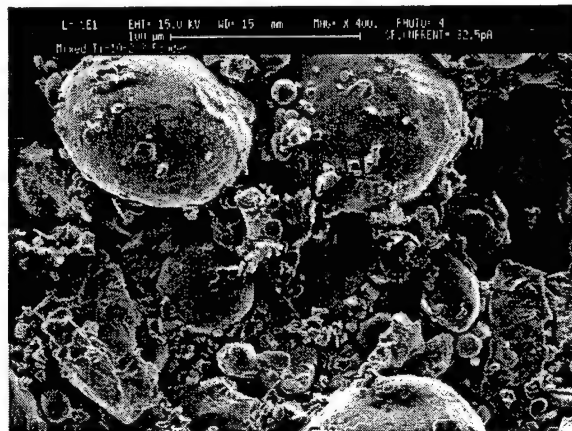
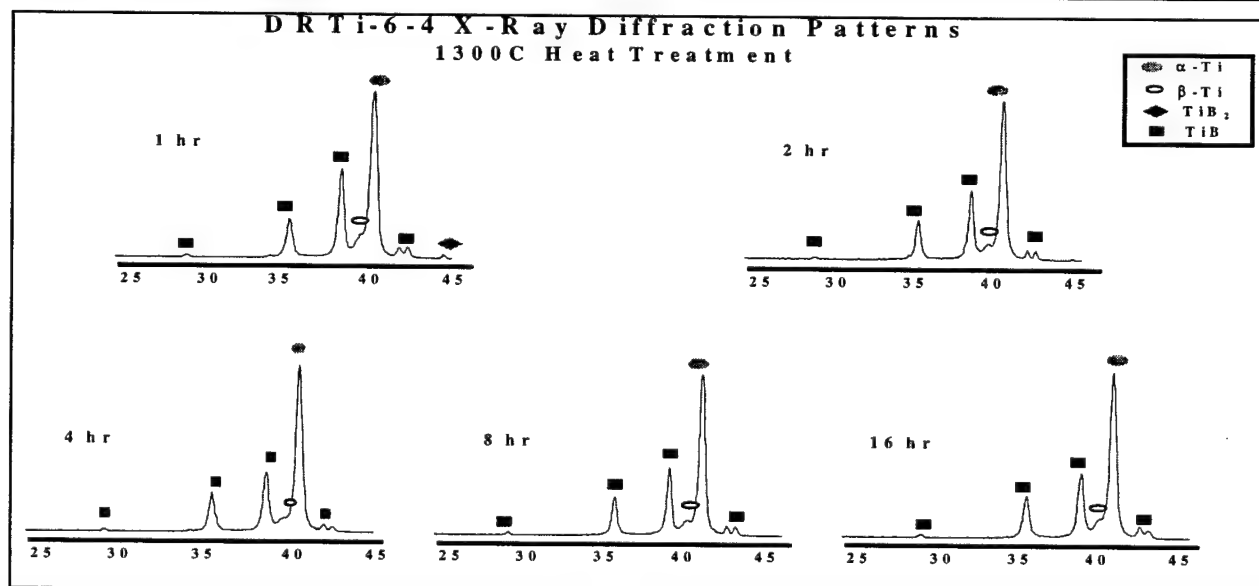
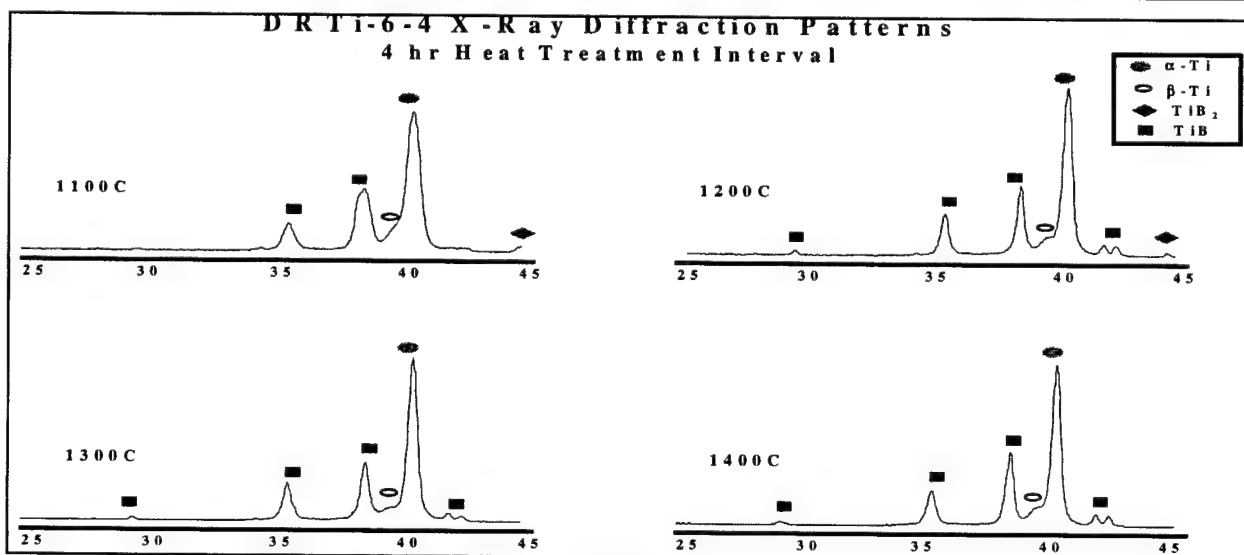
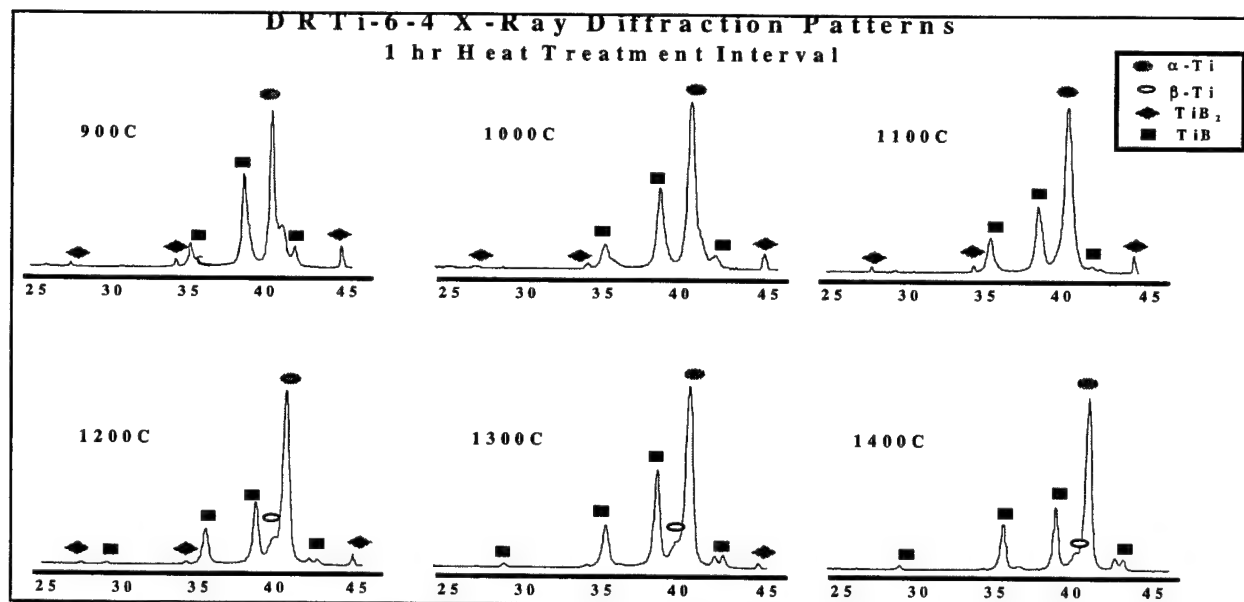


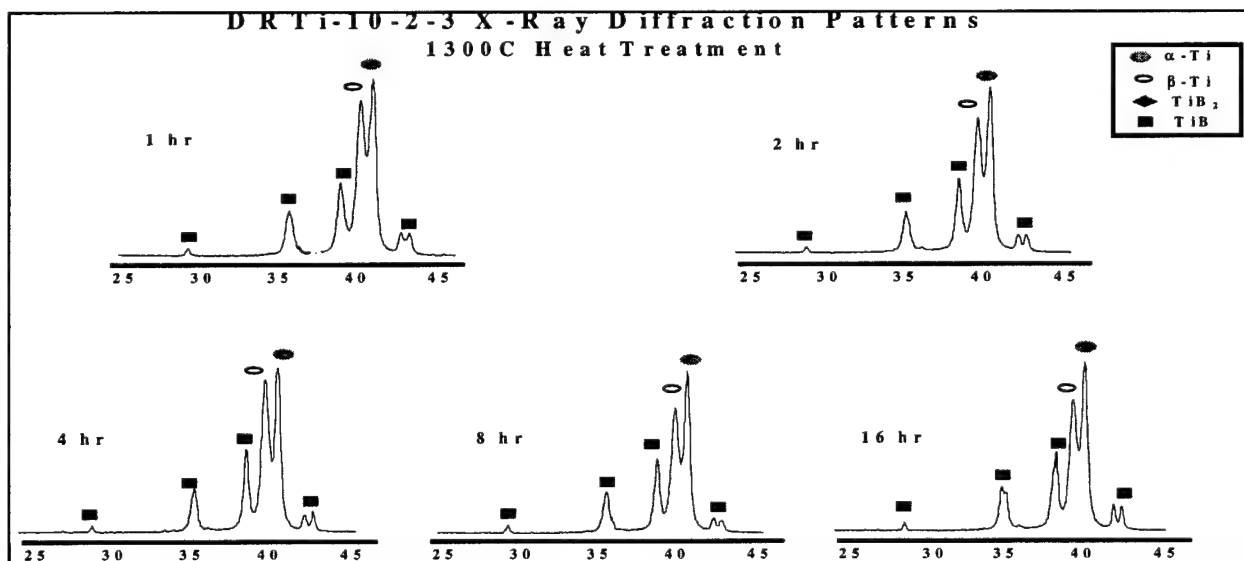
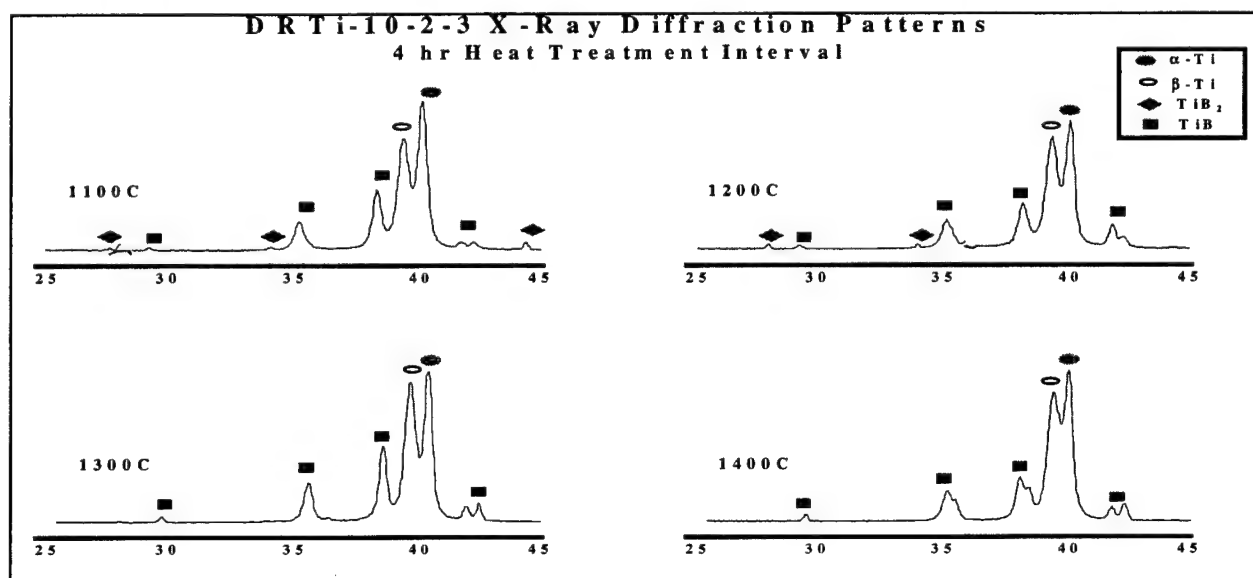
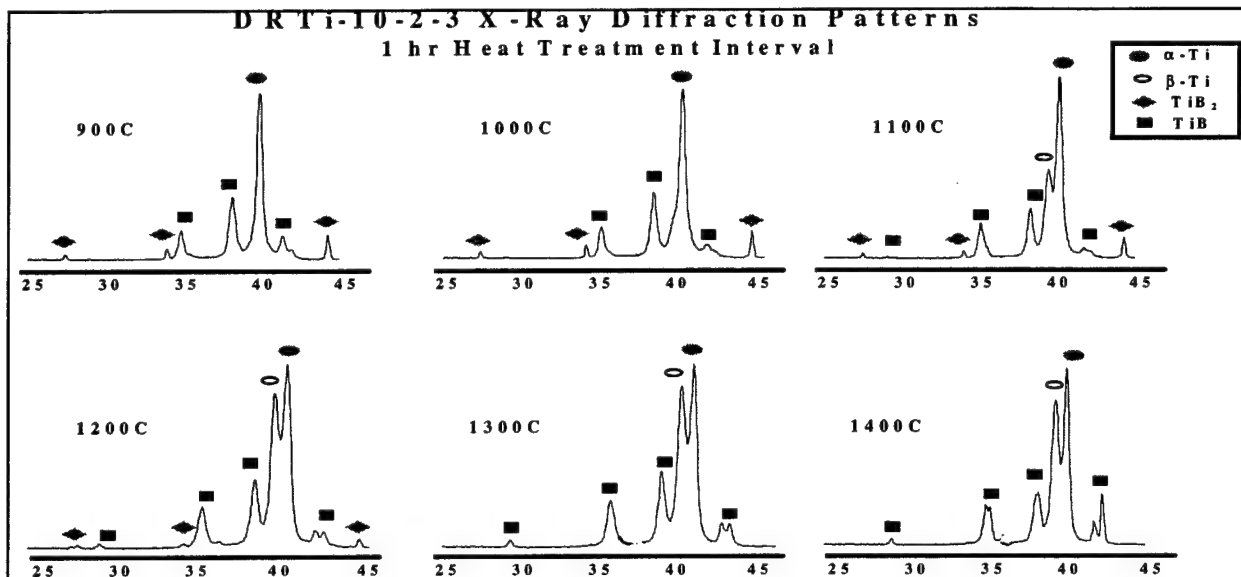
Figure 9-8

Blended Ti-10V-2Fe-3Al/TiB₂

Heat Treatment Mapping

A heat treatment mapping study was undertaken to determine the transformation temperature of TiB₂ to TiB particles. Cold compacts of approximately 0.5-inch diameter by 0.25-inch thick were used for this purpose. Compacts from each alloy were vacuum heat treated for one hour at temperatures of 900, 1000, 1100, 1200, 1300 and 1400°C and furnace cooled at a rate of 25 °C/min. Additionally, compacts of each alloy were vacuum heat treated for 4 hours at 1100, 1200, 1300 and 1400°C. X-ray diffraction was accomplished on each of the compacts and the diffraction patterns for each of the alloys are shown on pages 9-8 and 9-9.





Results show a definite transformation of TiB_2 to TiB in the Ti-10V-2Fe-3Al alloy after one hour at 1300°C , but not in the Ti-6Al-4V alloy. After four hours at 1300°C transformation is complete in the Ti-6Al-4V alloy. Additional heat treatments for 2, 8 and 16 hours were also conducted at 1300°C verifying complete transformation of the TiB_2 to TiB in the Ti-6Al-4V alloy after 2 hours. These additional heat treatments for both alloys will assist in analyzing TiB particle growth during extended periods at 1300°C . This confirms previous work by Saito documenting the TiB_2 to TiB transformation temperature of 1300°C [3-5].

Extrusion

In conjunction with the above activities efforts were undertaken to make the composite by extrusion. The powders were filled in 7.6 cm (3-inch) diameter extrusion cans fabricated from commercially available Ti-6Al-4V round stock, vacuum outgassed and sealed. The vacuum outgassing occurred in a two step sequence; first the powder was backfilled twice with argon prior to heating, and then backfilled twice again with argon while heating at 300°C for 24 hours [7,8]. Each can contained approximately 1.1 kg (2.5 pounds) of powder. The cans were heated to 1065°C for 1.5 hours and blind die compacted. For the extrusion itself the cans were reheated to 1065°C for 1 hour and extruded through a square die at a reduction ratio of 10.2:1. The temperature of 1065°C was chosen in order to compare with previous extrusions done at the same temperature [1,9].

Hot Isostatic Pressing

Hot isostatic pressing (HIPing) of the powders was used as an alternative approach to make the composites. The powders were filled in 2.5 cm (1-inch) diameter HIP cans fabricated from commercially available Ti-6Al-4V round stock, vacuum outgassed and sealed. The outgassing sequence was the same as that for the extrusion process. Each can contained approximately 160 grams (0.35 pounds) of powder. The cans were then HIP'd at 1065°C for 3 hours at 103.4 MPa (15 ksi). This would enable a direct comparison between the extruded and HIP'd microstructures of the composites.

Results

The as-extruded chemical composition is shown in Table 1. For both alloys the major alloying constituents fell short of the specification values. The values represented are in weight percent.

	Al	V	Fe	O	C	N	B
Ti-6Al-4V	5.29	3.37	0.049	0.159	0.0548	0.013	2.72
Spec	5.5-6.75	3.5-4.5	0.3	0.08-0.2	0.05-0.1	0.05	---
Ti-10V-2Fe-3Al	2.49	8.14	1.55	0.173	0.0522	0.008	2.52
Spec	2.6-3.4	9-11	1.6-2.2	0.13	0.05	0.05	---

Table 1

Constituent Weight Percentages of As-Extruded Composites

The as-extruded and as-HIP'd microstructures are shown in Figures 9-9 through 9-12. The micrographs reveal several clusters of reinforcing particles. X-ray diffraction of these samples confirmed the presence of TiB_2 and TiB as would be expected since the extrusion temperature was below the $1300^\circ C$ transformation temperature of TiB_2 to TiB . It appears that the clustered particles are in fact filling the voids between the titanium powder as the titanium powder boundaries are visible in the as-HIP'd microstructure. Additionally, it appears that there are very few TiB particles in what was formerly a titanium particle indicating limited solubility of

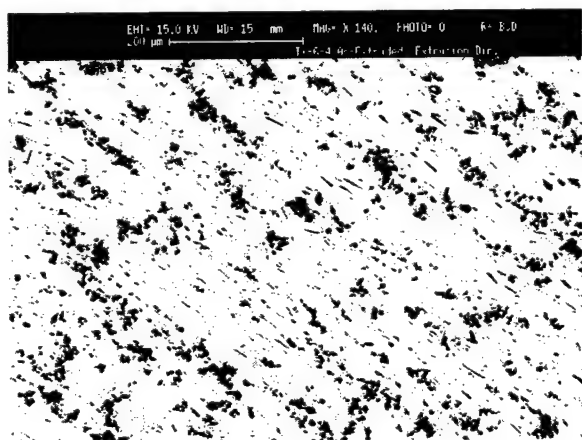


Figure 9-9

Ti-6Al-4V As-Extruded

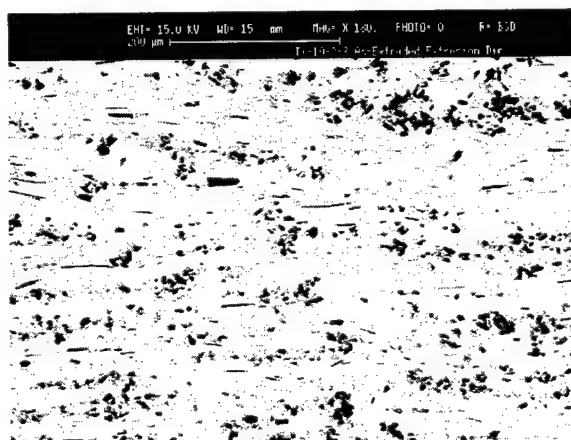


Figure 9-10

Ti-10V-2Fe-3Al As-Extruded

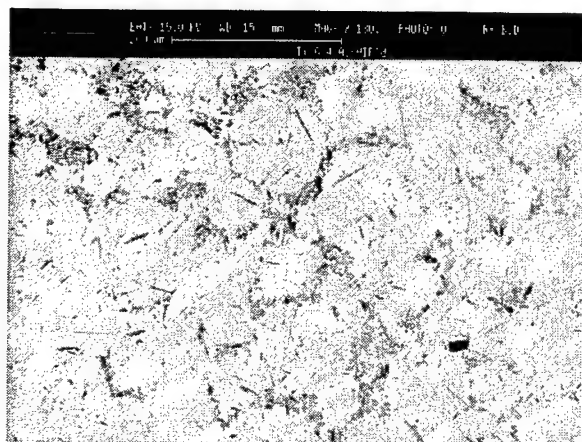


Figure 9-11

Ti-6Al-4V As-HIP'd

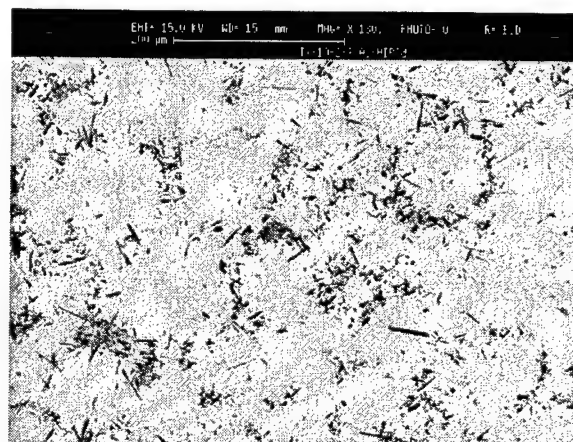


Figure 9-12

Ti-10V-2Fe-3Al As-HIP'd

boron in titanium and, quite possibly, a slow diffusion rate.

In order to investigate the transformation and reinforcement dispersal in the extruded product a series of heat treatments were conducted. Extruded samples were heat treated at 1100, 1200, 1300 and 1400°C for 1 hour, and at 1300°C for 2 and 4 hours in a vacuum furnace. X-ray diffraction confirmed the results of the cold compacts; i.e., complete transformation of TiB_2 in the Ti-10V-2Fe-3Al alloy at 1300°C after one hour and after two hours at 1300°C in the Ti-6Al-4V alloy. The completely transformed microstructures are shown in Figures 9-13 and 9-14. Clustering is still present in these microstructures and very few TiB particles are present in the areas where titanium powder particles once existed.. This is consistent with the extremely low solubility of boron in titanium of 0.001 a/o [5] to <0.003 a/o [10].

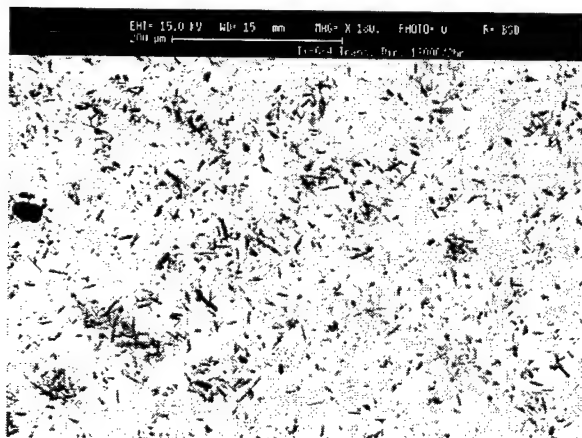


Figure 9-13

Ti-6Al-4V at 1300°C for 2 hours

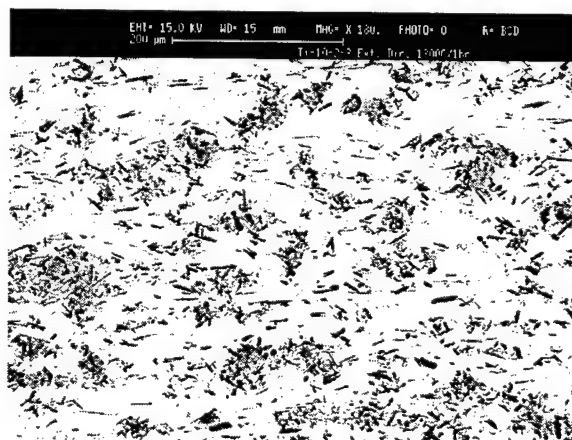


Figure 9-14

Ti-10V-2Fe-3Al at 1300°C for 1 hour

At this point attention was given to understanding how the transformation of TiB_2 to TiB takes place rather than evaluating the mechanical properties of the composites. It is obvious that the mechanical properties of the composites would be poor as the clustered reinforcement particles would promote crack initiation and propagation. Samples were cut from each of the heat treated extrusion specimens and electrolytically deep etched in a solution of methanol-7% HCL , dissolving the matrix and leaving behind either the TiB whiskers or remnants of the TiB_2 particles for further examination. Figures 9-15 through 9-18 document the TiB needle morphology at various heat treatment temperatures for the two alloys. It appears that at the lower temperature there is a mixture of TiB needles and a lacy-type morphology; i.e., very distinct from the needle morphology. This lacy morphology appears to decrease significantly, or eventually disappear, at the higher temperatures which are above the transformation temperature indicating that this may be TiB_2 transforming to TiB . Guillard and Rack [11] reported that TiB_2 evolved from a lacy to a needle- or plate-like morphology to a final blocky morphology in their studies of near- γ Ti-48Al-2Nb-2Mn . In their work [11], they formed TiB_2 reinforcement via the XDTM process, whereas in this case, the reverse is true.

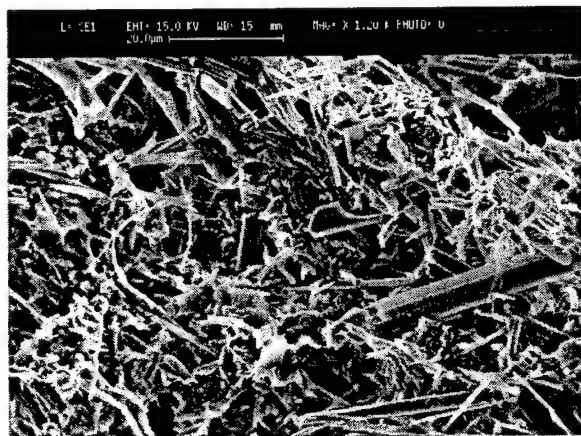


Figure 9-15

Ti-6Al-4V/1100C/1hr

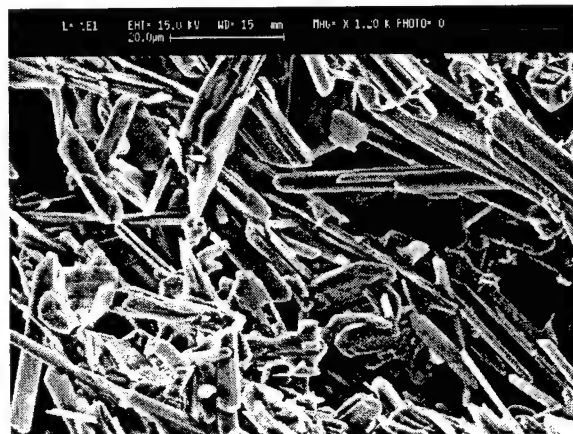


Figure 9-16

Ti-6Al-4V/1400C/1hr

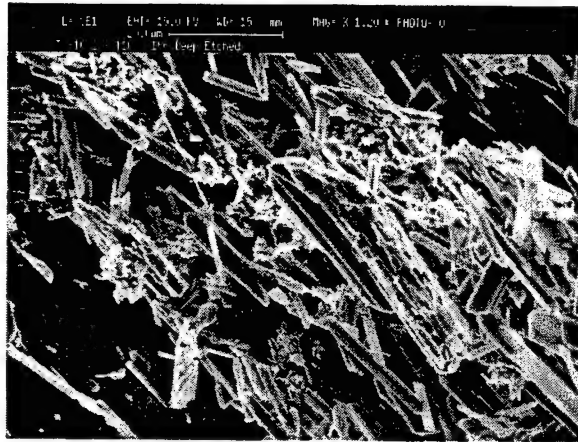


Figure 9-17

Ti-10V-2Fe-3Al/1100C/1hr

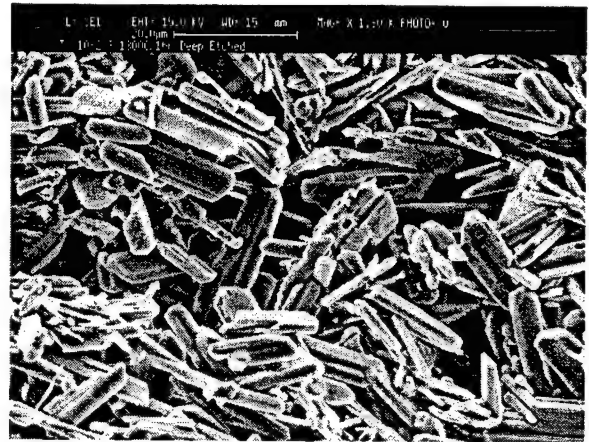


Figure 9-18

Ti-10V-2Fe-3Al/1300C/1hr

To further understand the clustering effect a second extrusion was accomplished. Approximately 454 grams (one pound) of each blended powder was left from the initial batch which provided enough material for a small extrusion. Filling, vacuum outgassing and blind die compaction of the extrusion cans proceeded as before. The difference came during the initial heating of the cans. Each can was heated at 1300°C for 3 hours prior to extruding; a time period confirmed to be long enough to obtain complete transformation of the TiB_2 . The billets were then

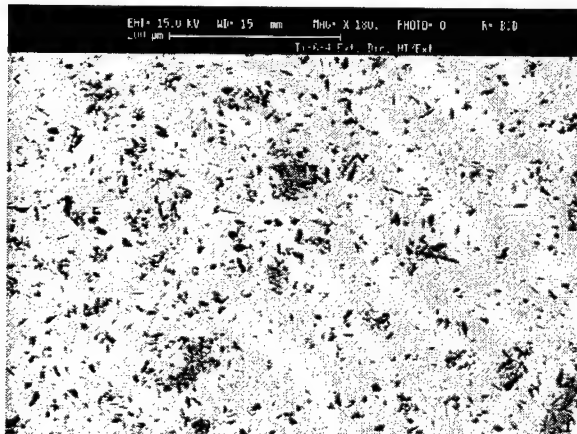


Figure 9-19

Ti-6Al-4V/15TiB Heat treated at 1300°C
then Extruded

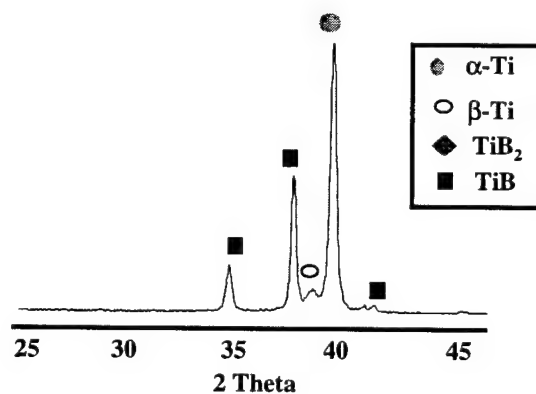


Figure 9-20

Diffraction Pattern Ti-6Al-4V/15TiB

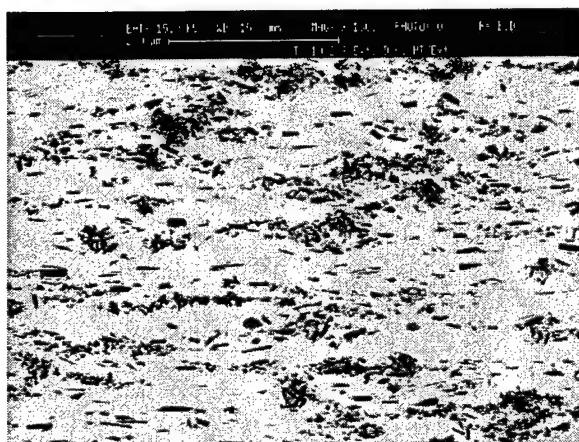


Figure 9-21

Ti-10V-2Fe-3Al Heat Treated at 1300°C
then Extruded

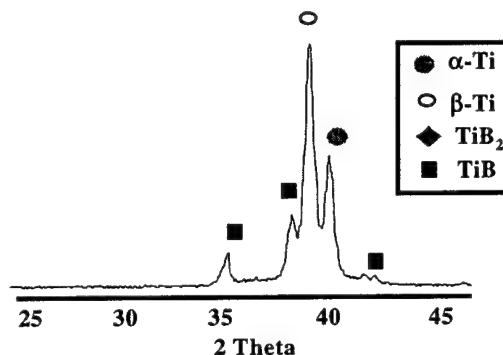


Figure 9-22

Diffraction Pattern Ti-10V-2Fe-3Al/15/TiB

extruded at 1065°C at a 10.2:1 reduction ratio. Figures 9-19 and 9-21 show the observed microstructure for the Ti-6Al-4V alloy and Ti-10V-2Fe-3Al alloy, respectively. It can readily be seen that the clustering is still present further supporting the low solubility of boron in titanium. Figures 9-20 and 9-22 are the x-ray diffraction patterns for this extruded material confirming complete transformation of the TiB_2 to TiB .

Conclusions

Two titanium alloys utilizing the blended elemental powder metallurgy approach and the in-situ synthesis of TiB from TiB_2 were successfully made. By using larger titanium powder particles the other smaller elemental powders were able to fill the voids between the titanium powder, but resulted in clusters of the reinforcement particles. The lack of uniformly dispersed reinforcement particles; i.e., few TiB particles in the area of previous titanium powder particles, can be attributed to the limited solubility of boron in titanium. These factors in combination will lead to deleterious effects on the mechanical properties of the composites. Using elemental powders of the same size may avoid the observed clustering effect.

Deep etching of heat treated extrusion samples definitely showed the formation of TiB particles and needles, thus confirming successful in-situ synthesis and a transformation

temperature for TiB_2 to TiB of 1300°C after 1 hour for the Ti-10V-2Fe-3Al alloy and after 2 hours for the Ti-6Al-4V alloy. This deep etching also revealed the presence of a lacy-type morphology interspersed with the TiB particles, believed to be TiB_2 in various phases of breakdown, in those samples heat treated below 1300°C .

The present results of this transformation study were used to provide complete transformation from TiB_2 to TiB prior to extruding expecting a relatively uniform distribution of TiB particles. Knowing the transformation temperature for TiB_2 to TiB will enable a heat treatment to be applied thus ensuring complete transformation prior to extruding, thereby avoiding the use of more costly rapidly solidified powders. A uniform distribution of reinforcement particles is expected to provide superior mechanical properties in discontinuously reinforced titanium metal matrix composites. Efforts are underway to achieve this goal.

Future Work

Continued emphasis will be placed on understanding the transformation kinetics of TiB_2 to TiB . Deep etching of the remaining heat treated extrusion samples, as well as the cold compacts used in the heat treatment mapping study, may shed some light on the transformation process. This may also provide useful information on the diffusion of boron in titanium, of which there is very limited information. Microprobe analysis will be accomplished on the lacy morphology to determine its composition.

Transmission electron microscopy will also be performed to analyze the interphase boundaries between the reinforcement particles and the matrix.

Elemental powders of the same size will be obtained and processed in the same manner to minimize, if not avoid, the observed clustering. A 1300°C heat treatment will be applied prior to extruding to ensure complete transformation of the TiB_2 to TiB . Mechanical properties of the composites will be determined after producing a uniform distribution of reinforcement particles.

Acknowledgments

I wish to thank Dr. Daniel Miracle, Dr. Awadh Pandey, Dr. Joel Philliber and the other members of the AFRL/MLLM team for their guidance, support, and continued encouragement in the pursuit of this research. I also wish to thank the Air Force Office of Scientific Research for allowing me the opportunity to participate in their Graduate Student Research Program.

REFERENCES

1. Srivatsan, T.S., Soboyejo, W.O., and Lederich, R.J. *Tensile Deformation and Fracture Behavior of a Titanium Alloy Metal Matrix Composite*. Composites Part A, 28A, 365-376, 1997.
2. Fan, Z., Miodownik, A.P., Chandrasekaran, L., and Ward-Close, M. *The Young's Moduli of In-Situ Ti/TiB Composites Obtained by Rapid Solidification Processing*. Journal of Materials Science, 29, 1127-1134, 1994.
3. Saito, T. *A Cost Effective P/M Titanium Matrix Composite for Automobile Use*. Advanced Performance Materials, 2, 121-144, 1995.
4. Saito, T., Furuta, T., Yamaguchi, T., and Ogino, K. *A New Low Cost MMC of TiB Particle Dispersed in Titanium Alloy*. Proc. Conf. 1993 Powder Met. World Congress, Y. Bando and L. Kosuge Eds., JPMA-JSPM, , 642-645, 1993.
5. Saito, T., Furuta, T., and Yamaguchi, T. *Development of Low Cost Titanium Matrix Composite*. Recent Advances in Titanium Matrix Composites, TMS, Warrendale, PA, F.H. Froes and J. Storer, Eds., 1995.
6. Sundrica, J. *Determination of the Optimal Rotational Speed for Powder Mixing*. Intl. J. Powder Met. Tech., 17, 291-294, 1981.
7. Kirchoff, S.D., Adkins, J.Y., Griffith, W.M., and Martorell, I.A. *Effective Method for Degassing Evaluation of Aluminum P/M Alloys*. Rapidly Solidified Powder Aluminum Alloys, ASTM STP 890, ASTM, Philadelphia, PA, M.E. Fine and E.A. Starke, Jr., Eds., 354-366, 1986.
8. Zimmer, W.H., Director of Engineering, Dynamet Technology, Inc., private communication.

9. Soboyejo, W.O., Lederich, R.J., and Sastry, S.M.L. *Mechanical Behavior of Damage Tolerant TiB Whisker Reinforced In-Situ Titanium Matrix Composites*. Acta Met., 42, 8, 2579-2591, 1994.
10. Larson, D.J., Liu, T., and Miller, M.K. *Boron Solubility and Boride Compositions in $\alpha_2 + \gamma$ Titanium Aluminides*. Intermetallics, 5, 411-414, 1997.
11. Guillard, S. and Rack, H.J. *Phase Transformations in XD TiB₂-Reinforced Near- γ Ti-48Al-2Nb-2Mn*. Materials Science and Engineering, A183, 181-194, 1994.

EVALUATION OF USING AGENTS FOR FACTORY LAYOUT AFFORDABILITY

Lisa Schaefer
Research Assistant
Department of Industrial and Management Systems Engineering

Arizona State University
Tempe, AZ 85287

Final Report for:
Graduate Student Research Program
Wright Research Site

Sponsored by:
Air Force Office of Scientific Research
Bolling Air Force Base, Washington, DC

and
Wright Research Site

August 1998

EVALUATION OF USING AGENTS FOR FACTORY LAYOUT AFFORDABILITY

Lisa Schaefer
Research Assistant
Department of Industrial and Management Systems Engineering
Arizona State University

Abstract

The Manufacturing Technology Division of the Air Force Research Laboratories is aiming toward improving the affordability of manufacturing military equipment. Autonomous agents have been used with increasing frequency in the past few years to model various manufacturing theories, such as scheduling and activity based costing.

The goal of this phase of the project was to evaluate the literature and the current state of factory layout methodologies and autonomous agent theories. A case study was performed to evaluate a preliminary model of agents applied to the layout of a helicopter blade manufacturing cell. The goal of the model was to determine a feasible factory layout design by applying agent rules to the entities (workers and machines) existing in the cell.

The long term goal of this research is to develop a tool to evaluate layout affordability which could be an extension for existing manufacturing software. The tool could determine the efficiency of work flow in a manufacturing facility by calculating the effects of overcrowded machines and congested walkways or transport areas vs. low floor space utilization.

EVALUATION OF USING AGENTS FOR FACTORY LAYOUT AFFORDABILITY

Lisa Schaefer
Research Assistant
Department of Industrial and Management Systems Engineering

Introduction

The Manufacturing Technology Division (ManTech) of the Air Force Research Laboratories is aiming toward improving the affordability of manufacturing military equipment. Old accounting practices are being reevaluated. A new accounting method called Activity Based Costing (ABC) is being reviewed by ManTech. The goal of ABC is to better define how costs should be distributed across products manufactured by the same company.

Autonomous agents have been used with increasing frequency in the past few years to model various manufacturing theories. Systems based on autonomous agents have the potential to produce robust, high quality solutions (Haynes and Erol 1997).

The goal of this phase of the project was to evaluate the literature and the current state of factory layout methodologies and autonomous agent theories. A case study was performed to evaluate a preliminary model of agents applied to the layout of a helicopter blade manufacturing cell. The goal of the model was to determine a feasible factory layout design by applying agent rules to the entities (workers and machines) existing in the cell.

The long term goal of this research is to develop a tool to evaluate layout affordability which could be an extension for existing manufacturing software. The tool could determine the efficiency of work flow in a manufacturing facility by calculating the effects of overcrowded machines and congested walkways or transport areas vs. low floor space utilization.

The performance measures would be quantities such as total floor space required (occupancy) per activity center and total distance and time of material transport. The output of this model could be used as input to an ABC model to calculate actual secondary activity (e.g. building maintenance) costs per product or to assist in determining whether jobs should be outsourced and if a long-term contract for a product would be profitable.

Hypothesis

Due to the rules programmed for the entities, the behavior that will emerge during a computer analysis of a factory layout will be a steady-state system. The machines will eventually converge to a location and will not deviate from that location more than a small distance.

Literature Review

Literature in the areas of autonomous agents, emergent behavior, factory layout, and relevant work in the Manufacturing Technology Division was reviewed. The three main categories of mathematical and simulation

models reviewed were: live beings, computer animation, and robots. This review contains descriptions of each publication reviewed in these categories along with a discussion of their implications.

Autonomous Agents

Musse and Thalmann (1997), modeled a crowd of pedestrians in a museum. They determined that while walking through the exhibits, the emergent behavior of the system is that people form social groups.

Musse and Thalmann used multiresolution collision avoidance for navigating the people in the simulation. Type 1 collision avoidance involved calculating the intersection of two lines and distance from two points to determine possible collision events. Type 2 collision avoidance is similar to type 1, however instead of stopping, the slower pedestrian changes its angular velocity when a potential collision is detected.

Microscopic models of ant trails have been widely researched (Parunak 1996, Schweitzer et. al. 1997, Millonas 1992). The simulated ants are programmed to follow pheromone trails left behind by ants which previously occupied nearby locations. The emergent behavior of the ants is that they eventually navigate their way to food, even though the rules do not specifically force the ants to find food.

Table 1 defines the categories of models that are used to describe models in the literature that could be modified to simulate agents. Each of these categories appear in Tables 2 through 5 which summarize algorithms in the literature.

CATEGORY	DEFINITION
cells	Cellular automata, or discrete squares. The space which entities may occupy is not continuous. Entities may travel to adjacent cells or skip cells each time step.
link-node	The space which entities may occupy is not continuous. Entities may travel to adjacent nodes at each time step.
flocking	The algorithm has rules to promote grouping of objects as they navigate toward a goal location.
navigation	The focus of the algorithm is selecting a path toward a specified goal location.
object-oriented	In the sense of object-oriented programming. Although most of the object-oriented models could be more specifically defined by placing them in other categories, some of the object-oriented models were too general to place in other categories.
curved path	The path that an object follows is swept out by a curve vs. rigid discrete changes in direction.
obstacle avoidance	The focus of the algorithm is avoiding collisions with stationary or non-stationary objects.
predefined terrain	The locations of all obstacles on the map are defined before the simulation.
force field	Objects avoid collisions by changing their direction or acceleration depending upon their distance from the obstacle. Their sensitivity to upcoming obstacles is proportional to the distance from the obstacle.
consensus-making	Several objects communicate to decide which action to take next.
blooming	An imaginary boundary is extended around the surface of each obstacle at a distance equal to the radius of the navigating entity.

Table 1: Definitions of Model Categories

Summary of Animal Agent Algorithms

Table 2 summarizes the relevant algorithms in the literature that may be used for modeling pedestrians.

AUTHOR	MAIN CONCEPTS	CATEGORY
Gipps and Marksjo, (1985)	How changes in environment affect pedestrian flow Route generation: shortest path, no collision with fixed obstacles Link movement: density, speed, benefit	cells, link-node
Lovas, (1994)	Stochastic queueing network EVACSIM discrete event simulation	link-node
Millonas, (1992)	Ants: energy states Route choices: length, quality	link-node
Musse and Thalmann, (1997)	Generic population, specific environment (museum) Emergent behavior (grouping at exhibits) Collision detection	flocking
Schweitzer et. al., (1997)	Ants: chemical communication Microscopic local interactions: emergence of trail system Triangular lattice Geocentric: landmarks, Egocentric: dead reckoning	cells
Schweitzer and Schimansky-Geier, (1994)	Potential function: particle interaction decisions- deterministic and probabilistic Langevin and Fokker-Planck, reaction-diffusion equations Hexagonal lattice	cells

Table 2: Algorithms in the Literature Used for Modeling Pedestrians

Computer Animation:

Parent (1998) discusses characteristics of modeling birds as a particle system. He lists the following traits objects must have:

- Be aware of itself and two or three of its neighbors
- Be aware of what's in front of it (some limited field of view)
- Have, if nothing is in view, a general migratory urge
- Have distance-limited field of view
- Be affected by things using a distance-squared or distance-cubed weighting function
- Not follow a designated leader
- Not have knowledge about a global flock center

In addition to collision avoidance and flock centering, a third force which is useful in controlling the object's behavior is velocity matching helps to avoid collision.

In his course notes for physically based modeling, Reynolds (1988) discusses some techniques for directing the paths of objects moving around an environment, such that they do not collide with either static obstacles or other moving objects. Rather than the traditional view of inert geometrical objects being moved

according to a centralized, pre-existing plan, we can model the objects to be active independent entities capable of directing their own motion.

The following is a list of the obstacle avoidance techniques described in Reynolds (1988).

- Steering-around-obstacles: accelerations are not bounded
- Steer-away-from-surface: agents are accelerated away from the surface of obstacles by a force field inversely related to distance
- Steer-away-from-center: considers the obstacles as points and causes agents to steer in the direction opposite to the center point of the obstacle
- Steer-along-surface: analogous to curb feelers
- Steer-towards-silhouette-edge: causes the intelligent agent to head toward an object's nearest silhouette edge rather than consider surface orientation or centroid location

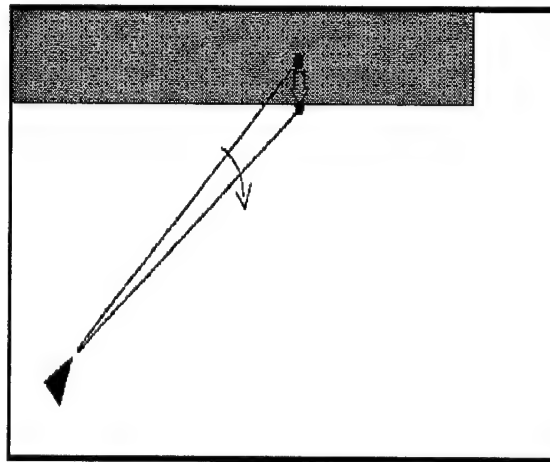


Figure 1: Steer-Along-Surface Technique: Analogous to Curb Feelers (Reynolds 1988)

Summary of Computer Animation Algorithms

Table 4 summarizes the algorithms in the literature for computer animation of autonomous agents.

Robots

Mataric, 1992, conducted an experiment with mobile robots to understand the types of simple local interactions which produce complex and purposive group behaviors. All agents had the same set of rules and goals. All communication was based upon the agents sensing the external state of nearby agents. This type of sensing is analogous to vision in humans. Agents were able to distinguish between two types of objects: mobile robots and anything else.

AUTHOR	MAIN CONCEPTS	CATEGORY
Badler (1993)	Curved path walking Basic, sequential, control, and planar algorithms	curved path
Lozano-Perez and Wesley (1979)	Collision avoidance: forbidden regions	link-node
Noser, et. al. (1995)	3-D, global & local navigation 3 Algorithms: path searching, path extension, shortest path	cells
Parent (1997)	Collision detection, conservation of momentum Particle systems, flocking	flocking
Badel et. al. (1994)	Computing steering vector	curved path
Reiter (1995)	Path planning Matrix: obtain curve - arclength, speed, curvature Collision resolution	obstacle avoidance
Reynolds (1988)	Intermediate goals, individual object Steer away from surface, away from center, along surface, towards silhouette edge	obstacle avoidance
Reynolds (1987)	Particle system, gravity in coordinate system, centrifugal force, simulated perception, collision avoidance rules	flocking

Table 4: Algorithms in the Literature Used for Computer Graphics

The robots had six capabilities: collision avoidance, following, dispersion, aggregation, homing, and flocking. Assuming the robots have the ability to sense objects in front of it on the right and on the left, the algorithm for collision avoidance can be described as follows:

```

If robot is in path
  If at the right
    turn left, go forward
  else turn right, go forward
If other object is in path
  If at the right only
    turn left, go forward
  If at the left only
    turn right, go forward
  If on both sides
    wait

```

The algorithm for homing was the following:

```

Turn toward direction of goal location
go forward
If at goal, stop

```

Robots in Manufacturing Environments

Automated guided vehicles (AGVs) are driverless vehicles which are becoming an increasingly popular type of material handling device in flexible manufacturing systems. (Krishnamurthy, 1993). Link-node models for uni-

directional or bi-directional paths on a grid network have been documented (Egbelu and Tanchoco, 1986, Krishnamurthy, 1993, Taghaboni and Tanchoco, 1988).

Taghaboni and Tanchoco (1988) developed rules to dispatch and schedule a fleet of AGVs in real time. The paths are defined on a grid network of nodes and arcs. A route planner determines the shortest route for each AGV with a branch-and-bound algorithm. The input is the grid pattern and the output is the list of paths.

Summary of Robot Modeling Algorithms

The following table summarizes the articles in the literature for modeling robots and AGVs.

AUTHOR	MAIN CONCEPTS	CATEGORY
Bobrow (1988)	Optimal Path: time control Non-linear equations of motion, B-spline polynomials, Obstacle avoidance constraints: distance functions	force field
Chattergy (1985)	Probe along straight line or parallel to barrier, Scan for break in barrier, Navigate toward image point	obstacle avoidance
Crowley (1985)	Composite local model: line segments Global path planning Local navigation, obstacle avoidance	predefined terrain
Egbelu and Tanchoco (1986)	Bi-directional, arcs and nodes Routing through an intersection Nodes have infinite buffer capacity	link-node
Gilbert and Johnson (1985)	Optimize performance indices, numerical solution Plan path around obstacles based on distance function Steps: path plan, path track	force field
Guldner and Utkin (1995)	Obstacle security zones Gradient of harmonic potential field approaches goal	force field
Ishiguro, et. al. (1997)	Decentralized consensus-making Immune network for action selection Collects, consumes energy	consensus-making
Krishnamurthy, et. al. (1993)	Constrained shortest path Bi-directional network: link, node, buffers	link-node
Mataric (1992)	Collision avoidance, Following, Dispersion, Aggregation, Homing, Flocking	flocking
Nageswarwa, et. al. (1994)	Terrain acquisition, path planning	predefined terrain
Shih (1985)	Repulsion: $1/d$ Passage with obstacles, deviation from ideal path	force field
Taghaboni and Tanchoco (1988)	Free-range AGVs, real time scheduling Dispatch, shortest route, schedule Network: link-node, collision avoidance: on same link	link-node
Uttal, et. al. (1997)	Approach nearest object Dead reckoning (straight line), curved path Route planning, obstacle avoidance: blooming	blooming
Vagenas (1996)	Bi-directional lane segments, Dijkstra's shortest path Safety distances between AGVs	link-node

Table 5: Algorithms in the Literature Used for Robot Navigation

Common Characteristics of General Autonomous Agent Algorithms for Navigation

There are four important items that must be represented in a 2-D spatial simulation. These are: the path, the objects on a spatial map, collision avoidance, and the goal of the objects. The objects and spatial map are placed in the same category because obstacles could be static or dynamic entities, or they could be forbidden regions on the map. Each item consists of a set of features which could be used to describe the item.

The path is the trail an agent forms as it navigates through its environment. The following tables define the features of the six main items for a simulation model which could be used to describe the path of a particle system.

Feature	Definition
Free range	Travel space is not limited to a predefined track.
Link-node	Travel paths-intersections •Cellular automata is a type of grid-shaped link-node architecture. •Robots on tracks are a link-node system.
Discrete angular changes	During each time step, the entity travels in a straight line, versus a curved path, according to a given velocity. At the end of the time step, the entity may choose a different direction and velocity to travel dependent upon the conditions of the system at that time step.

Table 6: Features of Paths of Particle Systems

The map is the 2-dimensional space over which the agent navigates. The following table defines the features of a simulation model which could be used to describe the representation of objects and map of a particle system.

Feature	Definition
More than 1 object	Objects are defined as entities that have a position in Euclidean space that can be defined with x and y coordinates. Objects can occupy points, lines, or areas. Each object can be an obstacle to the other objects. In our study, objects represent material transporters and machines. Objects are actual portions of code (classes) programmed in an object-oriented language.
More than 1 type of object	True if not all the objects follow the same rules. In this study, material transporters and machines are two different types of objects.
Forbidden regions / boundaries / obstacles	These are stationary restricted areas, such as a wall.
Cells	Entities occupy entire squares of space. Each square is the same size and exists at discrete intervals.
Points	Each entity is considered as occupying a point on a 2-D surface.
Areas	Each entity is considered as occupying an area of space on a 2-D surface. Entities may vary in size and may exist at any point in continuous space.

Table 7: Features of Representation of Objects and Maps of Agent Systems

Rules must be included in the simulation to prevent collisions. The following table defines the features of a simulation model which could be used to describe collision avoidance rules of a particle system.

Feature	Definition
Follow behind	Entities follow the path of another nearby entity. Possibly the opposite of the butterfly effect in chaos, this could be called the caterpillar effect. Instead of a butterfly causing a chain of events, the rules cause the entities to form a chain resembling caterpillar.
Maintain distance from other objects	Entities maintain a given distance from other objects.
Attention distance	Entities can only detect obstacles within a given distance.
Avoid surface	Entities explicitly avoid the edge of obstacles vs. Avoiding a given distance from the center.
Avoid center	Entities avoid coming within a given distance from the center of the obstacle.
Buffer zone	Either the entities, the obstacles, or both have a given distance around their perimeters which cannot be intruded.
Stop	Entities stop navigating to allow a moving entity to pass.
Acceleration/ deceleration	Entities may change their velocities gradually.
Maneuver around object	Entities may steer away from a goal temporarily to avoid colliding with another entity or obstacle.

Table 8: Features of Collision Avoidance Rules of Agent Systems

A simulation of agents needs to have a means to specify the approximate direction of motion of agents at any given time step. The following table defines the features of a simulation model which could be used to describe the goal location of an agent.

Feature	Definition
Location	Entities navigate toward a location.
Match average velocity	Entities speed up or slow down toward average velocity of the group.
Aggregation	Entities try to gather into a group of objects.
Intermediate goals	Entities try to reach another destination before traveling toward the point at which the object may leave the system.
Collect a virtual substance	Virtual substances such as food or chemicals can be located at certain points of a 2-D system. Entities navigate toward these substances. When an entity reaches the substance, it is removed from the environment and given to the entity as an attribute such as energy.

Table 9: Features of Goal Locations for Agent Systems

Emergence

Emergent Behavior

In many systems of autonomous agents, the system behavior converges to a certain state. This convergence is called emergent behavior. The definition of emergent behavior differs widely across the literature from various field of research. One such definition from literature describing a cellular automata model of chemical reactions

is: "the global behaviors of a system of agents, situated in an environment, that require new descriptive categories beyond those that describe the local behavior of each agent." (Hoskins 1995).

There are usually three classes of techniques which are discussed in the literature depending on the number of elements being controlled and the sophistication of the control strategy: particle systems, flocking, and autonomous behavior. The following table summarizes a comparison of these three classes.

Type of Animation	Participants	Intelligence	Physics-based	Collision	Control
Particle Systems	many	none	yes	detect & respond	force fields
Flocking	some	some	some	avoidance	global tendency
Behavioral	few	high	no	avoidance	rules

Table 10: Three Classes of Agent Modeling Techniques (Parent 1998).

Emergent Computation

Different authors suggest different definitions of emergent computation. Forrest (1990) and Sulis (1995) suggest three properties which must exist in a set of calculations in order to consider the results of the calculations as emergent computation:

- 1) A collection of agents, each following explicit instructions
- 2) interactions among the agents (according to the instructions) which form implicit global patterns at the macroscopic level, i.e., epiphenomena
- 3) A natural interpretation of the epiphenomena as computations.

Crutchfield and Mitchell (1994) use the phrase "emergent computation" to mean the appearance of global information processing in systems of locally interacting processors. Local interactions are the rules that determine the values of each cell at each subsequent time step.

Traditional Factory Layout Methods

There are four main categories of facility layouts: fixed position, product, process, and group technology. Fixed position is for very large products, such as airplanes, where all the equipment is brought to the product.

When one or a few specific products are produced in a factory, the machines are oriented so that the product flows to consecutive adjacent machines. This is called a product layout.

In factories that produce many products but small quantities of each product, machines must be able to perform a variety of production operations and work on a variety of parts. For these situations, a process layout system is required. Departments must be composed of machines with similar capabilities that perform similar functions. Grouping of similar machines allows for higher machine utilization.

Group technology is a combination of product and process layout. Similar parts are grouped together in sufficient quantity to justify their own machines. Manufacturing cell layout is designed to produce only each set of similar parts (Askin and Standridge, 1993).

Current Factory Layout Software

Four brands of software are known to exist for determining factory layouts: Planet, Core Lap, Craft, and BlocPlan. These are all DOS-based. No recent software is known to exist. There is no factory layout software mentioned on the internet.

Related Work in this Team

Industrial Technology Institute used agents to model Activity-Based Costing for Agile Manufacturing Control. The plan was to install Activity Based costing systems in six companies, then measure the success and the impact. The most significant benefit was a better understanding and awareness of costs in each company (Arnsdorf et. al., 1997).

Intelligent Automation, Inc. used agents to model factory scheduling. The Autonomous Agents for Rock Island Arsenal (AARIA) project showed the feasibility of agent-based factory automation. The AARIA project considered the basic feasibility of using the internet for modeling trade of goods (Haynes and Erol, 1997).

Summary

Rules of motion and space from research in computer animation or robot modeling can be applied to any object that could be defined as an intelligent agent. Factory layout design is a promising areas to apply these rules.

System Description

A case study was performed on an example factory floor. The system modeled for this initial experiment was the McDonnell Douglas/Boeing helicopter blade manufacturing cell which is located at the plant in Mesa, Arizona.

Table 11 lists the workstations with their approximate sizes and quantity of workspaces required at each workstation. Most of the workstations require long tables, although some require special machinery. There are 19 different workstations total, 3 of which are large and stationary, 16 which can be moved to different locations of the manufacturing cell.

Thirteen workers are available to work on blades and transport the blades around the manufacturing cell. Approximately one blade is completed every two hours.

Figure 2 is the layout of the helicopter blade manufacturing cell. Some areas of the floor were not used in this study since they were assumed to be reserved for products not considered in this analysis. The areas that were used in this study are outlined in bold.

Workstation	Workspace Size	Quantity
1 st Stage	15' x 3'	2
1 st Stage Fixtures	15' x 3'	4
Ultrasonic Inspection	10' x 3'	1
Saw	room	
Sheffield Inspection	5' x 5'	1
Doubler	15' x 3'	1
Doubler Fixtures	4' x 2'	3
Drill, Rout, Chamfer, Ream, Bolt, Rivet	15' x 3'	2
Root End	15' x 3'	1
Root End Fixtures	4' x 2'	2

Workstation	Workspace Size	Quantity
Tip End	15' x 3'	1
	3' x 3'	1
Tip End Fixtures	3' x 3'	1
Abrasion Strips	15' x 2'	1
	3' x 3'	1
Abrasion Fixtures	15' x 1'	5
Mill	10' x 4'	1
Drill	15' x 3'	1
Pull Test	4' x 3'	1
Paint	40' x 20'	1
Oven	30' x 20'	1

Table 11: Workstation Processing Times

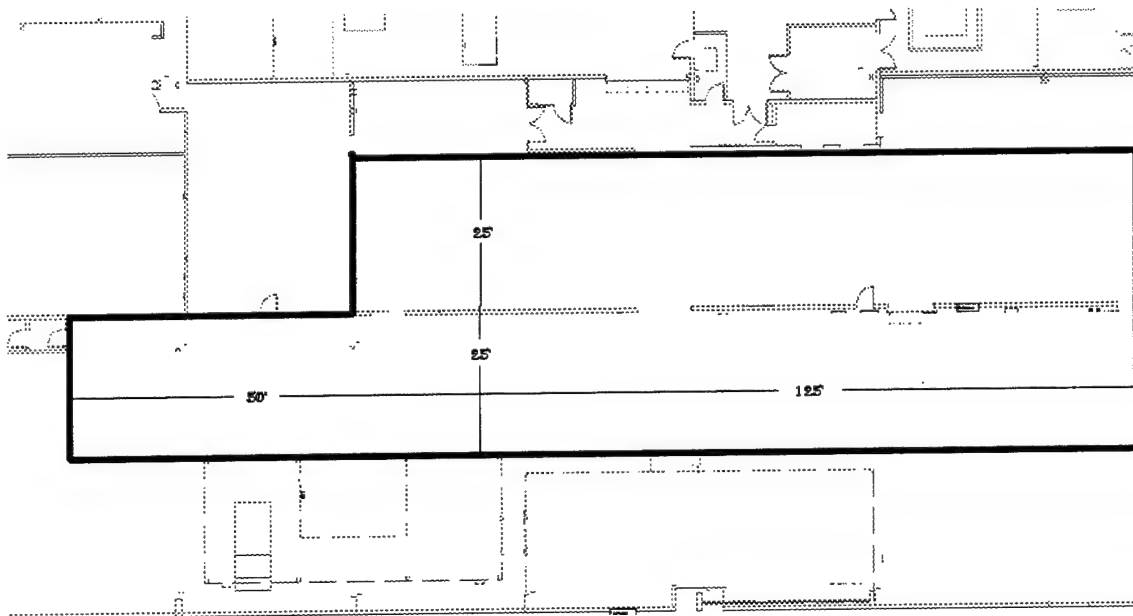


Figure 2: Blade Cell Floor Plan

Work Flow Description

The flow of the main blade processes is shown in Figure 3. The numbers which appear in each block correspond to the operation numbers which are also listed in Table 11. The laborers that can work on each operation are listed in all capital letters at the bottom of each block. The thirteen laborers are named A through M. The three inspectors are named X through Z. Names are listed to show that laborers can work on multiple operations. Workers bring material from their designated workstation to next workstation, then return to work on next material (blade).

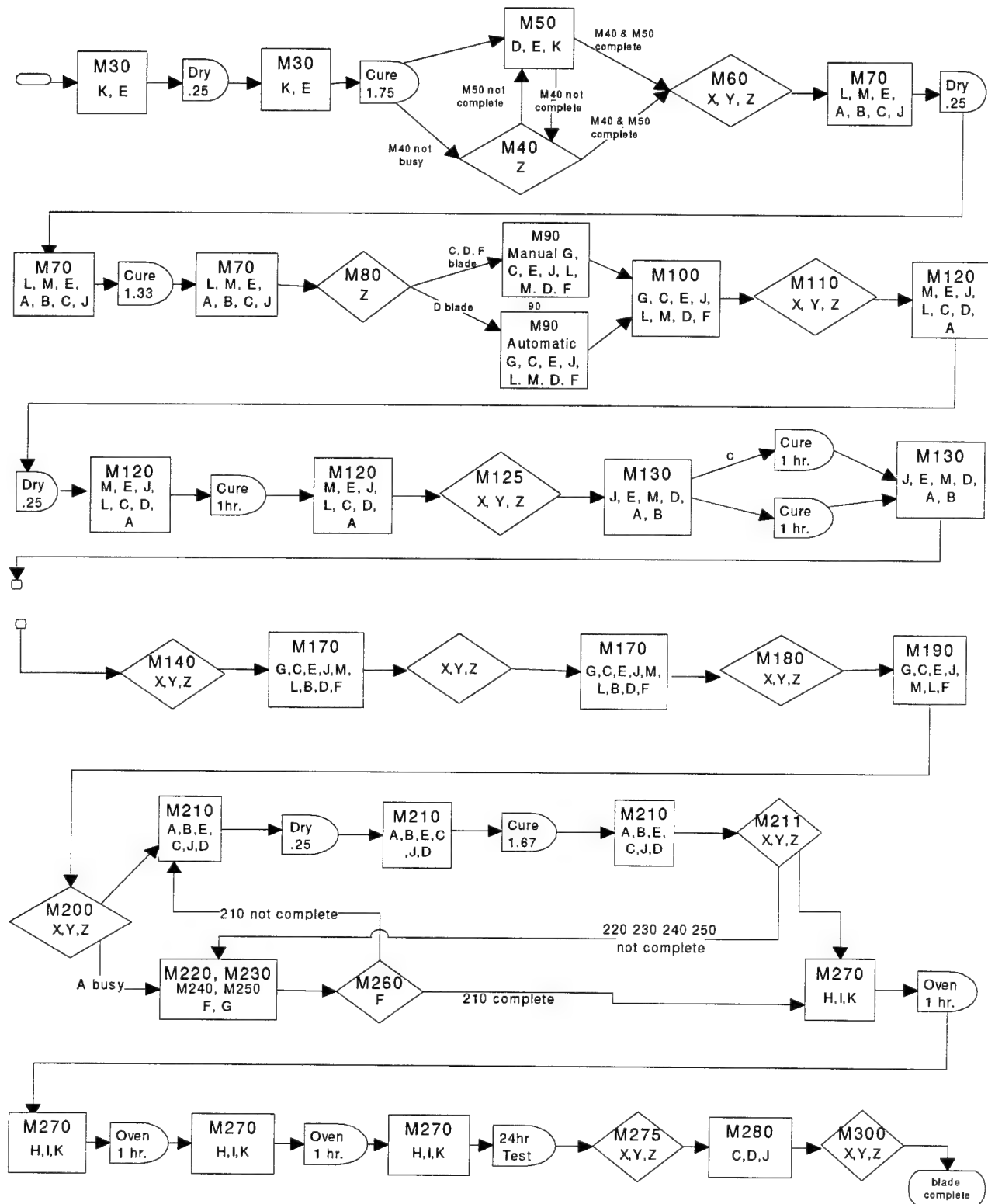


Figure 3: Process Flowchart of Main Blade

Input Data

Engineering plans were used to create a preliminary flowchart of the order of the flow around the blade cell. Blade cell workers were interviewed to verify details of each process to create process flowcharts.

Times clocked per operation per job order from 1996-1997 were fit to probability distributions with Arena distribution fitting software. Tables 1 and 2 lists the averages and the probability distributions for the processing times of each operation of the small and main blades. See ARENA documentation for definitions of standard probability distribution parameters (Kelton, et al. 1998). All values are in units of hours.

OPERATION	AVERAGE (hours)	PROBABILITY DISTRIBUTION
M 30	3.12	9 Beta (4.39, 8.12)
M 50	.47	Erlang (.235, 2)
M 70	.13	Normal (13, .779)
M 90	.91	2 Beta (3.44, 4.03)
M 100	.17	Lognormal (.193, .258)
M 120	1.73	Lognormal (1.72, .742)
M 130	1	Normal (1, .968)
M 170	.71	Lognormal (.702, .359)
M 190	.45	Gamma (.195, 33)
M 210	1.53	Lognormal (1.49, .999)
M 220	.96	12 Beta (.602, 6.95)
M 230	.5	Erlang (.166, 3)
M 240	.35	Gamma (.146, 39)
M 250	.57	2 Beta (1.16, 95)
M 270	.92	Lognormal (94, 1.73)
M 280	.91	Gamma (.461, 1.98)
M 290	.57	4 Beta (46, 13.5)

Table 12: Averages and Probability Distributions of Processing Times for Main Blades

Assumptions

For the sake of the initial analysis, some simplifying assumptions were made.

- The blades were assumed to flow from the 1st stage cure cycle to the saw then to the ultrasonic inspection station. Inspection operations that are conducted at workstations were considered part of the previous operation.
- All blades have the same machine sequence through all machines in the manufacturing cell.
- All workstations are assumed to occupy a total of a 15' x 3' space, regardless of the existence of multiple tables.
- Some of the workstations were lumped, such as fixtures that were associated with certain operations.
- Processing times were not considered, rather number of blade moves per hour affect layout
- The paint and balance work stations were not included in this analysis since they occur at large, stationary locations at the end of the process cycle.

Code / Rules

Simple rules were coded in the preliminary model described in this research. Some enhancements for future work on this model are also mentioned below.

Current Model

The following rules are in the existing model:

- When blade is completed at machine, blade is moved to next machine - the material handling device (person, in this case) is assumed to already be at the machine.
- Material handler is associated with each machine, the material handler must move back to its home machine location after dropping off.
- Initial location of material handler is its home machine
- The blades are not objects in the sense of object oriented programming. Instead, process times and pick-up times are stored in the machine objects and material handling objects.
- At each time step, all machines move toward the average location of material handlers traveling toward that machine.
- At each time step, all persons/material handlers move toward goal machine, defined as either the home machine or the machine after the home machine in the process, depending upon whether the material handler is delivering material or returning from dropping off material.
- Objects cannot go outside the system boundaries (walls).
- Machine centerpoints cannot be closer than five feet (20 pixels) from another machine.

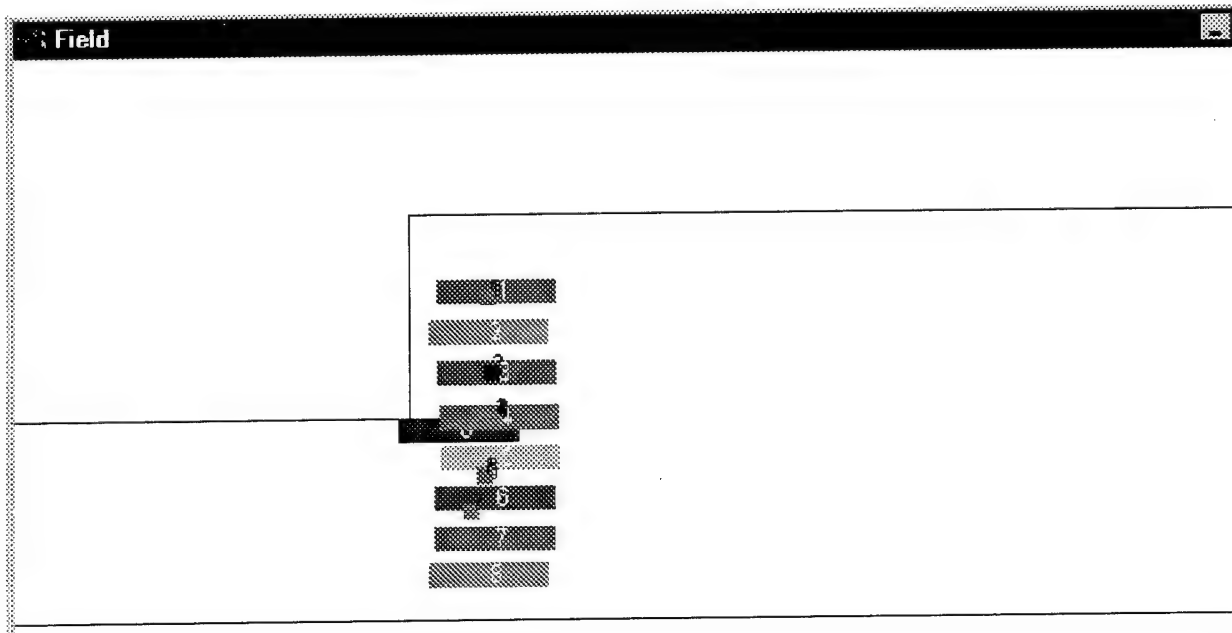
Future Enhancements

- When a blade arrives at each machine, it stays there for a certain number of time steps, dependent upon a probability distribution which describes the time between jobs finishing processing.
- When machine is idle, the machine could move toward parts that must be processed next on that machine. The goal location of each machine would then be the average location of all relevant jobs instead of material handlers.
- Some material handlers may be associated with more than one machine.
- Different products could have different machine sequences and may not visit each machine in the manufacturing cell.

Results

The performance measures for this system are total floor space required, total travel time, and total distance traveled by the material handlers.

The following figure is a screen shot of the final location determined by the analysis. The layout shown is the visual output which occurred after approximately 200 iterations. Each machine has a steady-state location that it eventually arrived at. The machines stopped at a location nearest to the machines in the machine sequence, i.e. the machines arrived at a linear layout.



Future Goals

The long term goal is to develop a tool to evaluate layout affordability. This could be an extension for existing software, such as Witness, to calculate the efficiency of work flow in a manufacturing facility. The tool could determine the effects of overcrowded machines and congested walkways or transport areas vs. low floor space utilization.

Required Input for such a model would be:

1. Select from a list of rules for material flow policies and how they would be mathematically represented.
2. Quantity of machines
3. Machine sizes
4. Time between starting a new job

Since the time frame for accomplishing this objective is not in the near future, this is not necessarily the approach to the problem, rather is included to spawn ideas for the direction of such a project and what could be accomplished.

The medium term goal is to determine how layout affects efficiency of manufacturing processes with respect to time and to determine recommended amount of open floor space per distance of material travel. The model should be improved to consider the four future enhancements mentioned above.

REFERENCES

- Annesley T., Dix, M., Beswick A. 1989. Development and Application of Pedestrian Assignment Models in London Railway Station Studies. *Traffic Engineering and Control*. **30 (7/8)**, 345-35
- Arnsdorf D. R., Erickson R. A., Fox M. J. 1997. *Activity-Based Costing for Agile Manufacturing Control*. Air Force Report 94-31-4
- Askin R. G., Standridge C. R. 1993. Modeling and Analysis of Manufacturing Systems. New York: John Wiley & Sons, Inc.
- Badal S., Ravela S., Draper B., Hanson A. 1994. A Practical Obstacle Detection And Avoidance System, *Proceedings of the IEEE Workshop on Applications of Computer Vision*, Sarasota, Florida, Dec. 5-7. 97-104.
- Badler N., Phillips C., Webber B. 1993. *Simulating Humans*. New York: Oxford University Press, Inc.
- Bobrow J. E. 1988. Optimal Robot Path Planning Using the Minimum-Time Criterion. *IEEE Journal of Robotics and Automation*. **4(4)**, 443-455.
- Chattergy R. 1985. Some Heuristics for the Navigation of a Robot. *The International Journal of Robotics Research*. **4(1)**, 59-65.
- Crowley. 1985. Navigation. *IEEE Journal of Robotics and Automation*. **RA-1(1)**, 31-41.
- Crutchfield J. P., Mitchell M. 1995. The Evolution of Emergent Computation. *Proceedings of the National Academy of Sciences*. **92**, 10742-10746.
- Egbelu P. J., Tanchoco J. M. A. 1986. Potentials for Bi-directional Guide-Path for Automated Guided Vehicle Based Systems. *International Journal of Production Research*. **26 (2)**, 1075-1097.
- Forrest S. 1990. Emergent Computation: Self-Organizing, Collective, and Cooperative Phenomena in Natural and Artificial Computing Networks. *Physica D*. **42**, 1-11.
- Gilbert E.G., Johnson D. 1985. Distance Functions and Their Application to Robot Path Planning in the Presence of Obstacles. *IEEE Journal of Robotics and Automation*. **RA-1(1)**, 21-31.
- Gipps P.G., Marksjo B. 1985. A Micro-Simulation Model for Pedestrian Flows. *Mathematics and Computers in Simulation*. **27**, 95-105.

- Guldner J., Utkin V. I. 1995. Sliding Model Control for Gradient Tracking and Robot Navigation Using Artificial Potential Fields. *IEEE Transactions on Robotics and Automation*. **11(2)**, 247-254.
- Haynes L., Erol K. 1997. *Factory Scheduling and resource Allocation by Autonomous Agents*. Air Force Report WL-TR-97-8035.
- Hoffmann C. M., Hopcroft J. E. 1987. Simulation of Physical Systems from Geometric Models. *IEEE Journal of Robotics and Automation*. **RA-3(3)**, 194-206.
- Hoskins D. A. 1995. An Iterated Function Systems Approach to Emergence. *Evolutionary Computation IV: The Edited Proceedings of the Fourth Annual Conference on Evolutionary Programming*.
- Ishiguro A., Kondo T., Watanabe Y, and Uchikawa Y. 1996. Immunoid: An Immunological Approach to Decentralized Behavior Arbitration on Autonomous Mobile Robots. *Parallel Problem Solving From Nature PPSN IV*, Y. Davidor, H.-P. Schwefel, and R. Manner, editors, Lecture Notes in Computer Science, Springer-Verlag, Berlin, 666-675.
- Krishnamurthy N. N., Batta R., Karwan M. 1993. Developing Conflict-Free Routes for Automated Guided Vehicles. *Operations Research*. **41**, 1077-1090.
- Levin B. M., Groner N. 199 *Human Behavior Aspects of Staging Areas for Fire Safety in GSA Buildings* NIST-GCR-92-606 George Mason University
- Lozano-Perez T., Wesley M.A. 1979. An Algorithm for Planning Collision-Free Paths Among Polyhedral Obstacles. *Communications of the ACM*. **4(3)**, 334-339.
- Lovas G. G. 1994. Modeling and Simulation of Pedestrian Traffic Flow. *Transportation Research Part B: Methodological*. **28**, 429-443.
- Kelton, W. D., Sadowski R. P., Sadowski D. A. 1998. *Simulation with Arena*. New York: McGraw-Hill.
- MacGregor Smith J. 1991. State-Dependent Queueing Models in Emergency Evacuation Networks. *Transportation Research Part B: Methodological*. **25**, 373-389.
- Mataric M. J. 199 Designing Emergent Behaviors: From Local Interactions to Collective Intelligence, *Proceedings, From Animals to Animats 2, Second International Conference on Simulation of Adaptive Behavior (SAB-92)*, J-A. Meyer, H. Roitblat and S. Wilson, eds., MIT Press, 432-441.
- Millonas M. M. 199 A Connectionist Type Model of Self-Organized Foraging and Emergent Behavior in Ant Swarms. *Journal of Theoretical Biology*. **159**, 529-55
- Musse S. R., Thalmann D. 1997. A Model of Human Crowd Behavior: Group Inter-Relationship and Collision Detection Analysis. *Eurographics Workshop on Computer Animation*.
- Nageswarwa S. V., Rao V., Iyengar S. S., Oommen B. J., Kashyap R. L. 1988. On Terrain Model Acquisition by Two Point Robots Amidst Polyhedral Obstacles. *IEEE Journal of Robotics and Automation* **4(4)**. 450-455.
- Noser H., Renault O., Thalmann D., Magnenat-Thalmann N. 1995. Navigation for Digital Actors Based on Synthetic Vision, Memory, and Learning. *Computers & Graphix*. **19 (1)**, 7-18.

- Parent R. 1998. *Computer Animation: Algorithms and Techniques*. Proposed book, Columbus, Ohio. <http://www.cis.ohio-state.edu/~parent/book> [accessed June 29, 1998].
- Parunak V. 1996. Go To the Ant. *Conference Proceedings*.
- Reynolds C.W. 1987. Flocks, Herds, Schools: A Distributed Behavioral Model. *ACM SIGGRAPH Computer Graphics*. **21 (4)**, 25-34.
- Reynolds C.W. 1988. *Not Bumping Into Things*. In the notes for the SIGGRAPH course Developments in Physical-Based Modeling. Published by ACM SIGGRAPH. Pages G1-G13.
- Schweitzer F., Lao K., Family F. 1997. Active Random Walkers Simulate Trunk Trail Formation by Ants. *Biosystems*. **41**, 153-166.
- Schweitzer F., Schimansky-Geier L. 1994. Clustering of "Active" Walkers in a Two-Component System. *Physica A*. **206**, 359-379.
- Selim S. Z., Al-Rabeh A. H. 1991. On the Modeling of Pedestrian Flow on the Jamarat Bridge. *Transportation Science*. **25 (4)**, 257-26
- Shih L. Y. 1985. Automatic Guidance of Mobile Robots in Two-Way Traffic. *Automatica*. **21(2)**, 193-198.
- Sullis W. 1995. Driven Cellular Automata. *1993 Lectures in Complex Systems*. SFI Studies in the Sciences of Complexity, Lectures **(VI)**, Addison-Wesley, 565-578.
- Taghaboni F., Tanchoco J. M. A. 1988. A LISP-Based Controller for Free-Ranging Automated Guided Vehicle Systems. *International Journal of Production Research*. **26 (2)**, 173-188.
- Uttal W. R., Kakarala R., Dayanand S., Shepherd T., Kalki J., Lunsikis C., Liu N. 1997. *The SWIMMER*. New York: Wiley.
- Vagenas N. 1996. Simulation Modeling of a Fleet of Remote-Controlled/Automatic Load-Haul-Dump Vehicles in Underground Mines. *Simulation*. **67(5)**, 331-34

SYNTHESIS OF 7-BENZOTHAZOL-2-YL-9,9-DIDECYLFLUORENE-2-YLAMINE:
A VERSATILE INTERMEDIATE FOR A NEW SERIES OF TWO PHOTON ABSORBING
MATERIALS & THREE NOVEL TPA DYES

Katherine J. Schafer
Department of Chemistry

University of Central Florida
4000 Central Florida Blvd., P.O. Box 162366
Orlando, FL 32816-2366

Final Report for:
Graduate Student Research Program
Air Force Research Laboratory

Sponsored by:
Air Force Office of Scientific Research
Bolling AFB, Washington, DC

and

Air Force Research Laboratory (AFRL/ML)

July 1998

SYNTHESIS OF 7-BENZOTHAZOL-2-YL-9,9-DIDECYLFLUORENE-2-YLAMINE:
A VERSATILE INTERMEDIATE FOR A NEW SERIES OF TWO PHOTON ABSORBING
MATERIALS & THREE NOVEL TPA DYES

Katherine J. Schafer
Department of Chemistry
University of Central Florida

Abstract

The synthesis of a new, useful intermediate, 7-benzothiazol-2-yl-9,9-didecylfluorene-2-ylamine, was accomplished starting with fluorene. Regiospecific nitration of fluorene with HNO_3 and $\text{CH}_3\text{CO}_2\text{H}$ at 85°C led to formation of 2-nitrofluorene in 80% yield. Regiospecific iodination of 2-nitrofluorene with I_2 , NaNO_2 , H_2SO_4 , and $\text{CH}_3\text{CO}_2\text{H}$ at 115°C afforded 7-iodo-2-nitrofluorene in 79% yield, after recrystallization. Alkylation of 7-iodo-2-nitrofluorene was accomplished with 1-bromodecane and KOH in DMSO at room temperature, yielding 9,9-didecyl-7-iodo-2-nitrofluorene in 77% yield (after column chromatographic purification). 2-(Tri-n-butylstannyl)benzothiazole was synthesized in 90% yield (after distillation) by reaction of benzothiazole with $n\text{-BuLi}$ at -78°C in THF , followed by addition of tri-n-butyltin chloride. 9,9-Didecyl-7-iodo-2-nitrofluorene and 2-(tri-n-butylstannyl)benzothiazole were subjected to Stille coupling with either tetrakis(triphenylphosphine)palladium (0) or dichlorobis(triphenylphosphine)palladium (II) in toluene at 110°C under Ar , providing 2-(9,9-didecyl-7-nitrofluorene-2-yl)benzothiazole in 61% yield. Quantitative reduction of 2-(9,9-didecyl-7-nitrofluorene-2-yl)benzothiazole with NH_2NH_2 and 10% Pd/C in EtOH/THF at 70°C produced 7-benzothiazol-2-yl-9,9-didecylfluorene-2-ylamine in 30% overall yield from fluorene.

SYNTHESIS OF 7-BENZOTHAZOL-2-YL-9,9-DIDECYLFLUORENE-2-YLAMINE: A VERSATILE INTERMEDIATE FOR A NEW SERIES OF TWO PHOTON ABSORBING MATERIALS & THREE NOVEL TPA DYES

Katherine J. Schafer

Introduction

Multiphoton absorption can be defined as a simultaneous absorption of two or more photons via virtual states in a medium.¹ The process requires high peak power which is available from pulsed lasers. Even though multiphoton processes have been known for some time, materials that exhibit a multiphoton absorption have yet to find widespread application. The discovery of multifunctional organic materials with large multiphoton absorption cross sections has spawned a new area of research in the photonic and biophotonic fields. In particular, two photon pumped upconverted fluorescence (Figure 1) has enormous implications for multiphoton absorption-induced optical power limiting, curing of polymeric materials, stereolithography, fabrication of microelectromechanical devices, and nondestructive imaging of coating and composite interfaces.

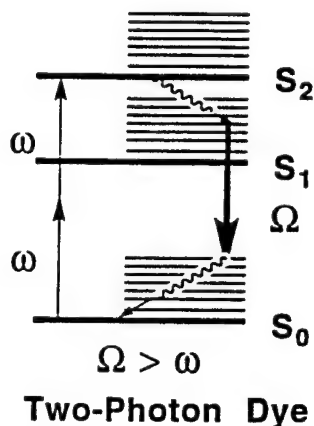


Figure 1. Illustration of upconverted fluorescence via two photon absorption.

Polymers for Optical Limiting

The optical response of an ideal optical power limiter is shown in Figure 2. The ideal optical limiter is completely transparent at low light intensities until a certain intensity level is reached. Above this threshold, the transmitted intensity remains at a constant value. Most current materials available for photonic and biophotonic applications suffer from speed, concentration, phase separation, or solubility problems. To overcome shortcomings of current materials, new, efficient two photon-absorbing chromophores could be covalently attached to polymers, affording good film forming materials which can be fabricated in a variety of configurations.

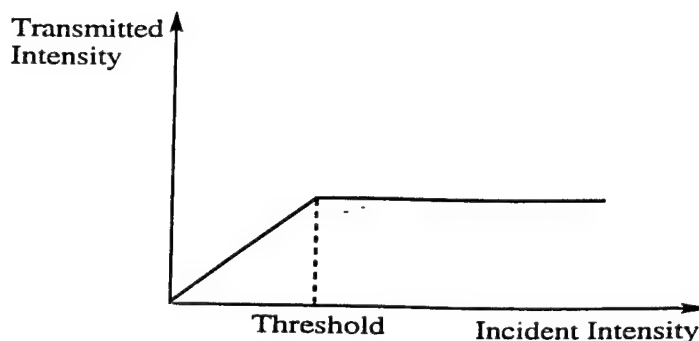


Figure 2. The optical response of an ideal optical power limiter.

Multiphoton Microscopic Fluorescence Imaging

Two photon induced fluorescence has been coupled with laser scanning microscopy to probe surfaces.² The major advantage of this method over single photon scanning is that the fluorescence intensity of a two photon process is quadratically dependent on the illumination intensity. This makes the fluorescence emission limited to the vicinity of the focal point and, hence, it is possible to achieve depth discrimination. Multiphoton confocal laser scanning microscopy could be a useful, nondestructive tool to study surfaces, interfaces, and fractures in polymer or glass specimens. Recently, fractures in polymer samples and polymer coatings layers (Figure 3) were imaged by this technique.³ The images were of a methacrylate polymer matrix containing organic fluorophores. Two photon multichannel confocal microscopy was demonstrated to be useful to probe and construct images of these multilayered coatings. In principle, the dye can be covalently attached to a monomer, hence be permanently and uniformly incorporated into a polymer at high concentrations.

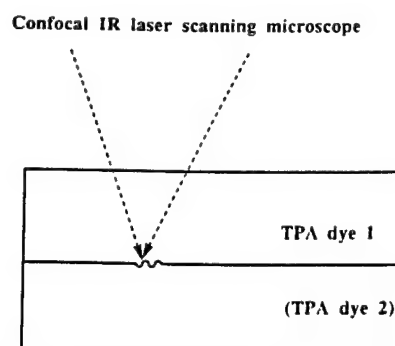


Figure 3. Interfacial imaging of coatings using two photon absorbing (TPA) coatings and confocal laser scanning microscopy.

Two Photon Curing

In many cases, thermal curing of monomers is impractical due to the size or nature of the composite, sealant, or adhesive structure, e.g., damaged aircraft parts or seams between panels. Moreover, photocuring is impractical for large objects because of the limited absorption depth of UV light. Two photon pumped upconverted fluorescence has potential for 3-D or spatially resolved photoinitiated polymerization, particularly in composites, adhesives, and sealant applications. For example, if an IR absorbing two photon dye is used, IR radiation could be used to induce two photon absorption of the dye, followed by subsequent emission of a visible photon. The visible photon could be absorbed by a photoinitiator, as illustrated in Figure 4. The two

photon absorption and fluorescence emission can be tuned by varying the molecular structure of the dye. Hence, IR radiation can be used to facilitate visible-initiated polymerization. The deep penetration of IR radiation could, potentially, be exploited to achieve deep curing of monomers, for example, in obstructed cracks and seals. With utilization of a confocal configuration, true three-dimensional (stereolithographic) and near isotropic polymerization should be possible. A logical next step would be the synthesis of monomers bearing two photon dyes and demonstration of their two photon-induced polymerization.

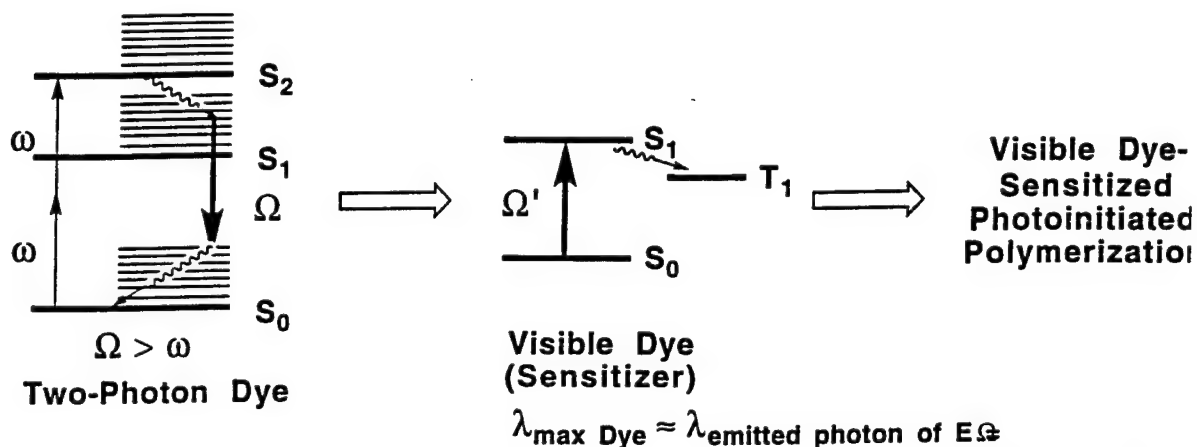


Figure 4. Schematic illustration of two photon absorption, fluorescence emission, one photon absorption, and photoinitiated polymerization.

Fluorene-based Two Photon Absorbing Chromophores

Recently, Reinhardt *et al.*⁴ have prepared and characterized a number of asymmetric fluorene-based dyes that exhibit two photon absorption at 800 nm. The dyes are comprised of a polarizable π electron bridge flanked by an arylamine π electron donor functionality and a heteroarylamine π electron donor functionality and a heterocyclic π electron accepting moiety, as illustrated in Figure 5. In general, large two photon absorption cross sections are realized in such systems with strong electron-donating functionality conjugated effectively with strong electron-withdrawing functionality. Thus, the π electron bridge should be planar to facilitate effective conjugation, a condition fulfilled sufficiently well by the fluorene framework.

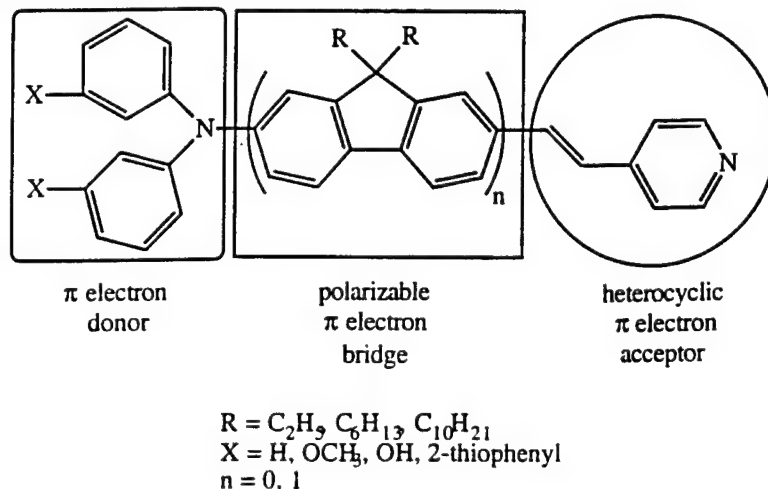


Figure 5. Generic structure of asymmetric fluorene-based chromophore.

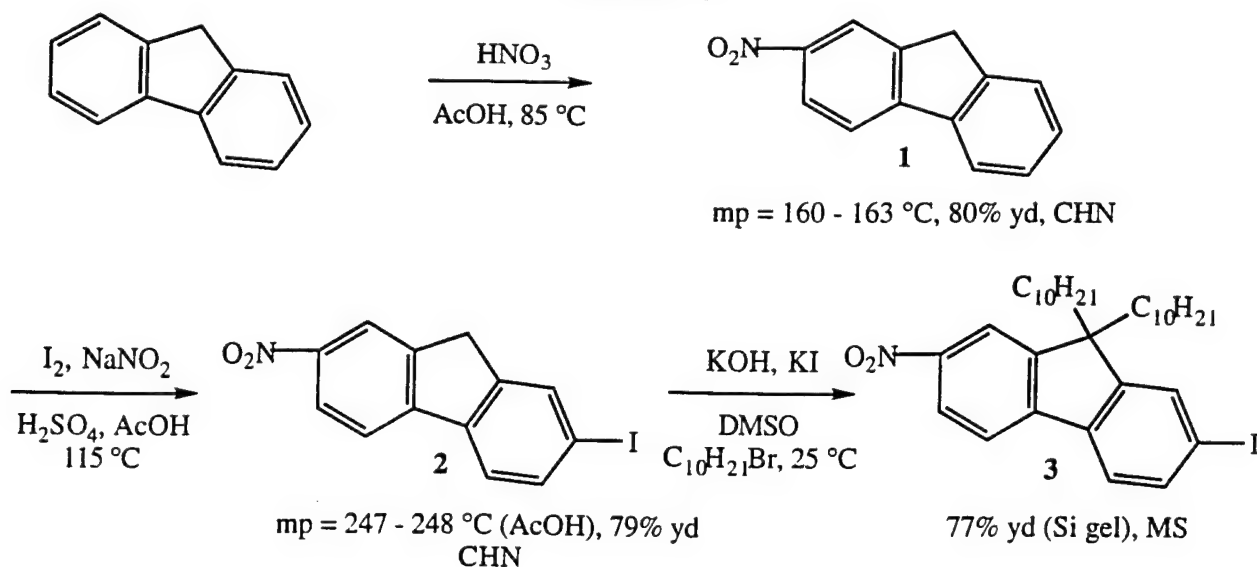
Objectives

The aim this summer was to synthesize a versatile intermediate which possessed the fluorene π electron bridge, electron-donating amine functionality, and electron-withdrawing benzothiazole moiety. In addition, long alkyl groups at the 9-position of the fluorene ring system will be incorporated to impart solubility, inhibit aggregation and crystallization, and, in suitable derivatized compounds, lead to the formation of amorphous glasses. The synthesis should be efficient, allowing for ready and economical scale-up. Functionalization of the intermediate will provide novel two photon absorbing materials. 7-Benzothiazol-2-yl-9,9-didecylfluorene-2-ylamine (**6**) was designed and selected to be the target intermediate. In addition, three novel two photon absorbing dye motifs were designed to be prepared straight away from the versatile intermediate **6**.

Results and Discussion

Two versatile fluorene-based intermediates, 7-iodo-9,9-didecyl-2-nitrofluorene (**3**) and 7-benzothiazol-2-yl-9,9-didecylfluorene-2-ylamine (**6**), were prepared in a relatively efficient multistep synthesis from readily available fluorene (Schemes 1, 5, and 6). The synthesis and characterization of these intermediates are discussed below, as are the preparations of three derivatives (**8**, **10**, and **11**) which should serve as two photon absorbing dye candidates.

Scheme 1

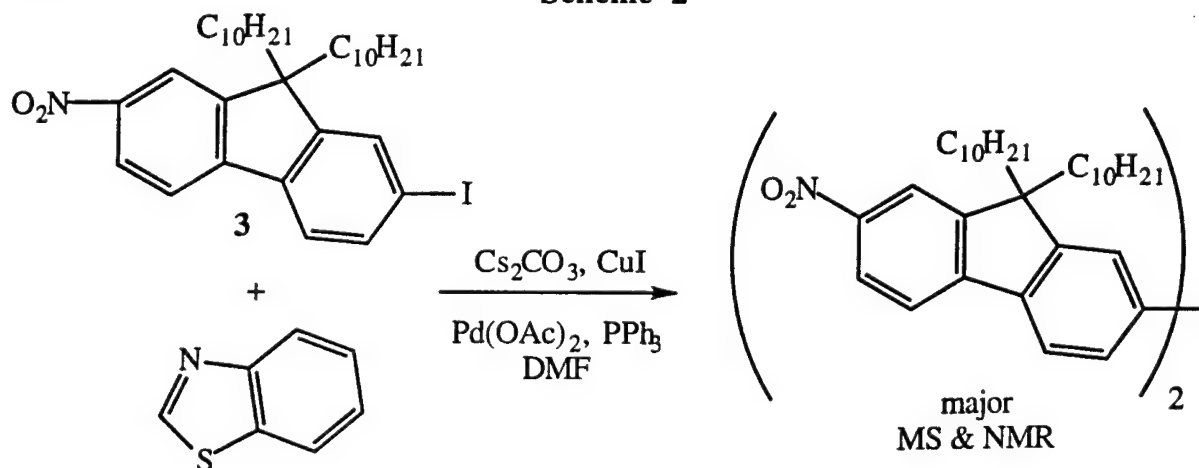


2-Nitrofluorene (**1**) was prepared in 80% yield by regiospecific nitration of fluorene with nitric acid in AcOH at 85°C . The melting point ($160\text{--}163^\circ\text{C}$) was comparable with the literature value (157°C),⁵ while CHN analyses were in accord with calculated values. The next step in the multistep synthesis involved regiospecific iodination of 2-nitrofluorene with iodine, sodium nitrite, AcOH and H_2SO_4 at 115°C , affording 7-iodo-2-nitrofluorene (**2**) in 77% yield after recrystallization from AcOH. Again, the melting point ($245\text{--}246^\circ\text{C}$) was consistent with the literature value ($244\text{--}245^\circ\text{C}$),⁶ while CHN analyses were in good agreement with calculated values. Dialkylation of **2** was accomplished by generation of the fluorenyl anion with KOH in DMSO and subsequent alkylation with 1-bromodecane in the presence of KI at room temperature.⁴ 7-Iodo-9,9-didecyl-2-nitrofluorene (**3**) was obtained as a yellow solid in 77% isolated yield, after column chromatography. MS analysis and ^1H NMR confirmed formation of

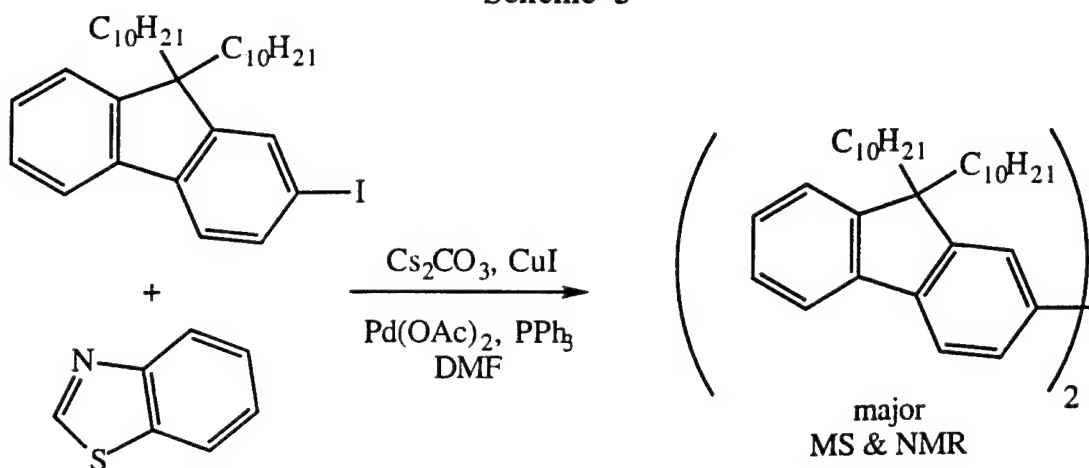
the desired product.

Next was formation of 2-(9,9-didecyl-7-nitrofluoren-2-yl)benzothiazole (**5**) from 7-iodo-9,9-didecyl-2-nitrofluorene (**3**). Although conversion of the iodide to carboxaldehyde, followed by condensation with 2-aminothiophenol was a "stand by" option, it was desirable to develop a more expeditious, direct synthetic method for the conversion of **3** to **5**. A direct coupling reaction,⁷ mediated by Pd(OAc)₂, CuI, PPh₃, and Cs₂CO₃, was attempted between **3** and benzothiazole (Scheme 2). Surprisingly, a nitrofluorene dimer was isolated as a yellow crystalline solid as the major product, as confirmed by MS and ¹H NMR. To probe what effect the nitro group may have on the reaction, 9,9-didecyl-2-iodofluorene (prepared from decylation of 2-iodofluorene) was subjected to Pd-catalyzed coupling with benzothiazole. Consistent with the nitro analog, 9,9-didecyl-2-iodofluorene underwent reaction to form, predominantly, the dimer, as illustrated in Scheme 3.

Scheme 2



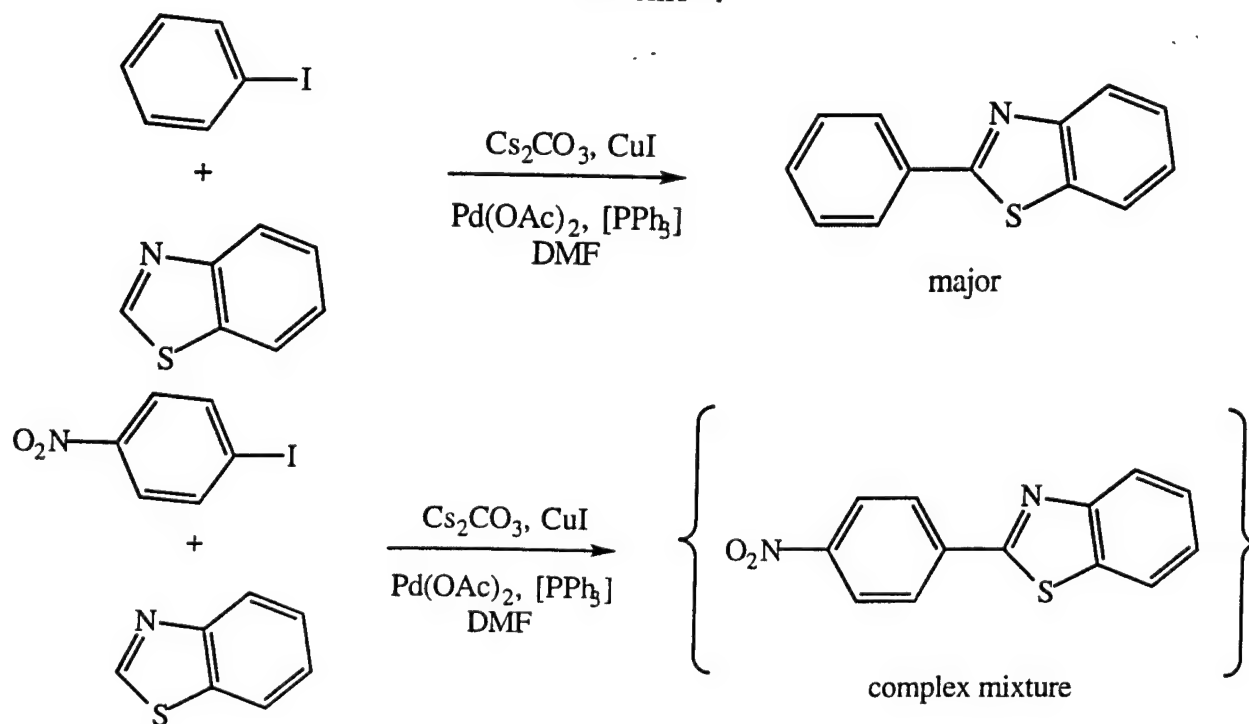
Scheme 3



To further assess the feasibility of the direct coupling, the reported example was carried out.⁷ Thus, iodobenzene was reacted with benzothiazole (Scheme 4), mediated by Pd(OAc)₂, CuI, and

Cs_2CO_3 , both in the presence and absence of PPh_3 (in one experiment tri-*o*-tolylphosphine was employed). In all cases, the expected coupling product, 2-phenylbenzothiazole, was secured. A similar set of experiments were conducted with 4-iodonitrobenzene, resulting in a complex mixture of products (by TLC). Hence, the direct coupling strategy was abandoned.

Scheme 4

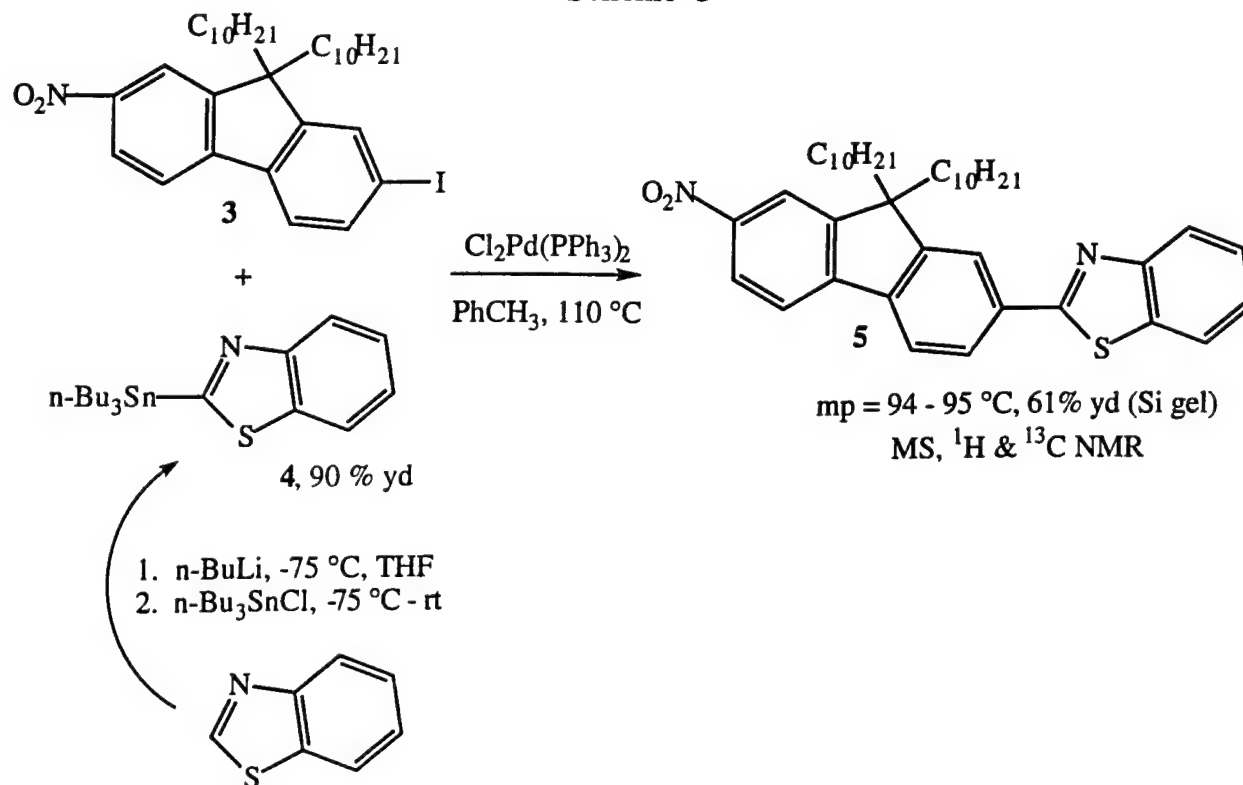


Finally, a Stille coupling procedure was devised to prepare **5**, as illustrated in Scheme 5. (2-Tri-*n*-butylstannyl)benzothiazole (**4**) was prepared in 90% yield by treating benzothiazole with *n*-BuLi in THF at -75°C , followed by addition of tri-*n*-butyl tin chloride.⁸ Pd-catalyzed coupling was then performed between **4** and 7-iodo-9,9-didecyl-2-nitrofluorene (**3**) in refluxing toluene with either tetrakis(triphenylphosphine)palladium (0) or dichlorobis(triphenylphosphine)palladium (II).⁹ 2-(9,9-Didecyl-7-nitrofluoren-2-yl)benzothiazole (**5**) was obtained as yellow crystals in 61% yield, after column chromatographic purification ($\text{mp} = 94 - 95^\circ\text{C}$). Clearly evident in the IR spectrum were absorptions attributable to asymmetric and symmetric NO_2 stretching vibrations at 1519 and 1337 cm^{-1} , respectively. Also present was the benzothiazole $\text{C}=\text{N}$ stretching vibration at 1589 cm^{-1} . Nitro analog **5** exhibited a UV-visible absorption ranging from 220 to 420 nm with $\lambda_{\text{max}} = 365\text{ nm}$. The diagnostic ^{13}C NMR resonance of the carbon in the 2-position in the benzothiazole ring was present at 168 ppm .¹⁰

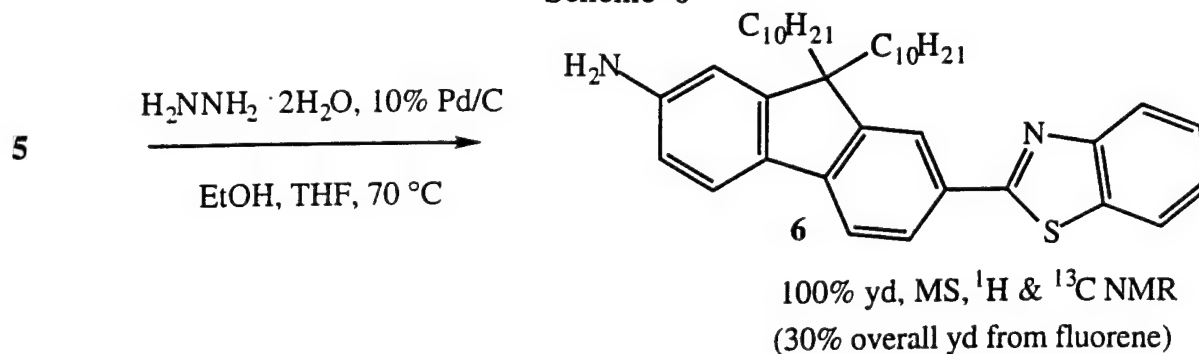
Fast, quantitative reduction of **5** was achieved using hydrazine hydrate¹¹ and 10% Pd/C in a 1:1 mixture of EtOH and THF at 70°C (Scheme 6), providing 7-benzothiazol-2-yl-9,9-didecylfluorene-2-ylamine (**6**) as a bright yellow sticky, viscous oil. As expected, **6** exhibited a 15 nm bathochromic shift in its UV-visible spectrum relative to **5** ($\lambda_{\text{max}} = 380\text{ nm}$, ranging from $210 - 450\text{ nm}$). Characteristic stretching absorptions were observed in the IR spectrum for NH_2 (3741 and 3383 cm^{-1}) and benzothiazole $\text{C}=\text{N}$ (1603 cm^{-1}). MS and ^1H NMR provided

additional confirmation of structure. Conclusive proof of structure was garnered by the anticipated upfield shift in the ^{13}C NMR of carbons *ortho* and *para* to the amine in the fluorene ring of **6**. *Ortho*-carbons 3 and 1 were observed at 109.8 and 114.3 ppm, respectively, compared to the corresponding carbons in **5** at 118.6 and 122.0 ppm, respectively. Even more pronounced was the chemical shift of *para*-carbon 11 of **6** at 125.0 ppm relative to that of **5** at 147.9 ppm. Amine **6** displayed a brilliant blue fluorescence in solution upon radiation with long wavelength UV radiation.

Scheme 5

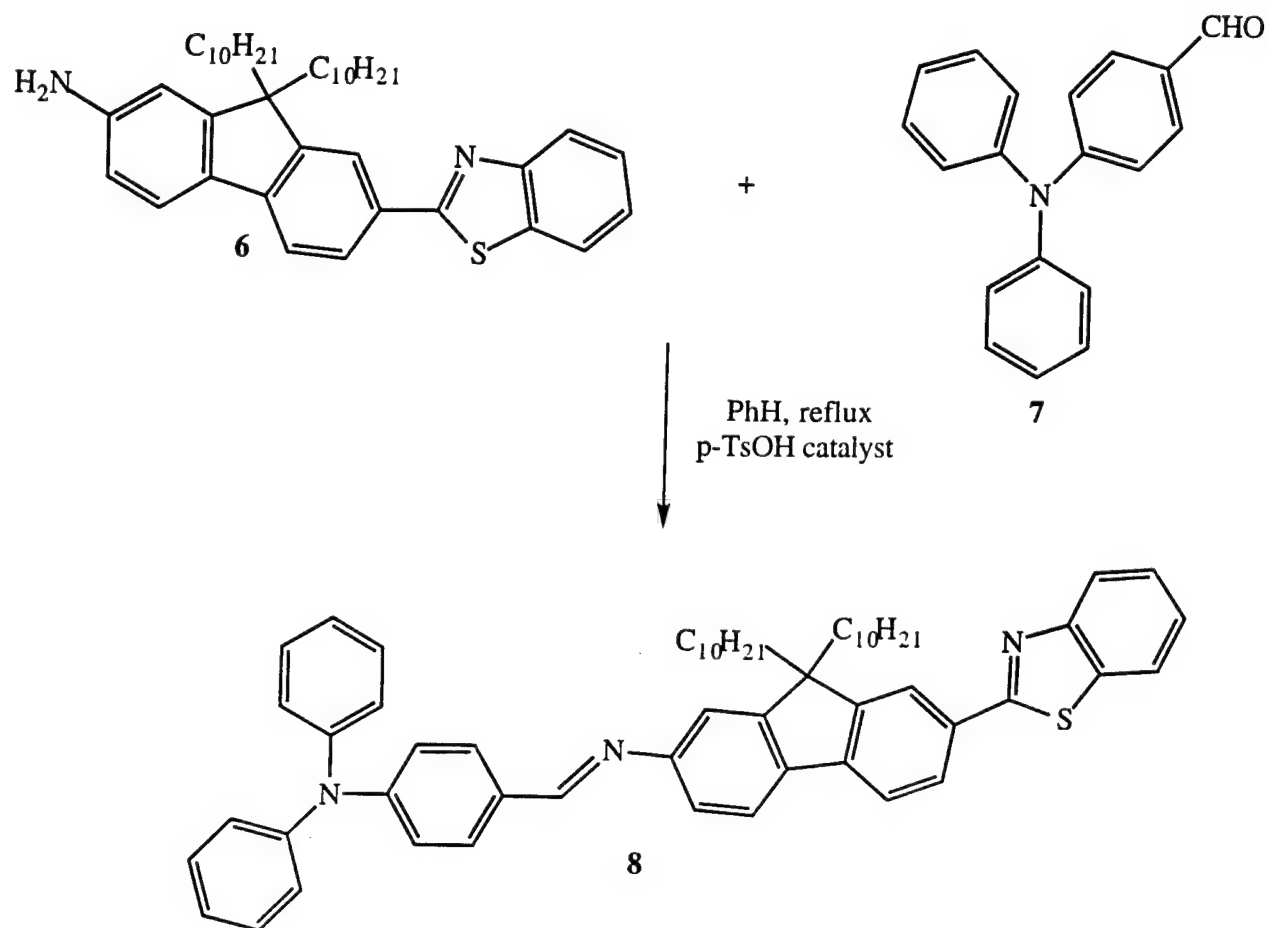


Scheme 6



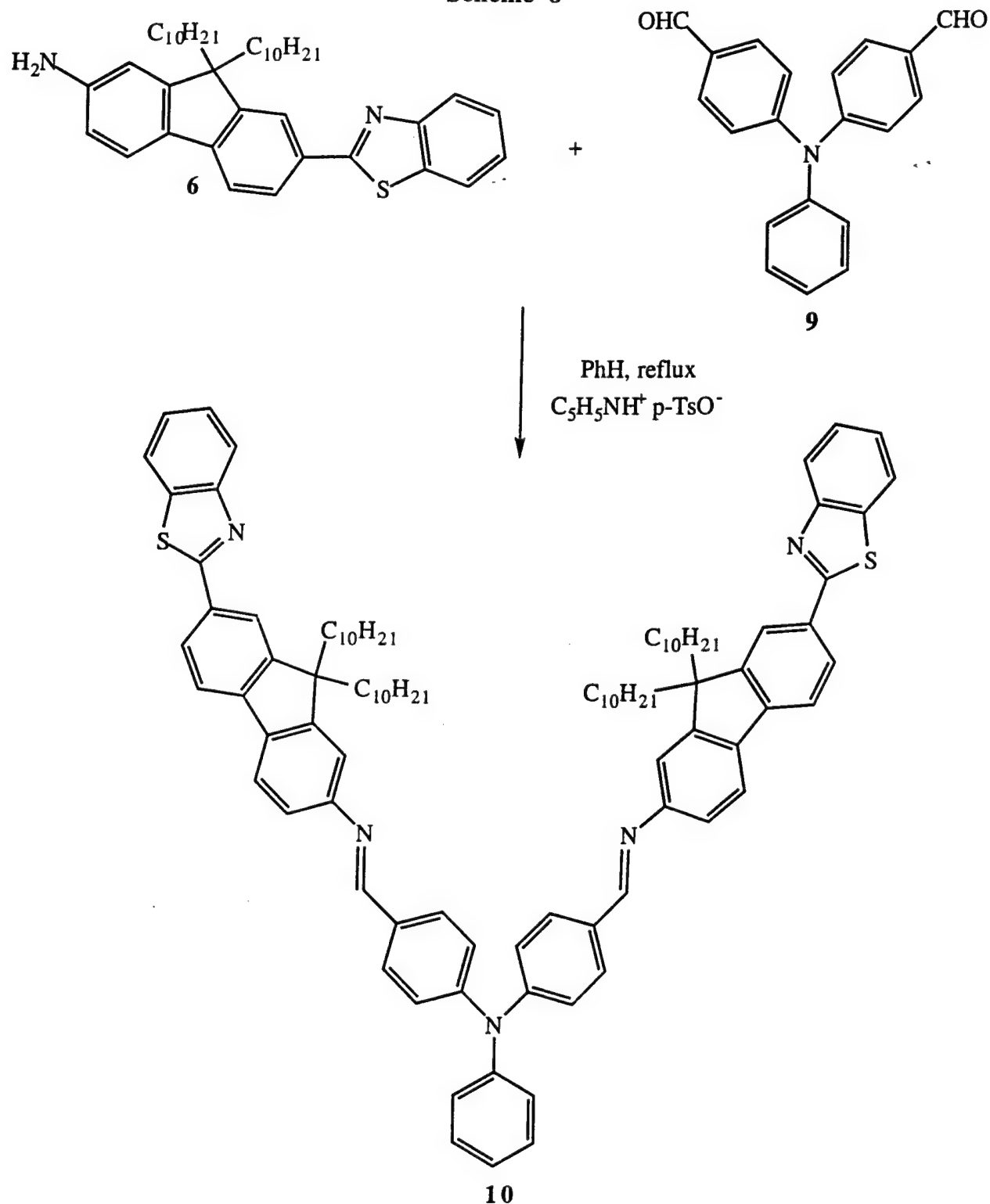
Derivatization of amine **6** was executed with three substrates, resulting in three new chromophores. First, p-TsOH-catalyzed condensation of **6** with 4-(N,N-diphenylamino)benzaldehyde (**7**, triphenylamine carboxaldehyde, prepared by Vilsmeier bisformylation of triphenylamine)¹² afforded the 4-(N,N-diphenylamino)benzaldehyde/7-benzothiazol-2-yl-9,9-didecylfluorene-2-ylamine azomethine dye (**8**) as a bright yellow solid (Scheme 7).

Scheme 7



In similar fashion, **6** underwent pyridinium toluene sulfonate-catalyzed condensation with triphenylamine biscaldehyde (**9**),¹² prepared by Vilsmeier bisformylation of triphenylamine, as depicted in Scheme 8. Triphenylamine biscaldehyde/7-benzothiazol-2-yl-9,9-didecylfluorene-2-ylamine azomethine dye (**10**) was produced as a bright orange solid.

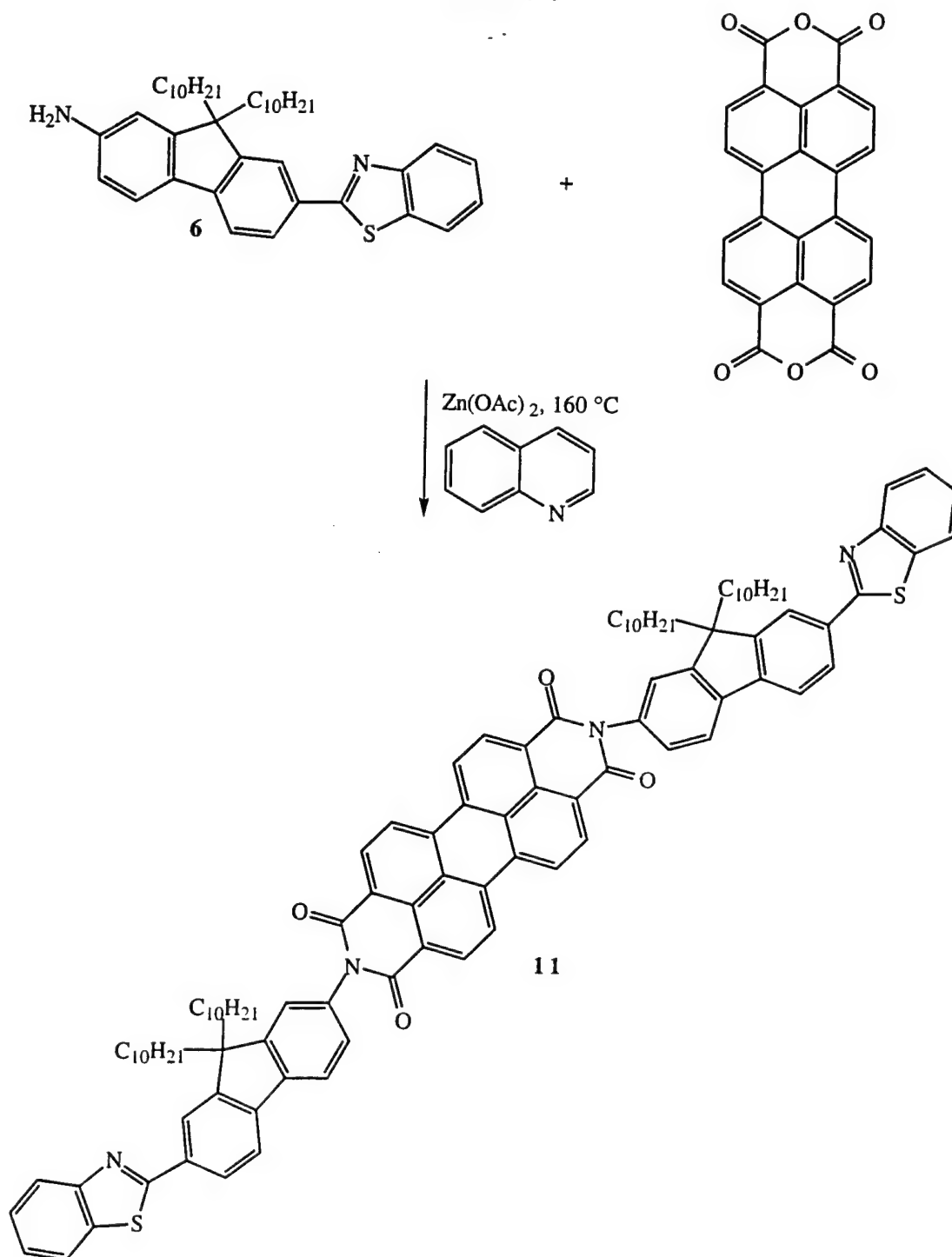
Scheme 8



In an attempt to synthesize a longer wavelength absorbing dye, **6** was subjected to $Zn(OAc)_2$ -catalyzed condensation imidization with 3,4,9,10-perylenetetracarboxylic dianhydride (Scheme 9).¹³ The 3,4,9,10-perylenetetracarboxylic dianhydride/7-benzothiazol-2-yl-9,9-didecylfluorene-

2-ylamine imide dye (**11**) was formed as a deep red-pink solid, after column chromatographic purification. Azomethine dye (**11**) exhibited two strong, broad absorption bands, one in the UV from 270 to 385 nm ($\lambda_{\text{max}} = 345$ nm) and another in the visible from 410 to 545 nm with λ_{max} at 457, 486, and 522 nm.

Scheme 9

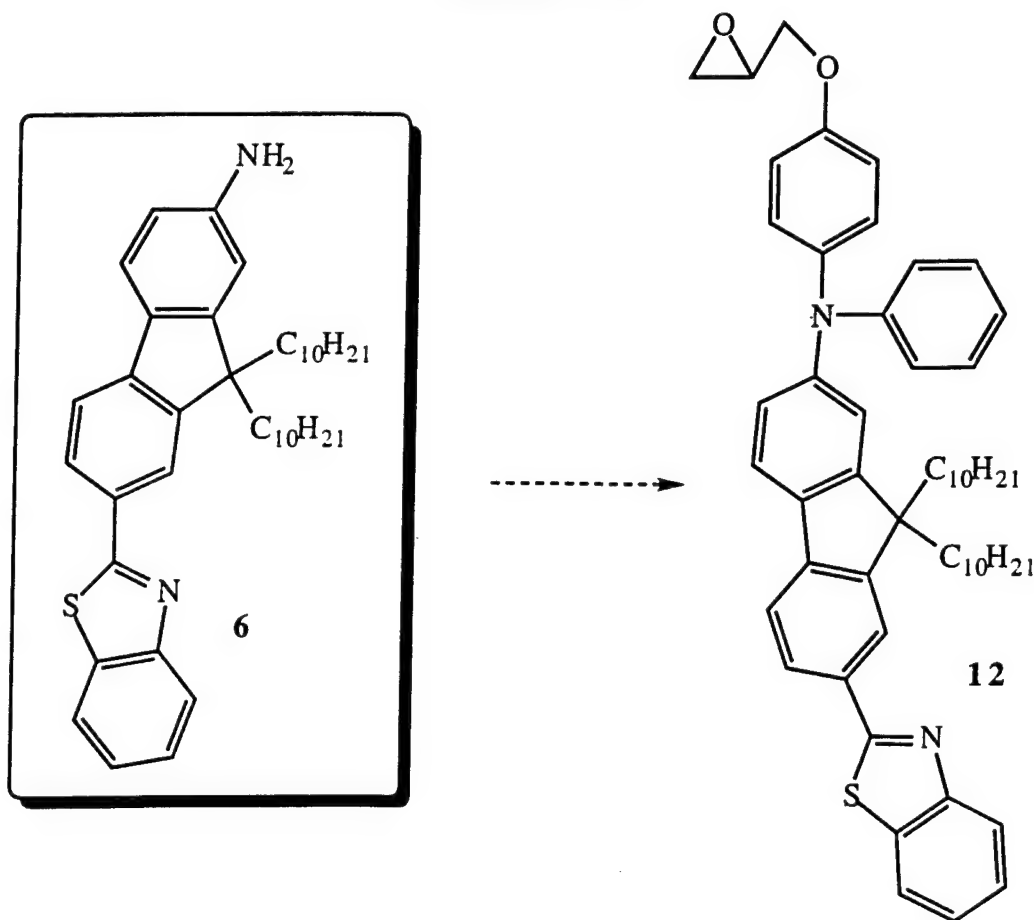


Conclusions

An efficient synthesis of two key intermediates (**3** and **6**) for the creation of new two photon absorbing dyes was accomplished, starting from readily available fluorene. All intermediates were fully characterized, including mp, UV-vis, FT-IR, MS, elemental analysis, ^1H and ^{13}C NMR, photoluminescence (fluorescence emission). Three novel dyes (**8**, **10**, and **11**), with varying UV-vis and fluorescence emission spectral characteristics, were prepared from the penultimate product **6** in good yield. A remarkable feature of these materials is their excellent solubility in common organic solvents, an important criterion for processing and potential device fabrication.

The efficient synthesis of aminofluorene **6** and iodofluorene **3** has opened the possibility of creating a diverse range of nonlinear optical, including multiphoton absorbing, materials, both low molar mass and polymeric. Work is underway to synthesize an epoxy derivative of **6** (Scheme 10) that will be copolymerized with an optical grade epoxide to produce a polymeric material for optical power limiting expected to have a high laser damage threshold. Importantly, monomer **12** will be a key component in two photon curing experiments to be performed in my laboratory at the University of Central Florida, in which it will serve as the two photon dye, providing upconverted fluorescence for absorption by a visible photoinitiator. Since it will then be covalently bound to the resulting polymer, it can also serve as a chromophore for subsequent two photon fluorescence imaging.

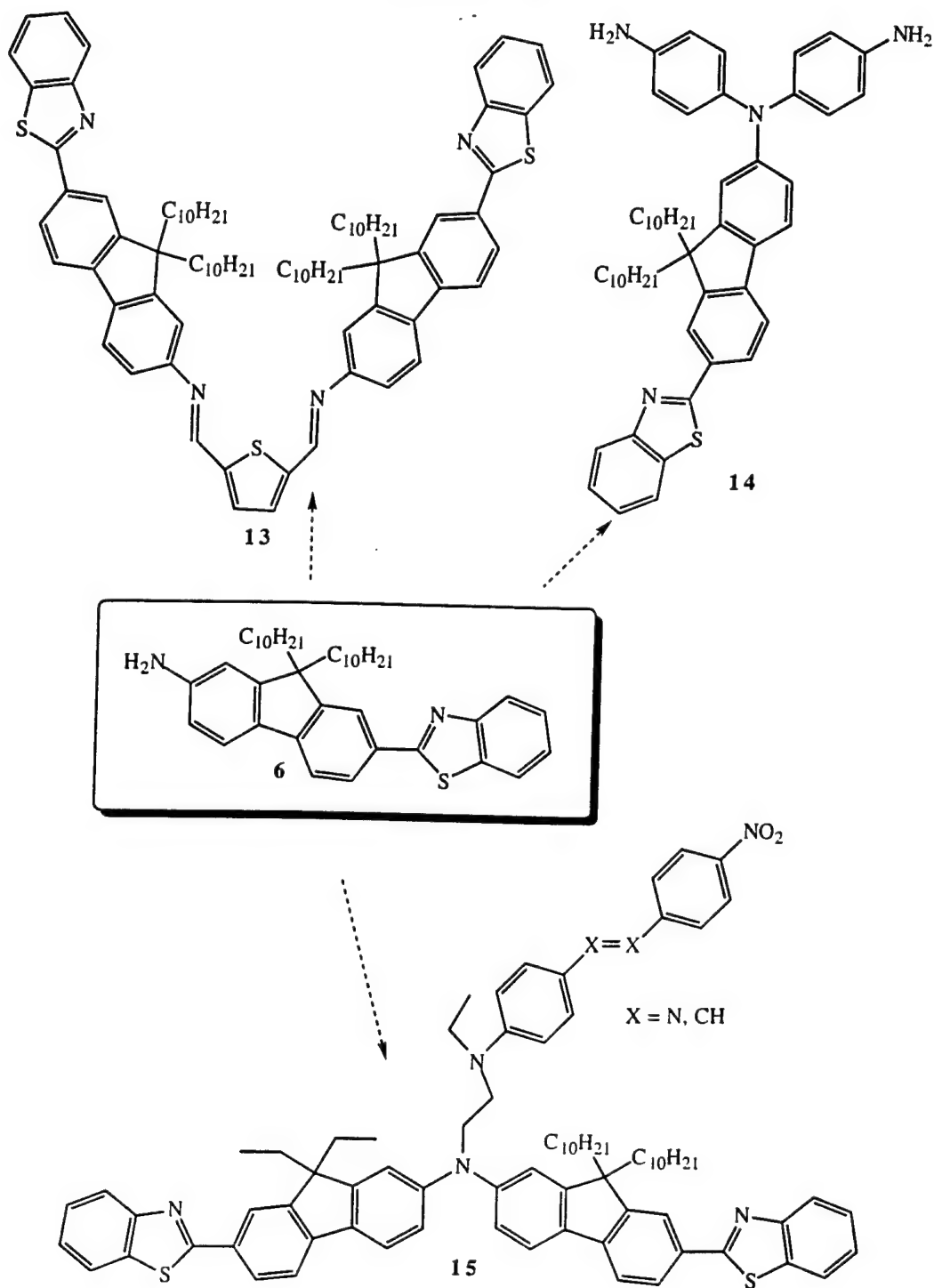
Scheme 10



Since the amine functionality of **6** can be readily functionalized, two photon absorbing dyes can be prepared whose absorption and emission properties are tailored through judicious choice of

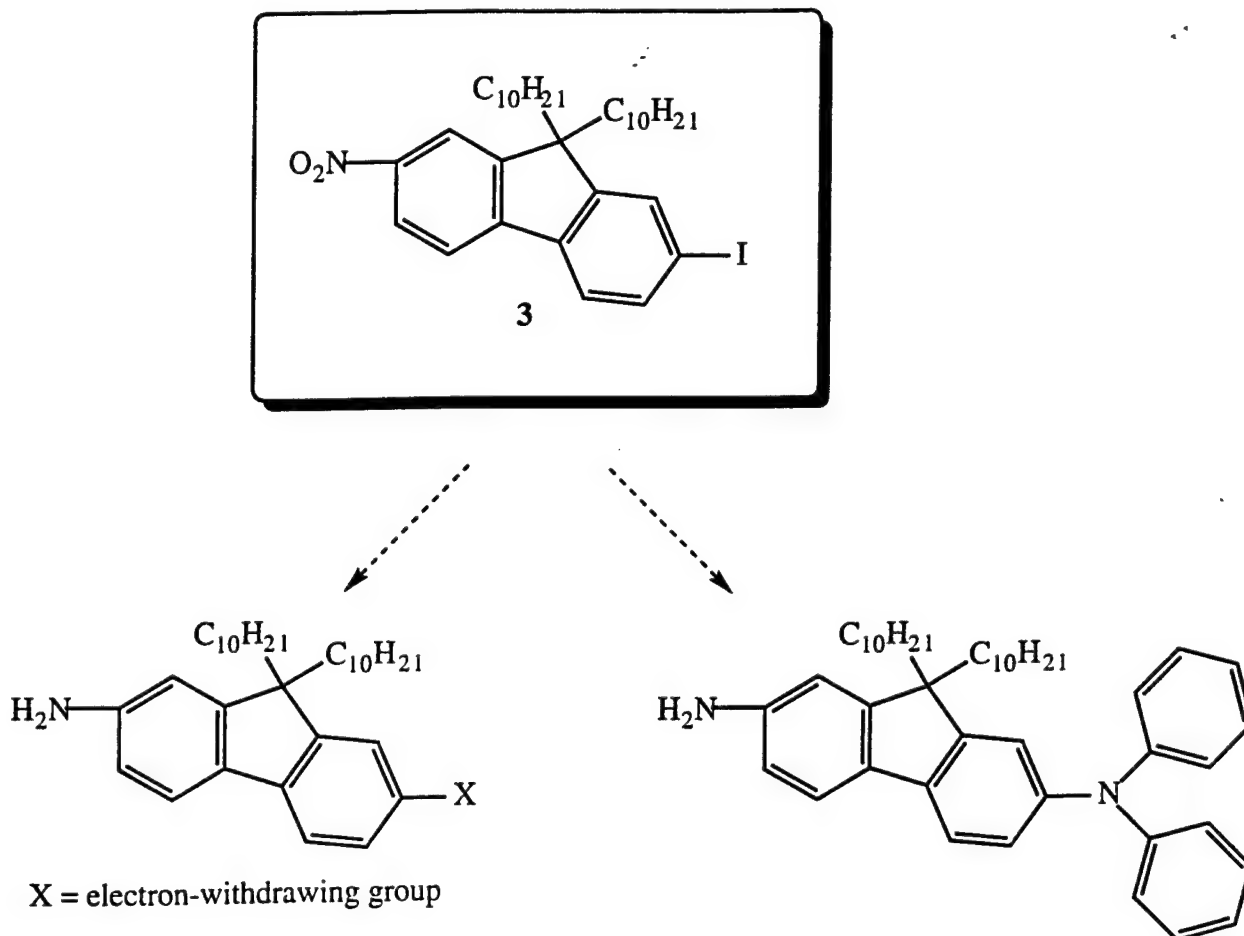
derivatization constructs (see e.g., Scheme 11). Future plans include preparation of a thiophene-based Schiff base with extended conjugation (**13**), a diamine (**14**) for the preparation of high thermal stability polyurethanes and polyimides for optical limiting, and a multifunctional compound (**15**) bearing two photon absorbing chromophores and a donor/acceptor NLO chromophore capable of being poled.

Scheme 11



Iodo derivative **3** will also serve as a key intermediate, as this can also be functionalized to provide access to wide range of multiphoton absorbing materials. A few of these possibilities are presented in Scheme 12, including conversion of the iodo functionality to either electron-withdrawing or electron-donating moieties, a compelling testament to the versatility of **3**.

Scheme 12



Experimental

General. Reactions were conducted under N_2 or Ar atmospheres. Benzothiazole was distilled under reduced pressure prior to use. THF was distilled over sodium before use. All other reagents and solvents were used as received from commercial suppliers. ^1H and ^{13}C NMR were recorded in CDCl_3 on Bruker AM-200 or Varian 300 NMR spectrometers, at 200 and 300 MHz, respectively, for ^1H (referenced to TMS at $\delta = 0.0$ ppm), and at 50 and 75 MHz, respectively, for ^{13}C (referenced to CDCl_3 at $\delta = 77.3$ ppm). UV-visible spectrophotometric measurements were recorded on a Hewlett-Packard Model 8453A spectrophotometer. Elemental analyses and MS analyses were performed at Wright-Patterson Air Force Base Materials Laboratory.

Synthesis of 2-nitrofluorene (1). Fluorene (60 g, 361 mmol) and 500 mL AcOH were heated, under N_2 , to 85°C in a 1 L 3-necked flask fitted with a mechanical stirrer, addition funnel, and thermometer. HNO_3 was added over 20 min via an addition funnel, maintaining the

temperature at 85 °C. The reaction mixture was allowed to cool to room temperature over 2 h, resulting in a yellow suspension. This was filtered, washed with 50 mL AcOH containing 1.3 g KOAc, then slurried in water and filtered. The yellow product was dried in a vacuum oven, affording 60.5 g (80% yield); mp = 160 - 163 °C (lit. 157 °C⁵). Anal. Calcd: 73.92% C, 4.29% H, 6.63% N; Found: 73.72% C, 3.72 % H, 6.52% N.

Synthesis of 7-iodo-2-nitrofluorene (2). 2-Nitrofluorene (6.4 g, 30 mmol) and 200 mL AcOH were stirred at room temperature in a 500 mL 3-necked flask fitted with N₂ inlet, condenser, stir bar, and stopper. I₂ (3.74 g, 14.7 mmol) was added and stirred for 20 min. An orange-brown liquid formed with some undissolved starting material remaining suspended. H₂SO₄ (20 mL) and 2.2 g NaNO₂ were then added, and the reaction mixture was heated to 115 °C for 1 h. Yellow precipitate formed. The suspension was cooled to room temperature and poured into 200 g ice, filtered, washed with water, and dried in a vacuum oven. The crude product (9.51 g) was recrystallized from AcOH (1200 mL), resulting in 8.0 g (79% yield) of yellow needles (mp = 245 - 246 °C, lit. 244-245 °C⁶). Anal. Calcd: 46.32% C, 2.39% H, 37.64 % I, 4.15% N; Found: 46.37% C, 2.18 % H, 37.96% I, 3.94% N. MS (EI, 70 eV) m/z: 337 (M+).

Synthesis of 7-iodo-9,9-didecyl-2-nitrofluorene (3). 7-Iodo-2-nitrofluorene (9.6 g, 28 mmol), 12.58 g 1-bromodecane (57 mmol), 0.49 g KI (3 mmol), and 65 mL DMSO were placed in a 250 mL 3-necked flask containing a stir bar at room temperature. Powdered KOH (6.65 g, 119 mmol) was slowly added via a solid addition funnel under N₂. The color of the reaction mixture changed from bright yellow to dark green immediately after addition of the KOH. TLC analysis (10:1 hexanes/EtOAc) indicated dialkylation was complete after 1 h. The reaction mixture was poured into H₂O and extracted with hexanes. The organic extract was washed with H₂O, dried over MgSO₄, and concentrated, affording 16.5 g of a viscous dark orange oil that crystallized on standing. Purification was accomplished by column chromatography (40:1 hexanes/EtOAc), providing 13.6 g of yellow solid (77% yield). MS (EI, 70 eV) m/z: 617 (M+); 477 (M - C₁₀H₂₀); 476 (M - C₁₀H₂₁); 350 (M - C₁₉H₄₀); 336 (M - C₄₀H₄₁); 85 (C₆H₁₃+); 71 (C₅H₁₁+); 57 (C₄H₉+); 43 (C₃H₇+). ¹H NMR (300 MHz, CDCl₃) δ: 8.25 (d, 1H, ArH), 8.18 (d, 1H, ArH), 7.79 (s, 1H, ArH), 7.72 (m, 2H, ArH), 7.53 (d, 1H, ArH), 1.99 (m, 4H, CH₂), 1.18 (bm, 14H, CH₂), 1.05 (bm, 14H, CH₂), 0.83 (t, 6H, CH₃), 0.56 (m, 4H, CH₂)

Synthesis of 2-(tri-n-butylstannyl)benzothiazole (4). Benzothiazole (20 g, 148 mmol) was dissolved in 150 mL dry THF and cooled to -75 °C in a 500 mL 3-necked flask, containing a stir bar and fitted with a low temperature thermometer, addition funnel, and N₂ inlet. n-BuLi (111 mL 1.6 M in hexanes) was slowly added, over 50 min, via the addition funnel, maintaining the temperature <-65 °C. During this time the reaction mixture turned from orange to brown. Tri-n-butyltin chloride (58 g, 178 mmol) was added slowly via the addition funnel, maintaining the temperature <-60 °C. The dark green reaction mixture turned yellow. After addition was complete, the reaction mixture was allowed to slowly warm to -20 °C, at which time it turned green again. It was then stirred at -10 °C for 1 h and turned yellow again. A solution of 100 mL of 3 wt% KF(aq) was added and stirred at 10 °C for 1 h. The layers were separated, in the presence of a ubiquitous polymeric gel. The organic phase was diluted with toluene, dried over MgSO₄, filtered, and concentrated. An orange-brown liquid resulted which was purified by vacuum distillation (bp 155-158 °C/0.2 mmHg, lit. 144-146 °C/0.15 mmHg). A yellow liquid was collected (56.3 g, 90% yield).

Synthesis of 2-(9,9-didecyl-7-nitrofluoren-2-yl)benzothiazole (5). 7-Iodo-9,9-didecyl-2-nitrofluorene (10.1 g, 16 mmol) and 8.5 g 2-(tri-n-butylstannyl)benzothiazole (20 mmol) were dissolved in 200 mL toluene and degassed under vacuum and Ar. $\text{Pd}(\text{PPh}_3)_4$ (0.47 g, 0.4 mmol) was added and degassed. The reaction mixture was heated to 110 °C under Ar. The reaction was monitored by TLC (10:1 hexanes/EtOAc) and found to be complete after about 4.5 h (reaction mixture turned black). The toluene was removed *in vacuo*, and the resulting dark orange oil was passed through a Si gel column, eluting with hexanes. An orange solid formed which was recrystallized from hexanes, affording 6.24 g of bright yellow crystals (61% yield, mp = 94-95 °C). MS (EI, 70 eV) m/z: 624 (M⁺); 497 (M - C₉H₁₉); 483 (M - C₁₀H₂₁); 357 (M - C₁₉H₃₉); 343 (M - C₂₀H₄₁); 311 (M - C₂₀H₄₃ - NO); 297 (M - C₂₀H₄₁ - NO₂); 71 (C₅H₁₁⁺); 57 (C₄H₉⁺); 43 (C₃H₇⁺). UV-vis (THF): λ_{max} = 365 nm (220 - 420 nm); ¹H NMR (200 MHz, CDCl₃) δ : 8.32, 8.37 (dd, 1H, ArH), 8.24, 8.18 (dd, 1H, ArH), 8.14 (m, 1H, ArH), 8.10 (m, 1H, ArH), 7.96, 7.92 (dm, 1H, ArH), 7.91, 7.88 (dd, 1H, ArH), 7.87, 7.84 (dd, 1H, ArH), 7.57, 7.38 (dd, 1H, ArH), 7.53, 7.42 (dm, 1H, ArH), 7.49, 7.46 (dd, 1H, ArH), 2.14 (m, 4H, CH₂), 1.14 (bm, 14H, CH₂), 1.04 (bm, 14H, CH₂), 0.81 (t, 6H, CH₃), 0.62 (m, 4H, CH₂); ¹³C NMR (50 MHz, CDCl₃) δ : 168.0 (C2), 154.4 (C9), 153.4 (C7'), 152.9 (C13'), 147.9 (C12'), 146.7 (C10'), 141.6 (C11'), 135.3 (C2'), 134.6 (C8), 127.8 (C1'), 127.6 (C5'), 126.7 (C4'), 125.6 (C3'), 123.6 (C6), 123.5 (C5), 122.0 (C8'), 121.8 (C7), 120.6 (C4), 118.6 (C6'), 56.4 (C9'), 40.2 (Ca), 32.0 (Ch), 30.4 (Cc), 30.0 (Cd), 29.7 (Ce,f), 29.4 (Cg), 24.0 (Cb), 22.8 (Ci), 14.3 (Cj); FT-IR (KBr, cm⁻¹): 3066 (ν_{arCH}), 2924, 2852 (ν_{alCH}), 1589 ($\nu_{\text{C=N}}$), 1519 (ν_{NO_2} as), 1337 (ν_{NO_2} sy).

Synthesis of 7-benzothiazol-2-yl-9,9-didecylfluorene-2-ylamine (6). 2-(9,9-Didecyl-7-nitrofluoren-2-yl)benzothiazole (4.0 g, 6.4 mmol) was dissolved in a mixture of 15 mL EtOH and 15 mL THF at room temperature. To this 0.2 g 10% Pd/C was added. The mixture was heated to 70 °C under Ar. Hydrazine hydrate (2 mL, 38 mmol) was added dropwise via syringe over 20 min. The reaction mixture was stirred for 12 h at 70 °C, cooled to room temperature, and concentrated, affording a yellow-green oil. TLC (10:1 hexanes/EtOAc) indicated the reaction was quantitative. Purification was accomplished by passing a hexane solution of the amine through a Si gel plug, eluting with hexanes, providing 3.6 g of viscous, sticky yellow material (95% yield). MS (EI, 70 eV) m/z: 594 (M⁺); 453 (M - C₁₀H₂₁); 327 (M - C₁₉H₃₉); 313 (M - C₂₀H₄₁); 163 (C₁₃H₇⁺); 57 (C₄H₉⁺); 43 (C₃H₇⁺). UV-vis (THF): λ_{max} = 380 nm (210 - 450 nm); ¹H NMR (200 MHz, CDCl₃) δ : 8.09, 8.05 (dm, 1H, ArH), 8.04 (d, 1H, ArH), 7.99, 7.95 (dd, 1H, ArH), 7.90, 7.86 (dm, 1H, ArH), 7.63, 7.59, 7.56, 7.51 (dd, 1H, ArH), 7.51, 7.44, 7.39, 7.32 (dq, 1H, ArH), 7.48, 7.35 (dm, 1H, ArH), 7.19 (m, 1H, ArH), 6.67 (m, 2H, ArH), 3.82 (bs, 2H, NH₂), 1.98 (m, 4H, CH₂), 1.15 (bm, 14H, CH₂), 1.04 (bm, 14H, CH₂), 0.82 (t, 6H, CH₃), 0.66 (m, 4H, CH₂); ¹³C NMR (50 MHz, CDCl₃) δ : 169.3 (C2'), 154.5 (C9'), 153.8 (C2), 150.8 (C10), 147.1 (C13), 145.1 (C12), 131.6 (C7), 130.8 (C8'), 129.2 (C8), 128.4 (C4), 127.3 (C5), 126.4 (C6), 125.0 (C11), 123.0 (C6'), 121.5 (C5'), 121.5 (C7'), 118.8 (C4'), 114.3 (C1), 109.8 (C3), 55.4 (C9), 40.8 (Ca), 32.1 (Ch), 30.4 (Cc), 30.3 (Cd), 29.8 (Ce), 29.7 (Cf), 29.5 (Cg), 24.0 (Cb), 22.8 (Ci), 14.3 (Cj); FT-IR (KBr, cm⁻¹): 3741, 3383 (ν_{NH_2}), 2926, 2855 (ν_{alCH}), 1603 ($\nu_{\text{C=N}}$).

Synthesis of 4-(N,N-diphenylamino)benzaldehyde/7-benzothiazol-2-yl-9,9-didecylfluorene-2-ylamine azomethine dye (8). Condensation of 200 mg 7-benzothiazol-2-yl-9,9-didecylfluorene-2-ylamine (0.34 mmol) and 93 mg 4-(N,N-diphenylamino)benzaldehyde (7) (0.34 mmol) was conducted at reflux in 15 mL benzene with a Dean-Stark trap. After 64 h of reflux, TLC (10:1 hexanes/EtOAc) indicated presence of starting materials and product, hence, ca. 5 mg p-TsOH was added. The reaction mixture immediately turned from bright yellow to deep orange, and water droplets were observed in the condenser. Heating continued for 9 h, after which time the mixture was cooled to room temperature, passed through a Si gel plug (CH_2Cl_2), and concentrated. An orange-yellow oil was obtained (0.39 g).

Synthesis of triphenylamine biscalboxaldehyde/7-benzothiazol-2-yl-9,9-didecylfluorene-2-ylamine azomethine dye (10). Condensation of 1.6 g 7-benzothiazol-2-yl-9,9-didecylfluorene-2-ylamine (2.7 mmol) and 405 mg triphenylamine biscalboxaldehyde (9) (1.3 mmol) was conducted at reflux in 15 mL benzene with a Dean-Stark trap. After 64 h of reflux, TLC (10:1 hexanes/EtOAc) indicated presence of starting materials and product, hence, ca. 10 mg pyridinium p-toluene sulfonate was added. The reaction mixture immediately turned from bright yellow to bright orange, and water droplets were observed in the condenser. Heating continued for 21 h, after which time the mixture was cooled to room temperature, passed through a Si gel plug (CH_2Cl_2), and concentrated. An orange oil was obtained (1.85 g).

Synthesis of 3,4,9,10-perylenetetracarboxylic dianhydride/7-benzothiazol-2-yl-9,9-didecylfluorene-2-ylamine imide dye (11). Condensation of 1.0 g 7-benzothiazol-2-yl-9,9-didecylfluorene-2-ylamine (1.7 mmol) and 300 mg 3,4,9,10-perylenetetracarboxylic dianhydride (0.8 mmol), 145 mg $\text{Zn}(\text{OAc})_2 \cdot 2\text{H}_2\text{O}$ (0.7 mmol), and 6 mL quinoline was carried out at 160 °C for 20.5 h. The reaction mixture was cooled to room temperature, diluted with EtOH, filtered, washed with MeOH, and air dried, affording 0.93 g of pink-red solid. UV-vis (THF): 270 to 385 nm ($\lambda_{\text{max}} = 345 \text{ nm}$) and 410 to 545 nm with $\lambda_{\text{maxima}} = 457, 486, \text{ and } 522 \text{ nm}$.

Acknowledgments

Support from the Air Force Office of Scientific Research, in the form of a Summer Research Graduate Student Fellowship, is gratefully acknowledged. Special thanks are due Bruce Reinhardt, the lab focal point, and Dr. Robert Evers, MLBP Branch Chief, for generous assistance, and facilitating a productive, and truly collaborative summer research experience. Credit is also due to Dr. Kevin D. Belfield, Associate Professor of Chemistry at the University of Central Florida, who received an AFOSR Summer Faculty Fellowship, and collaboratively facilitated this research.

References

1. See, e.g., Bhawalkar, J. D.; He, G. S.; Prasad, P. N. "Nonlinear Multiphoton Processes in Organic and Polymeric Materials" *Rep. Prog. Phys.* **1996**, *59*, 1041-1070.
2. Denk, W.; Strickler, J. H.; Webb, W. W. "Two-Photon Laser Scanning Fluorescence Microscopy" *Science* **1990**, *248*, 73-76.
3. Bhawalkar, J. D.; Shih, A.; Pan, S. J.; Liou, W. S.; Swiatkiewicz, J.; Reinhardt, B. A.; Prasad, P. N.; Cheng, P. C. "Two-Photon Laser Scanning Fluorescence Microscopy - from a Fluorophore and Specimen Perspective" *Bioimaging* **1996**, *4*, 168-178.
4. Reinhardt, B. A.; Brott, L. L.; Clarson, S. J.; Dillard, A. G.; Bhatt, J. C.; Kannan, R.; Yuan, L.; He, G. S.; Prasad, P. N. "Highly Active Two-Photon Dyes: Design, Synthesis and Characterization Toward Application" *Chem. Mater.* **1998** (in press).

5. Kuhn, W. E. "2-Nitrofluorene and 2-Aminofluorene" *Organic Synthesis, Coll. Vol. 2*; Blatt, A. H., Ed.; Wiley: New York, 1943, pp. 447-448.
6. Marhevka, V. C.; Ebner, N. A.; Sehon, R. D.; Hanna, P. E. "Mechanism-Based Inactivation of N-Arylhydroxamic Acid N,O-Acyltransferase by 7-Substituted-N-hydroxy-2-acetamidofluorenes" *J. Med. Chem.* **1985**, *28*, 18-24.
7. Pivsa-Art, S.; Satoh, T.; Kawamura, Y.; Miura, M.; Nomura, M. "Palladium-Catalyzed Arylation of Azole Compounds with Aryl Halides in the Presence of Alkali Metal Carbonates and the Use of Copper Iodide in the Reaction" *Bull. Chem. Soc. Jpn.* **1998**, *71*, 467-473.
8. Kosugi, M.; Koshiba, M.; Atoh, A.; Sano, H.; Migita, T. "Palladium-Catalyzed Coupling between Organic Halides and Organotin Compounds Involving C-N Unsaturated Bonds at the Reaction Center" *Bull. Chem. Soc. Jpn.* **1986**, *59*, 677-679.
9. Hark, R. R.; Hauze, D. B.; Petrovskaja, O.; Joullie, M. M.; Jaouhari, R.; McCormiskey, P. "Novel Approaches toward Ninhydrin Analogs" *Tet. Lett.* **1994**, *35*, 7719-7722.
10. Tan, L.-S.; Srinivasan, K. R.; Bai, S. J. "New Aromatic Benzazole Polymers. I. Benzobisthiazole and Benzobisoxazole Polymers with Main-Chain Triarylamino Units" *J. Polym. Sci.: Part A: Polym. Chem.* **1997**, *35*, 1909-1924.
11. Yang, C.-P.; Lin, J.-H. "Syntheses and Properties of Aromatic Polyamides and Polyimides Based on N-Phenyl-3,3-bis[4-(p-aminophenoxy)phenyl]phthalimidine" *J. Polym. Sci.: Part A: Polym. Chem.* **1994**, *32*, 369-382.
12. Belfield, K. D.; Najjar, O. M. unpublished results.
13. Bohm, A.; Arms, H.; Henning, G.; Blaschka, P. "1,7-Disubstituted Perylene-3,4,9,10-tetracarboxylic Acids and Dianhydrides and Diimides of Said Acids" WO 97/22608, World Patent Application.

**THEORY OF ENVELOPE-FUNCTION WITHIN 6X6 LUTTINGER MODEL
IN HOLES SUBBAND STATES OF Si/Ge QUANTUM WELLS AND
SUPERLATTICES.**

**Aboubakar Traore
Graduate Student
Department of Physics and Engineering Physics**

**Stevens Institute of Technology
Castle Point on Hudson
Hoboken, NJ 07030**

**Final Report for:
Summer Graduate Research Program
Hanscom AFRL**

**Sponsored by:
AFOSR SUMMER RESEARCH PROGRAM
Bolling Air Force Base, DC**

August 1998

Theory of Envelope-function within 6X6 Luttinger model in holes subband states of Si/Ge quantum wells and superlattices.

Abstract.

We derive the exact envelope-function from the Luttinger-Kohn effective-mass Hamiltonian including the split-off band to calculate the valence band structure for semiconductor quantum wells and superlattices. A unitary transformation is used to block diagonalize the 6X6 Hamiltonian matrix into two 3X3 blocks. The results are applicable to silicon/germanium. The envelope functions are analytically given as linear combination of Bulk wavefunctions. Boundary conditions imposed on the envelope functions yield a 12X12 matrix for quantum wells, 24X24 matrix for superlattices, and from the zeros of its determinant the in plane energy dispersion is obtained as a function of inplane wavevector $k_{||}$. We discuss the mixing between the heavy-holes and light-hole states at finite $k_{||}$.

Introduction

Significant progress in semiconductor physics in recent years has stimulated great interest in the use of high speed electronic and optoelectronics devices such as quantum well lasers, superlattice photodetectors etc... To study the electronic structure of these devices, several theoretical methods such as the envelope function method [1], using the effective mass theory, the tight-binding method [5], and the pseudopotential method [8] have been used.

The envelope function method based on effective-mass theory from Luttinger Hamiltonian is convenient for the description of valence subbands near the center of the Brillouin zone, and expresses the nonparabolicity in k space, causing the mixing of heavy and light holes away from $k = 0$ [2,3].

Our concern in this paper is the valence band structure of Si/Ge semiconductor quantum wells and superlattices. They have recently aroused great interest because of their optoelectronics properties and their compatibility with the mature Si-based integrated circuit fabrication technology. The progress in epitaxy growth technology such as chemical vapor deposition (CVD) and molecular-beam epitaxy (MBE) have made new Si/Ge alloy materials potentially useful optoelectronics properties.

We use six-components envelope function method to study the valence subband structure of semiconductor quantum wells and superlattices.

The Si/Ge semiconductors have a valence band maximum at the Γ point, similar to

zinc-blende structure. It is therefore important to consider in the effective-mass Hamiltonian, the contribution of interactions of Γ_{15} with states of $\Gamma_1, \Gamma_{12}, \Gamma_{25}$ symmetry. The contribution of These symmetry types are contained in the dimensionless quantities σ, π , and δ which are related to the Luttinger parameters as[6]:

$$\begin{aligned}\gamma_1 &= -1 + 4\pi + 4\delta + 2\sigma \\ \gamma_2 &= \sigma - \pi + 2\delta \\ \gamma_3 &= \sigma + \pi - \delta\end{aligned}\tag{1}$$

The envelope functions in the well(Ge) and the barrier(Si) are expressed as linear combination of their bulk wavefunctions, The boundary conditions, continuity of envelope functions and current conservation at interfaces are used in order to get the energy eigenstates.

Analytical solution of effective-mass equation.

We consider an isolated quantum well grown in $\langle 001 \rangle$ direction. The well extend from $-L/2$ to $L/2$. The effective mass Hamiltonian including the uniaxial stresses along $\langle 001 \rangle$ for the Γ_8 and Γ_7 valence band zone center is the 6X6 matrix [6,7]:

$$M(k_x, k_y, k_z) \equiv \begin{bmatrix} P+Q & L & M & 0 & i\frac{L}{\sqrt{2}} & -i\sqrt{2}\cdot M \\ L & P-Q & -iC & M & -i\sqrt{2}\cdot Q & i\sqrt{\frac{3}{2}}\cdot L \\ M & iC & P-Q & -L & -i\sqrt{\frac{3}{2}}\cdot L & -i\sqrt{2}\cdot Q \\ 0 & M & -L & P+Q & -i\sqrt{2}\cdot M & -i\frac{L}{\sqrt{2}} \\ -i\frac{L}{\sqrt{2}} & i\sqrt{2}\cdot Q & i\sqrt{\frac{3}{2}}\cdot L & i\sqrt{2}\cdot M & D & iC \\ -i\sqrt{2}\cdot M & -i\sqrt{\frac{3}{2}}\cdot L & i\sqrt{2}\cdot Q & i\frac{L}{\sqrt{2}} & -iC & D \end{bmatrix}\tag{2}$$

where

$$\begin{aligned}
 P &= \frac{\hbar^2}{4\pi m_0} \gamma_1 \left[(k_x)^2 + (k_y)^2 + (k_z)^2 \right] \\
 Q &= \frac{\hbar^2}{4\pi m_0} \gamma_2 \left[(k_x)^2 + (k_y)^2 - 2(k_z)^2 \right] + \xi(z) \\
 L &= -i\sqrt{3} \frac{\hbar^2}{4\pi^2 m_0} \gamma_3 (k_x - i k_y) \cdot [(\sigma - \delta) \cdot k_z + k_z \cdot \pi] \\
 M &= \sqrt{3} \frac{\hbar^2}{4\pi^2 m_0} \left[\gamma_2 \left[(k_x)^2 - (k_y)^2 \right] - i 2 \gamma_3 k_x k_y \right] \\
 C &= (k_x - i k_y) \cdot [k_z (\sigma - \delta - \pi) - (\sigma - \delta - \pi) \cdot k_z] \\
 D &= P + \Delta
 \end{aligned} \tag{3}$$

Δ is the spin-orbit splitting, ζ is the shear-strain splitting energy, m_0 is the free electron mass, \hbar is Planck's constant and $\gamma_1, \gamma_2, \gamma_3$ are Luttinger parameters.

The Γ_8 and Γ_7 Bloch functions at zone center are given by

$$\begin{aligned}
 |3/2, 3/2\rangle &= (1/2)^{1/2} (X + iY) |+\rangle \\
 |3/2, 1/2\rangle &= i/(6)^{1/2} [(X + iY) |-\rangle - 2Z |+\rangle] \\
 |3/2, -1/2\rangle &= 1/(6)^{1/2} [(X - iY) |+\rangle + 2Z |-\rangle] \\
 |3/2, -3/2\rangle &= i/(2)^{1/2} (X - iY) |-\rangle \\
 |1/2, 1/2\rangle &= 1/(3)^{1/2} [(X + iY) |-\rangle + Z |+\rangle] \\
 |1/2, -1/2\rangle &= i/(3)^{1/2} [-(X - iY) |+\rangle + Z |-\rangle]
 \end{aligned} \tag{4}$$

X, Y, and Z are the Γ_{15} zone center p states.

$|+\rangle$, and $|-\rangle$ are spin 1/2 spinors.

The Luttinger-Kohn 6X6 Hamiltonian matrix can be block-diagonalize into two 3X3 blocks, using a unitary transformation. This transformation is possible in the new basis $|u_i\rangle$ related to the old as [6]

$$\begin{aligned}
 |u_1\rangle &= \alpha|3/2, -3/2\rangle - \alpha^*|3/2, 3/2\rangle \\
 |u_2\rangle &= \beta|3/2, 1/2\rangle + \beta^*|3/2, -1/2\rangle \\
 |u_3\rangle &= \beta|1/2, 1/2\rangle + \beta^*|1/2, -1/2\rangle \\
 |u_4\rangle &= \alpha|3/2, -3/2\rangle + \alpha^*|3/2, 3/2\rangle \\
 |u_5\rangle &= \beta|3/2, 1/2\rangle - \beta^*|3/2, -1/2\rangle \\
 |u_6\rangle &= \beta|1/2, 1/2\rangle - \beta^*|1/2, -1/2\rangle
 \end{aligned}
 \tag{5}$$

where

$$\alpha = (1/2)^{1/2} e^{i(\pi/4 + \phi/2 + \eta)}$$

$$\beta = (1/2)^{1/2} e^{i(-3\pi/4 + \phi/2 - \eta)}$$

$$\phi = \arctan(k_x/k_y)$$

$$\eta = 1/2 \arctan[(\gamma_3/\gamma_2) \tan(2\phi)]$$

To eliminate off-block-diagonal elements it is necessary to have $\phi = \eta$. This assumption restrict the inplane angle to some finite values [6,13]

$$\phi = n\pi/4 \quad (n = 0, 1, 2, 3, \dots)$$

In the new basis, the Hamiltonian is given by,

$$\begin{bmatrix}
 P+Q & |M| - i \cdot |L| & \sqrt{2} \cdot |M| + i \cdot \frac{|L|}{\sqrt{2}} & 0 & 0 & 0 \\
 |M| + i \cdot |L| & P - Q - i \cdot C & -\sqrt{2} \cdot Q - i \cdot \sqrt{\frac{3}{2}} \cdot |L| & 0 & 0 & 0 \\
 \sqrt{2} \cdot |M| - i \cdot \frac{|L|}{\sqrt{2}} & -\sqrt{2} \cdot Q + i \cdot \sqrt{\frac{3}{2}} \cdot |L| & D + i \cdot C & 0 & 0 & 0 \\
 0 & 0 & 0 & P+Q & |M| + i \cdot |L| & \sqrt{2} \cdot |M| - i \cdot \frac{|L|}{\sqrt{2}} \\
 0 & 0 & 0 & |M| - i \cdot |L| & P - Q + i \cdot C & -\sqrt{2} \cdot Q + i \cdot \sqrt{\frac{3}{2}} \cdot |L| \\
 0 & 0 & 0 & \sqrt{2} \cdot |M| + i \cdot \frac{|L|}{\sqrt{2}} & -\sqrt{2} \cdot Q - i \cdot \sqrt{\frac{3}{2}} \cdot |L| & D - i \cdot C
 \end{bmatrix} \quad (6)$$

The electronic wave function, in the envelope-function theory is a linear combination of Γ_8 and Γ_7 Bloch functions assumed to be the same for Si and Ge layers at zone center ($k_{||} = 0$). In the new basis it is given by

$$\psi(r) = F_1(r)|u_1\rangle + F_2(r)|u_2\rangle + F_3(r)|u_3\rangle + F_4(r)|u_4\rangle + F_5(r)|u_5\rangle + F_6(r)|u_6\rangle \quad (7)$$

To build the microscopic wave function we require two linearly independent eigenvectors of bulk materials. We will use [4,7]

$$S_1(k) = \begin{bmatrix} 0 \\ \alpha_1 \\ \alpha_2 \\ \alpha_3 \\ \alpha_4 \\ \alpha_5 \end{bmatrix} \quad S_2(k) = \begin{bmatrix} \beta_1 \\ 0 \\ \beta_2 \\ \beta_3 \\ \beta_4 \\ \beta_5 \end{bmatrix} \quad (8)$$

$$\alpha_1 = (D+E-2Q) + \frac{\sqrt{3}}{2} \cdot L^2$$

$$\alpha_2 = -(D+E+Q) \cdot L - \sqrt{3} \cdot M \cdot L_c$$

$$\alpha_3 = \frac{\sqrt{3}}{2} \cdot L \cdot L_c + 2 \cdot Q^2 + R_1 \cdot (D+E)$$

$$\alpha_4 = i \cdot \frac{1}{\sqrt{2}} \cdot \left[\frac{\sqrt{3}}{2} \cdot L^2 - (R_1 + Q) \cdot M \right]$$

$$\alpha_5 = \frac{i}{\sqrt{2}} \left[\sqrt{3} \cdot M \cdot L_c + (2 \cdot Q - R_1) \cdot L \right]$$

(9)

$$\beta_1 = \alpha_1$$

$$\beta_2 = 2 \cdot M \cdot M_c + \frac{1}{2} \cdot L \cdot L_c - R_2 \cdot (D+E)$$

$$\beta_3 = -\sqrt{3} \cdot L \cdot M_c - L_c \cdot (D+E+Q)$$

$$\beta_4 = \frac{i}{\sqrt{2}} \cdot (3 \cdot M \cdot L_c + \sqrt{3} \cdot R_2 \cdot L)$$

$$\beta_5 = \frac{i}{\sqrt{2}} \cdot (2 \cdot R_2 \cdot Q - 2 \cdot M \cdot M_c + L \cdot L_c)$$

$$R_1 = Q - P - E$$

$$R_2 = Q + P + E$$

E is an eigenvalue of the Hamiltonian.

We build the envelope function in the quantum well by superposing bulk wave solutions for $+k_z$ and $-k_z$ for given $k_{//}$. It can be written as linear combinations of

$$F_1(p,z) = \exp(ik_{//}p) \cdot f_1(z) \quad \text{and} \quad F_2(p,z) = \exp(ik_{//}p) \cdot f_2(z)$$

where

$$f_1(z)_+ = S_1(k_{//}, k_z) \exp(ik_z z) + S_1(k_{//}, -k_z) \exp(-ik_z z)$$

$$f_1(z)_- = S_1(k_{//}, k_z) \exp(ik_z z) - S_1(k_{//}, -k_z) \exp(-ik_z z)$$

$$f_2(z)_+ = S_2(k_{//}, k_z) \exp(ik_z z) + S_2(k_{//}, -k_z) \exp(-ik_z z) \quad (10)$$

$$f_2(z)_- = S_2(k_{//}, k_z) \exp(ik_z z) + S_2(k_{//}, -k_z) \exp(-ik_z z)$$

From the definition of S_1 and S_2 the above linear combinations become standing waves

$$\begin{aligned} f_1(z)_+ = |S_1, +\rangle &= \begin{bmatrix} 0 \\ 2 \cdot \alpha_1 \cdot \cos(k_z \cdot Z) \\ 2 \cdot i \cdot \alpha_2 \cdot \sin(k_z \cdot Z) \\ 2 \cdot \alpha_3 \cdot \cos(k_z \cdot Z) \\ 2 \cdot \alpha_4 \cdot \cos(k_z \cdot Z) \\ 2 \cdot i \cdot \alpha_5 \cdot \sin(k_z \cdot Z) \end{bmatrix} & f_1(z)_- = |S_2, -\rangle &= \begin{bmatrix} 0 \\ 2 \cdot i \cdot \alpha_1 \cdot \cos(k_z \cdot Z) \\ 2 \cdot \alpha_2 \cdot \cos(k_z \cdot Z) \\ 2 \cdot i \cdot \alpha_3 \cdot \sin(k_z \cdot Z) \\ 2 \cdot i \cdot \alpha_4 \cdot \sin(k_z \cdot Z) \\ 2 \cdot \alpha_5 \cdot \cos(k_z \cdot Z) \end{bmatrix} \\ f_2(z)_+ = |S_2, +\rangle &= \begin{bmatrix} 2 \cdot i \cdot \beta_1 \cdot \sin(k_z \cdot Z) \\ 0 \\ 2 \cdot i \cdot \beta_2 \cdot \sin(k_z \cdot Z) \\ 2 \cdot \beta_3 \cdot \cos(k_z \cdot Z) \\ 2 \cdot \beta_4 \cdot \cos(k_z \cdot Z) \\ 2 \cdot i \cdot \beta_5 \cdot \sin(k_z \cdot Z) \end{bmatrix} & f_2(z)_- = |S_2, -\rangle &= \begin{bmatrix} 2 \cdot \beta_1 \cdot \cos(k_z \cdot Z) \\ 0 \\ 2 \cdot \beta_2 \cdot \cos(k_z \cdot Z) \\ 2 \cdot i \cdot \beta_3 \cdot \sin(k_z \cdot Z) \\ 2 \cdot i \cdot \beta_4 \cdot \sin(k_z \cdot Z) \\ 2 \cdot \beta_5 \cdot \cos(k_z \cdot Z) \end{bmatrix} \end{aligned} \quad (11)$$

By superposing $|S_1, +\rangle$, $|S_2, +\rangle$ and $|S_1, -\rangle$, $|S_2, -\rangle$ we obtain overall even and odd envelope function components,

$$\begin{aligned} F^+(\rho, z) &= \exp(ik_{//} \rho) [c_1 |S_1, +\rangle + c_2 |S_2, +\rangle] & (\text{even}) \\ F^-(\rho, z) &= \exp(ik_{//} \rho) [c_1 |S_1, -\rangle + c_2 |S_2, -\rangle] & (\text{odd}) \end{aligned} \quad (12)$$

We consider a quantum well having interfaces at $\pm L/2$. Due to the parity of the envelope function components, we have a symmetry problem with respect to the center of the quantum well. We only need to apply the boundary conditions at interface $z = (1/2)L$, then the solution for $z < 0$ can be obtained by reflection symmetry to the center.

The envelope function in the well will be a superposition of $F^+(\rho, z)$ and $F^-(\rho, z)$ for the heavy hole, light hole and spin split-off band, resulting in six expansion coefficients to be determined in the well [4].

In the barrier, we consider only evanescent states decaying for large z values, resulting in six unknown coefficients.

The general form of the envelope function in the well can be written,

$$\psi_w(r) = [F^+(\rho, z) + F^-(\rho, z)]_{hh} + [F^+(\rho, z) + F^-(\rho, z)]_{lh} + [F^+(\rho, z) + F^-(\rho, z)]_{so} \quad (13)$$

$$\psi_w(r) = \exp(i \cdot k_{//} \cdot \rho).$$

By factoring the components of the wavevectors, we may rewrite the function $f_w(z)$ as,

$$f_w(z) = A_1 \cdot \begin{bmatrix} 0 \\ \alpha_{1hw} \\ \alpha_{2hw} \\ \alpha_{3hw} \\ \alpha_{4hw} \\ \alpha_{5hw} \end{bmatrix} \cdot \exp(i \cdot k_{zh}) + A_2 \cdot \begin{bmatrix} 0 \\ \alpha_{1lw} \\ \alpha_{2lw} \\ \alpha_{3lw} \\ \alpha_{4lw} \\ \alpha_{5lw} \end{bmatrix} \cdot \exp(i \cdot k_{zl}) + A_3 \cdot \begin{bmatrix} 0 \\ \alpha_{1sw} \\ \alpha_{2sw} \\ \alpha_{3sw} \\ \alpha_{4sw} \\ \alpha_{5sw} \end{bmatrix} \cdot \exp(i \cdot k_{zs}) + \quad (14)$$

$$A_4 \cdot \begin{bmatrix} \beta_{1hw} \\ 0 \\ \beta_{2hw} \\ \beta_{3hw} \\ \beta_{4hw} \\ \beta_{5hw} \end{bmatrix} \cdot \exp(i \cdot k_{zh}) + A_5 \cdot \begin{bmatrix} \beta_{1lw} \\ 0 \\ \beta_{2lw} \\ \beta_{3lw} \\ \beta_{4lw} \\ \beta_{5lw} \end{bmatrix} \cdot \exp(i \cdot k_{zl}) + A_6 \cdot \begin{bmatrix} \beta_{1sw} \\ 0 \\ \beta_{2sw} \\ \beta_{3sw} \\ \beta_{4sw} \\ \beta_{5sw} \end{bmatrix} \cdot \exp(i \cdot k_{zs})$$

In the barrier, the function $f_b(z)$ has the form,

$$f_b(z) = B_1 \begin{bmatrix} 0 \\ \alpha_{1hb} \\ \alpha_{2hb} \\ \alpha_{3hb} \\ \alpha_{4hb} \\ \alpha_{5hb} \end{bmatrix} \cdot \exp(-q_{zh}) + B_2 \begin{bmatrix} 0 \\ \alpha_{1lb} \\ \alpha_{2lb} \\ \alpha_{3lb} \\ \alpha_{4lb} \\ \alpha_{5lb} \end{bmatrix} \cdot \exp(-q_{zl}) + B_3 \begin{bmatrix} 0 \\ \alpha_{1sb} \\ \alpha_{2sb} \\ \alpha_{3sb} \\ \alpha_{4sb} \\ \alpha_{5sb} \end{bmatrix} \cdot \exp(-q_{zs}) + \quad (15)$$

$$B_4 \begin{bmatrix} \beta_{1hb} \\ 0 \\ \beta_{2hb} \\ \beta_{3hb} \\ \beta_{4hb} \\ \beta_{5hb} \end{bmatrix} \cdot \exp(-q_{zh}) + B_5 \begin{bmatrix} \beta_{1lb} \\ 0 \\ \beta_{2lb} \\ \beta_{3lb} \\ \beta_{4lb} \\ \beta_{5lb} \end{bmatrix} \cdot \exp(-q_{zl}) + A_6 \begin{bmatrix} \beta_{1sb} \\ 0 \\ \beta_{2sb} \\ \beta_{3sb} \\ \beta_{4sb} \\ \beta_{5sb} \end{bmatrix} \cdot \exp(-q_{zs})$$

In the case of superlattices, the envelope function is written with twenty four unknown coefficients. Twelve unknown coefficients in the well, and twelve in the barrier:

The general form of the envelope function in the well can be written as:

$$\begin{aligned}
 f_w(z) = & A_1 \begin{bmatrix} 0 \\ \alpha_{1hw} \\ \alpha_{2hw} \\ \alpha_{3hw} \\ \alpha_{4hw} \\ \alpha_{5hw} \end{bmatrix} \cdot \exp(i \cdot k_{zh}) + A_2 \begin{bmatrix} 0 \\ \alpha_{1lw} \\ \alpha_{2lw} \\ \alpha_{3lw} \\ \alpha_{4lw} \\ \alpha_{5lw} \end{bmatrix} \cdot \exp(i \cdot k_{zl}) - A_3 \begin{bmatrix} 0 \\ \alpha_{1sw} \\ \alpha_{2sw} \\ \alpha_{3sw} \\ \alpha_{4sw} \\ \alpha_{5sw} \end{bmatrix} \cdot \exp(i \cdot k_{zs}) + \\
 & A_4 \begin{bmatrix} \beta_{1hw} \\ 0 \\ \beta_{2hw} \\ \beta_{3hw} \\ \beta_{4hw} \\ \beta_{5hw} \end{bmatrix} \cdot \exp(i \cdot k_{zh}) + A_5 \begin{bmatrix} \beta_{1lw} \\ 0 \\ \beta_{2lw} \\ \beta_{3lw} \\ \beta_{4lw} \\ \beta_{5lw} \end{bmatrix} \cdot \exp(i \cdot k_{zl}) + A_6 \begin{bmatrix} \beta_{1sw} \\ 0 \\ \beta_{2sw} \\ \beta_{3sw} \\ \beta_{4sw} \\ \beta_{5sw} \end{bmatrix} \cdot \exp(i \cdot k_{zs}) + \quad (16) \\
 & A_7 \begin{bmatrix} 0 \\ \alpha_{1hw} \\ \alpha_{2hw} \\ \alpha_{3hw} \\ \alpha_{4hw} \\ \alpha_{5hw} \end{bmatrix} \cdot \exp(-i \cdot k_{zh}) + A_8 \begin{bmatrix} 0 \\ \alpha_{1lw} \\ \alpha_{2lw} \\ \alpha_{3lw} \\ \alpha_{4lw} \\ \alpha_{5lw} \end{bmatrix} \cdot \exp(-i \cdot k_{zl}) + A_9 \begin{bmatrix} 0 \\ \alpha_{1sw} \\ \alpha_{2sw} \\ \alpha_{3sw} \\ \alpha_{4sw} \\ \alpha_{5sw} \end{bmatrix} \cdot \exp(-i \cdot k_{zs}) + \\
 & A_{10} \begin{bmatrix} \beta_{1hw} \\ 0 \\ \beta_{2hw} \\ \beta_{3hw} \\ \beta_{4hw} \\ \beta_{5hw} \end{bmatrix} \cdot \exp(-i \cdot k_{zh}) + A_{11} \begin{bmatrix} \beta_{1lw} \\ 0 \\ \beta_{2lw} \\ \beta_{3lw} \\ \beta_{4lw} \\ \beta_{5lw} \end{bmatrix} \cdot \exp(-i \cdot k_{zl}) + A_{12} \begin{bmatrix} \beta_{1sw} \\ 0 \\ \beta_{2sw} \\ \beta_{3sw} \\ \beta_{4sw} \\ \beta_{5sw} \end{bmatrix} \cdot \exp(-i \cdot k_{zs})
 \end{aligned}$$

The envelope function in the barrier has the same form as in the well by replacing the coefficients A_i by B_i and $i \cdot k_z$ by q_z .

k_{zh} , $k_{z\ell}$, and k_{zs} are solutions of The Hamiltonian eigenvalues equation for the well, and q_{zh} , $q_{z\ell}$, q_{zs} for the barrier. The coefficients A_i and B_i are determined for each eigenenergy for given inplane wave vector $k_{||}$. The envelope functions $f_w(z)$ and $f_b(z)$ must match at the interface $z = L/2$ and must also satisfy the current conservation condition. The current conservation matrix is obtained by differentiating with respect to k_z each element of the Hamiltonian matrix and then substituting $k_z = -i\delta/\delta z$. [4,6]

$$B_+ = \begin{bmatrix} (\gamma_1 - 2\gamma_2) \cdot \frac{\delta}{\delta z} & -2\sqrt{3} \cdot k_{11} & \sqrt{6} \cdot \pi \cdot k_{11} \\ 2\sqrt{3} \cdot (\sigma - \delta) \cdot k_{11} & (\gamma_1 + 2\gamma_2) \cdot \frac{\delta}{\delta z} - 2 \cdot (\sigma - \delta - \pi) \cdot k_{11} & -2\sqrt{2} \cdot \gamma_2 \cdot \frac{\delta}{\delta z} - \sqrt{2} \cdot (2\sigma - 2\delta + \pi) \cdot k_{11} \\ -\sqrt{6} \cdot (\sigma - \delta) \cdot k_{11} & -2\sqrt{2} \cdot \gamma_2 \cdot \frac{\delta}{\delta z} + \sqrt{2} \cdot (\sigma - \delta + 2\pi) \cdot k_{11} & \gamma_1 \cdot \frac{\delta}{\delta z} + 2(\sigma - \delta - \pi) \cdot k_{11} \end{bmatrix} \quad (17)$$

$$B_- = \begin{bmatrix} (\gamma_1 - 2\gamma_2) \cdot \frac{\delta}{\delta z} & 2\sqrt{3} \cdot k_{11} & -(\sqrt{6} \cdot \pi \cdot k_{11}) \\ -2\sqrt{3} \cdot (\sigma - \delta) \cdot k_{11} & (\gamma_1 + 2\gamma_2) \cdot \frac{\delta}{\delta z} + 2 \cdot (\sigma - \delta - \pi) \cdot k_{11} & -2\sqrt{2} \cdot \gamma_2 \cdot \frac{\delta}{\delta z} + \sqrt{2} \cdot (2\sigma - 2\delta + \pi) \cdot k_{11} \\ \sqrt{6} \cdot (\sigma - \delta) \cdot k_{11} & -2\sqrt{2} \cdot \gamma_2 \cdot \frac{\delta}{\delta z} - \sqrt{2} \cdot (\sigma - \delta + 2\pi) \cdot k_{11} & \gamma_1 \cdot \frac{\delta}{\delta z} - 2(\sigma - \delta - \pi) \cdot k_{11} \end{bmatrix}$$

B_+ and B_- are respectively the upper 3X3 block and lower 3X3 block of the 6X6 block-diagonal current conservation matrix.

For quantum wells, the continuity condition of the envelope function and the current conservation condition at the interface $z = L/2$, produce a set of 12 homogeneous linear equations with 12 unknowns.

In the case of superlattices, the boundary conditions produce a set of 24 homogeneous equations in 24 unknowns.

The consistency of the procedure require the vanishing of the 12X12 or the 24X24 determinant at the subbands eigenenergies for a given $k_{||}$.

The valence subbands energy dispersion is obtained by using the following procedure:

For a given k_y , we scan the energy in the range of the square well potential. At each step of energy, we use the equation (2) to determine the values for k_{zh} , k_{zi} , k_{zs} , q_{zh} , q_{zi} , and q_{zs} . We then evaluate the determinant of the 12X12 or 24X24 matrix.

The eigenenergies are the zeros of the determinant.

To evaluate the envelope function, we guess the value of a coefficient in order to avoid the trivial solutions, because the determinant vanishes.

For the Qw case, we now have a system of 12 linear equations in 11 unknowns. For example guessing $A_1 = 1$, we may use Cramer's rule to determine the

remaining 11 unknowns coefficients.

We normalize the envelope function by writing

$$\sum_{j=1}^6 \int_{-\xi}^{\xi} (|f_j(z)|)^2 dz = 1 \quad (18)$$

where ξ is chosen to be appropriate for the decay in the barrier, in the quantum well case, or ξ is the length of a period in the superlattice case.

Summary

The purpose of this work is to derive the wave functions in the well and barrier in order to study population inversion and laser gain in intersubband transition in Si/Ge.

Population inversion and lasing depend on lifetimes of carriers on upper and lower laser levels.

In the III-V materials the lifetimes are limited by strong longitudinal polar optical phonon scattering, which limits the lasing energies to less than the optical phonon energy [9, 11, 12]. But the absence of such strong polar optical phonon scattering in silicon-based materials results in longer lifetime on energy levels than in the III-V materials semiconductors.

The lifetime τ_i of subband i is determined by

$$\tau_i = [\Sigma(W_{ij}^a + W_{ij}^o)]^{-1} \quad (18)$$

where

$$W_{ij}^a = (\Xi_d^2 k_B T m^* / (4\pi c_L (h/2\pi)^3)) \Sigma |G_{ij}(q_z)|^2$$

is the acoustic phonon scattering rate

and

$$W_{ij}^o = m^* [n(\omega_0) + 1/2 -/+ 1/2] D^2 o / (4\pi p (h/2\pi)^2 \omega_0) \Sigma |G_{ij}(q_z)|^2$$

for nonpolar optical phonon scattering.

Ξ_d is the valence band deformation potential, m^* the heavy hole effective mass, c_L the elastic constant, k_B Boltzmann's constant, h Planck constant, T the absolute temperature, $n(\omega_0)$ is the phonon population of frequency ω_0 , D_0 is the valence band optical deformation potential, ρ the mass density, and q_z the phonon wavevector in the growth direction.

The term $G_{ij}(q_z) = \langle i | \exp(iq_z z) | j \rangle$ contains the spatial overlap of the wavefunctions involved in the transition. These wavefunctions are constructed in term of the thicknesses of the wells and barriers, hence the lifetimes of carriers on the energy levels are strongly influenced by the shape of the wells and barriers. Therefore the transition rate between different states involved in the lasing can be engineered by proper design of the wells and barriers[10]. It has been shown that intersubband lasing can be achieved, without total population inversion between different energy levels involved in the lasing[11], [13]. Due to valence band non-parabolicity, local k -space population inversion near $k=0$ is sufficient for laser action to take place. This feature may be exploited in Si/Ge quantum wells or superlattices, because of strong interaction between valence subbands. We expect such local population inversion near the anticrossing point of light and heavy hole bands.

Acknowledgments

I would like to thank Dr. Lionel Friedman and Dr. Philips Hemmer for their assistance and disponibility during the twelve weeks spent at AFRL,Hanscom. I thank Dr. Greg. Sun and Dr. Lu at Umass,Boston. I acknowledge the AFOSR Summer Research Program for the financial support during my stay at AFRL, Sensors Directorate,Hanscom AFB, Massachusetts.

References

- [1] L.C.Andreani, A.Pasquarello, and F.Bassani, Phys. Rev. B36 5887(1987).
- [2] G. Bastard, Phys. Rev. B24 5693(1981).
- [3] G. Bastard, Wave Mechanics Applied to semiconductor Heterostructures (Les Editions de physiques, Les Ulis, Paris,1988).
- [4] E.C. Valdares, Phys. Rev. B46 3935(1992).
- [5] J.H. Schulman, Y. C. Chang, Phys. Rev. B31 2056(1985).
- [6] Bradley A. Foreman, Phys. Rev. B48 4964(1993).
- [7] G. Edwards, E.C. Valdares,F.W.Sheard, Phys. Rev. B50 8493(1994).
- [8] M. Jaros,K.B.Wong,M.A.Gell, Phys. Rev. B31 1205(1985).
- [9] G. Sun, Lionel Friedman, Phys. Rev. B53 3966(1996).
- [10] Lionel Friedman, Richard A. Soref, J. Appl. Phys. 83 3480(1998)
- [11] G. Sun, Y. Lu, J.B. Khurgin, Appl. phys. Lett. 72 1481(1998)
- [12] G. Sun, L. Friedman, R.A. Soref, Appl. phys. Lett. 66(25) 3425(1995)
- [13] J. Faist, F. Capasso, Phys. Rev. Lett.76 411(1996).
- [14] A.T. Meney, B. Gonul, E.P. O'Reilly, Phys. Rev. B50 10893(1994).

MRF SEGMENTATION FOR FEATURE EXTRACTION
IN SAR CHIP CLASSIFICATION

Robert A. Weisenseel
Ph.D. Candidate
Electrical and Computer Engineering Department

Boston University
8 Saint Mary's St.
Boston, MA 02215

Final Report for:
Graduate Student Research Program
Air Force Research Lab
Sensors Directorate
Target Recognition Branch
AFRL/SNAT
Wright-Patterson AFB

Sponsored by:
Air Force Office of Scientific Research
Bolling Air Force Base, DC
and
Air Force Research Lab
Sensors Directorate
Target Recognition Branch

August 1998

MRF SEGMENTATION FOR FEATURE EXTRACTION IN SAR CHIP CLASSIFICATION

Robert A. Weisenseel
Ph.D. Candidate
Electrical and Computer Engineering Department
Boston University

Abstract

DARPA's Moving and Stationary Target Acquisition and Recognition (MSTAR) program has shown that image segmentation of Synthetic Aperture Radar (SAR) imagery into target, shadow, and background clutter regions can be a powerful tool in the process of recognizing targets in open terrain. Unfortunately, SAR imagery is extremely speckled. This impulsive noise can make traditional, purely intensity-based segmentation techniques fail. Introducing prior information about the segmentation image, such as its expected "smoothness" and anisotropy, in a statistically rational way can improve segmentations dramatically. Moreover, maintaining such statistical rigor throughout the recognition process can make combining multiple sources of information straightforward.

To this end, I introduce a Bayesian approach to image segmentation of MSTAR target chips based on a statistical observation model and a Markov Random Field (MRF) prior model. I then compare the results of this segmentation approach those from the MSTAR program and from human segmentation. Despite little optimization of the associated parameters, the Bayesian approach compares favorably to the MSTAR approach, opening a host of statistically based options for SAR image segmentation.

MRF SEGMENTATION FOR FEATURE EXTRACTION IN SAR CHIP CLASSIFICATION

Robert A. Weisenseel

1 Introduction

DARPA's Moving and Stationary Target Acquisition and Recognition (MSTAR) program is an effort to provide better automated tools for, as its name suggests, acquiring and recognizing targets, such as tanks or other military vehicles. One bonus of this program has been its freely distributed imagery and tools that have greatly advanced the image processing and recognition field, by providing a benchmark data set for comparing algorithms. Up until very recently, this data set has consisted entirely of Synthetic Aperture Radar (SAR) imagery. One of these public tools is been Predict Lite, a software package for predicting MSTAR imagery from a small set of parameters. The public program is named Predict Lite because it has only a small subset of the capabilities of the full prediction software which is ITAR restricted.

One area of study within MSTAR is image segmentation as a feature extraction tool for target recognition. MSTAR has shown that image segmentation of SAR imagery into target, shadow, and background clutter regions can be a powerful tool in the process of recognizing targets, although most of its robustness is lost outside of open terrain. Unfortunately, SAR imagery is extremely speckled, as evidenced in the small set of examples of measured data in Figure 1. Predict Lite attempts to simulate this noise with small success, as shown in Figure 2. This impulsive noise can challenge traditional, purely intensity-based segmentation techniques. The resulting segmentations of such traditional approaches are often noisy. Introducing prior information about the segmentation image, such as its expected "smoothness" and anisotropy, in a statistically rational way can improve segmentations dramatically. Moreover, maintaining such statistical rigor throughout the recognition process can make combining multiple sources of information straightforward.

In this report, I introduce a Bayesian approach to image segmentation of MSTAR target chips based on a statistical observation model and a Markov Random Field (MRF) prior model. I then compare the results of this segmentation approach those from the MSTAR program and from human segmentation. While I chose a set of operational parameters that produced reasonable segmentations in a reasonable time, I did not spend much effort to optimize of these parameters. Despite this, the Bayesian MRF approach compares favorably to the MSTAR approach, opening a host of statistically based options for SAR image segmentation.

2 Background

There are a number of ways to segment SAR imagery. Possibly one of the simplest to implement is human segmentation, where humans sit in front of a computers and painstakingly draw the regions that they believe

correspond to target, background, and shadow. Examples of such segmentations appear in Figures 3 and 4. The point of the MSTAR program is to automate processes such as these, since the sheer volume of data is too large compared to the number of available human analysts.

MSTAR has its own segmentation tools. The true MSTAR predictor can determine the "exact" segmentation of one of its predicted images, because the predicted images are determined in part by the segmentation. However, this tool is not available through Predict Lite, so I obtained MSTAR predicted segmentations off-line. These MSTAR segmentations provide a good baseline for testing algorithms on predicted imagery such as is shown in Figure 2. MSTAR segmentations of measured data and predicted imagery appear in Figures 5 and 6.

Another approach to segmentation is the one that I have chosen, the Bayesian approach. This approach incorporates information from sources other than data. For example, we might want to incorporate some knowledge of a physical model for the system, beyond just observations.

Assume first that a given SAR image y consists of N pixels, each of which can take on positive real values. Also, I assume a segmentation label field x where each element, x_i , corresponds to a particular element, y_i , of y , and where each element can take on one of three values corresponding to target, background, and shadow labels. Mathematically,

$$y_i \in \mathbb{R}^+ \text{ at pixel } i \quad x_i = \begin{cases} 3 & \text{pixel } i = \text{target} \\ 2 & \text{pixel } i = \text{background clutter} \\ 1 & \text{pixel } i = \text{shadow} \end{cases} \quad (1)$$

The Bayesian approach starts from the posterior probability density. One Bayesian approach that is appropriate to this problem is the Maximum A Posteriori (MAP) classifier. With x being the image where each pixel can take on three states, target, shadow, or background, and y being the SAR data image, the formula for determining the values of x is:

$$\hat{x} = \underset{x}{\operatorname{argmax}} p(x|y) = \underset{x}{\operatorname{argmax}} p(y|x)p(x) \quad (2)$$

where $p(x|y)$ is the posterior probability distribution of the segmentation label image conditioned on the SAR data image, $p(y|x)$ is the likelihood of the data image conditioned on the segmentation label image, and $p(x)$ is the prior probability distribution of the segmentation image. Thus, we just need three things: an observation probability model, a prior probability model, and an algorithm for maximizing over all possible segmentation images x .

3 Method

3.1 Observation Model

For the observation model, I assume that each pixel of data, y_i , is conditionally independent of all other data pixels, conditioned on knowledge of the segmentation label at that pixel, x_i . Formally,

$$p(y|x) = p(y_1, \dots, y_N | x_1, \dots, x_N) = \prod_{i=1}^N p(y_i | x_i) \quad (3)$$

where N is the number of pixels in the image. I also assume that each data pixel is a conditionally identically distributed Weibull random variable,

$$p(y_i | x_i) = \frac{\beta(x_i)}{\alpha(x_i)} \left(\frac{y_i}{\alpha(x_i)} \right)^{\beta(x_i)-1} \exp \left\{ - \left(\frac{y_i}{\alpha(x_i)} \right)^{\beta(x_i)} \right\} \quad \alpha, \beta > 0 \quad (4)$$

where $\alpha(x_i)$ and $\beta(x_i)$ are the scale and shape parameters, respectively, of the Weibull distribution, given that the observation is of segmentation label x_i . This label can be 1, 2, or 3 as stated in Equation 1.

I estimated the scale and shape parameters of each of the three distributions for both predicted and measured imagery from data, assuming the human segmentations described in Section 2 were correct. I used a maximum likelihood estimator to obtain these estimates. For example, using all of the pixels labeled by a human as target from every measured training image, I estimated the parameters of the probability distribution of a particular observation pixel, assuming it came from a target region within the measured data training imagery:

$$[\hat{\alpha}(3), \hat{\beta}(3)] = \underset{\alpha, \beta}{\operatorname{argmax}} g(\alpha, \beta) = \underset{\alpha, \beta}{\operatorname{argmax}} \log p(z | \alpha, \beta) \quad (5)$$

where z is that subset of all observation pixels y corresponding to a target region, and g is the objective function of the optimization. The function g is just the logarithm of the probability distribution of z , which is allowable since a logarithm does not affect the result of the maximization:

$$g(\alpha, \beta) = M \log \beta - \beta M \log \alpha + (\beta - 1) \sum_{i=1}^M \log z_i - \alpha^{-\beta} \sum_{i=1}^M z_i^{\beta} \quad (6)$$

M is the number of pixels in the training set labeled as target.

To accomplish this maximization, I used a Newton-type optimization algorithm,

$$\theta_{k+1} = [\alpha_{k+1}, \beta_{k+1}]^T = \theta_k - s_k [\nabla^2 g(\theta_k)]^{-1} \nabla g(\theta_k) \quad (7)$$

where s_k was the step size at each iteration, k , chosen by the Armijo rule. To initialize the optimization algorithm, I assumed the distribution was Rayleigh, i.e. the initial shape parameter, β_0 , was equal to 2 and the initial scale parameter, α_0 was given by

$$\alpha = \sqrt{\frac{1}{M} \sum_{i=1}^M y_i^2} \quad (8)$$

Please note that, for the estimation of the shadow distribution parameters, I chose to censor some of the shadow data that were clearly misclassified by the human segmenters, because these outliers would have resulted in a poor estimate of the shadow parameters. The target and background regions were much more robust to misclassifications and therefore did not require such censoring.

I show the fit of the Weibull model to measured target, background, and shadow histograms in Figures 7(a)-(c), respectively. Fits to predicted are similarly good, but I do not display them here for brevity. The parameter estimates appear in Table 1.

		α	β
Measured	Target	0.2182	0.9932
	Background	0.0542	1.7655
	Shadow	0.0202	1.3058
Predicted	Target	0.0337	0.8437
	Background	0.0110	1.7937
	Shadow	0.000122	1.6891

Table 1: Table of Predicted and Measured Parameter Estimates

3.2 Prior Model

For my prior model, I choose to introduce spatial correlation of target, background, and shadow regions using an anisotropic Markov Random Field (MRF) model [1, 2]. An MRF is a way of describing complex global structure through local pixel-to-pixel interactions in a statistically rigorous fashion. This concept is related to Markov chains. In a first-order Markov chain, each step in a one-dimensional series depends only on the previous step:

$$p(x_i | x_{i-1}, \dots, x_0) = p(x_i | x_{i-1}) \quad (9)$$

We can extend this concept to two dimensions with MRFs by saying a pixel depends only on its neighbors. For example, if x is an image, and $x_{i,j}$ is a pixel in that image, we can describe a first-order MRF,

$$p(x_{i,j} | x \setminus x_{i,j}) = p(x_{i,j} | \eta_{i,j}) \quad \eta_{i,j} = \{x_{i-1,j}, x_{i,j-1}, x_{i+1,j}, x_{i,j+1}\} \quad (10)$$

where \setminus denotes set subtraction and $\eta_{i,j}$ is the set of nearest neighbors to pixel i, j . This neighborhood is shown visually in Figure 8. While I could extend this to larger neighborhoods, in this research I have restricted the problem to the four nearest neighbors.

By using the equivalence between MRFs and Gibbs distributions, I write the probability function for the MRF in Gibbs form:

$$p(x) = \frac{1}{Z} \exp \left\{ -\alpha \sum_{i=1}^N \sum_{j \in \eta_i} f_{i,j}(x_i, x_j) \right\} \quad (11)$$

where I have simplified to a single index for denoting each pixel of the image. The variable α is just a weighting constant that can make the distribution "sharper" or "flatter," which correspondingly makes the segmentation field "smoother" or "noisier," respectively. Z is just a normalization constant called the partition function given by,

$$Z = \sum_x \exp \left\{ -\alpha \sum_{i=1}^N \sum_{j \in \eta_i} f_{i,j}(x_i, x_j) \right\} \quad (12)$$

where the first summation is over all possible segmentation label fields for x . Note that it is never necessary to compute the partition function.

The subscripts of the function $f_{i,j}(\cdot, \cdot)$, the potential function, make it possible for the MRF to be both inhomogeneous and anisotropic. In this work, I assume homogeneity, but not isotropy. For example, $f_{i,j}$ can be a different function depending on whether j is downrange of i or in one of the crossrange directions. By choosing an anisotropic, or directional, model, I incorporate prior knowledge about the structure of a SAR image segmentation field, i.e. that shadows usually fall downrange of targets and that there should be little or no background clutter between a target and its shadow. These functions appear in Table 2, with

$f_D(x_i, x_j)$		x_j			$f_U(x_i, x_j)$		x_j		
		S	B	T			S	B	T
x_i	S	0	-1	-2	x_i	S	0	-2	-1
	B	-2	0	-1		B	-1	0	-2
	T	-1	-2	0		T	-2	-1	0

$f_C(x_i, x_j)$		x_j		
		S	B	T
x_i	S	0	-1	-1
	B	-1	0	-1
	T	-1	-1	0

Table 2: Table of Potential Functions

f_D denoting the potential function corresponding to pixel j being downrange of pixel i , f_U denoting the potential function when j is uprange of i , and f_C denoting the potential for the case when j is in either of the cross-range directions from i . Note that f_U is just the transpose of f_D . The function f_C just implies that there is no penalty for two pixels of the same type neighboring in the cross-range direction, otherwise there is a penalty. The functions f_U and f_D are similar to f_C , but the cases of placing target downrange of shadow, background downrange of target, or background uprange of shadow are heavily penalized.

3.3 Simulated Annealing

I then combine the observation and prior models into a function proportional to the posterior distribution with α as a weighting constant between the prior and observation distributions:

$$p(x|y) \propto e^{-H(x|y)} \quad (13)$$

$$H(x|y) = \sum_{i=1}^N \left[\ln \beta(x_i) - \beta(x_i) \ln \alpha(x_i) + (\beta(x_i) - 1) \ln y_i - \left(\frac{y_i}{\alpha(x_i)} \right)^{\beta(x_i)} - \alpha \sum_{j \in \eta_i} f_{i,j}(x_i, x_j) \right] \quad (14)$$

This function is the function in Equation 2 that I said we need to optimize.

The last thing we need is a means to maximize this function, and hence the posterior distribution, for all x . I implement this maximization using a simulated annealing algorithm because the distribution of x is discrete [3]. Thus, I introduce a "temperature" parameter to the distribution:

$$p(x|y) \propto e^{-H(x|y)/T} \quad (15)$$

To obtain an optimal solution, T should start at a sufficiently high temperature and be reduced slowly according to a logarithmic cooling schedule that runs long enough to approach zero temperature,

$$T = \frac{c}{\ln(k+1)} \quad k = 1, 2, \dots \quad (16)$$

where c is a specific temperature determined by the maximum possible change in $H(x|y)$ caused by changing a single pixel in the segmentation label image, x . However, to reduce the number of computations necessary, I initialize the system at a relatively low temperature with a pixel-by-pixel Maximum Likelihood (ML) solution using the likelihoods given in Equation 4 and then decrease the temperature with a faster logarithmic cooling schedule for 1000 iterations. I control the lower starting temperature and faster cooling schedule by setting c . Lastly, I reduce the temperature to zero and run the algorithm for 5 iterations to force the system into the nearest local optimum.

While this approach is not guaranteed to achieve a globally optimal solution, the initialization makes this algorithm unlikely to do worse than the ML solution and the faster cooling schedule gives faster convergence. Because only local interactions are involved in this processing and the number of local operations required are small, this technique is well-suited to massive parallelization, either on multiple processors or on application specific ICs.

4 Results

The resulting segmentations appear for the T72 tank at a depression angle of 17° in Figures 9 and 10 at azimuths of 0° , 45° , 90° , 135° , 180° , 225° , 270° , and 315° . These values are approximate for the measured case. The segmentations shown are a subset of the total performed. I performed T72 segmentations at every

azimuth from 0° to 355° at a spacing of 5° (approximately in the measured case). Also I ran the MAP segmentation algorithm on the BTR70 transport and BMP2 tank predicted and measured imagery at the same spacing in azimuth and the same depression angle.

To compare the human, MSTAR, and MAP segmentations I chose to use a few simple techniques, two based on the areas of the target and shadow regions, and one on vehicle orientation as obtained from the target region. The orientation method involved estimating a two-dimensional covariance from the x-y locations of the target pixels and then finding the direction of the principal eigenvector of that covariance. This method has many flaws, but it is adequate for a simple comparison. Of course, there is also a 180° angular ambiguity in the estimate. Table 3 shows the standard deviations of the orientation estimates. I

Orient. Diff. from true		Human	MSTAR	MAP
Predicted	s.dev.	6.94	6.50	8.08
Measured	s.dev.	9.84	14.35	12.94

Table 3: Comparison of Orientation Estimates

obtained these by subtracting the mean, assumed to be the true angle since truth was known, and obtaining the square root of the variance of the new, zero mean orientation variable. Clearly, the human segmentation wins. While the MSTAR predicted segmentation clearly has less variability, it also has an unfair advantage because it is based on obtaining the "true" segmentation from the physical model. Note that MSTAR does worst on the measured imagery.

The first area-based comparison compares MSTAR to MAP based on the number of pixels in each region differing from the human. These results are displayed in Table 4. MSTAR consistently creates larger

Area Difference from Human			MSTAR	MAP
Predicted	Shadow	mean	37.6	-32.2
Predicted	Shadow	s.dev.	56.9	44.0
Predicted	Target	mean	78.8	-87.2
Predicted	Target	s.dev.	73.0	96.2
Measured	Shadow	mean	60.2	-52.3
Measured	Shadow	s.dev.	88.6	109.2
Measured	Target	mean	43.5	-79.4
Measured	Target	s.dev.	97.7	94.8

Table 4: MAP and MSTAR Area Comparison to Human (No. of pixels)

regions than a human, while MAP creates smaller regions. MAP also appears to have more variability than MSTAR. However, some of these results may be suspect, since on close inspection, the MSTAR predicted segmentations do not appear to be from the same models as used by Predict Lite.

The last comparison is based on the differences between the predicted areas and the measured areas for each segmentation region. Table 5 displays these results. It appears that the human and the MAP

Area Difference		Human	MSTAR	MAP
Shadow	mean	-39.4	-107.7	6.7
Shadow	s.dev.	136.8	91.4	159.5
Target	mean	-31.7	45.6	-47.7
Target	s.dev.	109.3	96.4	108.3

Table 5: Difference Between Predicted and Measured Areas

segmentations appear to have a much larger amount of variability. Again, however, this may have more to do with the difficulties of using Predict Lite than the efforts of the segmenters.

5 Conclusions

Without much effort spent on optimizing the MAP algorithm, I have achieved results that are reasonably comparable to the MSTAR program and human segmentation. With some effort the MAP algorithm should feasibly beat MSTAR on the quality of the segmentations. Particularly, some effort to redesign the a priori model could lead to large improvements, for example, by extending the model to include all singleton cliques (an 8 nearest neighborhood). Additionally, from this experience I feel that penalizing target falling downrange of shadow is an error. Only background between target and shadow should be penalized. Also, a MRF observation model could also improve segmentations.

6 Acknowledgments

I would like to thank Phil Douville for his support as my focal point for this program, Ben Booso for his assistance with the MSTAR segmentations, Greg Power and Doug Smith for their help with the human segmentations, and Lou Tamborino and Vince Velten for their helpful advice.

I would like to also thank AFOSR for supporting this research under the Summer Graduate Student Research Program.

References

- [1] G. Winkler, *Image Analysis, Random Fields, and Dynamic Monte Carlo Methods: a Mathematical Introduction*, Springer-Verlag, New York, (1995)
- [2] S.Z. Li, *Markov Random Field Modeling in Computer Vision*, Springer, New York, (1995)

- [3] S. Geman, D. Geman, "Stochastic Relaxation, Gibbs Distributions, and the Bayesian Restoration of Images", IEEE Transactions on Pattern Analysis and Machine Intelligence, v PAMI-6 no 6, pp721-741, 1984

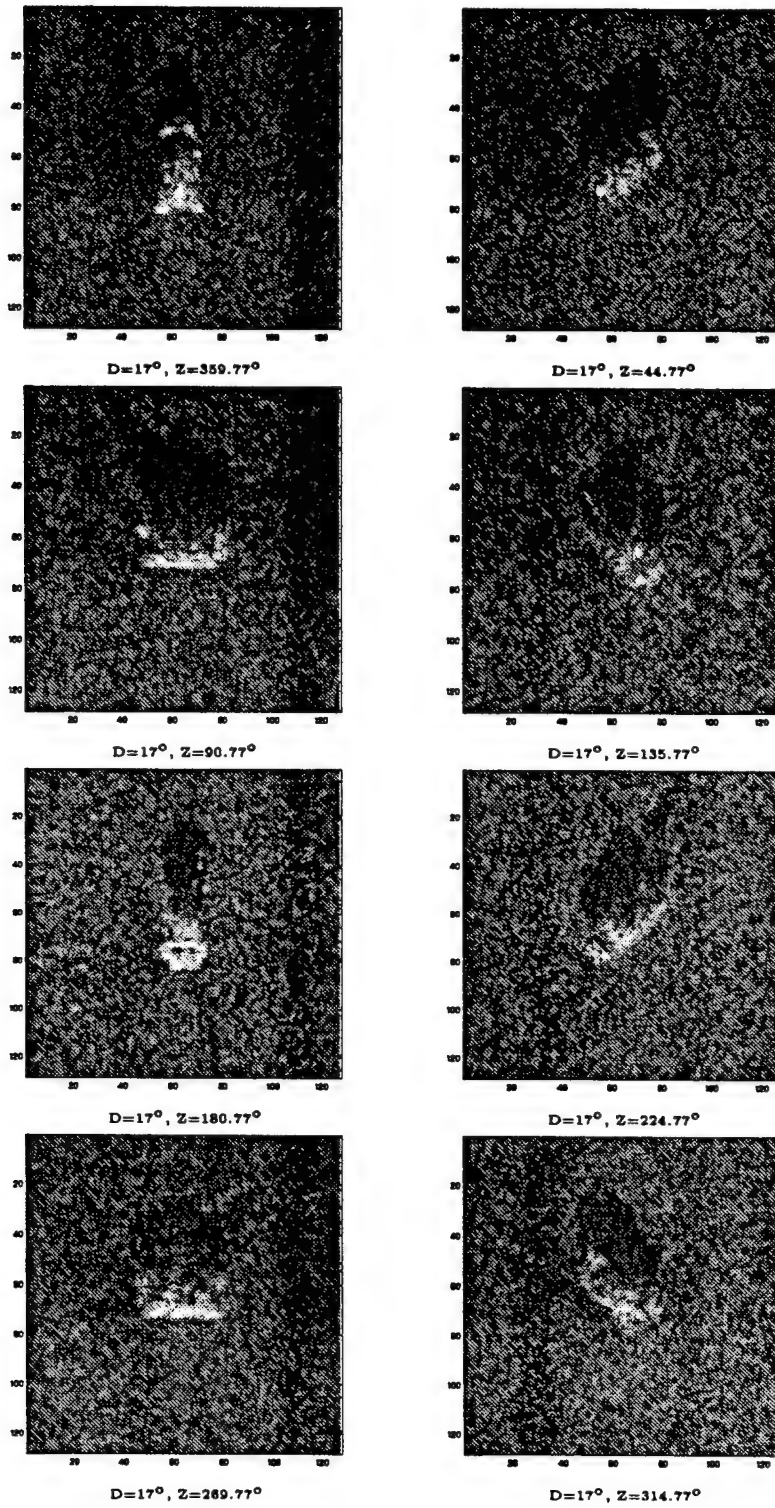


Figure 1: Example Logarithms of T72s from MSTAR's Public Data

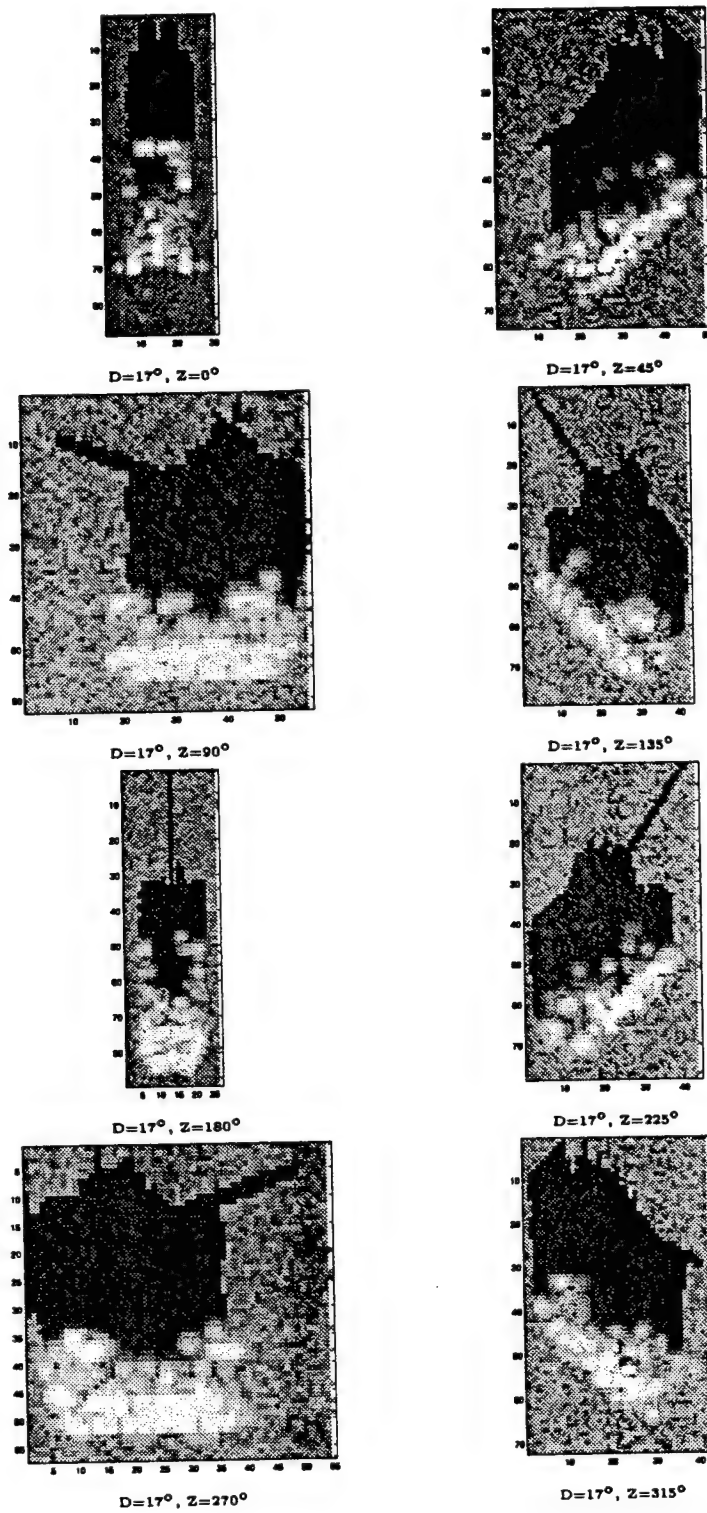


Figure 2: Example Logarithms of T72s from MSTAR's Predict Lite

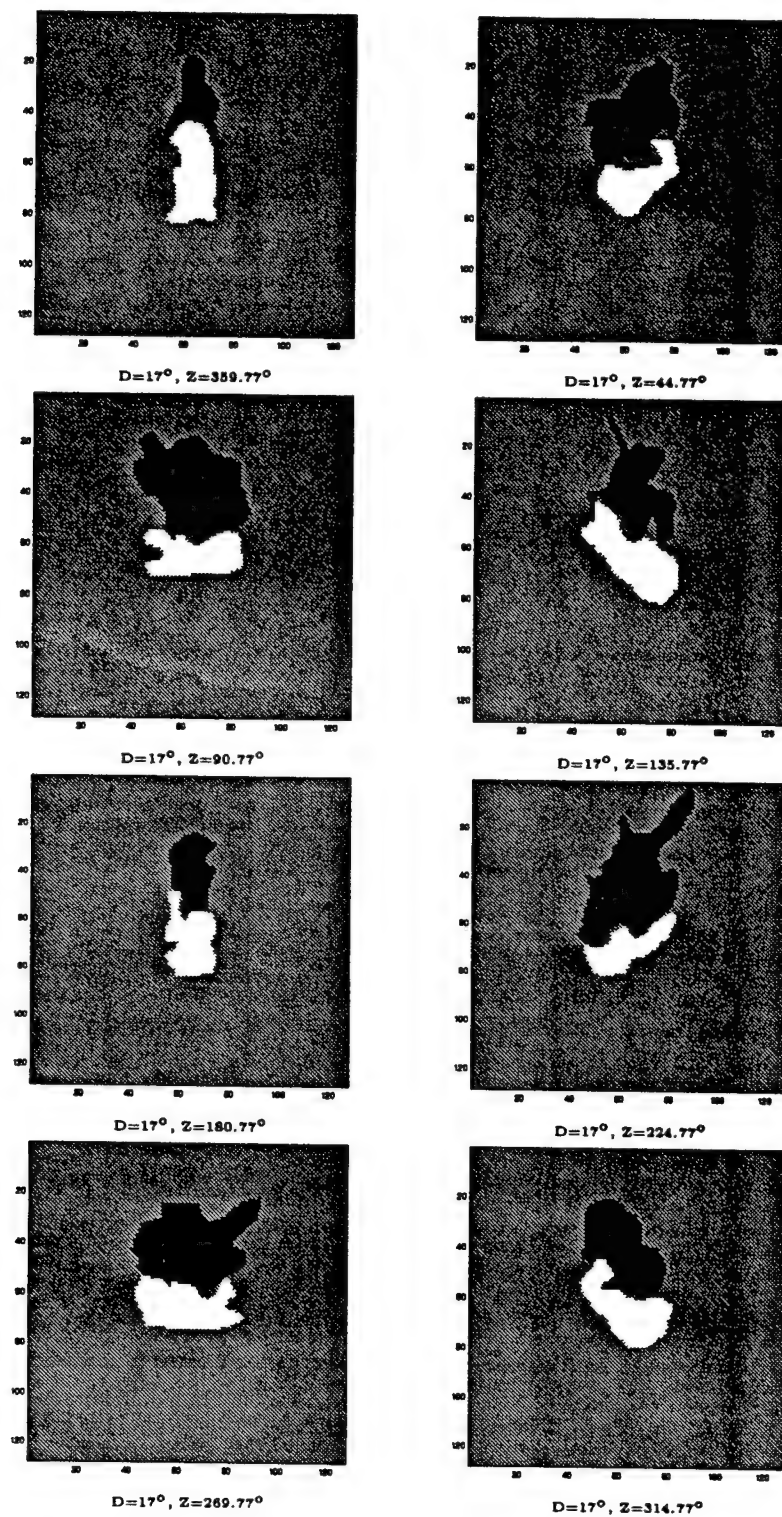


Figure 3: Example Human Segmentations of MSTAR Public Data

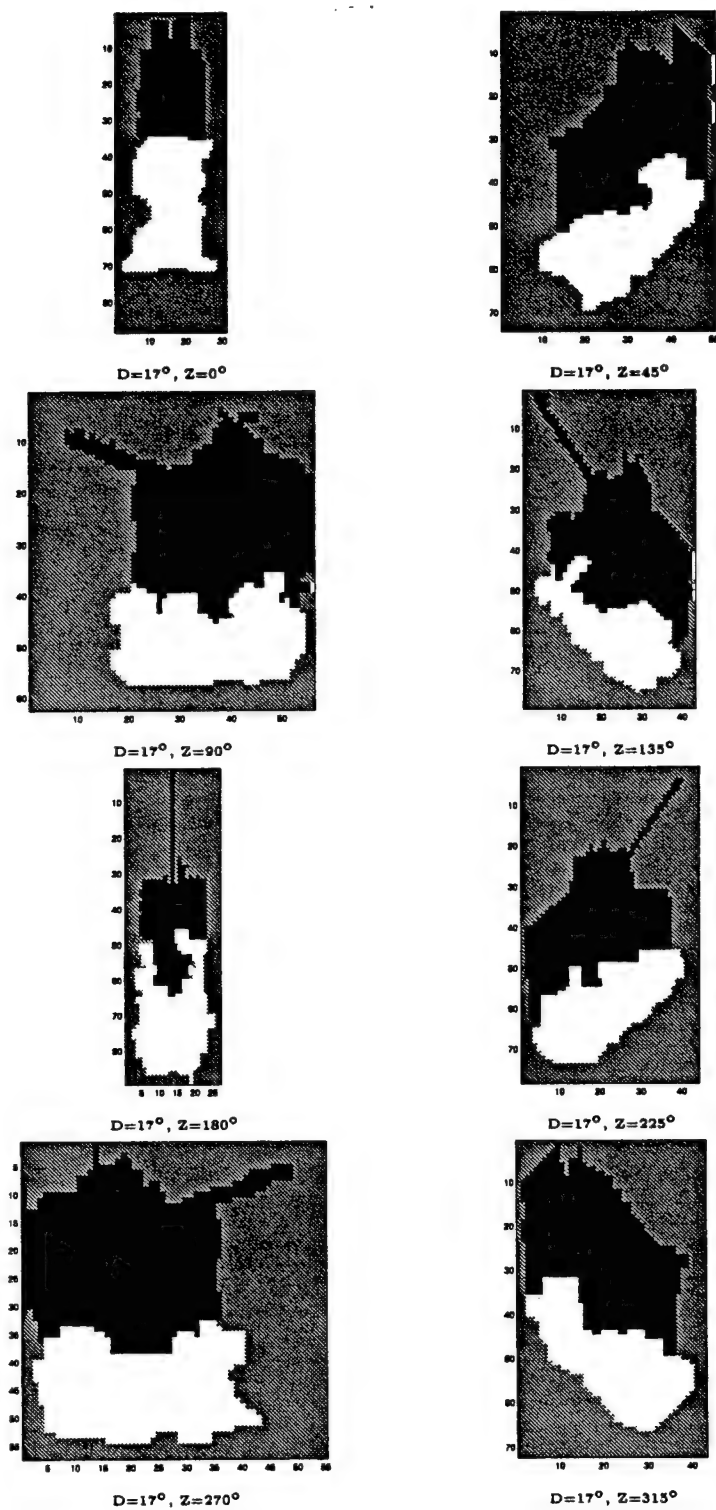


Figure 4: Example Human Segmentations of Predict Lite Imagery

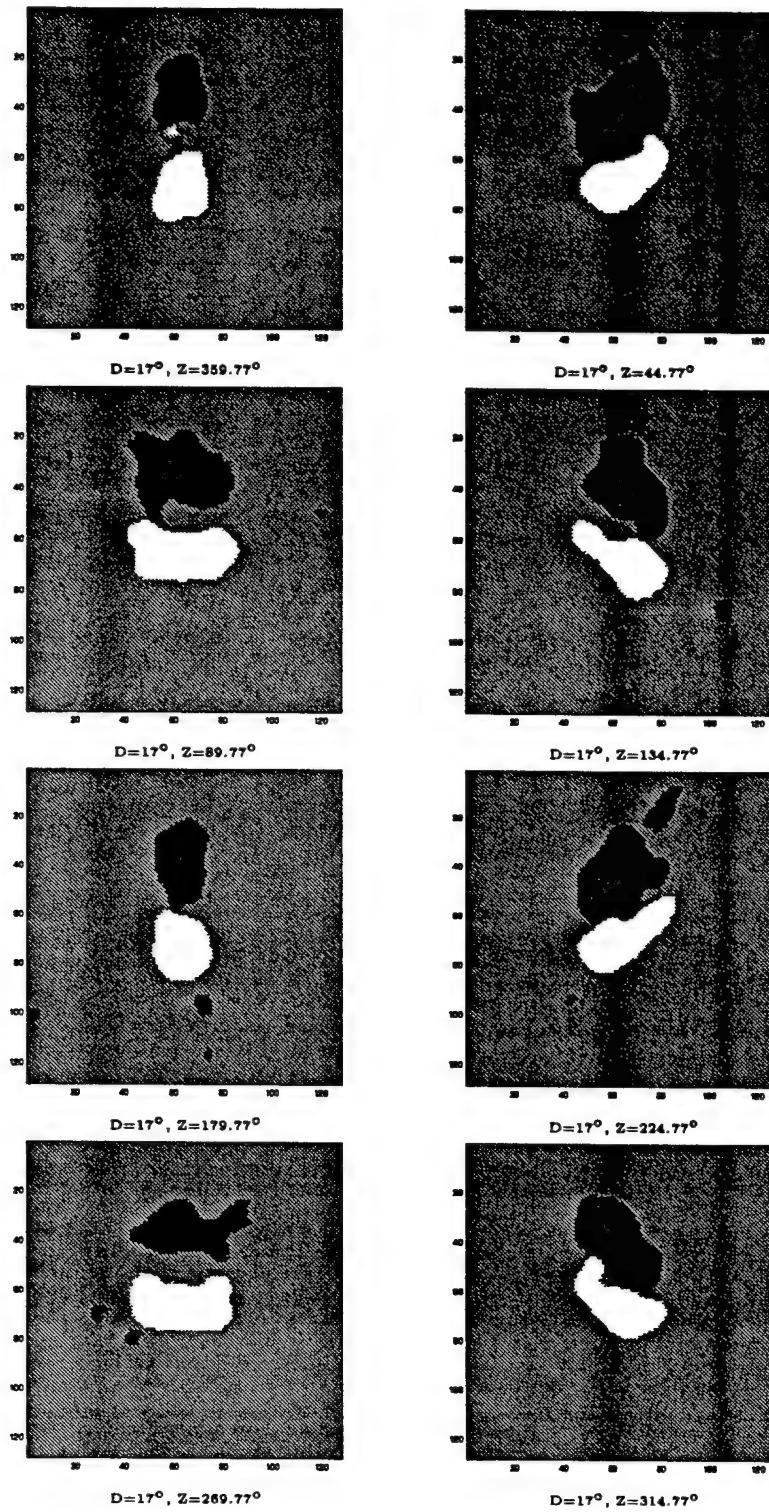


Figure 5: Example MSTAR Segmentations of Public Data

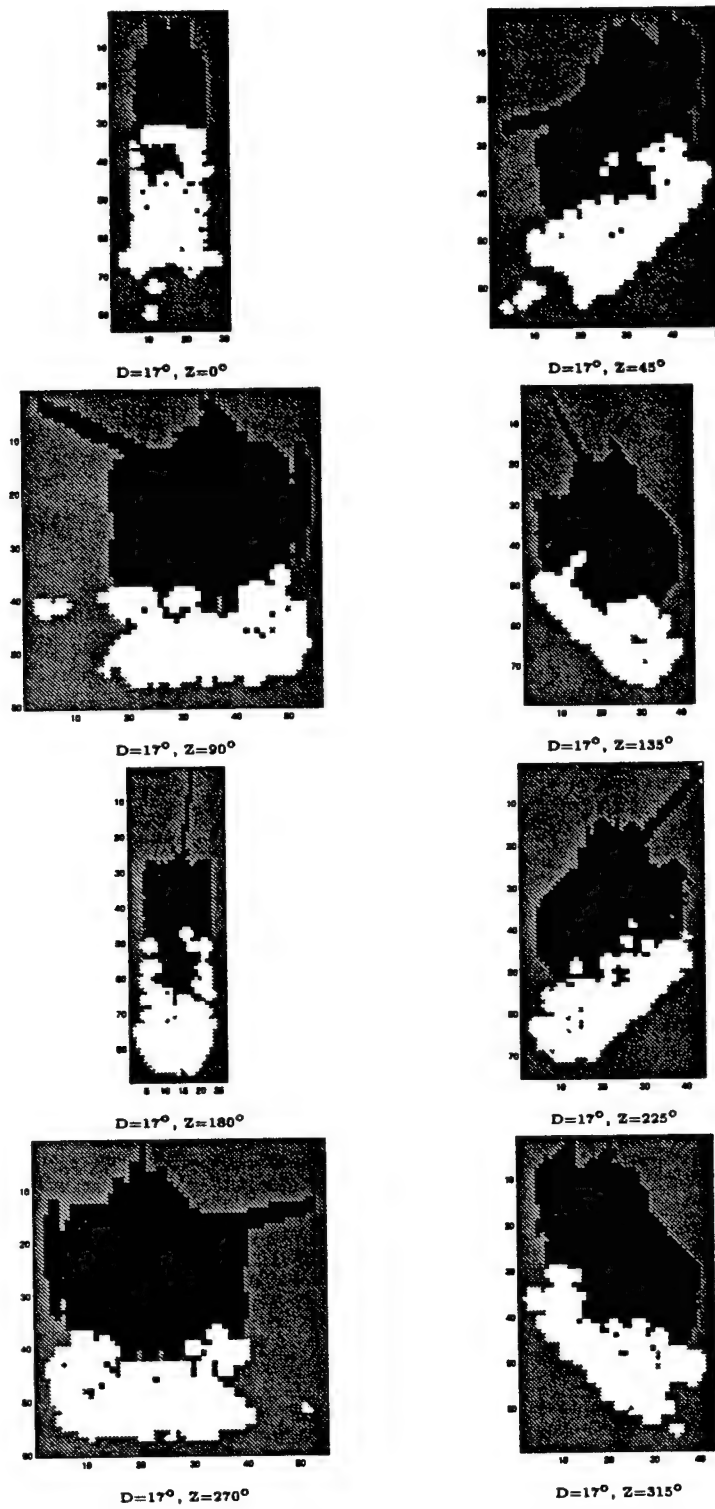


Figure 6: Example Predicted MSTAR Segmentations

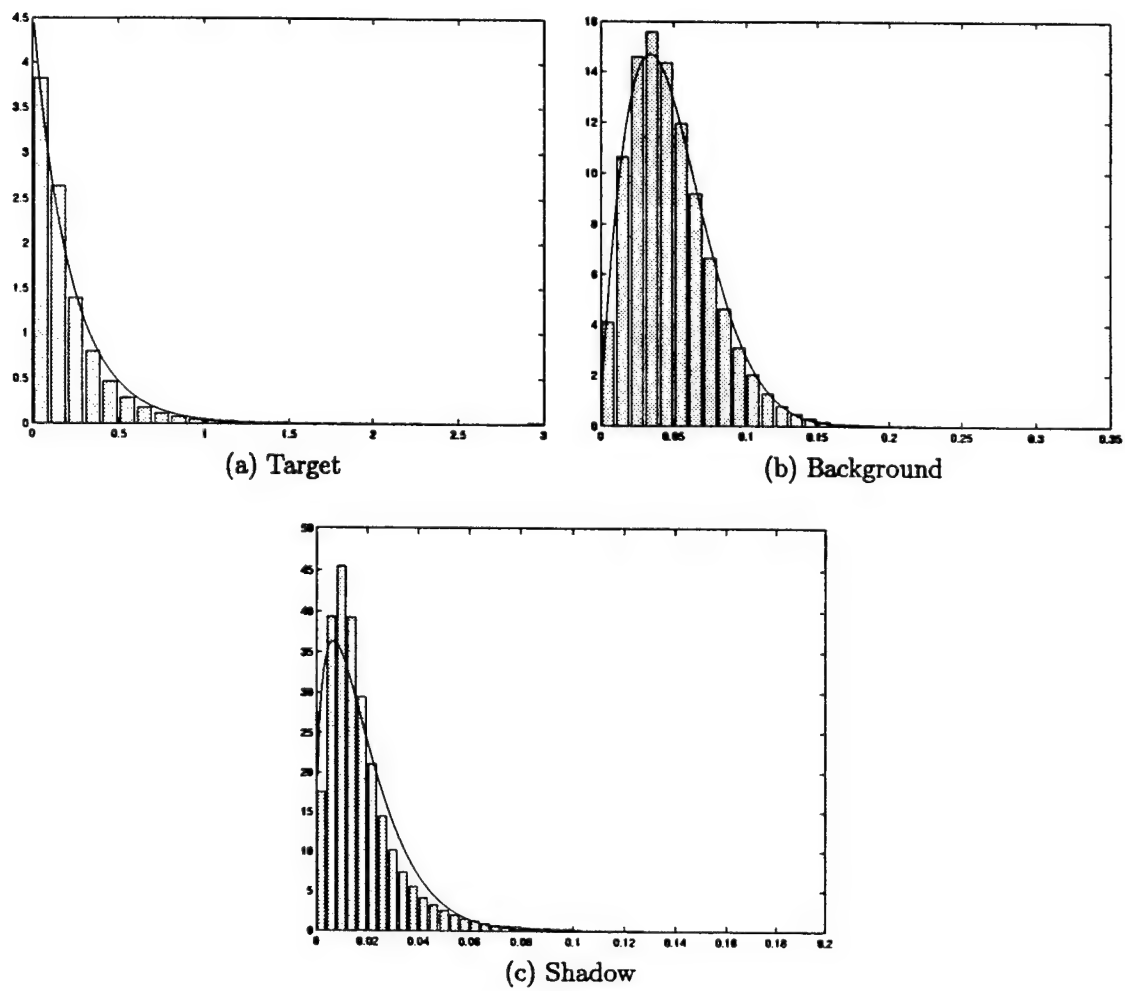


Figure 7: Weibull Fit to Measured Data (Probability vs. Intensity)

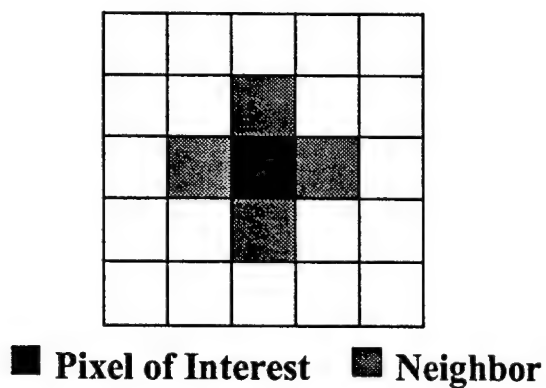


Figure 8: Neighborhood Structure of the Prior Model

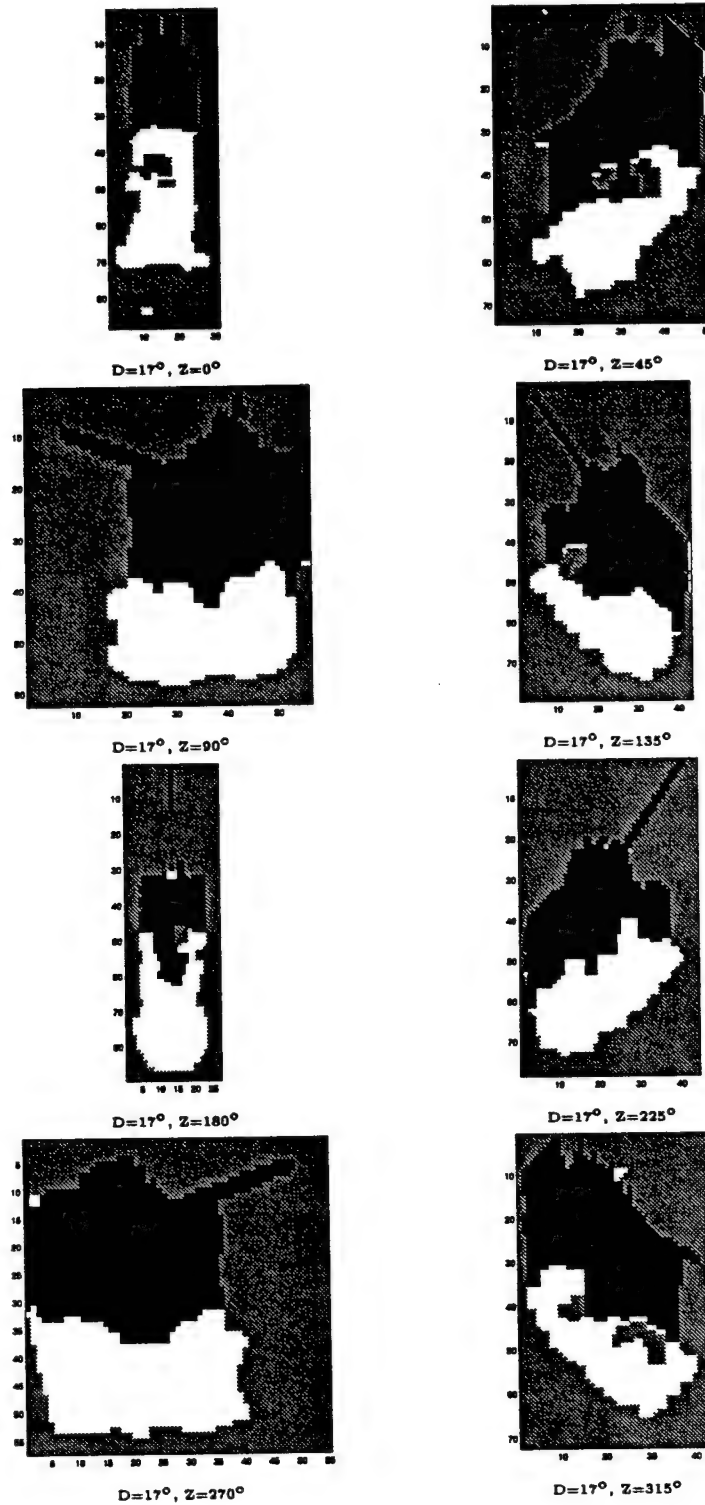


Figure 9: MAP Segmentations of predicted T72s, 17° dep

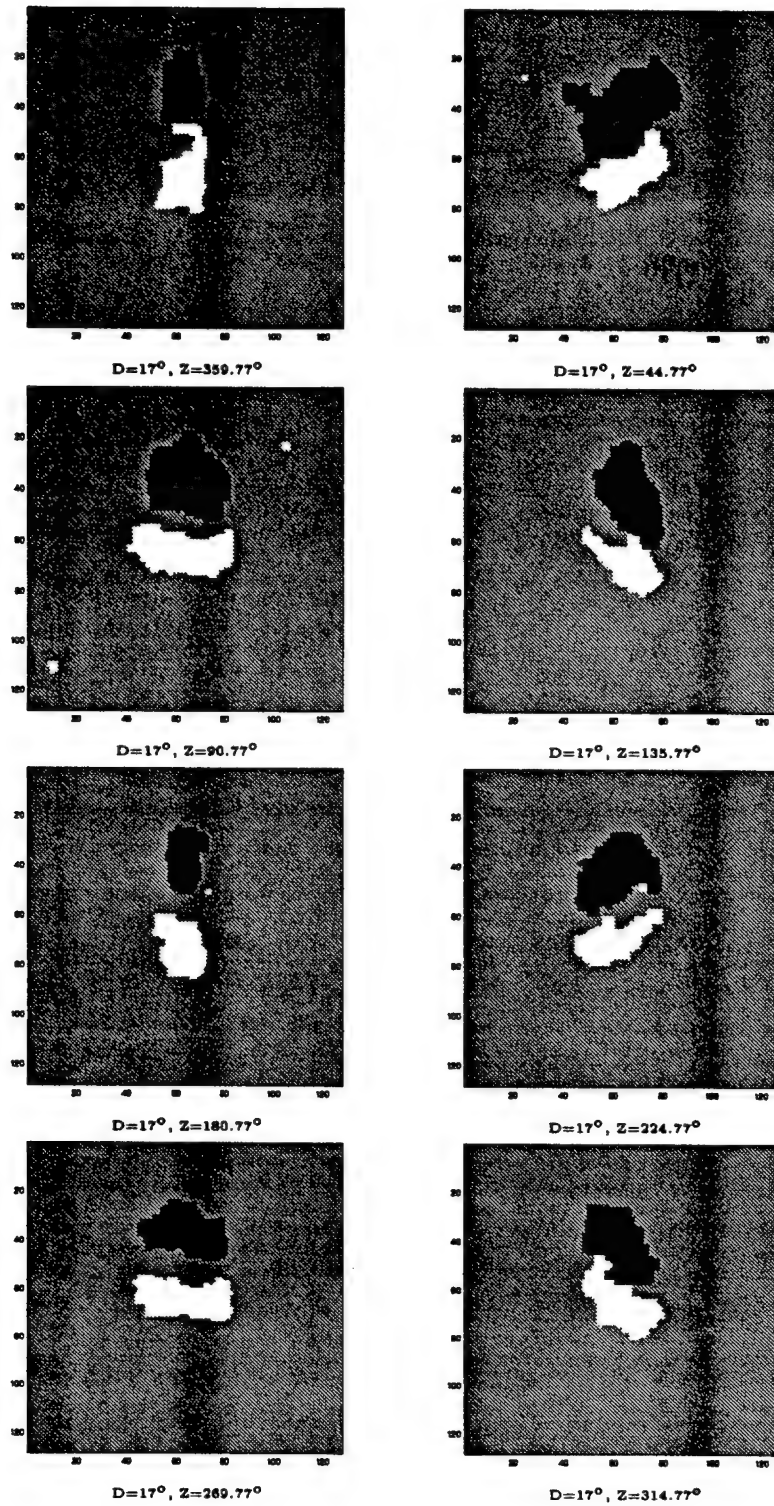


Figure 10: MAP Segmentations of measured T72s, 17° dep

Parameter Estimation for the Tailless Advanced Fighter Aircraft (TAFA)

Jerry M. Wohletz
Research Assistant
Aeronautics and Astronautics Department

Massachusetts Institute of Technology
77 Massachusetts Avenue
Cambridge, MA 02139

Final Report for:
Summer Graduate Research Program
Wright Research Site

Sponsored by:
Air Force Office of Scientific Research
Bolling Air Force Base, DC

And

Wright Research Site

August 1998

Parameter Estimation for the Tailless Advanced Fighter Aircraft (TAFA)

Jerry M. Wohletz
Research Assistant
Aeronautics and Astronautics Department
Massachusetts Institute of Technology

ABSTRACT

The goal of this summer research was to investigate the implementation of an online parameter estimation methodology for the Tailless Advanced Fighter Aircraft (TAFA). It was determined that the current in-house parameter estimation methodology for reconfigurable flight controls will require modifications in order to obtain reasonable estimates of the longitudinal stability derivative. The crux of the issue is that the longitudinal stability derivative varies rapidly with angle of attack, probably due to the canard influence, which is a unique characteristic of this aircraft. Furthermore, the control law design tends to reduce the stability derivative signature. A proposed modification would use the control law design canard preference to produce an equivalent pitch acceleration model for identification. The focus audience of this report is Air Force personnel who will continue to pursue this research.

Parameter Estimation for the Tailless Advanced Fighter Aircraft (TAFA)

Jerry M. Wohletz

1.0 INTRODUCTION

The objective of parameter estimation for reconfigurable flight control is to provide unbiased estimates of the aircraft stability and control derivatives with and without impairment. A parameter estimation methodology, which has been successfully applied to several flight vehicles, has been developed at the Air Force Research Lab. The foundation of this technique is based on minimum-variance parameter estimation, [1]. Static system identification is well suited for aircraft reconfiguration because aircraft states and state rates are measured. The underlying theory was then expanded to online estimation of stability and control derivatives, [2]. The fundamentals of obtaining real-time identification of aircraft parameters were addressed by exploiting the flight mechanics. The estimation is formulated as a constrained linear regression that is computed in either batch or recursively. The constraints to the linear regression can include relationships between stability and control derivatives, a priori estimates of derivatives, or restrictions on the rate of change of the estimate. This stage of the methodology was simulated for the pitch plane dynamics on the F-16 VISTA.

The next advancement to the methodology was the regularization techniques for real-time identification of aircraft parameters, [3]. The fundamentals of closed-loop identification for a moderate failure with tightly regulated control were addressed. Tight control attenuates the additional excitation caused by the failure, which is beneficial for identification. Also, the control is often a linear combination of the states, which results in biased estimates. To address this problem, singular value decomposition is used to reparameterize the model, and a priori data is used to

generate estimates of the original parameter set. This stage of the methodology was demonstrated on the F-16 VISTA simulation, and included both longitudinal and lateral-directional dynamics. Additionally, a version of this methodology was flight tested on the F-16 VISTA, [4].

The method has now been extended to aircraft with distributed control effectors, [5]. This advancement addresses the relationship between the system identification and control allocation modules. Traditional control allocation algorithms gang control surfaces while not exciting others; as a result, the control surfaces are correlated, which result in poor estimates of the control derivatives. This problem is circumvented by introducing additional excitation into the control surfaces without introducing residual motion to the aircraft. An additional advancement to the system identification algorithm is the separation of estimation tasks into two separate stages. The first stage estimates the stability derivative and a generalized loop gain for the purpose of rapid stabilization after the onset of failure. The second stage estimates the individual control effectors which is then used in the control allocation to optimize a performance metric. This version of the estimation methodology was demonstrated on the Innovative Control Effectors (ICE) tailless aircraft. This aircraft is a delta wing configuration with eleven individual control effectors.

Expanding on the previous effort, the objective of this summer research was to adapt the parameter estimation methodology to the Tailless Advanced Fighter Aircraft (TAFA) and implement it in the TAFA simulation. Section 2.0 details the parameter estimation methodology. Section 3.0 presents the results of the implementation, and section 4.0 provides conclusions. Due to report size limitations, all of the figures are contained in Appendix A along with short description of their relevance. Finally, Appendix B contains a brief description of the location of the script file and the modification required for this study.

2.0 METHODOLOGY

The purpose of this section is to outline the procedures of the parameter estimation algorithm that has been refined for aircraft with redundant control effectors. The procedures presented are for the first stage of the estimation; the generalized loop gain and the stability derivative are identified. Furthermore, only the pitch plane dynamics are considered for this initial study. The information contained herein was obtained from [1,2,3,5].

2.1 Aircraft Model

The modeled pitch acceleration equation of motion in body/stability axis with nonlinear kinematics and linear aerodynamics is as follows:

$$\dot{Q} = (I_{zz} - I_{xx})/I_{yy} PR + I_{xz}/I_{yy} (R^2 - P^2) + M_o + M_\alpha \alpha + M_q q + K \bar{M}_\delta \bar{\delta} + V$$

where: $\bar{M}_\delta \bar{\delta} = M_{\delta_{ptv}} \delta_{ptv} + M_{\delta_{tef}} \delta_{tef} + M_{\delta_{cnd}} \delta_{cnd} + M_{\delta_{ail}} \delta_{ail}$

For the 1st stage, the angle of attack derivative, M_α , and the loop gain, K , will be estimated. It is implied that the pitch rate derivative, angle of attack, body axis rates, and control surface deflections are measured. Furthermore, moments of inertia, the pitch-dampening derivative, and the control derivative are assumed known a priori. Modeling error, V , should be approximately represented by white noise if the linear aerodynamics is a good approximation to the nonlinear aerodynamics over the estimation interval. If the modeling error is colored, estimates may be biased.

2.2 Measurement Regressor Equation

The classical linear regression problem is:

$$Z = H\Theta + V, \quad V = \eta(0, R), \quad R > 0$$

For this particular problem, the measurement vector element at each sample time is:

$$Z' = [\dot{Q} - (I_{zz} - I_{xx})/I_{yy} PR - I_{xz}/I_{yy} (R^2 - P^2) - M_q q]$$

The regressor matrix row at each sample time is:

$$H(i,:) = [\alpha_i \quad \overline{M_\delta^T} \delta_i]$$

The parameters to be estimated are:

$$\Theta = [M_\alpha \quad K]^T$$

Note, for this particular formation, the zero lift moment, M_{α_0} , or equation intercept is not represented. The intercept is eliminated by removing the mean from the measurement vector and each of the columns of the regressor matrix. Thus,

$$Z = Z' - E\{Z'\}$$

$$H(:,i) = H'(:,i) - E\{H'(:,i)\} \quad i: 1,2$$

2.3 Stochastic Constraint: A Priori Data

The stochastic constraints are represented by:

$$b = N \Theta + W, \quad W = \eta(0, Q), \quad Q > 0$$

For this particular problem, the a priori information is used as a stochastic constraint. Thus, N is an identity matrix, b is the a priori estimates, and Q is a diagonal covariance matrix which represents the uncertainty in the relationship.

2.4 Classical Minimum Variance Parameter Estimation

The minimum variance parameter estimation is well documented in [1]. The estimate is:

$$\Theta_{mv} = (H^T R^{-1} H)^{-1} H^T R^{-1} Z$$

and the estimation error covariance is:

$$P_{mv} = (H^T R^{-1} H)^{-1}$$

An important property of this formulation is that because the multiple measurements are obtained by the same sensors at several time versus by different sensors at a single time, the covariance at each time is the same; thus, the R matrix is a scalar multiple of an identity matrix.

$$R = r I$$

This results in the minimum variance being independent of the measurement error covariance! This property is a key feature of the static system identification. Thus,

$$\Theta_{mv} = (H^T H)^{-1} H^T Z$$

$$P_{mv} = r (H^T H)^{-1}$$

The estimation procedure is as follows:

1. Calculate the minimum variance estimate, Θ_{mv} .
2. Using the new estimate, calculate the measurement error covariance:

$$\tilde{Z} = Z - H\Theta_{mv} \quad (\text{Referred to as return difference})$$

$$r = (\tilde{Z}^T \tilde{Z}) / (l - n)$$

3. Using the measurement error covariance, calculate the estimation error covariance, P_{mv} .

Given the minimum variance estimation, the stochastic constraint can be used as an additional parameter to obtain an update estimate or vice versa. This formulation follows the sequential minimum variance estimation in [1]. Here, the minimum variance estimation is updated using a priori data as an additional measurement.

A Priori Data: $\Theta_{apriori}, Q$

Minimum Variance Data: Θ_{mv}, P_{mv}

$$\Theta = \Theta_{mv} + P_{mv} N^T (N P_{mv} N^T + Q)^{-1} (\Theta_{apriori} - N \Theta_{mv})$$

$$P = [I - P_{mv} N^T (N P_{mv} N^T + Q)^{-1} N] P_{mv}$$

2.5 Removing Collinearity from Regressor Matrix

If the regressor matrix has a high condition number, which implies that the columns are collinear, the parameter estimates will be biased. Singular value decomposition is used to reduce the parameter set, which eliminates the high condition number.

$$H = U \Sigma V^T$$

If H is not full rank, the Σ will not be full rank. Collinearity is represented by the condition number of the matrix; thus, to remove the collinearity, small singular values must be removed. Engineering judgment must be used to decide what constitutes small. For the F-16 Vista, a singular value ratio or condition number of 250 was

considered to be a decorrelated matrix; however, a different ratio may be preferred depending on the application. Removing the small singular values and the accompanying columns of U and rows of V^T , the regressor matrix can be expressed as follows:

$$H \cong U_1 \Sigma_1 V_1^T$$

Define the following,

$$H_1 = U_1$$

$$K = \Sigma_1 V_1^T$$

$$\Theta_1 = K \Theta \Rightarrow \text{Reduced parameter formulation.}$$

As illustrated above, the minimum variance estimate for the reduced parameter is as follows:

$$\Theta_{1mv} = (H_1^T H_1)^{-1} H_1^T Z$$

$$P_{1mv} = r_1 (H_1^T H_1)^{-1}$$

where,

$$\tilde{Z}_1 = Z - H_1 \Theta_{1mv} \quad (\text{Referred to as return difference})$$

$$r_1 = (\tilde{Z}_1^T \tilde{Z}_1) / (1 - n)$$

At this point, we have an estimate of the reduced parameter along with a linear relationship with the desired parameter.

$$\Theta_{1mv} = K \Theta + V, \quad V = \eta(0, P_1), \quad P_1 > 0$$

To solve for θ , we could treat this equation as a linear regression; however, K is a flat matrix. Instead, we will treat this equation as a stochastic constraint on the a priori data. Thus, a priori data will represent an initial guess that is updated by the stochastic constraint in a sequential formation. The above equation should be viewed as an additional measurement.

Given the a priori data, θ_p and covariance Q , obtain an update to the a priori data using the measurement based reduced parameter estimate, $\Theta_{1_{mv}} = K \Theta + V$. From the sequential formulation above, the update estimate is obtained as follows:

$$\begin{aligned}\Theta &= \Theta_p + Q K^T (K Q K^T + P1)^{-1} (\Theta_{1_{mv}} - K \Theta_p) \\ P &= [I - Q K^T (K Q K^T + P1)^{-1} K] Q\end{aligned}$$

Important observations:

1. For $\theta \in \mathbb{R}^N$ and $\theta_1 \in \mathbb{R}^M$, if $M < N$ then $N-M$ parameters will be dominated by a priori data.
2. If the uncertainty in the a priori data is low, small Q , then estimates will be a priori data. As a result, the parameters will not change due to failures.
3. If the reduced parameter minimum variance covariance is large, the estimate will be dominated by a prior data.

3.0 RESULTS

A parameter estimation module was incorporated into the TAFA simulation. The TAFA configuration is a clipped delta wing with a canard, which differs from previous configurations. The system identification module was added to the baseline control law known as the Versatile Control Augmentation System. The module is currently setup in an open loop fashion; thus, the estimates are not feeding the feedback/feedforward augmentation or the control allocation modules. A single flight condition was chosen for evaluation: Mach=0.5, altitude=10,000 ft. The maneuver

performed is a simple pitch doublet. This is an idealized evaluation condition for parameter estimation because no sensor noise is introduced and the modeling error is very small. Note, due to report size limitations, all figures that are relevant to this section have been relegated to Appendix A. Furthermore, a brief description of the script files and modifications to the baseline TAFA simulation is contained in Appendix B.

The initial results of the system identification were mixed. The generalized loop gain was quite accurately estimated. If the aircraft is unfailed, the gain K should be very close to the identity matrix, which it is. However, the stability derivative had considerable bias and was variable compared to the truth-value. Based on these results, an extensive investigation was conducted into the potential source of the bias:

1. Persistency of Excitation,
2. Regressor Collinearity,
3. Nonwhite Modeling Error,
4. Parameter Variation, and
5. Regressor Column Scaling.

Because sensor noise was not included in the evaluation condition, it is obviously not a source of bias.

3.1 Persistency of Excitation

If the sensor measurements used in the regression does not have sufficient activity, the estimates will be biased and possibly diverge. The activity of the signal is quantified in terms of the signal's rms. To prevent this, rms thresholds are used to freeze the system identification for low excitation. For the current algorithm, the Z vector was used to measure the level of excitation; however, this was found to be inadequate for this aircraft. For certain situations, it was observed that while the Z vector had sufficient rms, the α column of the regressor matrix had a near zero rms. Thus, the system

identification needs to be frozen if the Z vector or if any of the individual columns of the regressor matrix fall below an acceptable rms threshold. Modifications to the estimation algorithm were performed; however, biased stability derivatives persisted.

3.2 Regressor Collinearity

Regressor collinearity leads to biased results. Thus, to circumvent this problem, singular value decomposition is used to monitor and reduce the collinearity of the regressor matrix if needed. The primary indicator of collinearity is the condition number of the regressor matrix. For the particular maneuver investigated, the condition number remained well below 10; thus, collinearity does not appear to be the source of bias.

3.3 Modeling Error

It is assumed that the equation error in the regressor system is zero mean white noise. If this is not the case, then estimates may be biased. The modeling error was checked using two separately generated a priori models. Though these models have different traits — each model has unique deficiencies — the modeling error using the a priori models is small and is approximately white noise. As a result, it is believed that the modeling error is not the source of the biased estimates.

3.4 Parameter Variation

If the parameter being estimated varies in the regressor window, the parameter estimate will be an average. This situation is referred to as mixed window estimation, and will always occur when a derivative being estimated changes in a window. Viewing the a priori data, one model suggests that the true stability derivative is constant with angle of attack and the other model has the derivative varying significantly with angle of attack. The question posed is which a priori model is more

accurate. The a priori model with derivatives that vary significantly with angle of attack, which is based on differentiation of wind tunnel data, is believed to be the more accurate model. However, the model with constant derivatives has the lower return difference. One possible explanation for these variations in parameters, which are normally constant versus angle of attack, is attributed to the fact that the canard's trailing vortexes are interacting with the flow field over the wing. Thus, parameter variation in the data window is a source of biased estimates. One solution to the variation problem is to reduce the size of the window. This was accomplished, and it was shown that the estimate does get better for smaller window sizes. For a window with 5 data points, the estimate, while not excellent, was reasonable. However, such a small window size is not advisable with realistic sources of errors.

3.5 Regressor Column Scaling

Naturally, if one column is large when compare to another column in the regressor matrix, the parameter associated with the larger column will impact the minimum variance objective function more than the other parameter. This can lead to considerable bias and variations in the parameter associated with the smaller column. For this application, it was found that the Z vector and the $M_\delta \delta$ vector in the regressor matrix are nearly two orders of magnitude greater than the α vector in the regressor matrix. This attribute has been traced back to the control design philosophy. For this aircraft, the canard is used as the primary longitudinal trim device. This is represented mathematically as:

$$0 \cong M_o(\alpha) + M_\alpha(\alpha) \alpha + M_{\delta_{cnd}}(\alpha) \delta_{cnd}$$

When the above relationship holds, the pitch acceleration equation reduces to:

$$q_{dot} \cong M_q(\alpha) q + \sum M_{\delta_i}(\alpha) \delta_i$$

As a result, the pitch acceleration is dominated by the control power excluding the canards, and regressor column scaling is a potential source of estimation bias. One solution is not to estimate the M_α α contribution when it is small.

3.6 Summary of Results

The generalized loop gain was quickly estimated; however, the stability derivative had considerable bias. At this point, the sources of the biased stability derivative estimates have been attributed to parameter variation in the data window and inappropriate scaling of the regression matrix columns. The design parameters of the system identification algorithm were modified. The window size was reduced to operationally unrealistic sizes, and the control power term was removed from the regressor matrix; however, the resulting estimate of the stability derivative still contained some bias. Based on this analysis, the estimation methodology, used successfully to estimate stability and control derivatives for different aircraft, will require modifications for this application.

3.7 Proposed Modifications

It is proposed that the estimation algorithm should be modified to directly account for the control law design philosophy. Recall that the canard is used as the primary trim device; thus, the no failure static trim equation is:

$$0 \cong M_o^{uf}(\alpha) + M_\alpha^{uf}(\alpha)\alpha + M_{\delta cnd}^{uf}(\alpha)\delta cnd^{pref}$$

which implies

$$\delta cnd^{pref} = -\frac{M_\alpha^{uf}}{M_{\delta cnd}^{uf}}\alpha - \frac{M_o^{uf}}{M_{\delta cnd}^{uf}}$$

The actual canard deflection can be represented as follows:

$$\delta_{cnd} = \delta_{cnd}^{pref} + \Delta\delta_{cnd}$$

The $\Delta\delta_{cnd}$ represents a perturbation to the preference command, and could result from either a fixed or floating failure or canard excitation. Expanding the modeled pitch acceleration equation to include the canard preference:

$$\dot{Q} = \left(M_o - \frac{M_o^{uf}}{M_{\delta_{cnd}}^{uf}} M_{\delta_{cnd}} \right) + \left(M_\alpha - \frac{M_\alpha^{uf}}{M_{\delta_{cnd}}^{uf}} M_{\delta_{cnd}} \right) \alpha + M_{\delta_{cnd}} \Delta\delta_{cnd} + M_q q + \tilde{K} \tilde{M}_\delta \tilde{\delta} + V$$

$$\text{where: } \tilde{M}_\delta \tilde{\delta} = M_{\delta_{ptv}} \delta_{ptv} + M_{\delta_{tef}} \delta_{tef} + M_{\delta_{ail}} \delta_{ail}$$

Define:

$$M_\alpha^{equiv} = \left(M_\alpha - \frac{M_\alpha^{uf}}{M_{\delta_{cnd}}^{uf}} M_{\delta_{cnd}} \right)$$

$$M_o^{equiv} = \left(M_o - \frac{M_o^{uf}}{M_{\delta_{cnd}}^{uf}} M_{\delta_{cnd}} \right)$$

Thus, for an unfailed aircraft, the equivalent dimensional derivatives are zero. For failures that do not affect the lifting surface area or the canards, this relationship should still hold. However, for failures to the lifting surface or the canard, the equivalent dimensional derivatives will not longer be equal to zero.

For this situations when the equivalent derivatives are no longer zero, there will be a dynamic inversion error because the nominal controller does not account for M_α in the deaugmentation. Thus, two options are available to eliminate the inversion error:

1. change the control law to include M_α^{equiv} in the deaugmentation, or
2. change the canard deflection preference to force $M_\alpha^{equiv} \rightarrow 0$.

The recommend option is to change the canard preference to force the equivalent dimensional derivatives to zero. This approach will work until the canard becomes saturate, and then, the pitch acceleration due to angle of attack must be used in the deaugmentation to reduce the inversion error further.

To update the preference, the canard control power derivative needs to be estimated. This can be accomplished by adding the perturbation canard deflection to the regressor matrix. With the canard control power derivative identified, the equivalent dimensional derivatives can be used to determine the new pitch acceleration due to angle of attack and the pitch acceleration intercept:

$$\begin{aligned} M_{\alpha}^f &= \left(M_{\alpha}^{\text{equiv}} + \frac{M_{\alpha}^{\text{uf}}}{M_{\delta\text{cnd}}^{\text{uf}}} M_{\delta\text{cnd}}^f \right) \\ M_o^f &= \left(M_o^{\text{equiv}} + \frac{M_o^{\text{uf}}}{M_{\delta\text{cnd}}^{\text{uf}}} M_{\delta\text{cnd}}^f \right) \end{aligned}$$

Finally, the new canard deflection preference is as follows:

$$\delta\text{cnd}^{\text{fpref}} = -\frac{M_{\alpha}^f}{M_{\delta\text{cnd}}^f} \alpha - \frac{M_o^f}{M_{\delta\text{cnd}}^f}$$

4.0 CONCLUSIONS

The goal of the summer research was to investigate the implementation issues associated with incorporating the in-house parameter estimation module into the TAFa simulation. For this investigation, only the pitch plane dynamics were considered. The results of the parameter estimation revealed that the proposed methodology did produce acceptable results of the generalized pitch loop gain, which is the major determination of stability and performance, but produced unacceptable estimates of the pitch stability derivative. The sources of the biased stability derivative estimates have been attributed to

parameter variation in the data window and inappropriate scaling of the regression matrix columns. The parameter variation is caused by the pitching moment derivative being nonlinear at small angles of attack, and the regressor scaling problem is attributed to the control law design philosophy. Even after the design parameters of the system identification algorithm were modified, the resulting estimate of the pitch stability derivative still contains some bias. The conclusion drawn from this study is that the estimation methodology needs to be modified to account for the strong interactions between the control law design and the identification performance. A proposed modification would use the control law design canard preference to produce an equivalent pitch acceleration model for identification.

5.0 REFERENCES

1. Mendel, J.M., "Discrete Techniques of Parameter Estimation," Marcel Dekker, Inc., NY, 1973.
2. Chandler, P. R., Pachter, M., and M. Mears, "System Identification of Adaptive and Reconfigurable Control," *Journal of Guidance, Control, and Dynamics*, Vol. 18, No. 3, May-June 1995.
3. Smith, Capt. L., Chandler, P. R., and M. Pachter, "Regulation Techniques for Real-Time Identification of Aircraft Parameters," *ALAA Guidance, Navigation, and Control Conference*, 1997.
4. D. Ward, J. Monaco, R. Barron, R., et al, "Self-Designing Controller: Design Simulation, and Flight-Test Evaluation," Final Tech. Rep. for Air Force Office of Scientific Research, Contract F49620-94-C-0087, Barron Associates, Inc., Nov., 1996.

5. Buffington, J., Chandler, P. R., and M. Pachter, "On-Line System Identification for Aircraft with Distributed Control Effectors," *AIAA Guidance, Navigation, and Control Conference*, 1997.